Impurities and Inhomogeneities in Nanoelectronic Systems

Dissertation

zur Erlangung des Doktorgrades

des Fachbereichs Physik

der Universität Hamburg

vorgelegt von
Tim O. Wehling
aus
Stadthagen

Hamburg
2010

Gutachter der Dissertation	Prof. Dr. Alexander Lichtenstein
	JP Dr. Frank Lechermann
	Prof. Dr. Alexander Mirlin
Gutachter der Disputation	Prof. Dr. Alexander Lichtenstein
	Prof. Dr. Mikhail Katsnelson
Datum der Disputation	11.01.2010
Vorsitzender des Prüfungsausschusses	PD Dr. Alexander Chudnovskiy
Vorsitzender des Promotionsausschusses	Prof. Dr. Jochen Bartels
Dekan der Fakultät für Mathematik, Informatik und Naturwissenschaften	Prof. Dr. Heinrich Graener

Abstract

The research on atomic scale solid state structures has developed into a highly dynamic field that is driven by fundamental questions as well as applications. In this thesis, the electronic properties of different nano scale systems are theoretically investigated and distinct physical effects determining their electronic structure will be encountered.

In the first part, effects of inhomogeneities and impurities in graphene are addressed by means of first-principles theory and analytical models. We give an explanation for an unexpected gap reported in recent scanning tunneling spectroscopy (STS) experiments on graphene. A particular type of electron-phonon coupling is shown to cause huge inelastic contributions in STS on graphene. As graphene exhibits long range ripples, we investigate the electronic properties of corrugated graphene. We show that quenched ripples induce pseudo-magnetic fields and that these can lead to the formation of flat bands near the Fermi level, which are destroyed upon annealing. Being crucial for any application, we then turn to impurity effects in graphene. Different interaction mechanisms of impurities with graphene are introduced and the requirements for impurity states in the vicinity of the Fermi level are worked out. We find that open-shell and inert impurities affect graphene very differently: the former interact directly with graphene, strongly hybridize, cause midgap states or become charged, whereas inert impurities usually physisorb and substrate mediated doping effects become important.

In the second part of this thesis, we address the electronic properties of magnetic ad-atoms and nanostructures on surfaces by combing density functional theory with many body approaches. For the model system of Ce ad-atoms on different transition metal surfaces, hybridization mechanisms are elucidated and recent photoemission experiments displaying a transition from localized to delocalized Ce $4f$ electrons upon changing the substrate are explained. Afterwards, we turn to the Kondo effect of Co atoms in different environments. In a joint STS and ab-initio theory investigation, we find that the Kondo temperature of Co atoms embedded in $CoCu_n$ clusters on Cu(111) exhibits a nonmonotonic variation with the cluster size and demonstrate the importance of the local inhomogeneous electronic structure for correlation effects in small clusters. Motivated by very recent experiments, we identify possible scenarios for the Kondo effect due to Co adatoms on graphene. We find that orbital physics controls the Kondo effect if Co is located in the center of a graphene hexagon. Characteristic signatures of the interplay of the orbital Co physics and the peculiar band-structure of graphene are predicted to occur in local probe experiments.

Zusammenfassung

Nanostrukturierte Festkörper bilden ein dynamisches Forschungsfeld, das sowohl durch grundlegende Fragen als auch durch Anwendungen motiviert wird. In der vorliegenden Arbeit werden die elektronischen Eigenschaften verschiedener Nanosysteme theoretisch untersucht und es wird herausgestellt, welche physikalischen Mechanismen ihre elektronische Struktur bestimmen.

Im ersten Teil wird der Einfluss von Inhomogenitäten und Störstellen auf Graphen mittels Dichtefunktionaltheorie und analytischer Modelle betrachtet. Wir erklären eine unerwartete Energielücke, die in Rastertunnelspektroskopieexperimenten (RTS) beobachtet wurde. Es wird gezeigt, dass eine spezielle Art der Elektron-Phonon-Wechselwirkung zu sehr großen unelastischen Beiträgen in der RTS führt. Da Graphen langreichweitige Riffeln aufweist, betrachten wir die elektronischen Eigenschaften von welligem Graphen. Wir zeigen, dass "eingefrorene" Riffeln pseudomagnetische Felder und flache Bänder am Fermi Niveau hervorrufen, welche durch Relaxation zerstört werden. Danach werden Störstelleneffekte in Graphen behandelt. Dabei werden verschiedene Wechselwirkungsmechanismen von Störstellen mit Graphen und die Voraussetzungen für die Erzeugung quasilokaler Zustände am Fermi Niveau herausgearbeitet: Störstellen mit offenen Elektronenschalen wechselwirken direkt mit Graphen, hybridisieren stark oder werden geladen, während inerte Störstellen indirekt mit Graphen wechselwirken und im Zusammenspiel mit dem Substrat zu Dotierung führen können.

Der zweite Teil dieser Arbeit behandelt die elektronischen Eigenschaften magnetischer Ad-Atome und Nanostrukturen auf Oberflächen, wobei Dichtefunktionaltheorie und Vielteilchenmethoden kombiniert werden. Für Ce Atome auf verschieden Übergangsmetalloberflächen werden Hybridisierungsmechanismen erläutert und Photoemissionsexperimente, die einen Übergang von lokalisierten zu delokalisierten Ce $4f$ Elektronen zeigen, erklärt. Im Weiteren wird der Kondo Effekt von Co Atomen in verschiedenen Umgebungen untersucht. Durch Kombination von RTS und ab-initio Theorie finden wir, dass die Kondo Temperatur von Co Atomen in $CoCu_n$ Clustern auf Cu (111) nicht monoton mit der Clustergröße variiert, und demonstrieren die Wichtigkeit der lokalen inhomogenen elektronischen Struktur für Korrelationseffekte in kleinen Clustern. Motiviert durch RTS Experimente, werden im letzten Teil der Arbeit mögliche Szenarien für den Kondo Effekt von Co Atomen auf Graphen diskutiert. Wir zeigen, dass orbitale Freiheitsgrade den Kondo Effekt kontrollieren, falls Co zentral über einem Graphen Hexagon adsorbiert. Für RTS Experimente werden charakteristische Signaturen des Wechselspiels von orbitaler Co Physik und der besonderen Bandstruktur von Graphen vorhergesagt.

Contents

Chapter 1

Introduction

Physics aims to describe phenomena on length scales ranging from Planck scale of 10^{-35} m up to astronomic length scales of more than 10^{24} m. The dominating physics strongly differs between the scales and transitions from one scale to a longer scale are often associated with the emergence of new phenomena, growing complexity and eventually coarse graining.

Solid state physics deals with phenomena spanning the range from the 10^{-10} m atomic scale up to some $1\,\mu$m or even more. Mechanical properties of solid state materials of some 10^{-3} m to 10^{1} m in size have been exploited since the ancient times. Similarly, magnetism has fascinated people and has been used in applications like compass needles for centuries. Starting about 100 years ago, increasingly smaller structures could be fabricated, studied and a found their way into technology. Semiconductors are one remarkable example in this respect, where advancing miniaturization revealed beautiful new physics and brought along novel applications: The quantum Hall effect has been discovered in the inversion layer of a metal-oxide-semiconductor field-effect transistor (MOSFET)[1], which is at the same time the building block of all modern computers. During the last decades, improvement of semiconductor devices meant miniaturization with typical dimensions of the smallest structures reaching $30-60$ nm in 2007. To date, the top-down production of structures of some nm in size is becoming possible and raises the question of how electronic and magnetic effects emerge on this previously inaccessible length scale.

In the opposite, bottom-up, direction, self assembly and atom manipulation using scanning tunneling microscopes (STM) provide a growing amount of possibilities to design and characterize nano scale structures: STM is capable of moving individual atoms along surfaces and to create structures in a well-directed manner [2]. In this way, electronic wave functions can be engineered in their size, shape and energy dependence [3, 4].

No matter from which direction, the nano scale, i.e. the range from a few atoms up to 100nm, is approached new questions of both, scientific and technological importance arise. If three dimensional materials like Si are structured on the nano scale the ratio of surface to bulk atoms becomes critical in a sense that surface effects might significantly determine the electronic properties of the whole

structure. For this reason, the conventional Si-based electronics is expected to encounter fundamental limitations at the spatial scale below 10 nm [5] and the search for so-called “nanomaterials” that are better suited for creating smaller structures than Si is of particular technological importance. This search extends over a diverse field of materials including nanoparticles with all three dimensions within the nanoscale, nanotubes having a nanosize cross-sectional area or nanofilms with a nanoscale thickness, but macroscopic extent in the other two dimensions.

In this context, carbon is an extremely promising element: It forms stable 4-fold coordinated sp^3 hybrids like diamond, 2-fold coordinated sp hybrids like acetylene, as well as stable 3-fold coordinated sp^2 hybrids like benzene or graphene. The latter allotrope, made up by carbon atoms arranged in a two dimensional (2-d) honeycomb lattice, is a building block for three dimensional graphite, ”one dimensional” carbon nanotubes and ”zero dimensional” fullerenes. These derived materials were discovered before graphene but their behavior already pointed towards one of graphene’s most remarkable properties: The carbon atoms in graphene ”are completely naked from above and below” but they are ”largely immune to further bonding”, as summed up by R. Smalley in his 1996 Nobel lecture [6].

The first experimental realization of graphene [7] about 8 years later initiated enormous interest in this material. In addition to being the first truly two dimensional material [8] and being surprisingly inert, graphene became famous for its remarkable electronic properties [9, 10, 11]. Its 2-d crystal structure leads to electrons behaving like massless fermions with the speed of light being replaced by the Fermi velocity $v \approx 10^6$ m/s. Electrons in graphene show extraordinarily high charge carrier mobility $\mu \sim 10^5\,\mathrm{cm^2V^{-1}s^{-1}}$ [7, 12, 13] which —in combination with the very high Fermi velocity— makes micron mean free paths routinely achievable. These properties make graphene a hotly debated candidate for silicon replacement in electronics industry. Moreover, graphene is particularly prospective for applications like ultra-high frequency transistors [14], gas sensors[15] or as transparent flexible electrode material for display technology. Indeed, as large scale high quality graphene samples grown by a technique called chemical vapor deposition [16] are becoming available, graphene applications are appearing very realistic today and are calling for an intense investigation of its electronic properties.

The effects of inhomogeneities in graphene are particularly important. First, inhomogeneities are widely used to functionalize materials. Impurities in semiconductors, e.g., can be used to control charge transport and are a key element for building transistors. Similarly, the giant magneto resistance (GMR) effect used in magnetic data storage employs that nm-thin layered ferromagnet non-ferromagnet structures exhibit extraordinarily strong magneto resistance.

At the same time, inhomogeneities are sources of electron scattering: At sufficiently low temperatures, impurity scattering is the most important contribution to the electronic resistance of usual metals or semiconductors.

Impurity effects can not only lead to new applications and determine their performance but they can also reveal the nature of exotic ground states, details of

electronic correlations or magnetic interactions. Impurities act as scattering centers which can locally destroy a coherent electronic state and create a real-space fingerprint of this state. Scanning tunneling microscopy (STM) images of the quasiparticle density of states close to Zn impurities in the high T_c superconductor $BiSr_2CaCu_2O_{8+\delta}$, for instance, revealed a four-fold symmetric quasi-particle cloud [17] and is one of the most direct proofs of *d*-wave pairing in these materials. Similarly, impurities uncovered the nature of an exotic surface state occurring on clean Cr (001) surfaces as being an orbital Kondo singlet formed by Cr d_{xz} and d_{yz} orbitals with the sp conduction electrons [18].

Inhomogeneities in graphene should be therefore studied to obtain a basic understanding of this material as well as they may present routes to applications. The first part of this thesis is devoted to impurity, phonon and structural inhomogeneity effects on electronic properties of this material. Moreover, we will address the interaction of graphene with magnetic impurities in the last part of this thesis and encounter a special Kondo effect controlled by graphene's particular symmetries.

Magnetism, in general, is major challenge in condensed matter physics, where the advance to the nano scale comes up with the possibility of new understanding as well as of novel applications. Techniques like x-ray magnetic circular dichroism (XMCD) or spin-polarized scanning tunneling microscopy allow to address magnetism element specifically and with atomic scale spatial resolution. In this way, magnetic interactions can be investigated in the range from individual atoms up to structures of some nm's in size. Such experiments can provide important insights for understanding the transition from atoms to solids, i.e. from electronic excitations being described by atomic multiplets to electronic excitations forming quasiparticle bands or collective excitations like spin-waves. A general theory of the magnetic properties of atoms, molecules or clusters in contact with substrate surfaces would be a big step in this direction but is still lacking. Moreover, understanding these magnetic systems will be important for data storage technology, where proceeding miniaturization brings up questions of how stable magnetic moments can formed in increasingly small structures and how the moments interact with their surrounding.

Many effects have been observed in this context. Single atoms can form magnetic moments on paramagnetic surfaces with the direction of the magnetic moment being stabilized by unexpectedly high magnetic anisotropies as found for Co ad-atoms on Pt (111) [19]. On other surfaces like Cu (111), Ag (111), Ag (100), or Au (111) [20, 21] the same Co ad-atoms appear to be best described as "Kondo impurities": below a characteristic temperature, T_K, the Co magnetic moment is screened by the conduction electrons which condense into a many-body ground state forming singlet with the ad-atom spin. The dominating physical effects appear to depend strongly on precise atomic configurations.

While this gives large freedom to design nanomagnetic structures with desired properties, the fact that "each atom matters" presents a major challenge for the theoretical description of these structures. The second part of this thesis addresses exactly this problem by combining ab-initio electronic theory and model based many-body approaches. We will investigate certain model systems like Ce ad-

atoms on different substrates or $CoCu_n$ nano structures on Cu (111) surfaces to find out which atomistic processes determine the physics of these systems and which quantities obtained from first-principles theory are the best starting point for getting a model based understanding of these systems.

The thesis is organized as follows: The description of impurities and inhomogeneities in graphene as well as the study of magnetic nanostructures presented in this work is in large parts based on ab-initio simulations in the framework of density functional theory (DFT). DFT as well as generalizations to deal with correlation phenomena like the Kondo effect are introduced in chapter 2. Afterwards we turn to the study of graphene with its basic electronic properties being introduced in chapter 3 followed by an investigation of structural inhomogeneities in chapter 4 as well as impurity effects in this material in chapter 5. Chapter 6 is devoted to magnetic nano structures on non-magnetic substrates such as Ce on different transition metal substrates, $CoCu_n$ on Cu (111) as well as Co on graphene. In this chapter the Anderson impurity model and the Kondo model are introduced, their basic physics is discussed and then combined with DFT calculations to describe these nanosystems. Ce on Ag (111), W (110), and Rh (111) as well as $CoCu_n$ on Cu (111) are investigated in joint experimental and theoretical studies.

Chapter 2

Ab-initio theory of solids

Deriving material properties from their atomistic structure presents a great challenge in theoretical physics: The full quantum mechanical description of any solid state material involves a many body Hamiltonian of the form

$$\hat{H} = \hat{H}_\mathrm{e} + \hat{H}_\mathrm{i} + H_\mathrm{ei}, \tag{2.1}$$

covering the dynamics of the electrons, $\hat{H}_\mathrm{e}$, the ion cores or nuclei, $\hat{H}_\mathrm{i}$ and their mutual interaction, $\hat{H}_\mathrm{ei}$. $\hat{H}$ is called first-principles or ab-initio Hamiltonian if it is only based on fundamental constants like the elementary charge, e, the electron mass m_e, the ion core masses M_μ, their charges Z_μ etc.. A nonrelativistic version [22] of this Hamiltonian containing the Coulomb-type ion-ion interaction V_I and electron-nucleus interaction $V_\mathrm{e-I}$ reads as

$$\hat{H}_\mathrm{e} = \sum_i \frac{\hat{p}_i^2}{2m_\mathrm{e}} + \sum_{j>i} \frac{e^2}{|\hat{r}_i - \hat{r}_j|}, \tag{2.2}$$

$$\hat{H}_\mathrm{i} = \sum_\mu \frac{\hat{P}_\mu^2}{2M_\mu} + \sum_{\nu>\mu} V_\mathrm{I}(\hat{R}_\mu - \hat{R}_\nu), \tag{2.3}$$

$$\hat{H}_\mathrm{ei} = \sum_{i,\mu} V_\mathrm{e-I}(\hat{R}_\mu - \hat{r}_i), \tag{2.4}$$

where ($\hat{r}_i$, $\hat{R}_\mu$) and ($\hat{p}_i$, $\hat{P}_\mu$) are position and momentum operators of the electrons and ion cores, respectively[1]. In any situation of practical interest to solid sate physics this Hamiltonian includes on the order of some 100 (nano system) to $\sim 10^{23}$ quantum degrees of freedom (macroscopic system) and obtaining physical observables by directly diagonalizing it or directly evaluating quantum statistical averages is intractable. The formidable task is rather finding approximations that make calculations of some desired quantity feasible while maintaining sufficient accuracy. As usual, the approximation of choice strongly depends on the physical observable of interest. A frequently used starting point is the Born-Oppenheimer

[1] In order to keep notations simple, vectors are not marked throughout this thesis. Whether a quantity is a vector or a scalar becomes clear from the context.

approximation (see section 2.1) to decouple the electronic and the ion core dynamics, which leads to a problem of interacting electrons in a static potential generated by frozen ion cores [23]. The latter problem, though simpler than the initial one, still comprises too much complexity for direct calculations of physical properties and various ways of treating it have been developed. These include ground state methods like DFT [24] or wave function Monte Carlo [25] as well as excited state methods like GW [26]. DFT is a particularly successful ground state approach that gives even good predictions for one-electron excitation spectra as long as correlations are not too strong. Large parts of this work rely on DFT and the formalism will be introduced in section 2.2.

Whenever the description of electrons in terms of independent particles breaks down the systems are called strongly correlated: The electronic wave function acquires many body character meaning that a description in terms of single Slater determinants is no more possible. The Kondo effect [27], where the conduction electrons form a singlet with a localized spin, is a famous example where the single particle picture fails qualitatively to describe the thermodynamic and spectral properties. Strongly correlated electrons have been traditionally studied by means of model Hamiltonians reading generally as

$$\hat{H}_e = \sum_{ij} t_{ij} c_i^\dagger c_j + \frac{1}{2} \sum_{ijkl} U_{ijkl} c_i^\dagger c_j^\dagger c_k c_l. \tag{2.5}$$

Here, c_i and $c_i^\dagger$ denote the usual fermionic annihilation and creation operators, respectively, which are labelled by a multi index, i, containing site, orbital and spin degrees of freedom. All one electron contributions to the Hamiltonian are included in the "hopping parameters", t_{ij}, whereas U_{ijkl} describes the two particle interactions.

Rewriting the full electronic Hamiltonian as obtained from Eq. (2.1) in Born-Oppenheimer approximation to a second quantized tight-binding basis yields a Hamiltonian in the form of Eq. (2.5). (See appendix B.) Frequently employed model Hamiltonians, like the Anderson impurity model or the Hubbard model [28], differ from this full Hamiltonian by considering only a truncated Hilbert space of one electron degrees of freedom, e.g. restricting the indices i to a particular set of orbitals, and using a simplified local Coulomb interaction. During the last decades great progress has been made in understanding the physics of the model Hamiltonians by various techniques: The behavior of Anderson impurities can be understood by means of renormalization group methods, large-N expansions or quantum Monte Carlo methods. Theoretical tools such as dynamical mean field theory (DMFT) [29, 30, 31], its cluster extensions [32, 33, 34, 35] or the recent dual fermion approach [36] for treating lattice models like the Hubbard model have been developed and allowed one to understand the physics of the Mott transition or the occurrence of complex ordered phases in these systems.

Originally, these approaches relied on hopping and Coulomb parameters being empirically adjusted, which hinders their applicability in cases, where the detailled atomistic structure is decisive. One way to address this problem is by

combining DFT with model approaches to obtain structure and material specific model Hamiltonians derived from first principles. One successful implementation of this idea is the "LDA+DMFT" method [37, 38]. The combination of DFT with model-based many body approaches is particular important for the understanding of magnetic nanostructures, which are addressed in chapter 6. In this context, we covercome limitations of prior combinations of many body methods with DFT, which relied on specific DFT implementations that did not allow to treat complex magnetic nanostructures.

In section 2.2 a derivation of DFT and important prerequisites for its practical use as well as an introduction of the implementation used for this work are given. Afterwards a theoretical background for combining DFT with model based approaches is given in terms of an effective action formalism and constraining fields.

2.1 Born-Oppenheimer Approximation

Since the electron mass is by a factor of 1800 less than the nucleon mass, the electrons should follow the nuclear motion quasi-instantaneously. This heuristic argument has been put on formal grounds by Born and Oppenheimer (see, e.g., [23] or [22].) who showed that electron and ion core dynamics can be separated in a lowest order approximation:

We consider the electrons moving in a static array of ion cores, i.e. the operators $\hat{R}_\mu \to R_\mu$ are replaced by real parameters. Solving the resulting Hamiltonian describing the electrons in presence of frozen ion cores,

$$(\hat{H}_\mathrm{e} + \hat{H}_\mathrm{ei})\psi_K(R_\mu, r_i) = E_K(R_\mu)\psi_K(R_\mu, r_i), \tag{2.6}$$

yields a basis of electronic eigenfunctions $\psi_K(R_\mu, r_i)$, which contain the nuclear coordinates, R_μ, as parameters. K denotes the overall electronic quantum number. Now, the following ansatz for eigenfunctions of the full Hamiltonian, Eq. (2.1), is chosen:

$$\Phi_Q(R_\mu, r_i) = \chi_Q(R_\mu)\psi_K(R_\mu, r_i), \tag{2.7}$$

where the wave function $\chi_Q(R_\mu)$ of the nuclei depends on the total system quantum number Q. Applying the full Hamiltonian to the ansatz for the full wave functions yields

$$\begin{aligned}
\hat{H}\Phi_Q(R_\mu, r_i) &= \left[E_K(R_\mu) + \hat{H}_\mathrm{i}\right]\Phi_Q(R_\mu, r_i) \\
&= \psi_K(R_\mu, r_i)\left[E_K(R_\mu) + \hat{H}_\mathrm{i}\right]\chi_Q(R_\mu) \\
&- \sum_\mu \frac{1}{2M_\mu}\left[2\nabla_\mu\psi_K(R_\mu, r_i)\nabla_\mu\chi_Q(R_\mu) + \chi_Q(R_\mu)\nabla_\mu^2\psi_K(R_\mu, r_i)\right].
\end{aligned} \tag{2.8}$$

The energy $E_K(R_\mu)$ acts on the ion core motion as an adiabatic potential, whereas the last line of Eq. (2.8) contains the non-adiabatic terms. The contribution $\sim \nabla_\mu\psi_K(R_\mu, r_i)\nabla_\mu\chi_Q(R_\mu)$ vanishes in first order perturbation theory but the term $\sim$

$\nabla^2_\mu \psi_K(R_\mu, r_i)$ is finite in this order. Since, by symmetry, ψ_K may only depend on differences $R_\mu - r_i$, this first order correction is by a factor of $m/M_\mu \lesssim 0.5 \cdot 10^{-3}$ smaller than the pure electronic kinetic energy. Up to corrections of this order, the electrons follow the ion core motions adiabatically (i.e. $K = const.$).

It is therefore in many circumstances an appropriate approximation to treat the electrons as moving in a static potential generated by the frozen ion cores, while the ion cores are considered as classical objects moving in the effective potential $E_K(R_\mu)$ and interacting via $V_I(R_\mu - R_\nu)$. In large parts of this thesis we will make use of this so-called Born-Oppenheimer approximation. Physically, it is equivalent to neglecting all effects of electron-phonon coupling. There are however famous examples, like BCS superconductivity, where this approximation breaks down. In chapter 4 we will deal with scanning tunneling spectra of graphene and show that electron-phonon coupling has an unexpectedly strong effect, there.

2.2 Density Functional Theory

Having separated the electronic dynamics from the nuclear motion one is in general still left with a problem of greatest complexity and the many body all electron wave functions $\psi_K(R_\mu, r_i)$ being quasi unmanageable objects. However, Hohenberg, Kohn and Sham showed that the groundstate of any interacting electron system can be properly described by the ground state density instead of the many body wave function (Hohenberg-Kohn Theorem I). They further showed that this density obeys a variational condition (Hohenberg-Kohn Theorem II), which can be used for mapping the many electron problem onto an effective single particle problem (Kohn-Sham equations).

A classical derivation, following Kübler [22], Jones [24] and Martin [39] will be given, here. An alternative derivation based on an effective action formalism will be discussed in the context of going beyond DFT in section 2.5.1.

Consider N electrons moving in an external potential $\hat{V}_{\text{ext}} = \sum_{i=1}^{N} v_{\text{ext}}(\hat{r}_i)$ being described by

$$\hat{H}_{\text{e}} = \hat{T} + \hat{V}_{\text{ee}} + \hat{V}_{\text{ext}}, \tag{2.9}$$

where $\hat{T}$ is their kinetic energy and $\hat{V}_{\text{ee}}$ is their interaction. (See Eq. (2.6.) For any N-electron state $|\Phi\rangle$, the density $n(r)$ at a point r is given by

$$n(r) = \langle\Phi| \left(\sum_{i=1}^{N} \delta(r - \hat{r}_i) \right) |\Phi\rangle. \tag{2.10}$$

A density $n(r)$ resulting from an N-electron wave function according to Eq. (2.10) is called N-representable. On the set of N-representable densities the functional

$$F[n] = \min_{|\Phi\rangle \in M(n)} \langle\Phi|\hat{T} + \hat{V}_{\text{ee}}|\Phi\rangle \tag{2.11}$$

is well defined with $M(n)$ being the set of N-electron states $|\Phi\rangle$ yielding the density $n(r)$. The contribution of the external potential $\langle\Phi|\hat{V}_{\text{ext}}|\Phi\rangle$ to the total energy $E =$

$\langle\Phi|\hat{H}_e|\Phi\rangle$ of the electronic system is given by

$$\langle\Phi|\hat{V}_{ext}|\Phi\rangle = \int n(r)v_{ext}(r)\mathrm{d}^3r. \tag{2.12}$$

With the ground state, $|\Phi_0\rangle$, for given $\hat{V}_{ext}$ and the corresponding density, n_0, Ritz's variational principle proves that

$$E_0 = \langle\Phi_0|\hat{H}_e|\Phi_0\rangle = \min_{|\Phi\rangle\in M(n_0)}\langle\Phi|\hat{H}_e|\Phi\rangle = F[n_0] + \int n_0(r)v_{ext}(r)\mathrm{d}^3r. \tag{2.13}$$

This is the Hohenberg-Kohn Theorem I: The ground state energy E_0 of an interacting electron system is a functional of the electron density

$$E_0 = E[n_0]. \tag{2.14}$$

Another application of Ritz's variational principle yields for any N-representable electron density $n \neq n_0$

$$E[n_0] = \min_{|\Phi\rangle\in M(n_0)}\langle\Phi|\hat{H}_e|\Phi\rangle < \min_{|\Phi\rangle\in M(n)}\langle\Phi|\hat{H}_e|\Phi\rangle = E[n]. \tag{2.15}$$

Therefore, the ground state density n_0 minimizes the energy functional $E[n]$ within the set of N-representable densities, which proves the Hohenberg-Kohn Theorem II. As consequence, the ground state density obeys the variational equation

$$\frac{\delta E[n]}{\delta n(r)} = \mu, \tag{2.16}$$

where μ is a Lagrange multiplier to ensure the desired number of electrons, $N = \int n(r)\mathrm{d}^3r$. This can be solved by mapping onto a single particle problem with a self-consistency condition. First, consider an auxiliary system of noninteracting particles described by the Schrödinger equation

$$\left[-\frac{\hbar^2}{2m}\Delta + v_{eff}(r)\right]\psi_i(r) = \epsilon_i\psi_i(r). \tag{2.17}$$

The ground state density of this system is obtained by occupying the N energetically lowest states

$$n(r) = \sum_{i=1}^{N}|\psi_i(r)|^2\,. \tag{2.18}$$

The effective potential $v_{eff}(r)$ has to be determined such, that the ground state density of the interacting electron system and of the auxiliary system coincide. To this end, the exchange-correlation functional $E_{xc}[n]$ is defined by splitting the energy functional of the interacting electrons according to

$$E[n] = T_0[n] + E_H[n](r) + E_{xc}[n] + \int \mathrm{d}^3r n(r)v_{ext}(r). \tag{2.19}$$

Here, $T_0[n]$ denotes the kinetic energy of noninteracting electrons with the density n and $E_{\mathrm{H}}[n]$ is the electrostatic energy (Hartree energy) of the charge distribution resulting from n. Defining the Hartree potential and the exchange-correlation potential by

$$v_{\mathrm{xc}}[n](r) = \frac{\delta E_{\mathrm{xc}}[n]}{\delta n(r)} \text{ and } v_{\mathrm{H}}[n](r) = \frac{\delta E_{\mathrm{H}}[n]}{\delta n(r)}, \tag{2.20}$$

respectively, Eq. (2.16) can be replaced by

$$\frac{\delta T_0[n]}{\delta \psi_i^*(r)} + (v_{\mathrm{xc}}[n](r) + v_{\mathrm{H}}[n](r) + v_{\mathrm{ext}}(r)) \frac{\delta n(r)}{\delta \psi_i^*(r)} = 0 \tag{2.21}$$

with $i = 1, 2, \ldots, N$ and the orthonormality constraint $\langle \psi_i | \psi_j \rangle = \delta_{i,j}$. As $\frac{\delta T_0[n]}{\delta \psi_i^*(r)} = -\frac{\hbar^2}{2m} \Delta \psi_i(r)$ Eq. (2.21) and (2.17) coincide for

$$v_{\mathrm{eff}}(r) = v_{\mathrm{ext}}(r) + v_{\mathrm{H}}[n](r) + v_{\mathrm{xc}}[n](r). \tag{2.22}$$

Therefore, the ground state density of the interacting electron system is given by a self consistent solution of the Eqs. (2.22), (2.17) and (2.18), known as Kohn-Sham equations. $\psi_i(r)$ and ϵ_i are referred to as Kohn-Sham eigenfunctions and eigenvalues, respectively.

The proof of the Hohenberg-Kohn theorems presented above holds also if the for electron density $n(r)$ is replaced by the spin density matrix

$$\tilde{n}_{\alpha\beta}(r) = \langle \Phi | \Psi_\alpha^\dagger(r) \Psi_\beta(r) | \Phi \rangle \tag{2.23}$$

as fundamental variable. Here $\Psi_\alpha(r)$ denotes the field operator for electrons with spin $\alpha = \uparrow, \downarrow$. This allows for more flexibility in formulating approximations to the exchange-correlation functional.

To generalize the Kohn-Sham theory to the spin dependent case (see Ref. [40]) the condition of vanishing variation of the total energy $E[\tilde{n}]$ under the constraint $N = \sum_\alpha \int \tilde{n}_{\alpha\alpha}(r) \mathrm{d}r$ is examined:

$$\frac{\delta T_0}{\delta \tilde{n}_{\beta\alpha}(r)} + v_{\mathrm{H}}[\tilde{n}](r)\delta_{\alpha\beta} + \frac{\delta E_{\mathrm{xc}}}{\delta \tilde{n}_{\beta\alpha}(r)} + v_{\alpha\beta}(r) = \mu \delta_{\alpha\beta}. \tag{2.24}$$

Comparison to a noninteracting auxiliary system, as in Eqs. (2.22) and (2.17), shows that Eq. (2.24) is equivalent to the coupled Pauli type equations

$$\sum_\beta \left[-\frac{\hbar^2}{2m} \delta_{\alpha\beta} \Delta + v_{\alpha\beta}(r) + v_{\mathrm{H}}[\tilde{n}](r)\delta_{\alpha\beta} + v_{\mathrm{xc}}^{\alpha\beta}[\tilde{n}](r) \right] \psi_\beta^{(i)}(r) = \epsilon_i \psi_\alpha^{(i)}(r).$$

In analogy to Eq. (2.18), the spin density matrix is given by $\tilde{n}_{\alpha\beta}(r) = \sum_{i=1}^N \psi_\alpha^{(i)*}(r) \psi_\beta^{(i)}(r)$ and self-consistency of the Hartree $v_{\mathrm{H}}[\tilde{n}]$ and exchange-correlation potentials $v_{\mathrm{xc}}[\tilde{n}]$ is required.

2.2.1 Approximations to the exchange-correlation functional

The total energy functional has been abstractly defined in Eqs. (2.11) and (2.13) but an explicit form necessary for practical applications of the theory is a-priori unknown. A very successful class of approximate functionals are the so-called (semi-)local exchange correlation functionals, which use exact exchange-correlation energies of the homogeneous electron gas as an approximation for inhomogeneous systems. The local-density approximation (LDA) implements this by assuming

$$E_{\mathrm{xc}}[n] = \int n(r)\epsilon_{\mathrm{xc}}(n(r))\mathrm{d}r, \tag{2.25}$$

where ϵ_{xc} is a *function* of the density $n(r)$. To obtain an explicit form of ϵ_{xc}, one separates exchange, E_{x}, and correlation, E_{c}, contributions to

$$E_{\mathrm{xc}} = E_{\mathrm{x}} + E_{\mathrm{c}} \tag{2.26}$$

and similarly $\epsilon_{\mathrm{xc}} = \epsilon_{\mathrm{x}} + \epsilon_{\mathrm{c}}$: The exchange energy E_{x} is defined as the Fock integral applied to the Kohn-Sham (KS) orbitals:

$$E_{\mathrm{x}}[n] = \langle \Phi^{\mathrm{KS}} | \hat{V}_{\mathrm{ee}} | \Phi^{\mathrm{KS}} \rangle - E_{\mathrm{H}}[n], \tag{2.27}$$

where $|\Phi^{\mathrm{KS}}\rangle$ is the Slater determinant of the occupied KS orbitals. This expression can be evaluated for the homogeneous electron gas, where the KS orbitals are plane waves [41]. The resulting exchange energy density is[2]

$$\epsilon_{\mathrm{x}}(n) = -\frac{3}{4\pi}(3\pi^2 n)^{1/3} = -\frac{3}{4\pi}\frac{(9\pi/4)^{1/3}}{r_s} \tag{2.28}$$

with the Wigner Seitz radius r_{s} being radius of a sphere containing one electron on average: $n = \frac{3}{4\pi r_{\mathrm{s}}^3}$. For ϵ_{c}, there are analytical expressions for the homogeneous electron gas in the limits of high and low densities. The high-density limit is the limit of weak interactions, in which

$$\epsilon_{\mathrm{c}}(n) = c_0 \log r_{\mathrm{s}} - c_1 + c_2 r_{\mathrm{s}} \log r_{\mathrm{s}} - c_3 r_{\mathrm{s}} + \ldots \tag{2.29}$$

and the constants c_i are obtained from many-body perturbation theory [41]. In the low-density, i.e., strong coupling limit, comparison to the electrostatic and the zero-point vibrational energies of a Wigner crystal yields [41]

$$\epsilon_{\mathrm{c}}(n) = -\frac{d_0}{r_{\mathrm{s}}} + \frac{d_1}{r_{\mathrm{s}}^{3/2}} + \ldots \tag{2.30}$$

and the constants d_i. An expression encompassing both limits is

$$\epsilon_{\mathrm{c}}(n) = -2c_0(1+\alpha_1 r_{\mathrm{s}}) \log\left[1 + \frac{1}{2c_0(\beta_1 r_{\mathrm{s}}^{1/2} + \beta_2 r_{\mathrm{s}} + \beta_3 r_{\mathrm{s}}^{3/2} + \beta_4 r_{\mathrm{s}}^2)}\right], \tag{2.31}$$

[2] In the following section atomic units are used: $\hbar = e = m_{\mathrm{e}} = 1$.

where $\beta_1 = \frac{1}{2c_0}\exp(-\frac{c_1}{2c_0})$, $\beta_2 = 2c_0\beta_1^2$. The remaining coefficients α_1, β_3 and β_4 are obtained by fitting Eq. (2.31) to Quantum Monte Carlo correlation energies by Ceperley and Alder. (See, e.g., [41] and references therein.)

The generalization of LDA to include spin densities, called local spin density approximation (LSDA), reads for the collinear case as

$$E_{\mathrm{xc}}[n] = \int n(r)\epsilon_{\mathrm{xc}}(n_\uparrow(r), n_\downarrow(r))\mathrm{d}r. \tag{2.32}$$

This LSDA functional can be obtained from the LDA functional using spin scaling relations for kinetic and exchange terms as well as a random phase approximation (RPA) motivated interpolation for the correlation energy. Widely used parameterizations can be found, e.g., in Ref. [41]. For DFT calculations including non-collinear spin configurations, an approximation to the exchange correlation potential is obtained by employing Eq. (2.32) and diagonalizing the spin density matrix $\tilde{n}_{\alpha\beta}(r)$ locally. (See [22] for details.)

To construct functionals beyond LDA, in particular the generalized gradient approximations (GGA) used in many parts of this work, the concept of the exchange-correlation hole, $n_{\mathrm{xc}}(r, r')$, has to be introduced [22]: Consider the two electron correlation function

$$\rho_2(r, r') = \operatorname*{Tr}_{\sigma,\sigma'}\langle\Phi|\Psi^\dagger_{\sigma'}(r')\Psi^\dagger_\sigma(r)\Psi_\sigma(r)\Psi_{\sigma'}(r')|\Phi\rangle \tag{2.33}$$

and define $n_{\mathrm{xc}}(r, r')$ by $\rho_2(r, r') = n(r)n_2(r, r')$ with $n_2(r, r') = n(r') + n_{\mathrm{xc}}(r, r')$. Hence, $n_{\mathrm{xc}}(r, r')$ describes the depletion of density at r', if there is an electron at r. Integrating Eq. (2.33) over r' yields the sum rule

$$\int \mathrm{d}^3r' n_{\mathrm{xc}}(r, r') = -1. \tag{2.34}$$

In analogy to Eqs. (2.26) and (2.27), $n_{\mathrm{xc}}(r, r') = n_{\mathrm{x}}(r, r') + n_{\mathrm{c}}(r, r')$ can be decomposed into the exchange hole, $n_{\mathrm{x}}(r, r')$, and the correlation hole, $n_{\mathrm{c}}(r, r')$. The exchange energy is defined as the Fock integral of the KS orbitals, Eq. (2.27), which implies

$$n_x(r, r') \leq 0 \tag{2.35}$$

in all space and

$$\int \mathrm{d}^3r' n_x(r, r') = -1. \tag{2.36}$$

Combination of Eqs. (2.34) and (2.36) yields

$$\int \mathrm{d}^3r' n_{\mathrm{c}}(r, r') = 0. \tag{2.37}$$

With the concept of coupling constant integration, $n_{\mathrm{xc}}(r, r')$ can be directly related to the functional $E_{\mathrm{xc}}[n]$: We generalize the density functional, Eq. (2.11), by introducing the coupling constant $\lambda \in [0, 1]$,

$$F_\lambda[n] = \min_{|\Phi\rangle\in M(n)}\langle\Phi|\hat{T} + \lambda\hat{V}_{\mathrm{ee}}|\Phi\rangle, \tag{2.38}$$

and define $|\Phi_n^\lambda\rangle$ as the N-electron state, which minimizes $\hat{T} + \lambda\hat{V}_{\mathrm{ee}}$ under the constraint of yielding the density $n(r)$. As

$$\frac{\mathrm{d}F_\lambda[n]}{\mathrm{d}\lambda} = \langle\Phi_n^\lambda|\hat{V}_{\mathrm{ee}}|\Phi_n^\lambda\rangle, \tag{2.39}$$

we obtain from $F[n] = F_0[n] + \int_0^1 \frac{F_\lambda[n]}{\mathrm{d}\lambda}\mathrm{d}\lambda$ by definition of the exchange-correlation functional, Eq. (2.19),

$$E_{\mathrm{xc}}[n] = \int_0^1 \mathrm{d}\lambda\langle\Phi_n^\lambda|\hat{V}_{\mathrm{ee}}|\Phi_n^\lambda\rangle - E_{\mathrm{H}}[n]. \tag{2.40}$$

With the replacements $|\Phi\rangle \to |\Phi_n^\lambda\rangle$ and $\rho_2(r,r') \to \rho_2^\lambda(r,r')$ in Eq. (2.33) we define the coupling constant dependent exchange-correlation hole, $n_{\mathrm{xc}}^\lambda(r,r')$, by $\rho_2^\lambda(r,r') = n(r)n_2^\lambda(r,r')$ and

$$n_2^\lambda(r,r') = n(r') + n_{\mathrm{xc}}^\lambda(r,r').$$

This yields the electron-electron interaction energy as function of λ:

$$\langle\Phi_n^\lambda|\hat{V}_{\mathrm{ee}}|\Phi_n^\lambda\rangle = \frac{1}{2}\int \mathrm{d}^3r\,\mathrm{d}^3r'\frac{n(r)n_2^\lambda(r,r')}{|r-r'|}.$$

By definition of the Hartree energy and Eq. (2.40), one finds that E_{xc} is determined by the coupling-constant averaged exchange-correlation hole $\overline{n}_{\mathrm{xc}}(r,r') = \int_0^1 \mathrm{d}\lambda n_{\mathrm{xc}}^\lambda(r,r')$:

$$E_{\mathrm{xc}}[n] = \frac{1}{2}\int \mathrm{d}^3r\,\mathrm{d}^3r'\frac{n(r)\overline{n}_{\mathrm{xc}}(r,r')}{|r-r'|}.$$

Hence an accurate approximation to the exchange-correlation functional $E_{\mathrm{xc}}[n]$ is equivalent an accurate description of $\overline{n}_{\mathrm{xc}}(r,r')$.

The fact that local approximations like L(S)DA give surprisingly accurate results even for systems, where the density varies strongly on the scale of the Fermi wavelength or the Thomas-Fermi screening length can be partly understood from properties of the corresponding exchange-correlation hole: L(S)DA is derived from the homogeneous electron gas, which is a real physical system. Therefore, the LDA exchange-correlation hole respects the sum rules of Eq. (2.36) and Eq. (2.37) as well as the negativity condition of Eq. (2.35).

These properties of the exchange-correlation hole need to be preserved when constructing of semilocal generalizations of LSDA: The first exchange-correlation functionals including density gradients ∇n - the so-called gradient expansion approximations (GEA) - were less accurate than LDA due to unphysical properties of $n_{\mathrm{xc}}(r, r+u)$ at large u [41]: There, $n_{\mathrm{x}}^{\mathrm{GEA}}$ exhibits undamped $\cos(2k_{\mathrm{f}}u)$ oscillations and violates the negativity condition, Eq. (2.35). The sum rule, Eq. (2.36), is only fullfilled with an additional convergence factor. Furthermore, n_c^{GEA} does not integrate to zero as required by Eq. (2.37) due to a positive u^{-4} tail at large u.

At small u, however, the GEA exchange-correlation hole is much better than LDA. Perdew, Wang, Becke et al. (see, e.g., [41]) succeeded in constructing

functionals that combine the desirable features of LDA with the more realistic exchange-correlation-hole from GEA at small u. This class of semilocal functionals, called generalized gradient approximations (GGA), is now widely applied from solid state physics to chemistry.

In calculations for this thesis GGA-functionals PW91 and PBE have been used. The basic step of getting from GEA to PW91-GGA is introducing a real-space cutoff on n_{xc}^{GEA} that enforces the sum rules and the negativity contition according to Eqs. (2.35) - (2.37). The explicit parameterization of PW91 is given in [42]. The newer PBE GGA-functional can be constructed more intuitively by using some known exact relations as starting point and not requiring the cutoff construction from PW91. Despite this quite different construction PW91 and PBE give very similar results [43].

2.3 Basis sets for Kohn-Sham Hamiltonians

The Kohn-Sham equation, (2.17), is formally a single-particle Schrödinger equation, which can be solved by expanding the wave functions to a basis set of the single particle Hilbert space. The basis set is infinite, in general, and a finite subset appropriate to the physical problem under consideration has to be chosen for numerical solutions. A preferably "small" basis set, which at the same time allows for an accurate description of the Kohn-Sham wave functions, is needed.

This requirement causes difficulties for many realistic solids and molecules, as the character of the wave functions near the nuclei differs drastically from the interstitial regions: In the vicinity of the nuclei, the wave function shows rapid oscillations but does not strongly respond to changes of the chemical environment. In the interstitial region, however, the wave function is smooth and very sensitive to its environment [44].

Besides the localized basis sets, widely used in quantum chemistry, various plane wave based approaches have been developed to deal with this problem: For periodic systems the crystal momentum k is a good quantum number and Bloch's theorem states that any eigenstate of the Kohn-Sham Hamiltonian, $\psi_{k,i}(r)$, can be represented by a discrete sum of plane waves

$$\psi_{k,i}(r) = \sum_G c_{i,k+G} e^{i(k+G)r}.$$

An obvious way of specifying a finite basis, is to truncate the full basis by imposing a kinetic energy cutoff E_{cut} such that only plane waves, $e^{i(k+G)r}$, with

$$\frac{\hbar^2(k+G)^2}{2m} < E_{\mathrm{cut}}$$

are considered. This approach suffers, however, from the problem that plane waves are poorly suited to reproduce the electronic wave functions near the nuclei. Correspondingly, large cutoffs E_{cut} are required [45]. Historically two distinct strategies - the pseudopotential (PP) and the augmented wave methods (see

sections 2.3.1 and 2.3.2, respectively) - have been developed to deal with this problem. The calculations presented in this work employ the so-called projector augmented waves (PAW), which can be viewed as unification of the PP and augmented wave approaches. The PAW method is described in section 2.3.3. The discussion in sections 2.3.1-2.3.3 follows mainly Refs. [22, 39, 44, 46].

2.3.1 Pseudopotentials

The scattering properties of the deep attractive ion core Coulomb potential, which is (almost) spherically symmetric and localized in a close vicinity of the nuclei, are fully characterized by the energy and angular momentum dependent phase shift $\eta_l(\epsilon)$. The eigenenergies of the KS Hamiltonian, Eq. (2.17), can be obtained solely from the wave functions in the interstitial regions as soon as all phase shifts are known. The essential point for PP approaches is that the wave functions outsite the scattering regions depend only on phase shifts modulo 2π: PPs are constructed such that they approximate $\eta_l(\epsilon)$ modulo 2π in a given energy range, where the freedom of adding integer multiples of 2π is used to remove nodes from the wave function in the scattering region. The PP can be much weaker and smoother than the original ion-core potential, which means that the plane wave expansion for the PP converges with significantly smaller plane wave cut-off than for the original problem.

This scattering theoretic view of pseudopotentials can be well illustrated by a cancellation theorem of kinetic and potential energy contributions to the energy of a valence electron wave function in the core region [39]: The Pauli repulsion of the core electrons (kinetic energy) and the attractive ion-core Coulomb potential have opposite sign and partly cancel each other. Their effect is combined in an approximate *pseudopotential* acting on the valence electrons. The core electrons are frozen and eliminated from the calculation.

In practice, *ab-initio* pseudopotentials can be constructed as follows [45, 39]: For a given atomic species, one solves the Kohn-Sham equations for the isolated atom and obtains the all-electron wave functions ψ_{lm}. Here, l denotes the total-angular momentum quantum number, m the angular momentum component about one quantization axis. For each valence electron state, ψ_{lm}, a pseudo-function ψ^{PS}_{lm}, which coincides with ψ_{lm} outside the core radius r_{c} and fulfills requirements like smoothness and absence of nodes inside r_{c}, is defined.

Exploiting the spherical symmetry of the ion core problem, the Schrödinger equation can be inverted for each angular momentum channel, l, at a reference energies ϵ_l to yield a potential $u_l(r)$ such that ψ^{PS}_{lm} is an eigenstate with energy ϵ_l:

$$u_l(r) = \epsilon_l + \frac{1}{\psi^{\mathrm{PS}}_{lm}(r)} \cdot \frac{\hbar^2}{2m_e} \nabla^2 \psi^{\mathrm{PS}}_{lm}(r). \tag{2.41}$$

Using a soft charge density $\tilde{Z}(r)$ mimicking the charge of the ion core and the pseudo charge density $\tilde{n}(r) = \sum f_n \psi^{\mathrm{PS}}_n(r) \psi^{\mathrm{PS}}_n(r)$ constructed from the pseudo wave

functions, we define a pseudo Kohn-Sham Hamiltonian[3]

$$\tilde{H}_l = -\frac{\hbar^2}{2m_e}\nabla^2 + v_l^{\mathrm{PS}}(r) + v_{\mathrm{H}}[\tilde{n} + \tilde{Z}](r) + v_{\mathrm{xc}}([\tilde{n}(r)], r) \tag{2.42}$$

with the pseudopotential, $v_l^{\mathrm{PS}}(r)$, such that the pseudo Kohn-Sham Hamiltonian produces the desired pseudo wave functions ψ_{lm}^{PS}, i.e.

$$v_l^{\mathrm{PS}}(r) = u_l(r) - v_{\mathrm{H}}[\tilde{n} + \tilde{Z}](r) - v_{\mathrm{xc}}([\tilde{n}(r)], r). \tag{2.43}$$

The construction of Eq. (2.43) is called unscreening. It is problematic since v_{xc} is non-linear in $\tilde{n}(r)$ and related ambiguities arise [39]. The final pseudopotential can be represented in the form

$$\hat{V}^{PS} = \hat{V}^{\mathrm{loc}} + \hat{V}^{\mathrm{SL}} \tag{2.44}$$

which consists of a local part $V^{\mathrm{loc}}(r, r') = v(r)\delta(r - r')$ and a semilocal part

$$V^{\mathrm{SL}}(r, r') = \sum_{lm} Y_{lm}(r) V_l(r) \frac{\delta(|r| - |r'|)}{|r|^2} Y_{lm}(r'). \tag{2.45}$$

Here, $Y_{lm}(r)$, denote the usual spherical harmonics. This construction fully defines the pseudopotential, which is non-local due to the explicit dependence of $V_l(r)$ on the angular momentum l. Evaluating expectation vales of the semilocal potential, Eq. (2.45), involves double integrals and is computationally expensive. Therefore, separable peusdopotentials, which can be decomposed according to

$$\hat{V}^{PS} = \hat{V}^{\mathrm{loc}} + \sum_{lm} \frac{|\psi_{lm}^{\mathrm{PS}} V_l\rangle\langle V_l \psi_{lm}^{\mathrm{PS}}|}{\langle \psi_{lm}^{\mathrm{PS}} | V_l | \psi_{lm}^{\mathrm{PS}}\rangle}, \tag{2.46}$$

are often used. The states $|\psi_{lm}^{\mathrm{PS}} V_l\rangle$ are projectors that operate upon the pseudized wave functions ψ^{PS}. Formally very similar expressions arise in the context of the projector augmented waves described in section 2.3.3.

Methods of constructing pseudopotentials differ by choosing pseudofunctions ψ_{lm}^{PS} for given ψ_{lm}. One widely used class of pseudopotentials are norm-conserving pseudopotentials, which impose the constraint that the total amount of charge within the core region is given correctly by ψ_{lm}^{PS}: $\int_{|r|<r_c} \mathrm{d}^3 r |\psi_{lm}^{\mathrm{PS}}(r)|^2 = \int_{|r|<r_c} \mathrm{d}^3 r |\psi_{lm}(r)|^2$. The pseudopotentials constructed in this way have the correct scattering properties to linear order in energy around the reference energies ϵ_l.

The total energy in the pseudopotential method reads as

$$E = \sum_n f_n \langle \psi_n^{\mathrm{PS}}| - \frac{\hbar^2}{2m_e}\nabla^2 + \hat{V}^{PS} |\psi_n^{\mathrm{PS}}\rangle + E_{\mathrm{self}} + E_{\mathrm{H}}[\tilde{n} + \tilde{Z}] + E_{\mathrm{xc}}[\tilde{n}], \tag{2.47}$$

where E_{self} is adjusted such that the energy of isolated atoms in the pseudopotential calculation equals the total energy of an all-electron calculation. The

[3] For clarity, $\tilde{H}_l$ is written for each angular momentum channel separately.

"pseudized" charge density $\tilde{Z}$ is chosen to mimic the charge of the nucleus and the core electrons in a smooth way. $\tilde{Z}$ is kept fixed, once the pseudopotential is constructed and does not change with the atomic environment.

PPs are very successful in the field of molecular dynamics simulations [45] and are widely used for large systems. However, there are some drawbacks of the PP method. First, within r_c around the nuclei (nearly) all information on the shape of electron density is lost. Moreover, so-called transferability problems arise that can be grouped into two classes:

- Energy transferability problems: The scattering properties of the reference system are reproduced accurately only within a given energy range.
- Charge transferability problems: The pseudopotential is constructed for a fixed atomic environment and errors arise, e.g., due to the pseudized charge density $\tilde{Z}$ being kept fixed to the spherically symmetric shape of the reference system.

For norm-conserving PPs, the capabilities of efficiently describing first row and 3d transition metal elements are limited, since no choice of r_c combining high (energy) transferability and accuracy with moderate energy cutoffs could be found. The mixed basis set approaches address this problem by including atom centered localized basis function in addition to the plane waves [47]. Vanderbilt's ultrasoft PPs do not impose norm conservation and overcome energy transferability problems in describing first row or 3d elements efficiently employing only plane waves [48].

Problems with charge transferability can be improved by including so-called non-linear core corrections [39] but for $\tilde{Z}$ being not adapted to the atomic environment systematic errors occur (see section 2.3.3.).

2.3.2 Augmented wave methods

In the augmented wave methods, a different approach is followed by constructing potential dependent basis sets: Space is again divided into atom-centered spheres and the interstitial region but, here, the basis functions are augmented with atomic orbital like functions within the atom-centered spheres. Today there is a variety of methods including linearized muffin tin orbitals (LMTO), linearized augmented plane waves (LAPW), and the Korringa-, Kohn- and Rostoker- (KKR) multiple scattering approach which implement this idea. These methods differ, e.g., in the way the wave functions in the interstitial region, called envelope functions, are described: plane waves in LAPW or solutions of the Laplace equation in LMTO.

Here we will illustrate the augmented wave methods with the example of the (linearized) augmented plane waves due to its formal similarities with the PAW method (see section 2.3.3), which has been used for calculations presented in this thesis. In the augmented plane wave (APW) methods, a model potential — often a so-called muffin-tin potential, which is constant in the interstitial and spherically symmetric in the muffin tin spheres — is chosen for the construction of the basis

functions. The resulting Schrödinger equation is solved in each region separately and the partial solutions are matched continuously at the border of interstitial and atomic regions. The solutions of the Schrödinger equation in the interstitial are plane waves. Inside the spheres, the Bessel functions occurring in the Rayleigh decomposition of the plane wave are replaced by radial functions, $u_l(E, r)$, which solve a radial Schrödinger equation

$$\left\{\frac{\hbar^2}{2m}\left(-\frac{\partial^2}{\partial r^2}+\frac{l(l+1)}{r^2}\right)+V^{\mathrm{MT}}(r)-E_l\right\} r u_l(E_l, r)=0 \tag{2.48}$$

involving the muffin-tin potential V^{MT} and the energy parameter E_l. For a given reciprocal lattice vector, K, and, k from the first Brillouin zone of the crystal, the corresponding APW basis function reads as

$$\phi_K(k, r)=\begin{cases} e^{i(K+k)r} & \text{interstitial} \\ \sum_{lm} a_{lm}^{\mu K}(k) u_l(E_l, r^\mu) Y_{lm}(r^\mu) & \text{muffin-tin } \mu, \end{cases} \tag{2.49}$$

where $r^\mu = r - \tau^\mu$ for the muffin-tin sphere μ centered at τ^μ. Using the Rayleigh decomposition of the plane wave about the sphere center τ^μ, the coefficients $a_{lm}^{\mu K}(k)$ are obtained from the requirement for continuous basis functions:

$$a_{lm}^{\mu K}(k)=4\pi e^{i(K+k)\tau^\mu} i^l Y_{lm}^*(K+k)\frac{j_l((K+k)R_{\mathrm{MT}})}{u_l(E_l, R_{\mathrm{MT}})}. \tag{2.50}$$

This defines the APW basis, where the energies E_l enter as parameters. For an accurate description of band structures in terms of APWs, it turns out to be necessary to set the expansion parameters E_l equal to the band energies $E_{k,\nu}$, where ν is a band index. As the basis functions depend then on the band energies, the solution of the equation resulting from the Schrödinger equation becomes a nonlinear problem, which is computationally much more demanding than a secular problem. Moreover, the APW basis functions are by construction discontinuous in slope at the muffin-tin boundaries. Therefore, the variational procedure of finding the expansion coefficients of the final wave functions in terms of APWs needs to be adjusted, such that the final wave functions have a continuous first derivative in the whole space.

The problem with discontinuities and — most important — the problems caused by nonlinear equations occurring in all augmented wave methods are avoided in the *linearized* augmented wave methods introduced by Andersen [49] in the 1970s. This development paved the way for realistic calculations of first row and 3d elements or complex systems [22]: On going from an APW to an LAPW basis, the radial basis functions $u_l(E_l, r^\mu)$ in the muffin-tins are supplemented by their energy derivatives $\partial_E u_l(E, r^\mu)|_{E=E_l} \equiv \dot{u}_l(E_l, r^\mu)$, and both, u_l and $\dot{u}_l$ are now evaluated at a *fixed* energy E_l. This yields basis functions of the form[4]

$$\phi_K(k, r)=\begin{cases} e^{i(K+k)r} & \text{interstitial} \\ \sum_{lm}(a_{lm}^{\mu K}(k) u_l(r^\mu)+b_{lm}^{\mu K}(k)\dot{u}_l(r^\mu)) Y_{lm}(r^\mu) & \text{muffin-tin } \mu, \end{cases} \tag{2.51}$$

[4]We skip the dependence of u_l and $\dot{u}_l$ on E_l in the following formulas, as the reference energies are fixed.

where there are now *two* expansion coefficients, $a_{lm}^{\mu K}(k)$ and $b_{lm}^{\mu K}(k)$, per muffin-tin sphere and angular momentum channel. These coefficients are fixed by requiring continuity in value and first derivative of the LAPW basis functions, which fully determines the LAPW basis set. Approaching from this formulation of LAPW, further improvements have been established like the so-called additive augmentation [50] or the implementation the so-called full-potential LAPW method (FLAPW) that allows to treat the full-potential and charge density without any shape approximations [51], efficiently. Today, methods like FLAPW enjoy great popularity for their high accuracy and are often used in problems where effects related to spin-orbit coupling play an important role. The main drawback of FLAPW and related methods lies in the bigger computational demands as compared to pseudopotential approaches or PAW.

2.3.3 Projector augmented waves

The pseudopotential and augmented wave methods approach the problem of solving the Schrödinger / Kohn-Sham equations from two opposite sides: In the pseudopotential approaches, the operators occurring in the Hamiltonian are transformed, whereas the augmented wave methods aim at constructing an efficient basis set but leaving the Hamiltonian unchanged. Pseudopotential theory can be derived with the so-called orthogonalized plane waves (OPW) which project atomic core states out of the variational Hilbert space. This procedure can be expressed in terms of a transformation operator $\mathcal{T}$ [39]:

$$|\Psi_n\rangle = \mathcal{T}|\tilde{\Psi}_n\rangle, \tag{2.52}$$

where $|\Psi_n\rangle$ denotes a physical all-electron wave function with its oscillations near the nuclei and $|\tilde{\Psi}_n\rangle$ is a smoother auxiliary wave function. Shifting the transformation $\mathcal{T}$ to the operators occurring in the Kohn-Sham Hamiltonian yields (after further approximations) pseudopotentials with the smooth functions remaining as variational degrees of freedom. However, the all-electron wave functions can be recovered from their smooth counterparts using $\mathcal{T}$ as in Eq. (2.52), which augments the auxiliary functions within the muffin-tin spheres. Exploiting this formal similarity of pseudopotential and augmented wave approaches, Blöchl [52] unified them in the *projector augmented waves* (PAW) method, which is discussed in the following section.

The central concept of the PAW method is a transformation mapping, $\mathcal{T}$, as in Eq. (2.52) with

$$\mathcal{T} = 1 + \sum_{\mu} \mathcal{T}_{\mu}, \tag{2.53}$$

where the summation is over all augmentation spheres μ and the operator $\mathcal{T}_{\mu}$ acts within the sphere μ. It applies projector functions $|\tilde{p}_i\rangle$ for augmenting auxiliary partial waves $|\tilde{\phi}_i\rangle$ with their physical counterparts $|\phi_i\rangle$:

$$\mathcal{T}_{\mu} = \sum_{i \in \mu} \left(|\phi_i\rangle - |\tilde{\phi}_i\rangle \right) \langle \tilde{p}_i|. \tag{2.54}$$

Here i denotes the quantum numbers specifying partial waves located in the muffin-tin-sphere μ. As in the construction of pseudopotentials, physical partial waves $|\phi_i\rangle$ are solutions of the Schrödinger equation of isolated atoms, while the corresponding auxiliary functions $|\tilde{\phi}_i\rangle$ are chosen to match $|\phi_i\rangle$ outside the augmentation spheres, being smooth inside and continuously differentiable in all space. The projector states $|\tilde{p}_i\rangle$ are finally defined by

$$\langle \tilde{p}_i | \tilde{\phi}_j \rangle = \delta_{ij}. \tag{2.55}$$

The explicit parameterizations of the auxiliary wave functions and the projector functions employed by the VASP code and used in this work are given in Ref. [53]. This leads to the PAW decomposition of the wave functions:

$$|\Psi\rangle = |\tilde{\Psi}\rangle + \sum_{\mu} \left(|\Psi^1_\mu\rangle - |\tilde{\Psi}^1_\mu\rangle \right) \tag{2.56}$$

with

$$|\Psi^1_\mu\rangle = \sum_{i \in \mu} |\phi_i\rangle \langle \tilde{p}_i | \tilde{\Psi}\rangle \tag{2.57}$$

$$|\tilde{\Psi}^1_\mu\rangle = \sum_{i \in \mu} |\tilde{\phi}_i\rangle \langle \tilde{p}_i | \tilde{\Psi}\rangle. \tag{2.58}$$

The PAW basis functions are continuously differentiable by construction. The augmentation done in PAW is similar to the additive augmentation in the context of LAPW [50] in the sense that $|\tilde{\Psi}\rangle$ extends into the augmentation spheres, where only those parts $|\tilde{\phi}_i\rangle$ are removed that are replaced by some all-electron counterpart $|\phi_i\rangle$.

Using the transformation operator $\mathcal{T}$ any observable A can be calculated from the auxiliary wave functions as

$$\langle A \rangle = \sum_n f_n \langle \tilde{\Psi}_n | \mathcal{T}^\dagger A \mathcal{T} | \tilde{\Psi}_n \rangle, \tag{2.59}$$

where f_n is the occupation number of the state $|\Psi_n\rangle$. For sufficiently local operators like the kinetic energy or the electron density and converged partial wave expansions this simplifies to[5]

$$\langle A \rangle = \sum_n f_n \langle \tilde{\Psi}_n | A | \tilde{\Psi}_n \rangle + \sum_\mu \sum_{i,j \in \mu} D_{ij} (\langle \phi_j | A | \phi_i \rangle - \langle \tilde{\phi}_j | A | \tilde{\phi}_i \rangle), \tag{2.60}$$

where all information about the augmentation channels enters with the one-center density matrices

$$D_{ij} = \sum_n f_n \langle \tilde{\Psi}_n | p_j \rangle \langle p_i | \tilde{\Psi}_n \rangle. \tag{2.61}$$

[5] We skip writing contribution from core states explicitly.

Correspondingly, the electron density decomposes as $n(r) = \tilde{n}(r) + \sum_\mu (n^1_\mu(r) - \tilde{n}^1_\mu(r))$ with

$$\begin{aligned} \tilde{n}(r) &= \sum_n f_n \left|\tilde{\Psi}_n(r)\right|^2 \\ n^1_\mu(r) &= \sum_{i,j\in\mu} D_{ij}\phi^*_i(r)\phi_j(r) \\ \tilde{n}^1_\mu(r) &= \sum_{i,j\in\mu} D_{ij}\tilde{\phi}^*_i(r)\tilde{\phi}_j(r). \end{aligned} \tag{2.62}$$

The Kohn-Sham equations in PAW representation are obtained by applying the variational principle to the total energy functional with respect to the auxiliary wave functions: Since the transformation operator $\mathcal{T}$ does not depend on the electron density, the Kohn-Sham equations transform according to Eq. (2.59) as

$$\mathcal{T}^\dagger H \mathcal{T}|\tilde{\Psi}_k\rangle = \epsilon_k \mathcal{T}^\dagger \mathcal{T}|\tilde{\Psi}_k\rangle. \tag{2.63}$$

Here, $H = -\frac{\hbar^2}{2m}\Delta + v_{\text{eff}}(r)$ is the Kohn-Sham Hamiltonian from Eq. (2.17), so that Eq. (2.63) is a Schrödinger type equation but with the overlap operator $\mathcal{T}^\dagger\mathcal{T}$ occurring on the right hand side. To solve Eq. (2.63) the auxiliary wave functions are expanded in terms of plane waves:

$$\tilde{\Psi}_k(r) = \langle r|\tilde{\Psi}_k\rangle = \sum_G c_{k,G} e^{i(k+G)r}. \tag{2.64}$$

For comparison to the pseudopotential approach (see section 2.3.1) it is useful to consider the PAW decomposition of the total energy functional. Similar to expectation values of single particle operators, Eq. (2.60), the total energy is divided into three parts

$$E = \tilde{E} + \sum_\mu E^1_\mu - \tilde{E}^1_\mu. \tag{2.65}$$

with

$$\tilde{E} = \sum_n f_n \langle\tilde{\Psi}_n| - \frac{\hbar^2}{2m}\nabla^2 + \bar{v}|\tilde{\Psi}_n\rangle + E_{\text{H}}[\tilde{n} + \tilde{Z}] + E_{\text{xc}}[\tilde{n}] \tag{2.66}$$

$$E^1_\mu = \sum_{i,j\in\mu} D_{ij}(\langle\phi_j| - \frac{\hbar^2}{2m}\nabla^2|\phi_i\rangle) + E_{\text{H}}[n^1_\mu + Z] + E_{\text{xc}}[n^1_\mu] \tag{2.67}$$

$$\tilde{E}^1_\mu = \sum_{i,j\in\mu} D_{ij}(\langle\tilde{\phi}_j| - \frac{\hbar^2}{2m}\nabla^2 + \bar{v}|\tilde{\phi}_i\rangle) + E_{\text{H}}[\tilde{n}^1_\mu + \tilde{Z}_\mu] + E_{\text{xc}}[\tilde{n}^1_\mu]. \tag{2.68}$$

The potential $\bar{v}$ enters the total energy in the form of an intelligent zero and is included to improve the plane wave convergence properties. The compensation charge density $\tilde{Z}(r) = \sum_\mu \tilde{Z}_\mu(r)$ plays the role of the pseudized charge density in the pseudopotential approach and is constructed such that the electrostatic multipole moments of the one-center contributions to the charge density, $n^1_\mu(r) + Z_\mu(r) - \tilde{n}^1\mu(r) - \tilde{Z}_\mu(r)$, vanish for each atomic site.

In contrast to the norm-conserving pseudopotentials, $\tilde{Z}_\mu(r)$ is non-spherical and adapts to its atomic environment. PAW can be therefore viewed as a pseudopotential method that adapts the pseudopotential to its instantaneous environment. It can be shown that the total energy expression in pseudopotential theory, Eq. (2.47), follows from the PAW total energy if a Taylor expansion in the on-site occupancy matrices D_{ij} is truncated after linear order [52, 53].

The main approximations in practical PAW implementations are the frozen core approximation, finite plane wave cut-offs and the finite number of augmentation channels being included. The latter two approximations can be well controlled by increasing the plane wave cut-off and/or the number of augmentation partial waves [52].

2.4 The Vienna Ab Initio Simulation Package

For all DFT calculations in this work the Vienna Ab Initio Simulation Package (VASP) has been applied. It is a complex software package for performing electronic structure and molecular dynamics simulations. The PAW method as well as Vanderbilt's ultrasoft pseudopotentials are implemented in VASP to expand the solutions of the Kohn-Sham equations [53]. In this work, the PAW basis-sets have been applied due to their higher accuracy and their suitability for many body calculations.

For iterative eigenvector optimization, VASP provides different algorithms based on the so-called "residual vector minimization schemes": The central quantity of all these algorithms is the residual vector

$$|R_n\rangle = (H - E)|\tilde{\Psi}_n\rangle \text{ with } E = \frac{\langle\tilde{\Psi}_n|H|\tilde{\Psi}_n\rangle}{\langle\tilde{\Psi}_n|\tilde{\Psi}_n\rangle},$$

where $|\tilde{\Psi}_n\rangle$ denotes a trial wave function. These vectors are used to expand a subspace of the bands followed by the diagonalization of the Kohn-Sham Hamiltonian in the expanded subspace, iteratively. There are the *conjugate gradient* (CG) and *Davidson block algorithm* as well as the *residual minimization method by direct inversion in the iterative subspace* (RMM-DIIS) available for this purpose in VASP. As the Davidson block algorithm turned out to be well suited for our parallel computer cluster, it has been used in this work.

Ionic relaxations can be performed in VASP by using damped Car-Parrinello molecular dynamics and related velocity quench algorithms, a quasi-Newton and a CG algorithm. For the graphene-adsorbate systems the velocity quench algorithm turned out to be the fasted and most reliable starting point. Near the total energy minimum, switching to CG could sometimes further speed up the relaxations. A flow diagram summarizing the VASP electronic and ionic relaxation cycle is shown in Fig. 2.1.

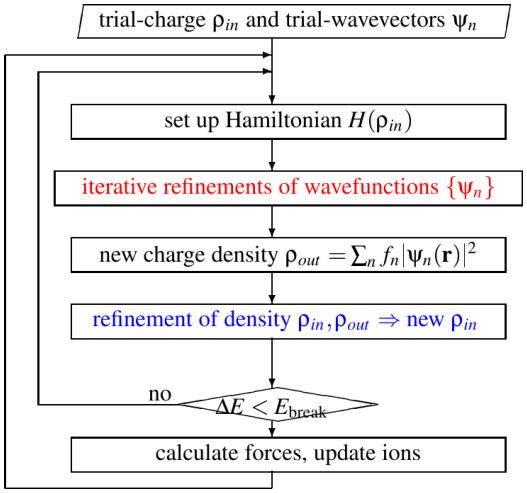

Figure 2.1: Flow diagram of the VASP loop. From [54].

2.5 Free energy functional formalism

To obtain a more general description of the electronic structure of solids and to construct approaches beyond DFT we consider the effective action formalism as introduced, e.g., in [55]. The discussion will follow mainly Refs. [56] and [31]. We start with a many electron Hamiltonian, $\hat{H}$ in second quantized form like Eq. (2.5). Such a Hamiltonian can be a fully first-principles Hamiltonian like Eq. (2.6) transferred to a second quantized notation or any simplified model Hamiltonian. With the particle number operator, $\hat{N}$, and the chemical potential, μ, the grand canonical partition function is

$$Z = \mathrm{Tr}\ e^{-\beta(\hat{H}-\mu\hat{N})}. \tag{2.69}$$

The corresponding thermodynamic potential is the grand canonical potential denoted by

$$F = -\frac{1}{\beta}\ln Z \tag{2.70}$$

and sometimes referred to as "free energy" in this context. The partition function can be expressed as a path integral of Grassmann numbers, η_i, by

$$Z = \int D[\eta_i^*(\tau)\eta_i(\tau)] e^{-\int_0^\beta \mathrm{d}\tau \left[\sum_i \eta_i^*(\tau)(\partial_\tau - \mu)\eta_i(\tau) + H(\eta_i^*(\tau),\eta_i(\tau))\right]}. \tag{2.71}$$

The integration measure is defined in Eq. (2.65) of Ref. [55] and $H(\eta_i^*(\tau), \eta_i(\tau)) = \langle\eta(\tau)|H|\eta(\tau)\rangle$, where

$$|\eta(\tau)\rangle = e^{-\sum_i \eta_i(\tau)c_i^\dagger}|0\rangle \tag{2.72}$$

is a coherent state created from the Fock vacuum, $|0\rangle$, with

$$c_i|\eta(\tau)\rangle = \eta_i(\tau)|\eta(\tau)\rangle. \tag{2.73}$$

Defining the action

$$S[\eta_i^*(\tau)\eta_i(\tau)] = -\int_0^\beta \mathrm{d}\tau \left[\sum_i \eta_i^*(\tau)(\partial_\tau - \mu)\eta_i(\tau) + H(\eta_i^*(\tau), \eta_i(\tau))\right] \tag{2.74}$$

the partition function is given by

$$Z = \int D[\eta_i^*(\tau)\eta_i(\tau)] e^{-S[\eta_i^*(\tau)\eta_i(\tau)]} \tag{2.75}$$

or in a symbolic short-hand notation

$$Z = \int D[\eta^*\eta] e^{-S[\eta^*\eta]}. \tag{2.76}$$

We choose now an observable of interest A, that couples to a source J, and consider the modified action $S + JA$. The corresponding partition function and free energy are now functionals of J:

$$F[J] = -\frac{1}{\beta} \ln \int D[\eta^*\eta] e^{-S[\eta^*\eta] - JA[\eta^*\eta]}. \tag{2.77}$$

Consequently, $\frac{\delta F[J]}{\delta J} = A[J]$, which can formally be inverted to yield $J = J[A]$. Using a Legendre transform, the source J can be eliminated from F in favor of A, which yields the new functional

$$\Gamma[A] = F[J[A]] - AJ[A]. \tag{2.78}$$

Variation of w.r.t. A yields $\frac{\delta \Gamma[A]}{\delta A} = J[A]$ and in case of stationary $\Gamma[A]$ the free energy is $F[J[A]] = \Gamma[A]$, i.e. the Legendre transformed functional gives the free energy. Moreover, $\Gamma[A]$ being stationary is equivalent to A taking its physical value corresponding to the original system, Eqs. (2.74) and (2.76).

We, now, split the action S according to $S = S_0 + \lambda S_1$, where λ plays the role of a coupling constant, as e.g. already done in the context of constructing exchange-correlation functionals in section 2.2.1. S_0 will serve as a "non-interacting" reference system for the full interacting problem. The functional $\Gamma = \Gamma_\lambda[A]$ depends now on the coupling constant and it is useful to express the fully interacting functional by means of coupling constant integration

$$\Gamma[A] = \Gamma_0[A] + \Delta\Gamma[A] \tag{2.79}$$

$$= \Gamma_0[A] + \int_0^1 \mathrm{d}\lambda \frac{\mathrm{d}\Gamma_\lambda[A]}{\mathrm{d}\lambda}. \tag{2.80}$$

As does Γ, so does $J = J_\lambda[A]$ depend now on λ. Substituting the definition of Γ, Eq. (2.78), for the non-interacting case $\lambda = 0$ into Eq. (2.79) yields

$$\Gamma[A] = F_0[J_0[A]] - AJ_0[A] + \Delta\Gamma[A]. \tag{2.81}$$

J_0 is called "constraining field", as it forces the non-interacting reference system described by the action $S_0[\eta^*\eta] + J_0 A[\eta^*\eta]$ to yield the desired expectation value

Theory	MFT	DFT	DMFT
Observable	local magnetization m_i	local density $n(r)$	local Green function $G_{ii}(\omega)$
Reference system	spin in effective field	non-interacting electrons in effective potential	Anderson impurity model
Constraining field	effective local field	Kohn-Sham potential	effective hybridization

Table 2.1: Comparison of theories in the unifying framework of functionals of physical observables.A-priori unrelated theories differ only in the physical observable of interest, the reference system, the constraining field and the functional relating the fully interacting problem with the reference system. From [56].

for A. At the physical value of A, $\Gamma[A]$ is stationary which determines by Eq. (2.81) the constraining field

$$J_0[A] = \frac{\delta \Delta\Gamma[A]}{\delta A}. \tag{2.82}$$

In turn, a given constraining field determines A by $\frac{\delta F_0[J_0]}{\delta J_0} = A[J_0]$ or, equivalently, by considering

$$\Omega_0[J_0, A] = F_0[J_0] - AJ_0 \tag{2.83}$$

as functional of two *independent* variables, J_0 and A, and requiring stationarity,

$$\frac{\delta \Omega_0[J_0, A]}{\delta J_0} = 0. \tag{2.84}$$

The physical expectation value of the observable A is, hence, a self-consistent solution of Eqs. (2.82) and (2.84).

This formalism can be applied to any physical system and it gives a unifying framework for theories from different areas of physics. These include the classical Weiss mean field theory (MFT) of Ising mangets, density functional theory and dynamical mean field theory (DMFT). In view of the effective action formalism, these theories differ only in the physical observable, A, they focus on, the reference system, S_0, the constraining field, J_0, and the functional $J_0 = J_0[A]$, Eq. (2.82). Table 2.1 contains a comparison of these theories. In the following we will shortly rederive DFT from this effective action approach and introduce extensions, such as LDA+U, LDA++ and LDA+DMFT.

2.5.1 Functional integral derivation of DFT

With the electron density, $\hat{n}(r) = \Psi^\dagger(r)\Psi(r)$, chosen as fundamental observable, the conjugated source field $J(r)$ modifies the action as

$$S'[J] = S + \int \mathrm{d}x J(r)\Psi^\dagger(x)\Psi(x), \tag{2.85}$$

where $x = (r, \tau, \sigma)$. The source term acts like an additional one-electron potential. From the electronic point of view and in the approximation of frozen nuclei

any materials differ only by external one-electron potentials, which are conjugate quantities of the electron density. This can be viewed as deeper reason behind the first Hohenberg-Kohn theorem.

The free energy becomes a functional of the source field $J(r)$,

$$F[J] = -\frac{1}{\beta} \ln \int D[\eta^* \eta] e^{-S'[\eta^* \eta]}, \tag{2.86}$$

and the Legendre transform w.r.t. $J(r)$ yields

$$\Gamma_{\mathrm{DFT}}[n] = F[J[n]] - \int \mathrm{d}r J(r) n(r). \tag{2.87}$$

In analogy to the preceding section, a non-interacting reference system has to be chosen,

$$\Gamma_{\mathrm{DFT}}[n] = \Gamma_{0,\mathrm{DFT}}[n] + \Delta\Gamma_{\mathrm{DFT}}[n], \tag{2.88}$$

and the self-consistency conditions, Eqs. (2.82) and (2.84), have to be imposed. In the Kohn-Sham approach to DFT, the reference system is formed by non-interacting electrons in an effective potential, $v_{\mathrm{eff}}(r) = v_{\mathrm{ext}}(r) + J_0(r)$, which is the sum of an external potential $v_{\mathrm{ext}}(r)$ and the constraining field $J_0(r)$. Comparison to Eq. (2.22) shows that finally we will obtain $J_0(x) = v_{\mathrm{H}}(r) + v_{\mathrm{xc}}(r)$.

We can calculate the free energy of the reference system and generalize as in Eq. (2.83) to the potential $\Omega_0[J_0, n]$ containing the potential and the density as independent variables:

$$\Omega_0[J_0, n] = -\sum_{\omega_n} \mathrm{tr}\, \ln[i\omega_n - \hat{t} - \hat{v}_{eff}] - \int \mathrm{d}r J_0(r) n(r), \tag{2.89}$$

where the tr denotes the trace over all single electron degrees of freedom, ω_n are the fermionic Matsubara frequencies. $\hat{t} \to -\nabla^2/2$ and $\hat{v}_{eff} \to v_{\mathrm{eff}}(r)$ are the single particle kinetic energy and effective potential operators, respectively.[6] By construction Ω_0 is stationary w.r.t. to $J_0(r)$ and $n(r)$ and performing the variation from Eq. (2.84) yields

$$n(r) = \frac{1}{\beta} \sum_n \langle r | [i\omega_n - \hat{t} - \hat{v}_{eff}]^{-1} | r \rangle, \tag{2.90}$$

which implicitly defines $J_0 = J_0[n]$ in terms of n. Obtaining the density from Eq. (2.90) is equivalent to solving the Kohn-Sham equation (2.17) and using the corresponding Green function of the Kohn-Sham particles

$$G_{\mathrm{KS}}(r, r', i\omega_n) = \sum_i \frac{\psi_i(r) \psi_i^*(r')}{i\omega_n - \epsilon_i} \tag{2.91}$$

to calculate the density according to $n(r) = \frac{1}{\beta} \sum_{\omega_n} G_{\mathrm{KS}}(r, r, i\omega_n) e^{i\omega_n 0^+}$.

[6] The chemical potential is understood to be included in $v_{\mathrm{eff}}(r)$.

The connection of the reference system to the fully interacting problem is given by means coupling constant integration, where Eqs. (2.79)-(2.82) yield Eqs. (2.38) -(2.40) when applied to the special case of DFT. Therefore, the Hartree and exchange correlation functional enter this general formalism as

$$\Delta\Gamma_{\mathrm{DFT}}[n] = E_{\mathrm{H}}[n] + E_{\mathrm{xc}}[n]. \tag{2.92}$$

The coupling constant integration appears here as natural link between the reference and the full system, whereas in the classical approach to DFT, as discussed in section 2.2.1, it had to be introduced ”by hand”. As in section 2.2 these arguments can be straightforwardly generalized to include the spin density $m(r)$ as additional variational quantity and to obtain spin density functional theory.

2.5.2 LDA+U

For many materials with delocalized s- and p-electrons ground state properties as well as excitation spectra obtained from LDA and the corresponding Kohn-Sham Green functions compare very well to experiments. However, LDA (as well as GGA) often fail qualitatively to describe systems containing strongly localized electrons including Mott insulating transition metal compounds and f-electron systems like lanthanides or Pu. This observation motivates the introduction of hybrid methods, which separate the electrons into weakly and strongly correlated: the weakly correlated electrons are described by means of DFT, whereas for the strongly correlated electrons many-body corrections beyond DFT, like DMFT, are included. This can be systemically achieved by including additional observables describing the strongly correlated electrons into the functional Γ.

In the L(S)DA+U method, the spin-dependent density matrix of a set of correlated orbitals, n^{σ}_{ab}, is considered as additional variational degree of freedom. With the conjugated constraining field λ^{σ}_{ab}, the total free energy is now a functional of the Kohn-Sham potential $v_{\mathrm{eff}}(x)$ and λ^{σ}_{ab}. Its Legendre transform with respect to the density, ρ, the spin density, m, and n^{σ}_{ab} reads as

$$\Gamma_{\mathrm{LDA+U}}[\rho, m, n_{ab}] = \Gamma_{0,\mathrm{LDA}}[\rho, m] - \lambda^{\sigma}_{ba} n^{\sigma}_{ab} + \Delta\Gamma_{LDA+U}[\rho, m, n^{\sigma}_{ab}], \tag{2.93}$$

where

$$\Delta\Gamma_{LDA+U}[\rho, m, n_{ab}] = E_{\mathrm{H}}[\rho] + E^{\mathrm{LDA}}_{\mathrm{xc}}[\rho, m] + \Phi_U[n^{\sigma}_{ab}] - \Phi_{\mathrm{DC}}[n^{\sigma}_{ab}]. \tag{2.94}$$

LDA Hartree and exchange correlation energy is corrected corrected by a term $\Phi_U[n^{\sigma}_{ab}] - \Phi_{\mathrm{DC}}[n^{\sigma}_{ab}]$ accounting for on-site Coulomb interaction effects. In the LDA+U scheme, the on-site Coulomb interaction energy is evaluated in the Hartree-Fock approximation,

$$\Phi_U[n_{ab}] = \frac{1}{2} \sum_{abcd \in C,\sigma} U_{acdb} n^{\sigma}_{ab} n^{-\sigma}_{cd} + (U_{acdb} - U_{acbd}) n^{\sigma}_{ab} n^{\sigma}_{cd}, \tag{2.95}$$

with the indices a, b, c, d including orbital and σ spin quantum numbers. C denotes the subspace of correlated orbitals and U_{abcd} is the local Coulomb interaction matrix element

$$U_{abcd} = \int \mathrm{d}r\mathrm{d}r' \chi_a^*(r)\chi_b^*(r')v_C(r-r')\chi_c(r')\chi_d(r), \tag{2.96}$$

where $v_C(r-r')$ is the screened Coulomb interaction and the functions $\chi_i(r)$, $i = a, b, c, d$, form a basis of correlated subspace. As L(S)DA contains already Coulomb interaction effects, the LDA contribution to the on-site Coulomb energy has be corrected for, which is done by the double-counting term, $\Phi_{\mathrm{DC}}[n_{ab}]$. The form of $\Phi_{\mathrm{DC}}[n_{ab}]$ is unknown a-priori and additional assumptions on the way the on-site Coulomb interaction is included in LDA need to be made. One widely used double-counting scheme, called fully localized limit, is based on two observations [57]: (1) LDA usually gives reliable total energies, while (2) orbital energies are often badly represented: One well known example is hydrogen atom with the orbital energy being -0.54 Ry instead of -1 Ry, but the total energy being -0.96 Ry which is very close to the exact value of -1 Ry. Related to this is the shortcoming of LDA that the potential $\frac{\delta\Gamma_{LDA}[n]}{\delta n(x)}$ varies continuously with particle number, N, whereas the (still unknown) exact density functional leads to an effective one-electron potential that jumps discontinuously when N passes through an integer value. One, therefore, constructs the double counting such that the total LDA+U energy is not changed w.r.t. LDA but the desired potential jump is created for integer filling of the correlated orbitals. It is assumed that L(S)DA correctly yields the total energy for *isolated atoms* with orbitally averaged Coulomb

$$\bar{U} = \frac{1}{(\dim C)^2} \sum_{ab\in C} U_{abba} \tag{2.97}$$

and exchange interaction

$$\bar{J} = \bar{U} - \frac{1}{(\dim C - 1)(\dim C)} \sum_{ab\in C} (U_{abba} - U_{abab}) \tag{2.98}$$

and uses the corresponding interaction energy as double counting correction [58]:

$$\Phi_{\mathrm{DC}}[n_{ab}] = \frac{1}{2}\bar{U}N(N-1) - \frac{1}{2}\bar{J}\left[N^{\uparrow}(N^{\uparrow}-1) + N^{\downarrow}(N^{\downarrow}-1)\right] \tag{2.99}$$

with $N^{\sigma} = \sum_a n_{aa}^{\sigma}$ for $\sigma = \uparrow, \downarrow$, $N = N^{\uparrow} + N^{\downarrow}$. This form of the double counting correction is implemented in VASP and will be used in section 6.5.

The generalized Kohn-Sham equations are derived in analogy to Eqs. (2.89) - (2.91) yielding

$$n(r) = \frac{1}{\beta}\sum_n \langle r|[i\omega_n - \hat{t} - \hat{v}_{eff} - \hat{\lambda}]^{-1}|r\rangle \tag{2.100}$$

$$n_{ab} = \frac{1}{\beta}\sum_n \langle \chi_a|[i\omega_n - \hat{t} - \hat{v}_{eff} - \hat{\lambda}]^{-1}|\chi_b\rangle. \tag{2.101}$$

Here, $\hat{\lambda} = \sum_{ab\in C} |\chi_a\rangle \lambda_{ab} \langle\chi_b|$ denotes operator form of the local constraining matrix field, which is given by

$$\lambda^{\sigma}_{ab} = \frac{\delta \Delta\Gamma_{LDA+U}[\rho, m, n^{\sigma}_{ab}]}{\delta n^{\sigma}_{ba}} = M_{ab,\sigma} - V^{\mathrm{DC}}_{ab,\sigma} \tag{2.102}$$

with

$$M_{ab,\sigma} = \sum_{cd\in C} U_{bcda} n^{-\sigma}_{cd} + (U_{bcda} - U_{bcad}) n^{\sigma}_{cd}, \tag{2.103}$$

$$V^{\mathrm{DC}}_{ab,\sigma} = \delta_{ab} \left[\bar{U}(N - 1/2) - \bar{J}(N^{\sigma} - 1/2) \right]. \tag{2.104}$$

Practical implementations of the LDA+U scheme are usually based on an LDA code which includes localized orbitals $|\chi_a\rangle$, for example as part of the employed basis set. In the original implementation, these localized states were LMTO partial waves [59], but can also be atomic centered augmentation functions as in FLAPW [60], mixed basis approaches [61] or PAW [62]. Using these localized states, the operator $\hat{\lambda}$ is added as additional orbital-dependent potential to the Kohn-Sham Hamiltonian:

$$\hat{H}_{KS} = \hat{H}_{LSDA} + \sum_{ab,\sigma} |\chi^{\sigma}_a\rangle \left(M_{ab,\sigma} - V^{\mathrm{DC}}_{ab,\sigma} \right) \langle\chi^{\sigma}_b|. \tag{2.105}$$

When going from DFT to spin density functional theory, the inclusion of the spin gives more flexibility in formulation of an accurate total energy functional. Similarly, the additional variational degrees of freedom in LDA+U allow one to obtain a more accurate total energy functional. Correspondingly, ground state properties of systems like Gd (type of magnetic order) or Mott Hubbard compounds (magnetic moments) are better described in LDA+U than in L(S)DA [58].

However, when interpreting the Kohn-Sham quasiparticles as excitations of the real system, L(S)DA, LDA+U and even the unknown exact density functional have a common intrinsic shortcoming: The Kohn-Sham potential playing the role of the self-energy is static and real in these approaches. Therefore, any phenomenon due to the energy dependence of the self-energy cannot be covered by these static theories. Correlation effects like mass enhancement, the Kondo effect, finite quasiparticle lifetimes, or the formation of Mott-Hubbard insulators cannot be explained by excitation spectra calculated within any of these approaches. A promising way to deal with these phenomena in an first-principles way is the generalization of LDA+U to include dynamical effects, called LDA++ [38].

2.5.3 LDA++

From a practical point of view, all LDA++ methods as well as in LDA+U base on a Hubbard type interaction being added to the Kohn-Sham Hamiltonian, which serves as bare, "non-interacting" starting point. As in the case of DFT or LDA+U, these approaches can be formally justified by deriving them within an effective action formalism. To explicitly include dynamics, the Green functions of correlated orbitals, $G_{ab}(\tau, \tau') = -\langle T_\tau c_a(\tau) c^{\dagger}_b(\tau') \rangle$, become variational quantities and replace

the local density matrices n_{ab}^{σ} from the LDA+U formalism. The electron density is maintained as a variational quantity. The action is, hence, modified by sources for the density, $L(r)$, and for the correlated Green functions, $J_{ba}(\tau,\tau')$:

$$S' = S + \int \mathrm{d}x L(r)\psi^*(x)\psi(x) + \sum_{ab}\int \mathrm{d}\tau\mathrm{d}\tau' J_{ba}(\tau,\tau')c_a^*(\tau)c_b(\tau'). \tag{2.106}$$

The Legendre transform of the corresponding free energy to eliminate the sources $L(r)$ and $J_{ba}(\tau,\tau')$ yields the functional

$$\Gamma_{\mathrm{LDA++}}[\rho,m,G_{ab}(\tau,\tau')] = \Gamma_{0,\mathrm{LDA}}[\rho,m] - \mathrm{Tr}(JG) + \Delta\Gamma_{LDA++}[\rho,m,G_{ab}(\tau,\tau')], \tag{2.107}$$

with

$$\mathrm{Tr}(JG) = \left[\int \mathrm{d}\tau\mathrm{d}\tau' J_{ba}(\tau,\tau')G_{ab}(\tau,\tau')\right] \tag{2.108}$$

and

$$\Delta\Gamma_{LDA++}[\rho,m,n_{ab}] = E_{\mathrm{H}}[\rho] + E_{\mathrm{xc}}^{\mathrm{LDA}}[\rho,m] + \Phi_U[G_{ab}(\tau,\tau')] - \Phi_{\mathrm{DC}}[G_{ab}(\tau,\tau')]. \tag{2.109}$$

This is the same as for LDA+U, Eqs. (2.93) and (2.94), apart from the fact that the local Coulomb interaction is not treated in Hartree-Fock approximation any more. A formally exact expression for this functional is [31]

$$\Phi_U[G_{ab}(\tau,\tau')] = \frac{1}{2}\int_0^1 \mathrm{d}\lambda \sum_{abcd\in C,\sigma,\sigma'} U_{abcd}\langle c_a^\dagger c_b^\dagger c_c c_d\rangle_\lambda. \tag{2.110}$$

As in the case of LDA+U, the double counting term is a-priori unknown and needs to be determined by assuming a particular form of local Coulomb interaction being included in LDA. The same double counting as in LDA+U might for example be used in LDA++.

As before, a Kohn-Sham decomposition allowing for full charge self-consistency can be made by performing the variation of the reference system like in Eqs. (2.83)-(2.84) or in the analog Eqs. (2.89)-(2.91):

$$n(r) = \frac{1}{\beta}\sum_n \langle r|[i\omega_n - \hat{t} - \hat{v}_{eff} - \hat{J}(i\omega_n)]^{-1}|r\rangle \tag{2.111}$$

$$G_{ab}(i\omega) = \langle\chi_a|[i\omega_n - \hat{t} - \hat{v}_{eff} - \hat{J}(i\omega_n)]^{-1}|\chi_b\rangle. \tag{2.112}$$

The constraining field, $\hat{J}(i\omega_n) = \sum_{ab\in C}|\chi_a\rangle J_{ab}(i\omega_n)\langle\chi_b|$, plays the role of a self-energy. It is given by

$$J_{ab}(i\omega_n) = \Sigma_{ab}(i\omega) - \Sigma_{ab}^{\mathrm{DC}} \tag{2.113}$$

with

$$\Sigma_{ab}(i\omega) = \frac{\delta\Phi_U[G_{ab}(i\omega)]}{\delta G_{ba}(i\omega)}, \tag{2.114}$$

$$\Sigma_{ab,\sigma}^{\mathrm{DC}} = \frac{\delta\Phi_{\mathrm{DC}}[n_{ab}]}{\delta n_{ba}}. \tag{2.115}$$

The explicit form of the functional $\Phi_U[G_{ab}(\tau,\tau')]$, Eq. 2.110, is unknown in general, but can be represented diagrammatically [31]. For lattices of correlated sites, one widely used approximation to the functional $\Phi_U[G_{ab}(\tau,\tau')]$ is provided by dynamical mean field theory (DMFT). It assumes $\Phi_U[G_{ab}(\tau,\tau')] \to \Phi_{\mathrm{DMFT}}[G_{ab}(\tau,\tau')]$ as the sum of two-particle irreducible graphs constructed from the local interaction and local Green functions [31] and is equivalent to assuming a local self-energy $\Sigma_{Ra,R'b}(i\omega) = \delta_{RR'}\Sigma_{ab}(i\omega)$ [56].

In the second part of this work we will be dealing with magnetic ad-atoms and nanostructures on metal surfaces. The metal hosts will provide sp-type bands at the Fermi level which are well described by LDA. However, the magnetic ad-atoms will require to include dynamic on-site correlation effects and will be studied by means of LDA++.

We will deal with one correlated site (the magnetic ad-atom) and use Anderson impurity model resulting from Eqs. (2.112) and (2.113) for the density frozen to its LDA form to obtain excitation spectra. In practice, this corresponds to considering Anderson impurity models (AIM) of the form

$$\hat{H} = \hat{H}_{\mathrm{KS}} + \hat{H}_U - \hat{H}_{\mathrm{DC}}, \tag{2.116}$$

where Kohn-Sham eigenstates $|K\rangle$ and energies ϵ_K, $H_{\mathrm{KS}} = \sum_K \epsilon_K |K\rangle\langle K| = \sum_K \epsilon_K c_K^\dagger c_K$ serve as bare starting point. The impurity site is treated as correlated subspace and the Coulomb interaction $\hat{H}_U = \sum_{abcd\in C,\sigma,\sigma'} U_{abcd} c_a^\dagger c_b^\dagger c_c c_d$ is added with double counting, $\hat{H}_{\mathrm{DC}}$, being corrected for. The methods to calculate specific physical quantities like spectral functions or Kondo temperatures from the AIM will be adapted to the specific physical problem and include continuous time quantum Monte Carlo [63], large N-expansions [64] as well as perturbative renormalization group [27].

Chapter 3

An overview of graphene physics

The existence of two-dimensional crystals like graphene and their stability at elevated temperatures [8] has been surprising, as the Mermin-Wager theorem forbids the formation of long range crystalline structures in two dimensions [65]. Dislocations are expected to destroy any 2d-crystals. Resolving this apparent contradiction between experiment and theory, was consequently a central problem during the first few years of graphene research. Two mechanisms explaining the stability of graphene appear very likely, today: First, graphene crystals can be viewed as trapped a metastable state because they are extracted from 3D materials and strong interatomic bonds prevent thermal fluctuations from generating dislocations or other crystal defects even at room temperature or above [9]. Moreover, 2d-crystals can be stabilized by anharmonic effects, which suppress long-wavelength bending fluctuations and minimize the total free energy for smoothly rippled configurations at moderate temperatures [66, 9]. Hence, graphene should not be flat but intrinsically rippled, which is supported by Monte Carlo simulations [67] and transmission electron microscopy [68].

In the light of these stabilization mechanisms, all actual graphene production processes can be viewed as circumvention of problems due to thermal fluctuations: All available fabrication techniques work by first growing a monolayer of graphene inside or on top of another three dimensional crystal and then removing the bulk at sufficiently low temperatures. This route to obtain graphene and other two dimensional crystals goes back to Geim and Novoselov [7, 8] who first isolated graphene by a technique called micromechanical cleavage. They started with three-dimensional graphite and extracted single layers by repeated peeling with adhesive tape. Later, automated cleavage techniques like sonification have been developed [69, 70]. Other promising recent techniques start with monolayer graphene grown epitaxially on top of other crystals surfaces like Ni(111) and transfer the graphene layers onto weakly binding substrates [71, 16]. These new techniques allow for industrial scale graphene production.

As outlined in the introduction, one main reason for the large interest in graphene is the surprisingly high electronic quality even of early samples. In present graphene samples, charge carriers can be tuned continuously between electrons and holes in concentrations up to $10^{13}\,\mathrm{cm}^{-2}$ and their mobilities can ex-

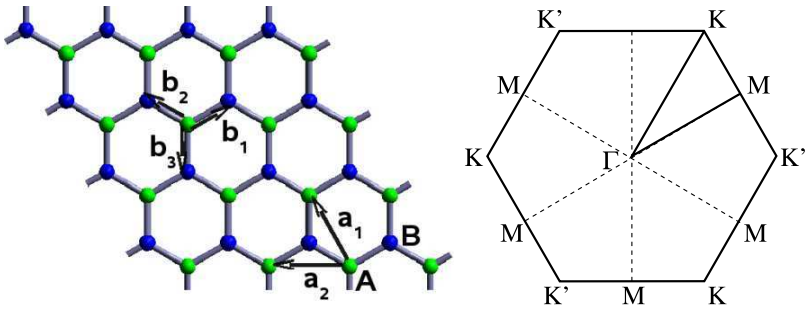

Figure 3.1: Left: Crystal structure of graphene. The carbon atoms are arranged in two degenerate sublattices A (green) and B (blue). These sublattices are connected by the vectors $b_{1,(2,3)}$. a_1 and a_2 indicate the Bravais lattice vectors. Right: Brillouin zone (BZ) of graphene, with high symmetry points Γ, M, K and K' marked. The irreducible part of the BZ is indicated by the solid line connecting Γ, K, M and Γ.

ceed $15,000\,\mathrm{cm^2V^{-1}s^{-1}}$ even under ambient conditions. These mobilities are expected to be significantly improvable but the values measured, so far, are still well below the highest mobilities of $77,000\,\mathrm{cm^2V^{-1}s^{-1}}$ obtained in bulk semiconductors like InSb [9]. However, the mobility of charge carriers in graphene appears to persist even high electrostatic and chemical doping [15]. A similarly important (and related) source of interest in graphene is the special electronic structure with low energy excitations resembling massless Dirac fermions.

3.1 The electronic structure of graphene

The crystal structure of graphene can be viewed as triangular lattice with two atoms per unit cell forming two sublattices A and B. In this arrangement the carbon atoms are sp^2 hybridized, with the carbon *s*-orbitals and the in-plane *p*-orbitals forming a network of σ-bonds. The resulting σ bands split into a bonding part forming deep fully occupied valence bands, which stabilize the crystal, and unoccupied high energy anti-bonding bands (see Fig. 3.2).

The remaining out-of-plane *p*-orbitals, p_z, form π bonds with their neighbors and determine the low energy electronic structure of graphene: As can be seen from the LDA band structure, there are two π-bands which intersect at the corners K and K' of the Brillouin zone[1]. The Fermi level of pristine graphene lies at this crossing point, called Dirac point. In the vicinity of the Dirac point, the electron energy depends linearly on the crystal momentum. The corresponding density of states (DOS), shown in Fig. 3.2, exhibits a "pseudogap" near the Fermi level. The DOS vanishes linearly for $E \to E_F = 0$ and is particle hole symmetric in this region.

This peculiar electronic structure, can be understood in terms of a π-band the tight-binding model. In the approximation of nearest-neighbor hopping, the

[1] K and K' are equivalent by symmetry. See below.

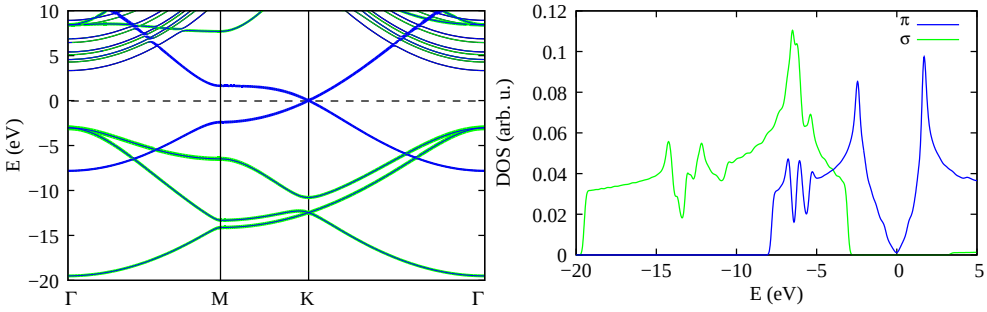

Figure 3.2: Left: Band structure of graphene as obtained from LDA. The blue lines are the graphene π, which determine the electronic structure of graphene in the vicinity of the Fermi level, $E_F = 0$. The σ-bands are marked in green and give rise to valence bands with $E < 3.0\,\text{eV}$ as well as high energy states above 7.7 eV. As the pendant of the graphite interlayer band, in graphene a quasi-continuum of nearly free electron states begins 3.3 eV above the Fermi level at the Γ-point (solid back lines). Right: LDA density of states of graphene. The projection on the σ-states is shown in green, the density of states of the π-bands in blue. The linear dispersion in the vicinity of the Fermi level gives rise to a characteristic V-shape density of states at low energies.

Hamiltonian can be expressed as [72, 73]

$$\hat{H} = t \sum_{<i,j>} a_i^\dagger b_j + a_j^\dagger b_i, \tag{3.1}$$

where a_i and b_i denote the Fermi operators of electrons localized in the carbon p_z orbital of sublattice atoms A and B in the cell at R_i, respectively. The sum includes all pairs of nearest-neighbor carbon atoms and $t \approx 2.7eV$ is the nearest-neighbor hopping parameter.

Using the Fourier transformed operators a_k (b_k), defined by $a_i = \int_{\Omega_B} \frac{\mathrm{d}^2k}{\Omega_B} e^{ikR_i} a_k$ and b_i analogously[2], the Hamiltonian reads as $\hat{H} = \int_{\Omega_B} \frac{\mathrm{d}^2k}{\Omega_B} \Psi_k^\dagger H_k \Psi_k$ with $\Psi_k = \begin{bmatrix} a_k \\ b_k \end{bmatrix}$ and the k-dependent 2×2 matrix

$$H_k = \begin{pmatrix} 0 & \xi(k) \\ \xi^*(k) & 0 \end{pmatrix}, \tag{3.2}$$

where $\xi(k) = t \sum_{j=1}^{3} e^{ik(b_j - b_1)}$ and b_j ($j = 1, 2, 3$) are the vectors connecting neighboring atoms [74]. As

$$H_k = -\sigma_3 H_k \sigma_3 \tag{3.3}$$

is chiral, its spectrum is symmetric about $E = 0$ and given by $\epsilon(k) = \pm|\xi(k)|$. The first important property of this disperion is that all low energy states are located near the K and K' points of the Brillouin zone. A Taylor expansion of $\xi(k)$ for k in the vicinity of these points yields the linear dispersion $\epsilon(k) \approx \pm\hbar v_f |k \mp K|$,

[2] Ω_B denotes the Brillouin zone volume.

where we used $K' = -K$ and v_f is the Fermi velocity $\hbar v_f = \frac{\sqrt{3}}{2} t a_0 \approx 5.8 eV\text{Å}$. ($a_0 = 2.465\text{Å}$ is the lattice constant of graphene.)

Doing this expansion with the Hamiltonian[3], $\hat{H}$, around K and K' yields the two dimensional (2D) Dirac equation for two species of *massless* fermions, ψ_1 and ψ_2 [74, 11]: With $\psi_1(k) = \psi(k - K)$ and $\psi_2(k) = \sigma_1\psi(k + K)$ the linearized Hamiltonian reads

$$H_{\text{lin}} = \hbar v_f \int_{\Omega_B} \frac{\mathrm{d}^2 k}{\Omega_B} \psi_1^\dagger(k)\boldsymbol{\sigma} \cdot \mathbf{k}\psi_1(k) - \psi_2^\dagger(k)\boldsymbol{\sigma} \cdot \mathbf{k}\psi_2(k), \tag{3.4}$$

where $\boldsymbol{\sigma} = (\sigma_1, \sigma_2)$ denote the "spatial" part of the Pauli matrices, σ_j. Note that the spinors, ψ_i, and Pauli matrices σ_j are not defined with regard to the real electron spin but to pseudo spin coming from the sublattice degree of freedom. In first quantized form each type of spinors, ψ_1 and ψ_2, fulfills a 2D Dirac equation of massless particles, which have the form

$$-i\hbar v_f \boldsymbol{\sigma} \cdot \nabla\psi_{1,2}(x) = \pm E\psi_{1,2}(x) \tag{3.5}$$

in position space representation. The treatment of these two distinct types of fermions can be unified by considering four-spinors of *chiral* 2D Dirac fermions. As in relativistic quantum mechanics, the eigenstates of these Dirac equations can be characterized by the projection of the momentum on the pseudospin, called helicity or chirality. This chirality, though related, is different from the chirality defined in Eq. (3.3), which does not include any momentum-pseudospin projection.

Each Dirac point is individually topologically stabilized by a combination of time reversal and inversion symmetry [75]: opening a gap while leaving the system translationally invariant requires breaking of time reversal or inversion symmetry or an external potential commensurate with the graphene lattice, which has a finite Fourier component at the wave vector $G = K - K'$ and thus hybridizes the two Dirac points.

One distinct property of graphene is the special symmetry of states at the Dirac point, which makes graphene behaving very different from usual metal surfaces as will be worked out in the context of inelastic tunneling and Kondo physics in sections 4.1 and 6.5, respectively. The point symmetry group of graphene is C_{6v}, which is generated by rotations of angle $\pi/3$, $C_{\pi/3}$, and a mirror reflection, S_x, e.g., about a horizontal axis going through the center of a hexagon in Fig. 3.1. As this group is non-abelian it has non-trivial, higher-dimensional irreducible representations. The group of the wave vector at the K and K' points is C_{3v}. The eigenstates, $\psi_{1,2}$, at K and K' are each twice degenerate and transform according to the two-dimensional irreducible representation E of C_{3v} [76].

Rotations like $C_{\pi/3}$ transform K into K' and require energies in both valleys to be equal. It is possible to form linear combinations involving wave functions from both valleys, which transform according to the to E_1 and E_2 representations

[3] A detailled derivation with the Taylor expansion being carried out, explicitly, is given in the context of corrugation effects in section 4.2.1.

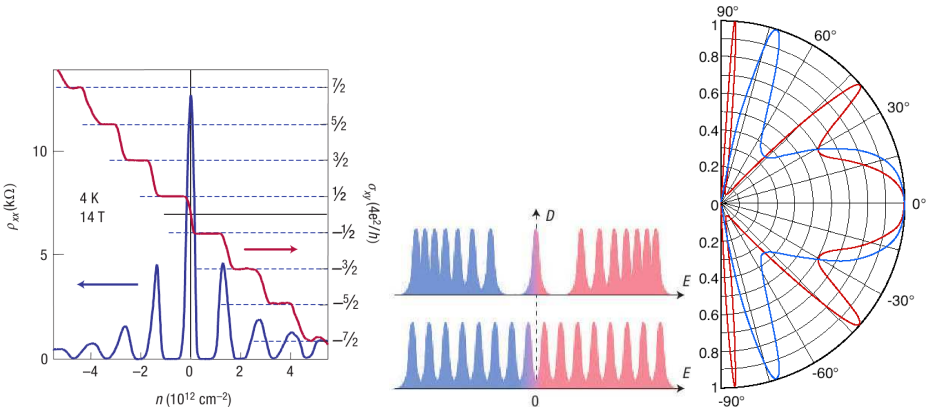

Figure 3.3: Left: Measurement of quantum Hall effect and Shubnikov-de-Haas oscillations in graphene. The plateaux in the Hall resistance σ_{xy} at half integer multiples of $4e^2/h$ are characteristic of massless Dirac fermions. (The factor 4 in $4e^2/h$ is due to valley and spin degeneracy.) From Ref. [9]. Middle: Comparison of Landau level quantization in graphene, $E_N \sim \pm\sqrt{N}$, (upper panel) to the standard Landau level sequence $E_N \sim N + 1/2$ (lower panel) for non-chiral particles with parabolic dispersion. From Ref. [9]. Right: Transmission probability as function of incident angle for electrons with energy 80 meV through a 100 nm wide potential barrier with height 200 meV (red curves) and 285 meV (blue curve). In addition to a broad transmission resonance at normal incidence there are additional resonances at finite angles. From [83].

of C_{6v}. Including translations, T, about Bravais lattice vectors to the symmetry group, it can be shown that the degenerate four states at the Dirac points K and K' form an irreducible representation of the extended symmetry group $G = C_{6v} \otimes T$ [76].

3.2 Quasirelativistic physics in graphene

These special properties of the low energy excitations in graphene result in interesting physical effects that started avalanche of research in this direction, which has been recently reviewed in [11], as well as earlier reviews including a special issue of Solid State Communications [77]. Unusual effects of quantum electrodynamics can manifest in graphene [78]: When subjected to a magnetic field, massless Dirac formions show an anomalous integer quantum Hall effect, with the ladder of plateaus in the Hall resistance being shifted by $1/2$ from the standard sequence [79, 80, 81, 82]. (See Fig. 3.3.) This shifted sequence of plateaus can be understood from the special Landau level (LL) quantization in graphene. In contrast to non-chiral particles with parabolic dispersion, where the N-th Landau level is at energy $E_N = \hbar(eB/m^*c)(N + 1/2)$, the N-th Landau level is at energy $E_N = \pm\hbar v_f \sqrt{2eBN/c}$. The lowest Landau level is at $E_0 = 0$ and shared by electrons and holes. From both, the viewpoint of electrons or holes, this zeroth Landau level exhibits only half the degeneracy of the higher Landau levels so that the Hall plateaus are shifted by 1/2 from the normal sequence of integer filling fac-

tors. The functional dependence of the cyclotron energies on the magnetic field for electrons in graphene being $E_N \sim \sqrt{B}$ results in markably higher LL separations than in usual semiconductors for typical fields, $B \sim 10T$, in the laboratory. This allowed for the observation of the QHE at room temperature [84]. We will encounter the physics of (pseudo)-Landau levels in section 4.2, in the context of graphene ripples.

Another practically important effect is the manifestation of the so-called Klein paradox in graphene: In relativistic quantum mechanics, this phenomenon refers to the process that particles can penetrate through potential barriers with transmission probability one as soon as the barrier height exceeds twice their rest energy, m_0c^2. Electrons in graphene having a gapless spectrum and zero effective mass thus penetrate through any potential barrier at normal incidence. The transmission through barriers at general angles has been investigated by Katsnelson et al. [83] and it has been shown that there are in general several directions with transmission probability 1. These transmission resonances are depicted in Fig. 3.3 for barrier parameters that might be typically encountered in graphene p-n junctions.

As a consequence of these transmission resonances, Anderson localization is suppressed in graphene. Moreover, it means that graphene is rather insensitive to external potentials that are smooth on the atomic scale and that a graphene field effect transistor cannot be closed like usual MOSFETs. To build graphene field effect transistors a gap needs to be opened in the spectrum, which can be achieved, e.g., by creating graphene nanoribbons [85, 86] or chemical functionalization [87].

3.3 Experiments on impurity effects in graphene

Any application exploiting graphene's unique electronic properties requires us to understand impurity effects in this material. Firstly, impurities are inevitable sources of electron scattering left from the production process and they might limit electron transport in graphene to a substantial extent. However, apart from being just undesirable obstacles, impurities provide a powerful tool for controlling and examining the electronic properties of solid state materials. Doping of semiconductors is one famous application of impurity states in this context. In addition, impurities in graphene allow to address fundamental questions in top-of-table experiments: Impurity states in this material are directly related to scattering of relativistic quasiparticles [78, 88, 89, 90, 91, 92] as well as to quasiparticles in the pseudogap phase of high Tc superconductors [88, 93].

Experiments showed that adsorbates on graphene and related materials can strongly affect charge transport by doping and causing scattering of electrons. Since 2000, carbon nanotube (CNT) based gas sensors have been reported [94, 95, 96]: By placing a semiconducting CNT on a SiO_2/Si substrate, contacting it by normal metal electrodes and using Si as a back gate a field effect transistor (FET) is created. (See Fig. 3.4.) A gate voltage V_g between the tube and the Si gate can used to charge the CNT and to tune the chemical potential inside it. The current through such CNT-FET turns out to be sensitive to gas exposure. Kong et

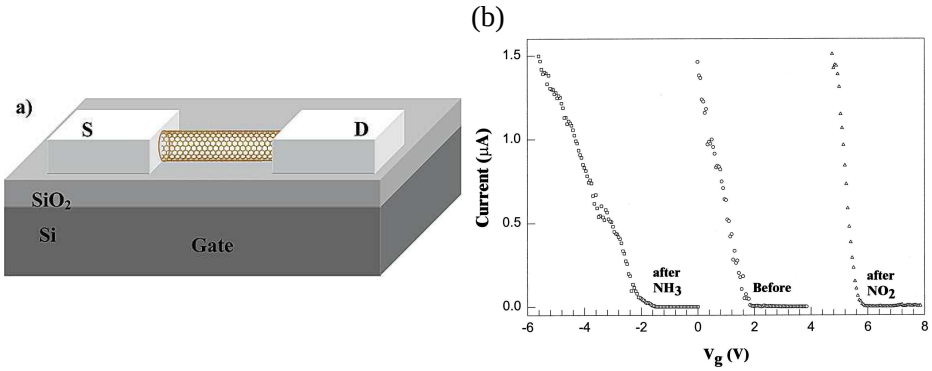

Figure 3.4: (a) Schematic structure of a carbon nanotube field effect transistor. From [96]. (b) Chemical gating effects to the semiconducting CNT. Current versus gate voltage curves before NO_2 (circles), after NO_2 (triangles), and after NH_3 (squares) exposures. The measurements with NH_3 and NO_2 were carried out successively after sample recovery. From [94].

al. [94] found shifting of the current vs. gate voltage curves in different directions upon NH_3 and NO_2 exposure. (See Fig. 3.4). Similarly, CNT-FETs are affected by other adsorbates including H_2O [96], K and O_2.

In a similar setup graphene has been proven to be strongly sensitive to gas exposure [7]: Changing resistance R of a graphene multilayer device has been measured upon H_2O, NH_3 and C_2H_5OH adsorption. R drops upon exposure to water, while ethanol and ammonia exposure as well as placement in vacuum increase it. Subsequent experiments [15] studied the sensitivity of graphene based devices to active gases in more detail: Combining measurements of the longitudinal and the Hall resistivity (ρ_{xx} and ρ_{xy}, respectively) the chemically induced charge carrier concentrations Δn and their signs were determined. The measurements (Fig. 3.5 a) show, that NO_2 and H_2O act as acceptors, while NH_3 and CO are donors. For NO_2 the adsorption of single molecules appeared to be detectable: The height of steps occurring in Hall resistance ρ_{xy} (Fig. 3.5 b) are peaked around the value corresponding to removal or addition of one electron to the graphene sample [15]. Such steps occur only, when the sample is exposed to NO_2 or annealed after exposure but not, e.g., for a clean the sample in He flow. Moreover, no such steps have been detected for H_2O, NH_3 or CO adsorbing on graphene. In section 5.2.1, we give a joint theoretical and experimental study clarifying the mechanism of this single molecule detection. In general, the response of graphene and CNT devices to gas exposure can be very different or caused by different mechanisms: For CNT devices Schottky barriers can control the response [97], whereas for graphene the Schottky effect is suppressed due to the vanishing gap.

In the limit of strong doping, ARPES with graphene on SiC observed lifting (lowering) of the chemical potential upon K (NO_2) exposure [98, 99] and showed that these adsorbates act as donor and acceptor, respectively. In room temperature transport measurements using graphene on SiO_2 substrates Schedin et. al. [15] find NO_2 induced hole doping up to concentrations of $1.5 \times 10^{12}\,\mathrm{cm}^{-2}$ and the

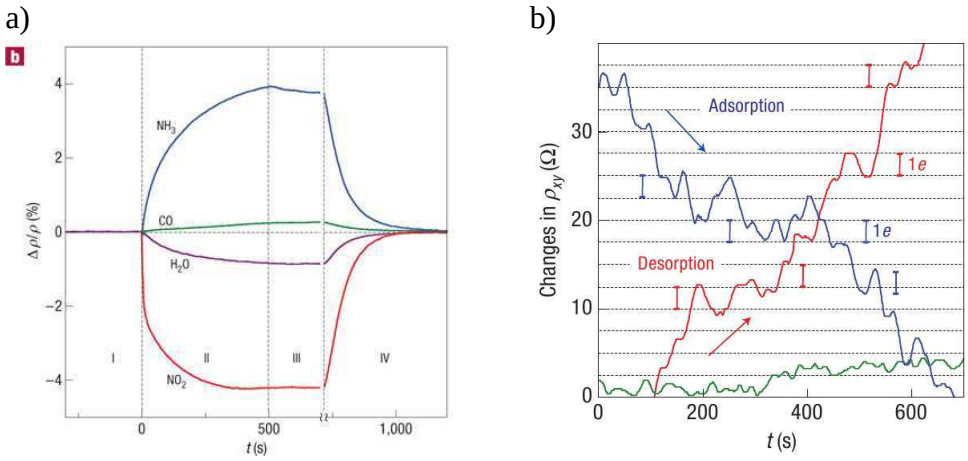

Figure 3.5: (a) Response in the resistivity ρ of single-layer devices to NO_2, H_2O, NH_3 and CO in concentrations of 1ppm in He at atmospheric pressure. The positive (negative) sign of changes in ρ were added to indicate electron (hole) doping. Region I - the device is in vacuum prior to its exposure; II - exposure to the diluted chemical; III - evacuation of the experimental setup; and IV - annealing at 150° C. From [15]. (b) Examples of changes in Hall resistivity observed near the neutrality point during adsorption of strongly diluted NO_2 (blue curve) and its desorption in vacuum at 50 °C (red curve). The green curve is a reference of the same device thoroughly annealed and then exposed to pure He. The curves are for a three-layer device in $B = 10$ T. The grid lines correspond to changes in ρ_{xy} caused by adding one electron charge. From [15].

electron mobility staying constant within 20% of its mean value. The charged NO_2 impurities do not seem to strongly affect electron scattering. However, depositing K on graphene at cryogenic temperatures [100] Chen et al. achieved electron doping up to $5 - 6 \times 10^{12}\,\mathrm{cm}^{-2}$ but found the electron mobility decreasing by more than a factor of 15 within this doping range. These seemingly contradictory experiments lead to a controversy on the importance charged impurities as limiting factor for the electron mobility in graphene. In section 5.2.3, we address the question of which impurities are naturally present in graphene by means of first-principles theory. We show that there is a close relation between migration barriers of impurities in graphene and whether they are covalently or ionically bond.

Impurities are naturally local perturbations and one route to understanding their effects is investigating the local electronic properties in their vicinity. The local density of states (LDOS) is therefore one central quantity in the study of impurity effects in chapter 5. Experimentally, STM provides a tool to measure the LDOS with atomic resolution.

3.4 Local probe experiments on graphene

During the time when thesis was prepared scanning tunneling microscopy characterizations of graphene samples have been reported [101, 102, 103, 104, 105, 106, 107, 108, 109]. Several results are in close relation to the theoretical studies

presented here:

These experiments have proven directly, that graphene of top of SiO_2 prepared by mechanical exfoliation as well as epitaxial graphene on SiC(0001) exhibit a high degree of crystalline order. For epitaxial single layer graphene on SiC(0001) height modulations stemming from the a reconstruction of the SiC layer underneath the graphene have been found. These corrugations occur on a typical length scale of 1.8 nm and lead to a root mean square (rms) roughness on the order of $0.01 - 0.02$ nm [104, 105]. Mechanically exfoliated graphene on SiO_2 exhibits corrugations on a larger length scale and more than an order of magnitude bigger roughness: The two experiments from Refs. [101, 102] found height fluctuations that mainly follow the roughness of the underlying substrate with rms roughness on the order of 0.2 nm and correlation length of approx. 30 nm. Later experiments [108] showed that graphene on SiO_2 can have partially suspended areas that do not follow the roughness of the underlying substrate but have the same rippling characteristics as found for fully suspended graphene sheets by Monte Carlo calculations [67] and microscopic electron diffraction [68]: there are corrugations on the length scale of 15 nm with rms roughness of $0.3-0.4$ nm and correspondingly typical height variations of ~ 1 nm between "valleys" and "hills" of the graphene sheet [108]. The roughness of graphene strongly depends on the preparation technique. Understanding the electronic properties of present graphene samples, therefore, requires a theory describing how corrugations affect the electronic structure. The question is addressed in section 4.2.

The concentration of impurities and the amount of atomic scale corrugations can depend strongly on fine details of the sample preparation. Nevertheless, the results by different groups on impurity concentrations in mechanically exfoliated graphene appear consistent. In Refs. [101, 102] defect free regions of a few nm^2 are reported. A larger scale transmission electron microscopy (TEM) study [110] found about 0.3% of the carbon atoms forming defects, which corresponds to approx. one defect per $10\,nm^2$. STM topographies in the vicinity of impurities in epitaxial bilayer graphene revealed complex scattering patterns and largely corrugated low energy scanning tunneling spectra at distances of a few nm from the nearest atomic defect [103]. (See Fig. 3.6.) This strong corrugation of the spectra, in particular the pronounced dI/dV minima, in the bias range of ± 40 meV are unexpected given the strong electron doping of the samples used in this experiment.

STS of graphene with in a larger range of bias voltages [104, 106] came up with a surprise that, with hindsight of the theory given in section 4.1, is possibly closely related to the corrugated low energy spectra reported in Ref. [103]: It is not the Dirac point with its linearly vanishing density of density of states, which causes the most prominent feature in the measured dI/dV spectra, but a gap of ± 60 meV pinned to the Fermi level [106] (see Fig. 3.6 right).

After initial speculations on the nature of this gap like feature including substrate and electric field effects [104], the most recent experiments indicate that this gap is caused by the opening of an inelastic tunneling channel due to graphene's out-of-plane at K and K' phonons [106]. This is highly unexpected in the light of the experience with inelastic effects in scanning tunneling spectroscopy: For tun-

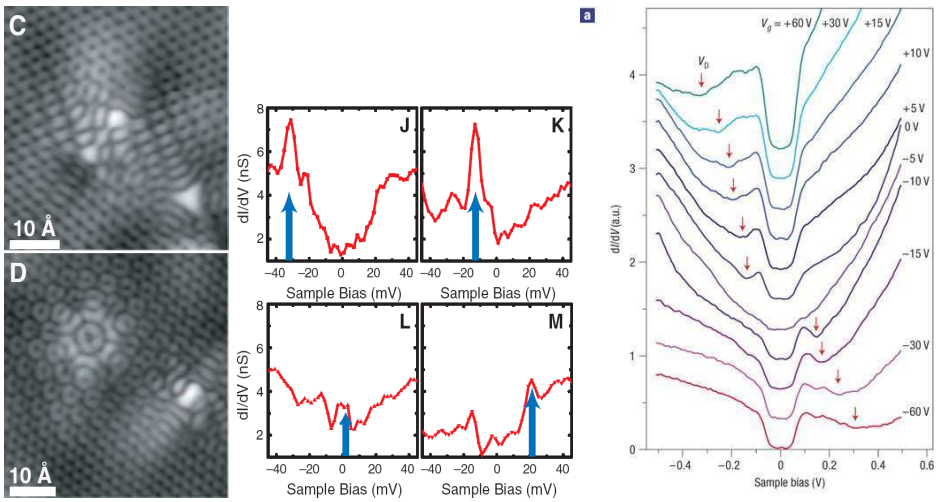

Figure 3.6: Left: STM constant current mode topographic images of defects in bilayer epitaxial graphene. Complex scattering patterns around atomic scale defects are found at bias voltage +300 meV. The sample is heavily electron doped with the Dirac point approx 300 meV below the Fermi level. From [103]. Middle: low energy dI/dV spectra taken at in different areas of the same sample as in the left part. The spectra are averages over lines of $2-3$ nm in length. The peaks in dI/dV marked by blue arrows correlate with maxima of longwavelength interference patterns. From [103]. Right: dI/dV spectra taken at the same point on the graphene surface for different gate voltages, V_G, by Zhang et al.. Curves are vertically displaced for clarity. Red arrows indicate the gate-dependent positions of the adjacent conductance minimum, V_D, outside the gap feature. From [106].

neling into normal metals [111] or Dirac materials like high Tc superconductors [112, 113] inelastic processes usually contribute on the order of a few percent or less to the total dI/dV signal. Section 4.1 will be devoted to a theory explaining this unexpected phenomenon.

Chapter 4

Lattice corrugations in graphene

In this chapter we discuss how deviations of graphene from its perfect lattice influence its electronic properties. Phonons present are dynamical lattice corrugations and turn out to be very important for understanding STM experiments. The first section of this chapter will be devoted to giving a theory of phonon effects manifesting in STM on graphene and to explain recent experiments. In this section will investigate Brillouin zone corner states inhibiting graphene's Dirac electrons being coupled to high energy states from the Brillouin zone center. It will be shown that tiny admixtures of zone center states to the Dirac electron states have a big impact on tunneling, while the overall electronic structure is only weakly affected.

In section 4.2, we study the question of which corrugations can strongly influence graphene's Dirac electrons as regards their intrinsic local electronic properties. We consider long wavelength graphene ripples and show how so called rippling-induced pseudomagnetic fields alter graphene's low-energy electronic properties. To this end, first principles calculations are combined with an effective field theory. The formation of flat bands near the Fermi level corresponding to "pseudo-Landau levels" is studied as a function of the rippling parameters. Quenched and relaxed ripples turn out to be fundamentally different is this respect: It is demonstrated, both numerically and analytically, that annealing of quenched ripples can destroy the flat bands.

4.1 Phonon mediated tunnelling into graphene

In the following sections a detailled theoretical study of the phonon mediated tunneling scenario is given and it is explained how inelastic contributions can dominate the dI/dU spectra from Refs. [104, 106]. Firstly, a derivation of a basic electron-phonon interaction Hamiltonian is given. Then, we present a simple model of graphene's electrons being coupled to K/K' phonons. Within this model the electron self-energy, the total density of states (DOS) and the density of states resolved in different tunneling channels are calculated. It turns out that the total DOS and the DOS in the channel of zone center states differ strongly: At low energies, the total DOS is dominated by the V-shape from the Dirac electron's DOS. However, the DOS of the zone center channel recovers the gapped experimental dI/dU spectra.

Motivated by this insight, the effect of different K/K' phonons on the electronic wave functions and their decay in the vacuum is investigated by means of first principles theory. It is shown why the electron-phonon coupling has such a large impact on STS as seen in Refs. [104, 106] and which phonon is responsible of the gap seen in STS. We show that the inelastic channel is strongly enhanced in the tunneling density of states (TDOS) by a very general mechanism of band mixing. This mechanism is not limited to dynamic processes but is also expected to occur, e.g., near short range corrugations of the graphene lattice.

4.1.1 Electron-phonon interactions

Any electron in a solid interacts with the lattice degrees of freedom and is sensitive to displacements of the ions from their minimum energy positions. A Hamiltonian describing the interaction of electrons and phonons is derived following the textbook by Mahan [28]. We start from a Hamiltonian

$$H = H_e + H_{ei} + H_p \tag{4.1}$$

containing the quantized normal modes of lattice vibrations

$$H_p = \sum_{\mathbf{k}} \omega_{\mathbf{k}} a^\dagger_{\mathbf{k}} a_{\mathbf{k}}, \tag{4.2}$$

the kinetic and Coulomb energy of the electrons

$$H_e = \sum_i \frac{p_i^2}{2m} + \frac{e^2}{2} \sum_{i \neq j} \frac{1}{r_{ij}}, \tag{4.3}$$

and the electron-ion interaction

$$H_{ei} = \sum_{iJ} V_{ei}(r_i - R_J). \tag{4.4}$$

Here, $\mathbf{k} = (k, \eta)$ contains the phonon wave vector k and the branch η. The indices i, j label the electrons, their momenta p_i, positions r_i and distances $r_{ij} = |r_i - r_j|$,

as well as the index J labels ions and their positions R_J. The ionic positions are decomposed, $R_J = R_J^0 + Q_J$, into their equilibrium positions R_J^0 and their displacement Q_J. For Q_J small as compared to interionic distances one can expand

$$V_{ei}(r_i - R_J) = V_{ei}(r_i - R_J^0) - Q_J \nabla V_{ei}(r_i - R_J^0) + O(Q^2). \tag{4.5}$$

This yields the electron-phonon interaction potential

$$V_{ep}(r) = -\sum_J Q_J \nabla V_{ei}(r - R_J^0). \tag{4.6}$$

The displacement $Q_J^{\mathbf{k}}$ of the ions due to a phonon mode $\mathbf{k}$ is given by

$$Q_J^{\mathbf{k}} = i\left(\frac{\hbar}{2MN\omega_{\mathbf{k}}}\right)^{1/2} \xi_{\mathbf{k}} e^{ik\cdot R_J^0}(a_{\mathbf{k}} + a_{-\mathbf{k}}^\dagger). \tag{4.7}$$

Here, M is the ionic mass, N the number of atoms in the crystal and $\xi_{\mathbf{k}}$ is the unit polarization vector of the phonon mode. We now introduce a basis of Bloch functions $\phi_{\mathbf{q}}(r) = u_{\mathbf{q}}(r)e^{iqr}$ for the single electron wave functions labelled by $\mathbf{q} = (q, \nu)$ including crystal momentum q and band index ν, where $u_{\mathbf{q}}(r)$ is required to have the periodicity of the Bravais lattice. Inserting Eq. (4.7) into Eq. (4.6) with $Q_J = \sum_{\mathbf{k}} Q_J^{\mathbf{k}}$ and using the density operator $\rho(r) = \sum_{\mathbf{q},\mathbf{q}'} \phi_{\mathbf{q}}^*(r)\phi_{\mathbf{q}'}(r)c_{\mathbf{q}}^\dagger c_{\mathbf{q}'}$ yields the electron-phonon interaction Hamiltonian

$$\begin{aligned} H_{ep} &= \int \mathrm{d}^3 r \rho(r) V_{ep}(r) && (4.8)\\ &= \sum_{\mathbf{k},\mathbf{q},\mathbf{q}'} \int \mathrm{d}^3 r \left(\sum_J Q_J^{\mathbf{k}} \nabla V_{ei}(r - R_J^0) u_{\mathbf{q}}^*(r) u_{\mathbf{q}'}(r) e^{i(q'-q)r}\right) c_{\mathbf{q}}^\dagger c_{\mathbf{q}'} && (4.9)\\ &= \sum_{\mathbf{k},\mathbf{q},\mathbf{q}'} M_{\mathbf{k},\mathbf{q},\mathbf{q}'} c_{\mathbf{q}}^\dagger c_{\mathbf{q}'}(a_{\mathbf{k}} + a_{-\mathbf{k}}^\dagger) && (4.10) \end{aligned}$$

with

$$M_{\mathbf{k},\mathbf{q},\mathbf{q}'} = i\left(\frac{\hbar}{2MN\omega_{\mathbf{k}}}\right)^{1/2} \int \mathrm{d}^3 r \xi_{\mathbf{k}} \nabla V_{ei}(r) u_{\mathbf{q}}^*(r) u_{\mathbf{q}'}(r) e^{i(q'-q)r} \delta_{k+q'-q}. \tag{4.11}$$

$M_{\mathbf{k},\mathbf{q},\mathbf{q}'}$ is called the electron-phonon interaction matrix element.

4.1.2 Perturbative treatment of electron-phonon interactions

The simplest model allowing us to understand how electron-phonon coupling due to the K/K' phonons in graphene affects STS deals with three electronic bands: the two graphene π-bands at K/K' and a band of states at the zone center Γ, which extend far into the vacuum above the sheet. The latter band is approximated by a flat band

$$H_\sigma = E_\sigma \sum_q d_q^\dagger d_q \tag{4.12}$$

at energy E_σ in the vicinity of Γ. Here, d_q is the annihilation operator of an electron with crystal momentum q this flat band. The Hamiltonian of the π-bands can be be written as

$$H_\pi = \sum_{\nu=\pm,q} \nu\epsilon(q) c^\dagger_{\nu,q} c_{\nu,q}, \tag{4.13}$$

where the index $\nu = +(-)$ denotes the conduction (valence) band and $c_{\nu,q}$ is the annihilator of an electron in this π-band with momentum q. Close to the Dirac points K and K', i.e. $q = \pm K + k$ with $|k| \ll |K|$, the dispersion is linear $\epsilon(k) \approx \hbar v_\mathrm{f}|k|$.

With the phonon Hamiltonian from Eq. (4.2) restricted to a close vicinity of the K/K' points and constant phonon energy $\omega_\mathbf{k} = \omega_a$ in this region, scattering of electrons between the π-states at K/K' and zone center states is accounted for in the following electron-phonon interaction Hamiltonian:

$$H_{ep} = \lambda \sum_{\nu,q,k} (d^\dagger_{k+q} c_{\nu,q} + c^\dagger_{\nu,k+q} d_q)(a_\mathbf{k} + a^\dagger_{-\mathbf{k}}). \tag{4.14}$$

As small spots of the Brillouin zone are involved, we assumed $M_{\mathbf{k},\mathbf{q},\mathbf{q}'} = \lambda\delta_{k+q'-q}$ which leads directly from Eq. (4.10) to the interaction at hand, Eq. (4.14). In this model dealing with three electronic bands, the non-interacting electron Green function is a diagonal 3×3 matrix and reads as

$$G^0(q, i\omega_n) = \begin{pmatrix} \frac{1}{i\omega_n - E_\sigma} & 0 & 0 \\ 0 & \frac{1}{i\omega_n - \epsilon(q)} & 0 \\ 0 & 0 & \frac{1}{i\omega_n + \epsilon(q)} \end{pmatrix}, \tag{4.15}$$

where $i\omega_n$ are fermionic Matsubara frequencies. With the non-interacting phonon Green function[1] $D^0(k, i\Omega_m) = D^0(i\Omega_m) = -\frac{2\omega_a}{\Omega_m^2 + \omega_a^2}$ on bosonic Matsubara frequencies, $i\Omega_m$, and the electron-phonon interaction from Eq. (4.14) transformed to the matrix form of Eq. (4.15),

$$H_{ep} = \sum_{\nu,q,k} (d^\dagger_{k+q}, c^\dagger_{-,k+q}, c^\dagger_{+,k+q}) \mathbf{M}_\nu (d_q, c_{-,q}, c_{+,q})^T (a_k + a^\dagger_{-k}). \tag{4.16}$$

with

$$\mathbf{M}_- = \begin{pmatrix} 0 & \lambda & 0 \\ \lambda & 0 & 0 \\ 0 & 0 & 0 \end{pmatrix} \text{ and } \mathbf{M}_+ = \begin{pmatrix} 0 & 0 & \lambda \\ 0 & 0 & 0 \\ \lambda & 0 & 0 \end{pmatrix}, \tag{4.17}$$

the lowest order contribution to the electronic self-energy is

$$\begin{aligned} \Sigma(q, i\omega_n) &= -\frac{1}{\beta} \sum_{k,\Omega_m,\nu,\nu'} D^0(k, i\Omega_m) \mathbf{M}_\nu G^0(q-k, i\omega_n - i\Omega_m) \mathbf{M}_{\nu'} \\ &= -\frac{1}{\beta} \sum_{\Omega_m,\nu,\nu'} D^0(i\Omega_m) \mathbf{M}_\nu G^0(r=0, i\omega_n - i\Omega_m) \mathbf{M}_{\nu'}, \end{aligned} \tag{4.18}$$

[1] See Mahan [28] for a detailled derivation.

where $G^0(r = 0, i\omega_n)$ is the non-interacting local Green function, $\beta = 1/k_\mathrm{B}T$ is the inverse temperature and the independence of D^0 and $\mathbf{M}_\nu$ on k has been exploited. The sum over bosonic Matsubara frequencies is carried out using the contour integration technique described in chapter 3.5 of Ref. [28]: We change to the spectral representation $G^0(r = 0, i\omega_n) = \int \mathrm{d}\omega' \frac{A(\omega')}{i\omega_n - \omega'}$ and obtain $\Sigma(q, i\omega_n) = \Sigma(i\omega_n)$ with

$$\begin{aligned}\Sigma(i\omega_n) &= -\frac{1}{\beta}\sum_{\Omega_m,\nu,\nu'}\int \mathrm{d}\omega' \mathbf{M}_\nu D^0(i\Omega_m)\frac{A(\omega')}{i\omega_n - i\Omega_m - \omega'}\mathbf{M}_{\nu'} \\ &= \sum_{\nu,\nu'}\int \mathrm{d}\omega' \mathbf{M}_\nu A(\omega')\mathbf{M}_{\nu'}\left(\frac{n_\mathrm{B}(\omega_a)}{i\omega_n - \omega_a - \omega'} - \frac{n_\mathrm{B}(-\omega_a)}{i\omega_n + \omega_a - \omega'} - \right. \\ &\quad \left. D^0(i\omega_n - \omega')n_\mathrm{B}(i\omega_n - \omega')\right). \end{aligned} \tag{4.19}$$

Here, $n_\mathrm{B}(z) = 1/(e^{\beta z} - 1)$ is the complex Bose function and $n_\mathrm{B}(i\omega_n - \omega') = -1/(e^{-\beta\omega'} + 1) \equiv -n_\mathrm{F}(-\omega')$, as $e^{i\beta\omega_n} = -1$. In the zero temperature limit, $\beta \to \infty$, we have $n_\mathrm{B}(\omega_a) \to 0$, $n_\mathrm{B}(-\omega_a) \to (-1)$, and $n_\mathrm{F}(-\omega') \to \Theta(\omega')$. Analytical continuation $i\omega_n \to \omega + i\delta$ with $\delta \to 0^+$ yields

$$\begin{aligned}\Sigma(\omega + i\delta) &= \sum_{\nu,\nu'}\int \mathrm{d}\omega' \mathbf{M}_\nu A(\omega')\mathbf{M}_{\nu'}\left(\frac{1}{\omega + i\delta + \omega_a - \omega'} + \right. \\ &\quad \left. D^0(\omega + i\delta - \omega')\Theta(\omega')\right) \\ &= \sum_{\nu,\nu'}\int \mathrm{d}\omega' \mathbf{M}_\nu A(\omega')\mathbf{M}_{\nu'}\left(\frac{\Theta(\omega')}{\omega + i\delta - \omega_a - \omega'} + \right. \\ &\quad \left. \frac{\Theta(-\omega')}{\omega + i\delta + \omega_a - \omega'}\right). \end{aligned} \tag{4.20}$$

These equations apply to the case of zero chemical potential, $\mu = 0$ which can be always achieved by shifting the spectral functions $A^0(\omega) \to A^0(\omega') = A^0(\omega + \mu)$. With the spectral function

$$A^0(\omega) = \mathrm{diag}\left(\delta(\omega + \mu - E_\sigma), 2\Theta(-\omega - \mu)\frac{|\omega + \mu|}{W}, 2\Theta(\omega + \mu)\frac{|\omega + \mu|}{W}\right) \tag{4.21}$$

belonging to the local unperturbed Green function $G^0(r = 0, \omega)$ the integrals in Eq. (4.20) can be easily evaluated. For energies, $\omega \ll W$, small as compared to the Dirac electron bandwidth $W \approx 6\,\mathrm{eV}$, the diagonal components read as $\Sigma_{1,1}(\omega + i\delta) = \Sigma'_{1,1}(\omega + i\delta) + i\Sigma''_{1,1}(\omega + i\delta)$, where

$$\Sigma'_{1,1}(\omega + i\delta) = \frac{2\lambda^2}{W^2}\begin{cases} (\omega + \mu - \omega_a)\log\left|\frac{\omega - \omega_a}{W}\right| + (\omega + \mu + \omega_a)\log\left|\frac{(\omega + \omega_a + \mu)^2}{W(\omega + \omega_a)}\right| & \text{if } \mu \geq 0 \\ (\omega + \mu - \omega_a)\log\left|\frac{(\omega + \mu - \omega_a)^2}{W(\omega - \omega_a)}\right| + (\omega + \mu + \omega_a)\log\left|\frac{\omega + \omega_a}{W}\right| & \text{if } \mu < 0 \end{cases} \tag{4.22}$$

and

$$\Sigma''_{1,1}(\omega + i\delta) = -\frac{2\pi\lambda^2}{W^2}\Theta(|\omega| - \omega_a)\left|\omega + \mu - \mathrm{sign}\,(\omega)\omega_a\right|. \tag{4.23}$$

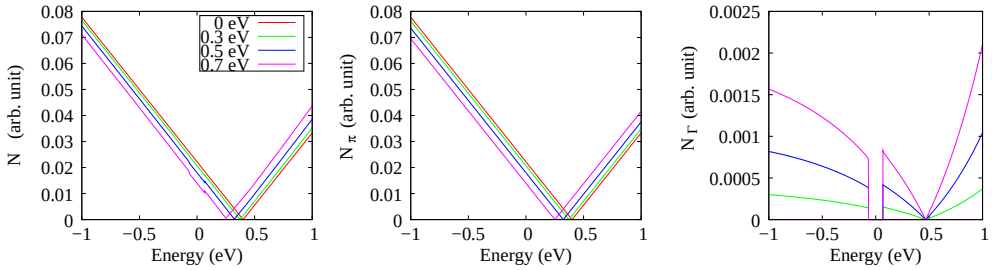

Figure 4.1: (Color online) DOS for different coupling strengths $\lambda = 0,\ 0.3,\ 0.5,\ 0.7$ eV. Left panel: Total DOS, $N(\omega)$. Middle panel: DOS in π-channel, $N_\pi(\omega)$. Right panel: DOS in channel of long range zone center states, $N_\Gamma(\omega)$.

The π block is

$$\Sigma_{i,i}(\omega + i\delta) = \lambda^2 \frac{1}{\omega + \mu - E_\sigma - \ \mathrm{sign}\,(E_\sigma - \mu)\omega_a} \approx -\frac{\lambda^2}{E_\sigma}, \tag{4.24}$$

with $i = 2, 3$ and causes a rigid shift of the band energies in regime important for STS. With the interacting Green function being $G^{-1}(p,\omega) = {G^{(0)}}^{-1}(p,\omega) - \Sigma(\omega)$, momentum space integration yields the density of states $\mathbf{N}(\omega) = -\frac{1}{\pi}\mathrm{Im}G(r = 0, \omega + i\delta)$.

For fixed chemical potential $\mu = -0.4eV$ and $E_\sigma = 3.3\,\mathrm{eV}$, Fig. 4.1 shows how the DOS is modified by the electron-phonon interaction as a function of the coupling strength λ. The total DOS, $N(\omega) = \mathrm{Tr}\,\mathbf{N}(\omega)$, and the DOS of the π-bands, $N_\pi(\omega) = \sum_{i=1,2}(\mathbf{N}(\omega))_{i,i}$, are virtually indistinguishable and exhibit the "V"-shape characteristic for Dirac fermions. The main modification of the total DOS is a shift to slightly lower energies with increasing coupling strength due to the π-block of $\Sigma(\omega + i\delta)$ — a consequence of level repulsion of the π bands and the flat band at E_σ, well known from second order perturbation theory.

However, the spectral properties in the channel of zone center states are strongly altered at low energies $|\omega| \ll W$. The density of states in this channel, $N_\Gamma(\omega) = (\mathbf{N}(\omega))_{1,1}$, reads as

$$\begin{aligned} N_\Gamma(\omega) &= -\frac{1}{\pi}\mathrm{Im}G_{1,1}(\omega) = -\frac{\Sigma''_{1,1}(\omega + i\delta)}{\pi|\omega - E_\sigma - \Sigma_{1,1}(\omega + i\delta)|^2} \\ &\sim \Theta(|\omega| - \omega_a)\left|\omega + \mu - \ \mathrm{sign}\,(\omega)\omega_a\right|. \end{aligned} \tag{4.25}$$

Without electron-phonon interaction $N_\Gamma(\omega)$ vanishes for $\omega \neq E_\sigma$. But, as soon as this interaction becomes effective and the energy of the electrons $\omega > \omega_a$ exceeds the phonon mode energy, the zone center states start mixing with the π bands. This leads to a gap of $\pm\omega_a$ around the Fermi level in the channel of zone center states. Outside this gap, $N_\Gamma(\omega)$ recovers the usual "V"-shape of graphene's DOS. (See Fig. 4.1, right panel.) Indeed, the shape of $N_\Gamma(\omega)$ is very similar to the gapped spectra found in STS on graphene. [106]

Comparing the scales in the left and right part of Fig. 4.1 one sees, that the DOS in the nearly free electron channel is for all coupling constants considered,

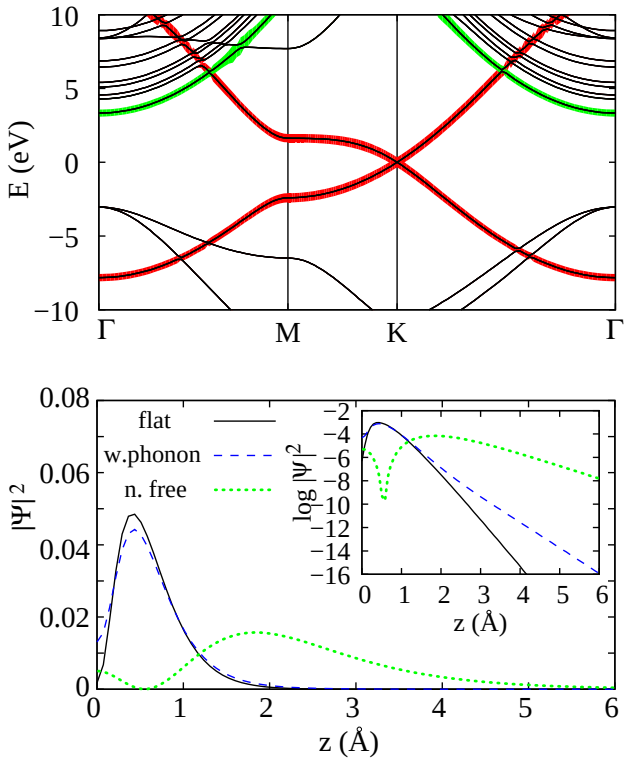

Figure 4.2: (Color online) Upper panel: Band structure of graphene. The π-bands inhibiting the Dirac electrons are marked with dark red lines. Instead of the graphite interlayer band, in graphene a quasi-continuum of nearly free electron states begins 3.3 eV above the Fermi level at the Γ-point (light green lines). Lower panel: Decay of the electronic wave functions $\Psi(z)$ as a function of height z above the graphene sheet. The laterally averaged density $|\Psi(z)|^2$ is shown for states near the Dirac point of flat graphene (solid line) and in presence of a K_6 out-of-plane frozen phonon (dashed line). The density belonging to the lowest quasi free electron band at Γ printed as dotted line.

here, smaller than the total DOS by a factor of less than 1/20. In the next section, it will be shown that in STS, however, this factor of 1/20 is by far overcompensated by the factor on the order of 10^4 coming from the different tunneling matrix elements in presence or absence of certain K/K' phonons.

4.1.3 Frozen-phonon simulations

To address the effects of the K/K' phonons on the electronic wave functions of graphene and related tunneling matrix elements, we performed density functional calculations within the framework of the local density approximation using VASP [48] with the PAW [53, 52] basis sets as described in sections 2.3.3 and 2.4. The corresponding plane wave expansions were cut-off at 928 eV and the Brillouin zone integrations were carried out with the tetrahedron-method on k-meshes denser than 20×20 when folded back to the simple graphene unit cell. The vertical extension of this cell was chosen to be 24Å.

To understand the phonon effects on tunneling it is insightful to revisit the band structure of flat graphene (Fig. 4.2) obtained from DFT: The π-bands exhibit the well known shape intersecting the Fermi level at the K point with linear dispersion in the vicinity. At the zone center Γ, a quasi continuum of free electron like bands starts 3.3 eV above the Fermi level. These bands correspond to the interlayer band of graphite, which is important in graphite intercalation compounds [114]. In contrast to graphite, the quasi free electron bands, here, are not limited by other graphene layers on top and extend far into the vacuum above the sheet.

To quantify the decay of the wave functions of different bands into the vacuum, we calculated the laterally averaged charge density $|\Psi(z)|^2$ of these wave functions as a function of distance z from the sheet. As shown in Fig. 4.2, lower panel, the wave functions at the Dirac point of flat graphene have their maximum at $z =$ 0.4 Å above the sheet. For $z \gtrsim 1.5$Å, their probability density starts decaying into the vacuum dominated by an exponential, $|\Psi_K(z)|^2 \sim e^{-\lambda_K^{-1} z}$, with decay constant $\lambda_K^{-1} = 3.9\text{Å}^{-1}$, which has been obtained from a linear fit of $\log|\Psi_K(z)|^2$ in this region. This decay constant follows from the single particle Schrödinger equation in presence of a constant potential given by the graphene work function [115]:

$$\lambda^{-1} = 2\sqrt{k_\parallel^2 + 2m_\mathrm{f}\phi/\hbar^2}, \tag{4.26}$$

where the in-plane crystal momentum is $|k_\parallel| = 1.7\text{Å}^{-1}$ for the electrons at K/K' and we obtained $\phi = 4.5$ eV for the work function from LDA.

States at the Γ point of the Brillouin zone, $k_\parallel = 0$, decay much slower into the vacuum: The lowest nearly free electron state is extremely long ranged (see Fig 1., lower panel) and spreads out into the vacuum with decay constant $\lambda^{-1} = 1.0\text{Å}^{-1}$. For states at the Fermi level with $k_\parallel = 0$, Eq. (4.26) yields $\lambda^{-1} = 2.2\text{Å}^{-1}$. Such states are absent in perfect graphene but they can be generated by perturbations mixing the Dirac-like π bands at K/K' with $k_\parallel = 0$ states at Γ. The nearly free electron states as well as the bonding s- and p_z states at Γ are examples of such $k_\parallel = 0$ states.

Selection rules determine which perturbations may generate $k_\parallel = 0$ admixtures to the Dirac bands: Firstly translational symmetry must be broken, with the perturbation having K/K' Fourier components. Moreover, a $k_\parallel = 0$ plane wave transforms under C_{6v} according to the identity representation. The Dirac states at the Brillouin zone corners belong the two-dimensional E_1 and E_2 representations of C_{6v}. So, the perturbation must also break C_{6v} symmetry and must have a component transforming according to $E_{1,2}$ under C_{6v} to achieve coupling of the Dirac bands to long ranged zone center states.

All phonons at K and K' break translational symmetry appropriately. Out of the six phonon modes at K/K' the two-fold degenerate modes K_5 at 151 meV and K_6 at 67 meV transform according to E_1 and E_2 under C_{6v} [116]. The K_1 and K_2 modes at 160 meV and 125 meV, respectively, belong to one-dimensional representations of C_{6v} and cannot couple states from graphene's Dirac point to long ranged zone center states.

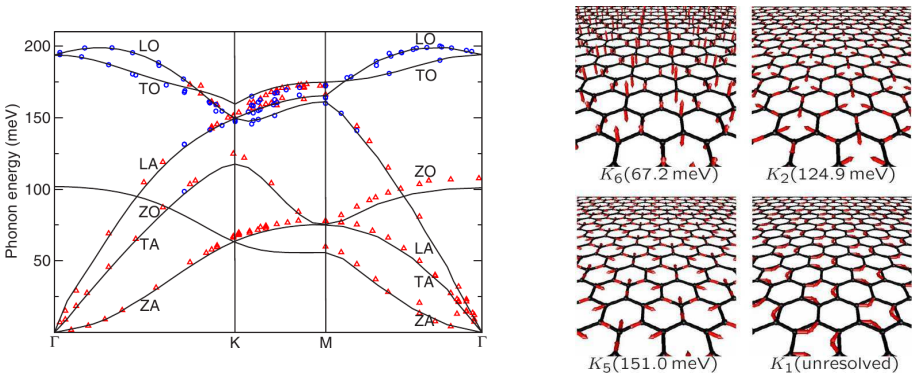

Figure 4.3: Left: Phonon dispersion of graphene obtained from DFT (solid lines) and in-plane phonon dispersion of graphite from inelastic x-ray scattering (triangles and circles). Right: Snapshot of eigenmodes of graphene at the K-point. From [116].

The coupling efficiency by the K_5 and K_6 phonons has been addressed in our first-principles calculations: In a frozen-phonon simulation, the displacement operator $Q_J^{\mathbf{k}}$ from Eq. (4.7) is replaced by a real number via $(a_{\mathbf{k}}e^{-i\omega_{\mathbf{k}}t} + a_{\mathbf{k}}^{\dagger}e^{i\omega_{\mathbf{k}}t}) \rightarrow \sqrt{n}e^{i\phi}$, where n is a positive number, $\phi \in [0; 2\pi)$ and $Q_i^{\mathbf{k}}(t) \rightarrow \mathrm{Re}Q_i^{\mathbf{k}}$. Then, the ion displacements read as

$$Q_J^{\mathbf{k}} = -\left(\frac{n\hbar}{2M_C N\omega_{\mathbf{k}}}\right)^{1/2} \mathrm{Im}\left(\xi_{\mathbf{k}}e^{i(k\cdot R_J^0+\phi)}\right), \tag{4.27}$$

where $M_C \approx 12\,\mathrm{u}$ is the atomic mass of carbon. The ratio $\tilde{n} = n/N$ is the number of phonons per unit cell. In the case of graphene, the unit polarization vector of the phonon mode is six-dimensional, $\xi = (\xi_A, \xi_B)$, as there are two atoms per unit cell. The two-fold degenerate $K_{5/6}$ modes can be represented by $\xi_A^{K_6} = \xi_B^{K_6}e^{-ik\cdot b_0} = \sqrt{1/2}\vec{e}_z$ and $\xi_A^{K_5} = (\xi_B^{K_5})^* = \frac{1}{3}\left(b_0 + b_1e^{i2\pi/3} + b_2e^{i4\pi/3}\right)$, where b_i with $i = 0, 1, 2$ are unit vectors connecting nearest neighbors.

The admixture of $k_{\|} = 0$ components to states at the Fermi level due K_5 and K_6 phonons manifests in changing slopes of $\log|\Psi(z)|^2$, shown in Fig. 4.4: Starting at 3 Å above the sheet the decay constant reduces to $\lambda^{-1} = 2.3\text{Å}^{-1}$ and 2.2Å^{-1} in presence of the K_5 and K_6 phonons, respectively. This is the decay constant expected for $k_{\|} = 0$ contributions from Eq. (4.26). Thus, both phonons fulfilling the above selection rules turn out to couple to states from the Dirac point to long range states at the zone center.

The coupling efficiencies can be obtained by analyzing the $k_{\|} = 0$ admixture as function of phonon concentration $\tilde{n}$: According to Eq. (4.10), a displacement field $Q_i^{\mathbf{k}}$ as in Eq. (4.27) generates a perturbation acting on the electrons:

$$H_{ep} = \frac{\sqrt{\tilde{n}}}{2}\left(\sum_{\mathbf{q},\mathbf{q}'} M_{\mathbf{k},\mathbf{q},\mathbf{q}'}e^{i\phi}c_{\mathbf{q}}^{\dagger}c_{\mathbf{q}'} + \mathrm{H.c.}\right). \tag{4.28}$$

To leading order, the changes in the local density $\delta|\Psi(z)|^2$ are quadratic in that perturbation and consequently $\delta|\Psi(z)|^2 = \alpha_{\mathbf{k}}(z)\tilde{n}$, where the constant of propor-

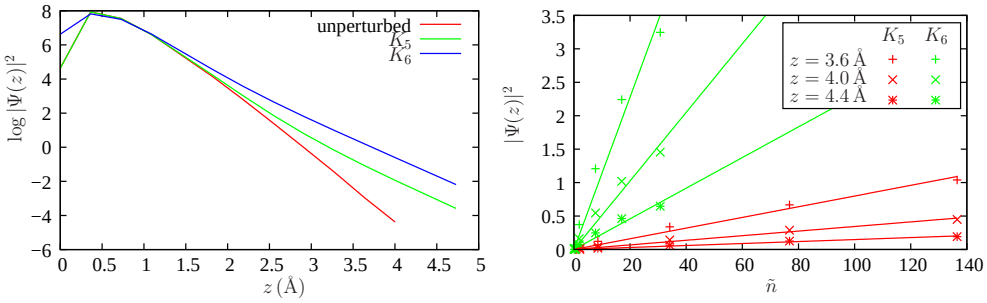

Figure 4.4: Left: Logarithm of the probability density $\log|\Psi(z)|^2$ as function of height z above the graphene sheet for an unperturbed graphene sheet as well as in presence of frozen K_5 and K_6 phonons. The amplitude of the frozen phonons is $|\mathbf{Q}_i^{\mathbf{k}}| \sim 0.1$Å in both cases. Right: Density $|\Psi(z)|^2$ as function of phonon density $\tilde{n}$ at different z. The data points for the K_5 and K_6 phonons are depicted in red and green, respectively. The solid lines in the respective color show linear fits to these data points.

	$\alpha_{K_5}(z)$	$\alpha_{K_6}(z)$	$\alpha_{K_6}(z)/\alpha_{K_5}(z)$
$z = 3.6$ Å	0.0080	0.114	14.3
$z = 4.0$ Å	0.0034	0.051	14.9
$z = 4.4$ Å	0.0015	0.023	15.5

Table 4.1: Linear fits of $|\Psi(z)|^2$ as function of phonon density $\tilde{n}$ at different heights z, as shown in Fig. 4.4. The ratio $\alpha_{K_6}(z)/\alpha_{K_5}(z)$ yields the relative intensity of the two different inelastic phonon processes and turns out to be quasi independent of z, as required.

tionality $\alpha_{\mathbf{k}}(z)$ is a measure for the efficiency of the inelastic phonon channel $\mathbf{k}$ under consideration. The relative efficiency of the K_5 and the K_6 phonon channels is given by the ratio $\alpha_{K_6}(z)/\alpha_{K_5}(z)$, where the z-dependence cancels out. As the wave functions of states from the Dirac point without any phonons decay almost twice faster into the vacuum than in presence of K_5 or K_6 phonons, $\delta|\Psi(z)|^2 = |\Psi(z)|^2$ is fulfilled to very good approximation for $z > 3.5$Å. (See Fig. 4.4 left.)

For both, the K_5 or K_6 phonons, our frozen-phonon calculations confirm $|\Psi(z)|^2 \sim \tilde{n}$ for the range of $\tilde{n}$ plotted in Fig. 4.4 right. This range corresponds in both cases to displacements $|\mathbf{Q}_i^{\mathbf{k}}| < 0.2$Å in each atomic coordinate. The linear fits to these data sets yield $\alpha_{\mathbf{k}}(z)$ and the corresponding relative efficiencies of the two phonon channels. These are given in table 4.1 and they show that the inelastic tunneling due to the K_6 phonon at 67 meV should be more efficient by a factor of approx. 15 than inelastic tunneling due to the 151 meV K_5 phonon.

According to Tersoff-Hamann theory [115], tunneling currents are determined by the tunneling density of states, which is the LDOS at the location of the tip - usually on the order 5Å above the sample. Thus, for each tunneling channel, the DOS inside the graphene sheet has to be weighted with the squared amplitude of the corresponding wave function about 5Å above the sample - which can be approximately written as

$$\mathrm{d}I/\mathrm{d}U \sim |\Psi_\Gamma|^2 N_\Gamma(E) + |\Psi_K|^2 N_K(E). \tag{4.29}$$

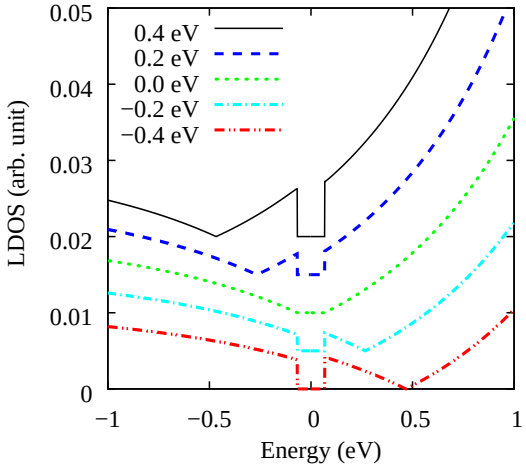

Figure 4.5: DOS in channel of long range zone center states, $N_\Gamma(\omega)$, for different chemical potentials $\mu = -0.4,\ -0.2,\ 0.0,\ 0.2$ and $0.4\,\mathrm{eV}$, phonon energy $\omega_a = 67$ meV, energy of zone center states $E_\sigma = 3.3\,\mathrm{eV}$, and the coupling strength $\lambda = 0.5$ eV fixed to the experimental value [106]. The curves are vertically displaced for clarity.

With the decay constants from above, the ratio of the exponential prefactors entering the tunneling matrix elements is $|\Psi_\Gamma/\Psi_K|^2 \propto e^{1.7\text{Å}^{-1}z}$. At $z = 5$Å this ratio is on the order of 10^4. Thus, the admixture of zone center states to the π-bands by electron-phonon coupling appears as greatly enhanced by this factor of 10^4 in STM spectra. The factor of 1/20 in the ratio $N_\Gamma(\omega)/N_\pi(\omega)$ resulting from Eqs. (4.22-4.24) and depicted in Fig. 4.1 is overcompensated by the matrix element effect on the order of 10^4. The STM spectra are therefore dominated by the inelastic phonon mediated channel of long range states from the zone center and the spectra are expected to exhibit the shape of $N_\Gamma(\omega)$.

As discussed above, the 67 meV phonon provides by a factor of 15 the most important contribution to this inelastic tunneling. It is therefore illustrative to consider $\omega_a = 67$ meV and study $N_\Gamma(\omega)$ according to Eq. (4.25) as a function of the chemical potential, as shown in Fig. 4.5. This presents a simulation of the STM spectra.

Here, we considered the nearly free electron bands as a realization of the long range zone center states and chose $E_\sigma = 3.3\,\mathrm{eV}$, consequently. The most prominent feature of the simulated STM spectra is a gap of $\pm\omega_a$ around the Fermi level, which is independent of doping. The minimum caused by zone center states being coupled with π-states at the Dirac point shifts with the chemical potential. This behavior is unaffected by the particular choice of E_σ as long as E_σ does not fall into the range of bias energies used in STS. So, including contributions from higher nearly free electron states $E_\sigma > 3.3\,\mathrm{eV}$ or the bonding σ-states $E_\sigma = -20\,\mathrm{eV}$ will not change these spectra qualitatively.

Experimentally, the chemical potential is shifted with the gate voltage [7, 106]. Thus, the spectra calculated, here, and the experimental STS from Ref. [106] (see Fig. 3.6) exhibit the same characteristic behavior. The good agreement of the simulated spectra, $\mathrm{d}I/\mathrm{d}U \sim N_\Gamma(eU)$, and the experimental STM spectra strongly

supports the correctness of the phonon mediated tunneling mechanism proposed in Ref. [106]. In addition, our calculations explain why the 67 meV K_6 phonon but not the 151 meV K_5 phonon appears as major inelastic feature in STS. Very recently, prediction of the ratio of the K_6- to the K_5 inelastic phonon signal being on the order of 10-15 has been confirmed experimentally [117].

Moreover, it becomes clear that the phenomenon of strongly enhanced tunneling currents may occur in various contexts in graphene. The Fermi surface of perfect graphene is located at the corner of the Brillouin zone. Any perturbation the mixing the Dirac electron states at the Brillouin zone corners with long range states at Γ may cause such enhancement. Therefore, corrugations on scale of the graphene lattice constant can be expected to affect the tunneling density of states enormously. This is quite in contrast to most metal surfaces, where the *projected* Fermi surface usually includes not only a few points of the surface Brillouin zone but extends over wide areas of the surface Brillouin zone. Therefore, the surprisingly huge inelastic phonon effect in STM on graphene, where the phonons circumvent the "momentum space selection rule for tunneling", Eq. (4.26), is intimately connected with graphene being truly two dimensional.

4.2 Midgap states in corrugated graphene

One of the biggest early puzzles about graphene was that two dimensional crystals were expected not to exist (see chapter 3). Thermal fluctuations in two-dimensional solids, in principle, should lead to macroscopic displacements of the carbon atoms from their perfect lattice arrangement and destroy any long range crystalline order. One very like solution of this problem has been given by Monte Carlo simulations [67] and transmission electron microscopy [68] which suggest that graphene is stabilized by intrinsic ripples. We now discuss how rippling affects the low energy electronic properties of graphene. and under which conditions midgap states do occur.

4.2.1 Rippling effects in a tight-binding model

A tight-binding (TB) Hamiltonian, Eq. (3.2), and a low energy theory, Eq. (3.4), describing electrons in graphene as two species of Dirac fermions have been introduced in section 3.1. These models can serve as basis for obtaining a field theoretical model of graphene's electronic properties in presence of ripples. A derivation suggested by A. Tsvelik will be sketched here:

The TB Hamiltonian from Eq. (3.2) can be rewritten in the form

$$H = \sum_k (a_k^\dagger, b_k^\dagger) \begin{pmatrix} t_{nnn}(k) & t_{nn}(k) \\ t_{nn}^*(k) & t_{nnn}(k) \end{pmatrix} \begin{pmatrix} a_k \\ b_k \end{pmatrix}, \tag{4.30}$$

where t_{nn} and t_{nnn} denote the Fourier transformed nearest and next-to-nearest hopping matrix elements, respectively. As in section 3.1, a_k (b_k) are the Fermi operators of electrons in sublattice A (B) with crystal momentum k.

We introduce a coordinate frame, where $e_1 = (-1, 0)$, $e_2 = (1/2, \sqrt{3}/2)$, $e_3 = (1/2, -\sqrt{3}/2)$ are vectors connecting atoms in sublattice A with their nearest neighbors in sublattice B. The nearest neighbor distance is defined as unit of length $\tilde{a}_0 = a_0/\sqrt{3} = 1.4\,\text{Å} \equiv 1$. In this coordinate system two non-equivalent corners of the Brillouin zone are at $\pm K = (0, \mp 4\pi/3\sqrt{3})$. Close to $\pm K$, the dispersion for the undeformed lattice vanishes linearly and a continuum theory describing low energy electronic states can be defined: Near the K point the undeformed hopping integral can be expanded as

$$\begin{aligned} t_{nn}(k) &= t_0 \sum_\mu e^{ike_\mu} \\ &= t_0 \left[e^{-ik_x} + 2\cos(\sqrt{3}k_y/2) e^{ik_x/2} \right] \\ &\approx \frac{3t_0\tilde{a}_0}{2}(q_y - iq_x) \to 2v_0\bar{\partial}, \end{aligned} \tag{4.31}$$

where $k = (k_x, k_y)$, $q = k - K$, $\bar{\partial} = \frac{1}{2}(\partial_x + i\partial_y)$, and $v_0 = 3t_0\tilde{a}_0/2$ is the Fermi velocity, involving explicitly the nearest-neighbor spacing. Lattice deformations which are smooth on the scale a_0 can be described by the in-plane displacement field u_a with $a \in \{x, y\}$ and the out-of-plane displacement field h. (x, y are the

usual real space cartesian coordinates.) Then, lattice deformations give rise to the deformation tensor field

$$u_{ab} = \frac{1}{2}\left[\partial_a u_b + \partial_b u_a + \partial_a h \partial_b h\right] \tag{4.32}$$

with $a, b \in \{x, y\}$, which quantifies the local strain of the graphene sheet. In particular, $\sum_{a,b} e_\mu^a u_{ab} e_\mu^b$ yields the local changes of bond lengths in e_μ direction ($\mu = 1, 2, 3$).

A change in bond length causes a change in the hopping integral $\partial \log t_0 / \partial \log \tilde{a}_0 = \beta \approx -2$ (see e.g. Harrison [118]), i.e. $\partial t_0 / \partial \tilde{a}_0 \approx 4\,\mathrm{eV/\AA}$. Therefore, local strains change the Fourier transformed hopping integrals according to

$$\begin{aligned}
&\delta t(K)/[\frac{\partial t_0}{\partial R}] = \sum_\mu e^{iKe_\mu} e_\mu^a \frac{\partial u^a}{\partial x^b} e_\mu^b \\
&= e_1^a e_1^b u_{ab} + e^{2i\pi/3} e_2^a e_2^b u_{ab} + e^{-2i\pi/3} e_3^a e_3^b u_{ab} \\
&= u_{xx} + e^{2i\pi/3}(\frac{1}{4}u_{xx} + \frac{3}{4}u_{yy} + \frac{\sqrt{3}}{2}u_{xy}) + e^{-2i\pi/3}(\frac{1}{4}u_{xx} + \frac{3}{4}u_{yy} - \frac{\sqrt{3}}{2}u_{xy}) \\
&= \frac{3}{4}(u_{xx} - u_{yy} - 2iu_{xy}) = 3u_{zz},
\end{aligned} \tag{4.33}$$

where $z = x + iy$. Thus, the nearest neighbor hopping matrix element near the point K becomes

$$t_{nn}(k) \to 2v_0\left(\bar{\partial} - \gamma u_{zz}\right), \tag{4.34}$$

where $\gamma = (1/t_0)\partial t_0 / \partial R$ plays a role of the charge, and u_{zz} can be interpreted as a vector potential:

$$\bar{A^3} = A_{\bar{z}}^3 \equiv A_x^3 - iA_y^3 = u_{zz}. \tag{4.35}$$

Curvature induced rehybridization of σ- and π bands leads to similar gauge fields acting on the Dirac fermions [119].

As in Ref. [120], we introduce a pair of two-dimensional spinors $\Psi_1 = \begin{pmatrix} a_K \\ b_K \end{pmatrix}$, $\Psi_2 = \begin{pmatrix} b_{-K} \\ -a_{-K} \end{pmatrix}$ describing electronic wave packets centered at the K and $-K$ point, respectively. Repeating the above derivations for gauge fields due to smooth lattice deformation for the $-K$ point leads to the same vector potential but with opposite sign. As shown in Ref. [120], all these distortion effects can be summarized in the low energy Hamiltonian

$$H = \Psi^\dagger \left\{ I \otimes IA_0 + v_0 \sigma_\mu \otimes [-iI\partial_\mu + \gamma \tau^a A_\mu^a] \right\} \Psi, \tag{4.36}$$

where the Pauli matrices σ_μ, $\mu = x, y$, act on the sublattice index and the matrices τ^a, $a = 1, 2, 3$, act on the valley index of the spinor $\Psi^\dagger = (\Psi_1^\dagger, \Psi_2^\dagger)$. Electrons in a deformed graphene lattice are a subject of a general vector potential A_μ^a. Its components A_μ^3 are generated by slow deformations, as described above. The other components $A_\mu^{1,2}$ are generated by abrupt changes of the nearest neighbor hopping integrals [120].

In general, the rippling induced gauge fields A^3 are nonuniform and affect the electrons in graphene like an *effective* magnetic field [121]:

$$\mathcal{B} = i(\partial A^3 - \bar{\partial}\bar{A}^3) = \nabla \times A. \tag{4.37}$$

This effective magnetic field couples to the graphene 2D Dirac spinors. The spin associated with them is the sublattice index rather than the real electron spin. Hence, these effective fields are formally similar but differ physically from real magnetic fields.

TB estimations on the effective magnetic field induced to graphene by rippling found the possibility of partially flat bands, which are the analog of Landau levels in real magnetic fields [122]. Therefore, these flat bands are referred to as *pseudo* Landau levels. In particular, zero-energy chiral states ($n = 0$ LL) at the Fermi level should occur in inhomogeneous (real and effective) magnetic fields, as was pointed out from topological considerations [81]. Guinea et al. [122] showed that one-dimensional ripples with height modulation on the order of $h \sim 1 - 5\,\text{nm}$ on a length scale of $l \sim 50$ nm gives rise to about one pseudo-magnetic flux quantum per ripple. They confirmed within the TB approach the occurrence of pseudo Landau levels within this regime. Moreover, it has been shown that rippling induced gauge fields accompanied by an modulated electrostatic field can open band gaps [122]. In graphene ripples, effective electrostatic fields are generated due to strain- and curvature induced changes in $t_{nnn}(k)$ [119].

The appearance of ripple-induced mid-gap states can lead to important consequences: The increased DOS at the Fermi level will enhance the tendency to spatial inhomogeneities [122] as well as it leads to strong resonant electron scattering [78, 123, 124]. Knowing the conditions under which midgap states occur is therefore important for the problem of electron scattering in graphene.[2]

The predictions on midgap states in Ref. [122] have been rather qualitative involving adjustable parameters, like hopping matrix elements or their change with strain and curvature. Moreover, they neglected rehybridization effects of the π and σ bands [122]. It is not clear *a priori* how essential these effects can be. Moreover, taking into account next-nearest-neighbor hopping leads to a *scalar* electrostatic potential induced by the ripples [122] which can cause opening a gap around the Fermi level [119]. To describe this electrostatic potential yet more adjustable parameters are required which makes predictions increasingly difficult. Here, complete first-principles calculations including all these different effects without any adjustable parameters can be very helpful, as they allow to judge how important corrections to the simplest nearest-neighbor TB model are.

In the next section, we present full potential DFT studies of quenched and annealed graphene ripples. We find flat bands very close to the Dirac point for quenched ripples, whereas in annealed ripples these midgap states turn out to be suppressed. Subsequently we will extend the low energy effective field theory description of graphene to include this relaxation effect and justify this extension by our DFT results.

[2] Impurity induced midgap states will be addressed in chapter 5.

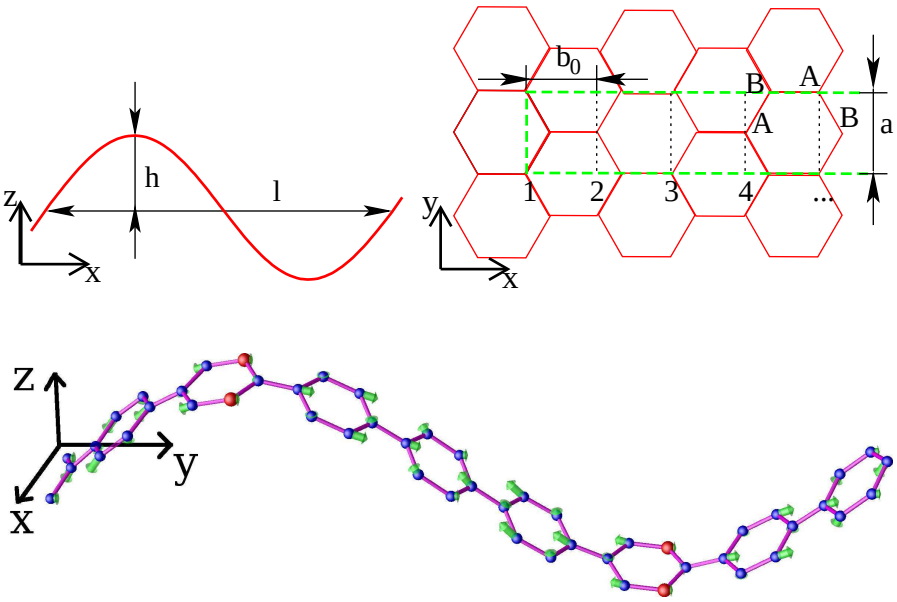

Figure 4.6: Upper Panel: Schematic top and side view of the sinusoidal graphene ripples. The rippling period is denoted by l and the amplitude by h. Lower panel: Perspective view of a relaxed graphene ripple. The green arrows show the displacement of the atoms during the relaxation. To enforce a constant rippling amplitude the vertical position of the atoms marked as big red dots has been fixed.

4.2.2 First principles simulations of graphene ripples

To model quenched ripples in our DFT calculations we consider sinusoidal graphene ripples with height field $h(x,y) = h_0 \sin(qx)$ (Fig. 4.6 upper panel). While the effective gauge field A is caused by strain and curvature, the strain in the ripple can be significantly reduced by allowing all atoms and the supercell shape to relax with the constraint of fixed rippling amplitude h_0.

This relaxation leads to our model of annealed graphene ripples, where "annealed" means that in these ripples possible external sources for energy barriers preventing the ripples from relaxation have been removed. Such sources might be impurities or bonding to a substrate with lattice mismatch [125, 105]. As starting point for the relaxed cell shape, we shortened the supercell in rippling direction such that the arc length of one sinusoidal graphene ripple period coincides with the equilibrium length of the same supercell for flat graphene. Then, standard relaxation of the atomic positions and the cell shape under the constraint of fixed rippling amplitude h_0.

In all calculations within this section we employ the generalized gradient approximation (GGA) [42] to DFT for supercells containing up to 160 carbon atoms. The resulting Kohn-Sham problems are solved within VASP [48] package by expanding the electronic bands into projector augmented waves (PAW) [53, 52], as described in sections 2.3.3 and 2.4. Plane wave cut-offs of 500 eV for band-structure calculations and 875 eV for the relaxations and total energy calculations were used. For the total energy calculations, the Brillouin zone integrations were

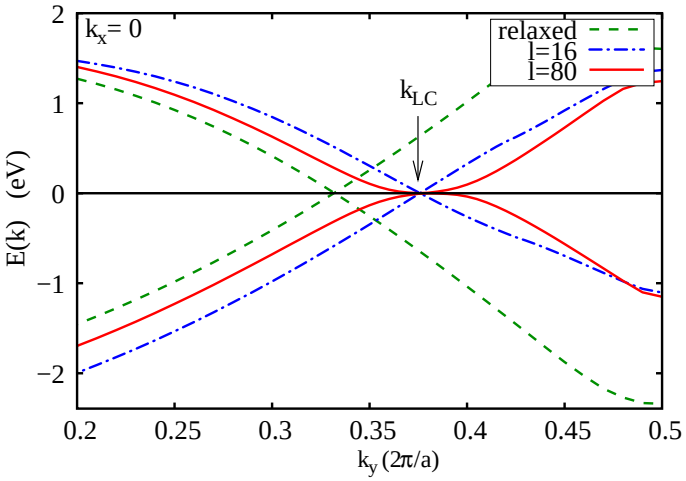

Figure 4.7: Band structure of corrugated graphene sheets: The highest valence and lowest conduction bands along the k_y direction (perpendicular to the rippling direction) are shown for different armchair ripples. The dash dotted (blue) and solid (red) lines correspond to unrelaxed sinusoidal ripples with fixed $h_0/l = 1\text{Å}/4b_0$ ratio for $l = 16,\ 80b_0$, respectively. Dashed lines: A ripple relaxed with the constraint $h_0 = 4\text{Å}$ and a rippling period of 16 graphene unit cells.

performed with 0.1 eV Gaussian smearing on k-meshes denser than 24×24 when folded back to the graphene first Brillouin zone, whereas for relaxations and input charge densities for band structure calculations k-meshes diluted by a factor of 2 turned out to be sufficient.

Firstly, the occurrence of the $n = 0$ LL in quenched ripples has been studied as function of the ripple length l and h_0/l. For $h_0/l = 1\text{Å}/4b_0$ with $b_0 = \sqrt{3}a_0/2$, i.e. $h_0/l \approx 0.1$, prominent changes in the high valance and the low conduction bands occur depending on the rippling period l (Fig. 4.7).

The shorter ripple ($l = 16b_0$) exhibits electron dispersion resembling massless particles with the Dirac point shifted from $k_y = 2\pi/3a_0$ to $k_y \approx 0.375(2\pi/a_0)$, where k_y is the crystal momentum perpendicular to the rippling direction, x. However, the bands of the $l = 80\,b_0$ ripple are flat near the Fermi level and exhibit all characteristics of the $n = 0$ LL of Dirac fermions: They are chiral, that is, fully sublattice polarized and localized in regions of maximum effective magnetic field B (see Fig. 4.8, left panel):

For a ripple of the form $h(x) = h_0 \sin(qx)$ with $q = 2\pi/l$ and l sufficiently large we have $u_{zz} \sim (h_0 q \cos(qx))^2$ and Eq. (4.35) yields the effective gauge field

$$A_y \sim (h_0 q \cos(qx))^2. \tag{4.38}$$

As ($A_x = A_z = 0$) and the pseudomagnetic field is

$$\mathcal{B} = \nabla \times A \sim h_0^2 q^3 \sin(2qx). \tag{4.39}$$

Thus, for $l = 80b_0$ the absolute value of the effective field is maximum around $x = 10, 30, 50, 70b_0$ which coincides with the regions of maximum probability density for the highest valence band electrons with $k_y = 0.385(2\pi/a_0)$.

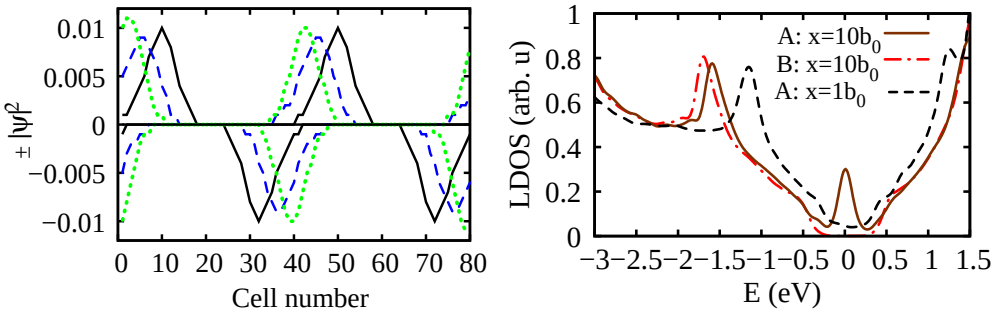

Figure 4.8: Real space properties of the pseudo Landau level wave functions for the ripple with length $l = 80b_0$ and $h_0/l = 1\text{Å}/4b_0$. Left panel: The squared projection of the highest valence band wave function onto both sublattices is shown as a function of the cell number. Sublattice A and B are denoted on the positive and negative ordinate, respectively. The different curves correspond to different crystal momenta $k_y = 0.385$ (solid), 0.4025 (dashed) and $0.4225(2\pi/a_0)$ (dotted) perpendicular to the rippling direction. Right panel: The local density of states (LDOS) inside the cells at $x = 1b_0$ (low eff. field) and at $x = 10b_0$ (high field region). For the low field region, the LDOS is the same in both sublattices (only sublattice A plotted is here, dashed line), whereas in the high field region the LDOS in sublattice A (solid) and B (dash-dotted) differ significantly.

This peculiar real space structure manifests also in the local density of states (LDOS) (Fig. 4.8, right panel). In the high field region, the spectrum is gapped around the Fermi level ($E = 0$) in one sublattice (here B) but exhibits a mid-gap peak in the other sublattice. Such an LDOS should lead to sublattice stripes in low bias STM images with sublattice A bright and B dark, which is very reminiscent of the midgap impurity states [92] to be discussed in section 5.1.2. The increased density of states at the Fermi level may cause instabilities, e.g. ferromagnetism as proposed by Guinea et al. [122]. To investigate this possibility by means of ab-initio theory we performed spin-polarized DFT calculations within the GGA as described above. Independent of the starting magnetization, mixing parameters etc., these calculations could not find any ferromagnetic state as self-consistent solution of the corresponding Kohn-Sham problem. This is very likely because of strong antiferromagnetic coupling between the sublattices A and B: It tends to spin-polarize atoms from the “dark” sublattice — an energetically unfavorable process because of the energy gap in this sublattice. Therefore, if local moments are formed in the “bright” sublattice, they will more likely arrange to noncollinear structures and prevent spin-polarization of their “dark” nearest neighbors.

In the low effective field region, the LDOS recovers the pseudogap shape typical for flat graphene and the two sublattices appear fully equivalent again. This transition from an inhomogeneous to a homogeneous local low energy electronic structure can be understood in terms of the band structure: For k_y away from the k-space center, $k_{LC} \approx 0.38(2\pi/a_0)$, of the $n = 0$ LL “plateau”, the real space center of the Landau level moves into regions of lower effective magnetic field (Fig. 4.8, left panel). This is very similar to the case of nanotubes in a magnetic field perpendicular to the tube axis [126]. For k_y such that the LL wave functions

from regions of opposite effective magnetic field start overlapping significantly, the corresponding band energies start to depend on k. Here, the wave function character changes back to that of the usual steep graphene π bands.

The band structures of the quenched ripples shown in Fig. 4.7 allow to estimate the strength of the involved pseudomagnetic fields: Given the shift of the Dirac point of $\delta k_y = 0.042(2\pi/a_0)$ away from the flat graphene value, we obtain the average gauge field $|A_0| = \hbar\delta k_y/e = 2.8 \cdot 10^3\,\mathrm{T}a_0$. With Eqs. (4.38-4.39) and for $q = 2\pi/80b_0$ this yields the amplitude sinusoidal pseudomagnetic field $\mathcal{B}_0 = A_0 q \approx 250$T. Due to $\mathcal{B} = \mathcal{B}_0 \sin(2qx)$ a pseudo Landau level wave function should be localized on a length less than $l/4$ corresponding to an area of $l^2/16 = 18\,\mathrm{nm}^2$ for the ripple under consideration. (See also Ref. [122].) The value of 250 T corresponds to approx. 2 (pseudo)magnetic flux quanta per $18\,\mathrm{nm}^2$.

The energy required to create the quenched ripples considered, here, is 0.5 eV/atom. They have maximum local strain of 24%, which is more than the average strain of approx. 1% measured in epitaxial graphene [125] or 4% found in other nanosized epitaxial materials [127]. Scaling down the pseudo magnetic field of the $l = 80b_0$ ripple with $h_0 = 20$Å to these strain values yields $\mathcal{B}_0 = 10\,\mathrm{T}$ and 40 T, respectively.

So far, we considered quenched ripples, but the pseudomagnetic field is sensitive not only to flexural deformations but also to in-plane distortions. In general, ripples will be accompanied by in-plane distortions: For the quenched ripple of length $l = 16b_0$ with $h/l = 1$Å$/4b_0$, we relaxed the atomic positions and the supercell shape of the ripple with the constraint of fixed rippling height. For this relaxed structure with atomic positions depicted in Fig. 4.6, lower panel, the "rippling" energy is 0.03 eV/atom. The structure is still sinusoidal but with all nearest neighbor bond lengths having relaxed back to 1.42-1.43Å — the value of flat graphene. During this relaxation process the effective gauge field decreases as can be seen from the band structure of the relaxed ripple in Fig. 4.7. The Dirac point for the relaxed ripple is at $k_y \approx 0.332(2\pi/a_0)$, which is by a factor of 40 closer the flat graphene value of $k_y = 1/3(2\pi/a_0)$ than the Dirac point of the quenched ripples. This corresponds to a decrease of the average effective gauge field the same factor. So, in the minimum energy structure of this still corrugated graphene sheet the different contributions to the rippling induced gauge field sum up to nearly zero average gauge field. This suppression of effective gauge and pseudomagentic fields in the annealed ripple turns out to be a very general effect and can be understood in terms of the model discussed in the next subsection.

4.2.3 Effective field theory for corrugated graphene

In section 4.2.1 we revisited the derivation of the low energy Hamiltonian of graphene and showed that strain and curvature cause gauge fields acting on graphene's Dirac fermions (see Eq. 4.35). We will now give an analytical model worked out by A. Tsvelik [128] to understand in which cases the ripple induced gauge fields lead to midgap states. We will restrict ourselves to the case of slow deformations when $A^{1,2} = 0$.

The zero energy wave functions in presence of a deformation induced vector potential can be found analytically for $A_0 = 0$. With $\mathcal{B}$ according to Eq. (4.37) and $\mathcal{B} > 0$ the zero energy wave functions can be expressed as

$$a_K = a_{-K} = z^n \exp\left[-\frac{\gamma}{\partial\bar{\partial}}\mathcal{B}\right], \quad b_K = b_{-K} = 0. \tag{4.40}$$

For $\mathcal{B} < 0$ one has to interchange a_K, a_{-K} with b_K, b_{-K} and z with $\bar{z}$. Inserting these wave functions into the effective Hamiltonian (4.36) shows that these are indeed $E = 0$ eigenfunctions. The condition of normalizability determines the range of allowed powers n: In two dimensions, the Green function of the Laplace operator is $(\partial\bar{\partial})^{-1} \sim \log|z|$. Consequently, $\frac{\gamma}{\partial\bar{\partial}}\mathcal{B} \sim \Phi \log|z|$, where $\Phi = \int \mathrm{d}z\mathrm{d}\bar{z}\, \mathcal{B}$ is the pseudomagnetic flux. Thus, we have $A_K = z^n \exp\left[-\frac{\gamma}{\partial\bar{\partial}}\mathcal{B}\right] = z^n|z|^{-\alpha\Phi}$, where the prefactor $\alpha = 1/\Phi_0$ turns out to be the inverse flux quantum Φ_0. These wave functions are normalizable for n ranging from 0 to the integer part of the pseudomagnetic flux. As many zero modes exist.

The expression for $\mathcal{B}$ and for the deformation tensor changes drastically depending on whether the elastic energy is at its minimum or not. The expression for the elastic energy density of a smooth surface compatible with the C_3 symmetry is given by [129, 66]:

$$\begin{aligned}
E &= (\lambda+\mu)(u_{xx}+u_{yy})^2 + \mu\left[(u_{xx}-u_{yy})^2 + 4u_{xy}^2\right] + \frac{K}{2}(\nabla^2 h)^2 \\
&= (\lambda+\mu)\left[\frac{1}{2}(\bar{\partial}u + \partial\bar{u}) + \partial h\bar{\partial}h\right]^2 \\
&\quad +\mu\left[\partial u + (\partial h)^2\right]\left[\bar{\partial}\bar{u} + (\bar{\partial}h)^2\right] + \frac{K}{2}(\nabla^2 h)^2 \\
&= \mu A\bar{A} + (\lambda+\mu)\left[\frac{1}{2\partial\bar{\partial}}(\bar{\partial}^2 A + \partial^2\bar{A}) + \frac{1}{\partial\bar{\partial}}\mathcal{R}[h]\right]^2 + \frac{K}{2}(\nabla^2 h)^2
\end{aligned} \tag{4.41}$$

where $\mathcal{R} = [\partial^2 h\bar{\partial}^2 h - (\partial\bar{\partial}h)^2]$ is the Gaussian curvature of the surface, λ, μ are in-plane Lamé constants and K is the bending rigidity of the surface. Integration over the whole surface is understood. If for given field h the membrane is at equilibrium, the elastic energy (4.41) is at its minimum, $\frac{\delta E}{\delta A} = \frac{\delta E}{\delta \bar{A}} = 0$, w.r.t. changes in A and $\bar{A}$:

$$\begin{aligned}
\frac{\delta E}{\delta \bar{A}} &= \mu A + (\lambda+\mu)\frac{\partial^2}{\partial\bar{\partial}}\left[\frac{1}{2\partial\bar{\partial}}(\bar{\partial}^2 A + \partial^2\bar{A}) + \frac{1}{\partial\bar{\partial}}\mathcal{R}[h]\right] \\
&= \mu A + (\lambda+\mu)\left[\frac{1}{2}A + \frac{\partial^4}{2(\partial\bar{\partial})^2}\bar{A} + \frac{\partial^2}{(\partial\bar{\partial})^2}\mathcal{R}[h]\right]
\end{aligned} \tag{4.42}$$

Consequently,

$$\begin{aligned}
0 &= \frac{\lambda+3\mu}{2(\lambda+\mu)}A + \frac{\partial^4}{2(\partial\bar{\partial})^2}\bar{A} + \frac{\partial^2}{(\partial\bar{\partial})^2}\mathcal{R}[h] \\
0 &= \frac{\bar{\partial}^4}{2(\partial\bar{\partial})^2}A + \frac{\lambda+3\mu}{2(\lambda+\mu)}\bar{A} + \frac{\bar{\partial}^2}{(\partial\bar{\partial})^2}\mathcal{R}[h],
\end{aligned}$$

or in matrix form $\underline{\mathrm{R}} = \underline{\mathrm{MA}}$ with

$$\underline{\mathrm{R}} = -\begin{pmatrix} \frac{\partial^2}{(\partial\partial)^2} \\ \frac{\partial^2}{(\partial\bar{\partial})^2} \end{pmatrix}\mathcal{R}[h],\ \underline{\mathrm{M}} = \begin{pmatrix} \frac{\lambda+3\mu}{2(\lambda+\mu)} & \frac{\partial^4}{2(\partial\partial)^2} \\ \frac{\partial^4}{2(\partial\bar{\partial})^2} & \frac{\lambda+3\mu}{2(\lambda+\mu)} \end{pmatrix}, \text{ and } \underline{\mathrm{A}} = \begin{pmatrix} A \\ \bar{A} \end{pmatrix}.$$

Thus the gauge field is

$$\begin{aligned} \underline{\mathrm{A}} &= \frac{(\lambda+\mu)^2}{\mu(\lambda+2\mu)}\begin{pmatrix} \frac{\lambda+3\mu}{2(\lambda+\mu)} & -\frac{\partial^4}{2(\partial\partial)^2} \\ -\frac{\partial^4}{2(\partial\bar{\partial})^2} & \frac{\lambda+3\mu}{2(\lambda+\mu)} \end{pmatrix}\underline{\mathrm{R}} \\ &= -\frac{(\lambda+\mu)^2}{\mu(\lambda+2\mu)}\begin{pmatrix} \frac{\mu}{\lambda+\mu}\frac{\partial^2}{(\partial\partial)^2} \\ \frac{\mu}{\lambda+\mu}\frac{\partial^2}{(\partial\bar{\partial})^2} \end{pmatrix}\mathcal{R}[h] \\ &= -\frac{\lambda+\mu}{\lambda+2\mu}\begin{pmatrix} \frac{\partial^2}{(\partial\partial)^2} \\ \frac{\partial^2}{(\partial\bar{\partial})^2} \end{pmatrix}\mathcal{R}[h]. \end{aligned} \tag{4.43}$$

$\mathcal{R}$ is the Jacobian of the coordinate transformation $\xi = \partial h$, $\bar{\xi} = \bar{\partial} h$:

$$\partial^2 h\bar{\partial}^2 h - (\partial\bar{\partial}h)^2 = \frac{\partial\left(\xi,\bar{\xi}\right)}{\partial\left(z,\bar{z}\right)}.$$

Thus, $\mathcal{R}$ as well as $A^3, \bar{A}^3$ vanish in any configuration of h which depends on just one Cartesian coordinate. This includes all plane wave configurations, in particular those studied by DFT in the previous section. Substituting Eq. (4.43) into (4.37) we get

$$\mathcal{B} = -i\frac{\lambda+\mu}{\lambda+2\mu}\frac{\partial^3 - \bar{\partial}^3}{(\partial\bar{\partial})^2}\mathcal{R}[h], \tag{4.44}$$

which is C_3 symmetric, as it must be.

This C_3 symmetry of $\mathcal{B}$ for a relaxed membrane leads to important qualitative differences with a real magnetic field. A local vortex of magnetic field with flux N carries N normalizable zero modes, but it is not possible to create such a flux by deforming a membrane and allowing for in plane relaxation: An analogue of a magnetic vortex is a point-like defect carrying local Gaussian curvature

$$h = h(|r-a|),\ \ \mathcal{R} = \mathcal{R}(|r-a|) = \int \frac{\mathrm{d}^2k}{(2\pi)^2}\mathcal{R}_k e^{ik(r-a)} \tag{4.45}$$

Then the argument in wave function (4.40) is

$$\frac{\gamma}{\partial\bar{\partial}}\mathcal{B} = \gamma\sin(3\phi)b(|r-a|) \tag{4.46}$$

$$b(r) = \int \frac{\mathrm{d}k}{(2\pi)k^2}J_3(kr)\mathcal{R}_k \tag{4.47}$$

where ϕ is the angle with respect to the crystalline axis. Since $\mathcal{R}_k$ is constant at small k, Eq. (4.47) yields $b(r) \sim r$ at distances larger than the size of the defect. Such wave function is not normalizable. On the other hand the wave function for

two defects with curvature of the opposite sign will be normalizable for the entire volume (as a plane wave). Such state is non-degenerate, that is we have $n = 0$ in (4.40).

So, if we allow the graphene membrane to relax there are only nondegenerate zero modes, which only exist for membrane configurations with nonzero Gaussian curvature. Therefore, the effect of relaxations on the electronic properties of the graphene ripples is qualitatively the same for 1D and 2D ripples. The *degenerate* zero modes are suppressed in relaxed ripples and no significant midgap peak in the total DOS of 2D ripples is expected to occur. The ab-initio calculations from the previous section reveal a perfect particle-hole symmetry at low energies and justify this nearest neighbor hopping based field theory for describing the electronic properties of graphene ripples.

Chapter 5

Impurities in graphene

In this chapter, we discuss how adsorbates affect the electronic properties of graphene and give a systematic theoretical investigation of impurity effects in this material. To this end, we go from simple models allowing for qualitative insights to more realistic models including full ab-initio descriptions of impurities on graphene. First, the Green function formalism is introduced which allows to address the local electronic properties of graphene in presence of impurities. A comparison of strongly schematized graphene with a model semiconductor and a model metal is given in this framework (section 5.1.1). We find that certain types of impurities create resonances in the vicinity of the Dirac point and discuss the nature of these "midgap states" in section 5.1.2. Predictions for STM experiments are given in this section. Within this model approach we also discuss impurities in superconducting graphene and describe how opening of a superconducting gap affects the low energy impurity states (section 5.1.5).

Section 5.2 is devoted to realistic DFT based studies of impurity effects in normal state graphene. We start with a detailled joint experimental and theoretical study addressing the interaction of NO_2 and N_2O_4 with graphene (section 5.2.1) and afterwards address the effect on H_2O on graphene in section 5.2.2. With these examples show that there are two distinct classes of impurities, open-shell impurities and inert impurities. The former interact directly with graphene and become charged or strongly hybridize. The latter interact weakly with graphene but may still lead to doping by mediating interactions between graphene and its substrate. In section 5.2.3 we give a broad investigation of open-shell impurities on graphene, discuss their electronic effects, their bonding energies and migration barriers. The latter will allow to judge which types of impurities are likely expected to occur in graphene samples.

5.1 Models of impurities in graphene

To study impurity effects in graphene we first compare impurities in a metal with rectangular DOS and a semiconductor with gapped DOS to the intermediate case of a graphene-type host with "V"-shape DOS. These models can be treated

fully analytically and allow us to understand the similarities and differences of graphene, normal semiconductors, and simple metals. In the next step (section 5.1.2), we consider impurities in a tight-binding model of graphene, which allows us to include atomistic details of the impurity; finally (section 5.1.3), we discuss the effect of impurities bringing along additional orbitals, which hybridize with the graphene bands.

5.1.1 Hosts with schematized electronic structure

Following [130], a simple model of a metal, a semiconductor and graphene is obtained from an unperturbed Hamiltonian

$$\hat{H} = \sum_k \epsilon_k c_k^\dagger c_k, \tag{5.1}$$

where c_k are Fermi operators of electrons labelled by the quantum number $k = (\vec{k}, \nu)$, which contains the crystal momentum $\vec{k}$ and the band index ν. The spin-index is omitted for simplicity. ϵ_k is the energy of the electron in the state k and the Fermi energy is defined to be $E_\mathrm{f} = 0$.

A short range spherically symmetric impurity can be imagined as a δ-function potential $V(x) = V\delta(x)$ and reads as $\hat{V} = V \sum_{k,k'} c_k^\dagger c_{k'}$ in this model.

The associated impurity effect on the electronic properties of the system can be obtained using Green function techniques: The unperturbed Green function is given by $\hat{G}^0(E) = (E - \hat{H} + i\delta)^{-1}$ and has matrix elements $G^0_{k,k'}(E) = \delta_{k,k'} \frac{1}{E-\epsilon_k+i\delta}$. The full Green function

$$\hat{G}(E) = (E - \hat{H} - \hat{V} + i\delta)^{-1} \tag{5.2}$$

is then

$$\hat{G}(E) = \hat{G}^0(E) + \hat{G}^0(E)\hat{T}(E)\hat{G}^0(E), \tag{5.3}$$

where the T-matrix is

$$\hat{T}(E) = \left(\mathbf{1} - \hat{V}\hat{G}^0(E)\right)^{-1} \hat{V}. \tag{5.4}$$

All single particle observables can be calculated from this Green function. Of particular interest is the LDOS, $N(r, E)$, in the vicinity of the impurity which is, e.g., probed by scanning tunnelling spectroscopy. At any point $\vec{r}$, the LDOS is given by $N(\vec{r}, E) = -\frac{1}{\pi}\mathrm{Im}\, G(\vec{r}, \vec{r}, E)$, where $G(\vec{r}, \vec{r}, E)$ is the real space representation of the Green function $\hat{G}(E)$:

$$G(\vec{r}, \vec{r}, E) = \sum_{k,k'} G_{k,k'}(E) e^{i(\vec{k}-\vec{k}')\cdot\vec{r}}. \tag{5.5}$$

As the unperturbed system is homogeneous and its real space Green function is independent of $\vec{r}$, we can define the local unperturbed Green function $g_0(E) = G^0(\vec{r}, \vec{r}, E) = \sum_k \frac{1}{E-\epsilon_k+i\delta}$. Using the Cauchy principal value $\mathcal{P}$, yields

$$g_0(E) = \mathcal{P} \sum_k \frac{1}{E - \epsilon_k + i\delta} - i\pi N_0(E), \tag{5.6}$$

where $N_0(E) = \sum_k \delta(E - \epsilon_k)$ is the unperturbed local density of states, and consequently

$$\mathrm{Re}\, g_0(E) = \mathcal{P} \int_{-\infty}^{\infty} \frac{N_0(E')}{(E - E')} \mathrm{d}E'. \tag{5.7}$$

Specifying the unperturbed LDOS is sufficient to determine the local unperturbed Green function. As the matrix elements of the localized perturbation $\langle k|\hat{V}|k'\rangle = V$ considered here are independent of k and k', Eq. (5.4) simplifies to $\langle k|\hat{T}(E)|k'\rangle = T(E)$ with

$$T(E) = (1 - V g_0(E))^{-1} V. \tag{5.8}$$

This formalism will be now used to compare impurity resonances in different model materials:

- a metal with rectangular and symmetric DOS with respect to the Fermi level $N_0^{\mathrm{m}}(E) = \frac{1}{2D} \cdot \Theta(D - |E|)$ and resulting Green function $g_0^{\mathrm{m}}(E) = \frac{1}{2D} \ln \left|\frac{D+E}{D-E}\right| - i\pi N_0^{\mathrm{m}}(E)$;
- a semiconductor with gap Δ in the DOS $N_0^{\mathrm{s}}(E) = \frac{1}{2D} \cdot (\Theta(D + \Delta - |E|) - \Theta(\Delta - |E|))$ and $g_0^{\mathrm{s}}(E) = \frac{1}{2D} \ln \left|\frac{(D+\Delta+E)(\Delta-E)}{(D+\Delta-E)(\Delta+E)}\right| - i\pi N_0^{\mathrm{s}}(E)$;
- graphene with DOS $N_0^{\mathrm{g}}(E) = \frac{|E|}{D^2} \cdot \Theta(D - |E|)$ and $g_0^{\mathrm{g}}(E) = \frac{E}{D^2} \ln \left|\frac{E^2}{D^2 - E^2}\right| - i\pi N_0^{\mathrm{g}}(E)$.

These unperturbed Green functions are depicted in Fig. 5.1. Eq. (5.3) shows that poles of the T-matrix cause impurity resonances, which occur according to Eq. (5.8) if

$$\mathrm{Re}\, g_0(E) = 1/V \text{ with } |\mathrm{Im}\, g_0(E)| \ll |\mathrm{Re}\, g_0(E)|. \tag{5.9}$$

The solutions to these conditions can be determined graphically (cf. [93]) as has been done in Fig. 5.1:

Weak impurities $|V_<| \ll D$ cause resonances close to the band edges and close to the gap edge of the model semiconductor, but no resonance in the middle of graphene's pseudogap is created. To obtain an impurity resonance in the vicinity of the Fermi level of graphene, the impurity potential has to exceed a threshold $|V| \gtrsim D$ on the order of the bandwidth. Concerning weak impurities $|V_<| \ll D$, graphene behaves like the model of the metal with no resonances close to the Fermi level and turns out to be robust against perturbations of this kind. As regards strong impurities $|V_>| \gg D$ graphene exhibiting an impurity state in the center of the (pseudo)gap is more similar to the model semiconductor than to the metal. This overall behavior of graphene is directly related to its local, unperturbed Green function g_0^{g}: The divergences of $\mathrm{Re}\, g_0^{\mathrm{g}}(E)$ are the same as for metal ($g_0^{\mathrm{m}}(E)$), but the structure of zeros $\mathrm{Re}\, g_0^{\mathrm{g}}(E) \to 0$ with $|\mathrm{Im}\, g_0^{\mathrm{g}}(E)| \ll |\mathrm{Re}\, g_0^{\mathrm{g}}(E)|$ is the same as for the semiconductor ($g_0^{\mathrm{s}}(E)$).

In the latter case of a strong impurity, the energy E_{imp} of the impurity resonance and its width Γ show a universal behavior. For $|V| \gg D$, Eq. (5.9) simplifies

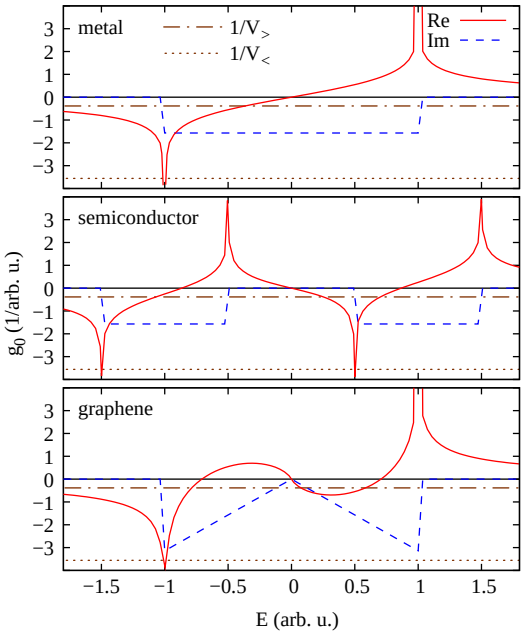

Figure 5.1: Unperturbed model Green functions for a metal g_0^{m}, a semiconductor g_0^{s}, and a graphene g_0^{g}. (Here, the bandwidth parameter is $D = 1$ and the semiconductor's gap is $\Delta = \frac{1}{2}$.) The real and imaginary parts are shown by solid and dashed lines, respectively. The real parts exhibit logarithmic divergences at band edges and have zeros in the center of the bands as well as in the middle of the gap (semiconductor) / pseudogap (graphene). Impurity resonances may occur at intersections of the $\mathrm{Re}\, g_0(E)$ with the $1/V$ lines. $|V_>| \gg D$ ($|V_<| \ll D$) illustrate strongly (weakly) attractive impurity potentials.

to $2E_{\mathrm{imp}} \ln\left|\frac{E_{\mathrm{imp}}}{D}\right| = \frac{D^2}{V}$ and consequently [93, 90, 92]

$$E_{\mathrm{imp}} \approx \frac{D^2}{2V \ln\left|\frac{D}{2V}\right|}. \tag{5.10}$$

This resonance is well-defined if its width Γ is small as compared to the distance to the closest Van-Hove singularity: $\Gamma \ll |E_{\mathrm{imp}}|$. An expansion of Eq. (5.8) about E_{imp} yields $T(E) \sim \frac{1}{(E-E_{\mathrm{imp}})+i\Gamma}$ with

$$\begin{aligned} \Gamma &= \mathrm{Im}\, g_0^{\mathrm{g}}(E_{\mathrm{imp}}) \cdot \left(\left.\frac{\partial \mathrm{Re}\, g_0^{\mathrm{g}}(E)}{\partial E}\right|_{E_{\mathrm{imp}}} \right)^{-1} \\ &\approx \frac{\pi}{2}|E_{\mathrm{imp}}| \left| \ln\left|\frac{E_{\mathrm{imp}}}{D}\right| + 1 \right|^{-1}. \end{aligned} \tag{5.11}$$

The criterion $\Gamma \ll |E_{\mathrm{imp}}|$ is best fulfilled for $|E_{\mathrm{imp}}|$ close to the Dirac point: With increasing potential strength $V \to \infty$, the impurity resonances approaches the Dirac point $|E_{\mathrm{imp}}| \to 0$ and becomes arbitrarily sharp $\Gamma \to 0$ with $\Gamma/|E_{\mathrm{imp}}| \to 0$.

5.1.2 The nature of midgap impurity state

The requirements to the discussion of the previous section were the bare density of states of the host material and that the matrix elements of the impurity potential are the same between all eigenstates $|k\rangle$ and $|k'\rangle$ of the unperturbed system. This leads to the possibly counterintuitively appearing conclusion that strong impurities, $V \to \infty$, cause midgap states in graphene and in semiconductors. Indeed, the same arguments can be made for impurities in the pseudogap phase of high-Tc superconductors [130, 93]. We now address the questions of what the nature of these impurity states is and why they occur.

In the language of Green functions, this question has been answered already: a host with unperturbed Green function $g_0(E)$ fulfilling $\mathrm{Re}\, g_0(E) \to 0$ and $|\mathrm{Im}\, g_0(E)| \ll |\mathrm{Re}\, g_0(E)|$ for $E \to E_{\mathrm{imp}} = 0$ is required.

The simplest system fulfilling this requirement is a two-level system with Hamiltonian $\hat{H} = \Delta\sigma_3$, where σ_i $(i = 1, 2, 3)$ are the usual Pauli matrices and σ_0 is the corresponding identity matrix. The eigenenergies of this system are $\pm\Delta$. In this system playing the role of the host, an "impurity potential" with the matrix elements between all eigenstates of the unperturbed system being the same reads as $\hat{V} = V(\sigma_0 + \sigma_1)$. The perturbed system $\hat{H} + \hat{V}$ is easily diagonalized and has eigenenergies $E_1 = 0$ and $E_2 = 2V$ in the limit $V \gg \Delta$. The state at zero energy $|-\rangle = (1, -1)/\sqrt{2}$ is the pendant of the midgap state in graphene and in the model semiconductor. So, a strong impurity forces the system into eigenstates of the impurity potential and the midgap states are those effectively decoupled $\hat{V}|-\rangle = 0$ from the impurity operator.

This result and its atomistic meaning can be translated to case of graphene by means of the tight-binding, Eqs. (3.1)-(3.2), model introduced in section 3.1. As $H_k = -\sigma_3 H_k \sigma_3$ is chiral, its spectrum is symmetric about $E = 0$ and given by $\epsilon(k) = \pm|\xi(k)|$. We will see that the chirality of this Hamiltonian manifests itsself in impurity induced midgap states.

Impurities acting as potential scatterers read in this model as $\hat{V}_{\mathrm{pot}} = \sum_{i,j} \Psi_i^\dagger V_{i,j} \Psi_j$, with $V_{i,j}$ being complex 2×2 matrices. The eigenstates of H_k are of the form $|k_\pm\rangle \sim (1, e^{i\phi(k)})$ with $\phi(k) \in [0, 2\pi)$. Therefore, impurities as discussed in section 5.1.1 with the matrix elements being the same between all eigenstates of the unperturbed Hamiltonian translate into this model as potentials localized at the origin and acting on one sublattice only: $V_{0,0} = V_{\mathrm{s}} = U_0 \begin{pmatrix} 1 & 0 \\ 0 & 0 \end{pmatrix}$, for a "single" impurity in sublattice A with potential strength U_0.

The Green function formalism introduced in section 5.1.1 can be directly applied to this tight-binding model of graphene with Eq. (5.8) involving now 2×2 matrices in sublattice space rather than complex numbers. The local Green function appearing in this context is $g_0(E) = \int_{\Omega_B} \frac{\mathrm{d}^2 k}{\Omega_B} (E - H_k + i\delta)^{-1}$.

Impurity resonances occur at $\mathrm{Re}\, \det T(E_{\mathrm{imp}}) = 0$ and a comparison of resonant energies E_{imp} in this tight-binding model to the purely DOS based model shows that single localized impurities acting one sublattice behave quasi identical in both models. (See Fig. 5.2.) E_{imp} approaches the Dirac point for $U_0 \to \infty$ in the same

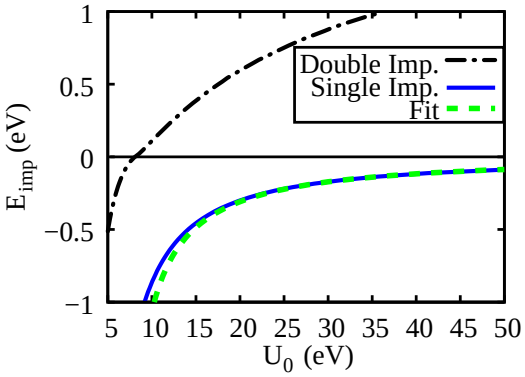

Figure 5.2: The energy E_{imp} of the impurity resonance as function of the potential strength U_0 is shown for single and double impurities. For the single scatterer E_{imp} obtained from the tight-binding model is compared to the result obtained from the DOS based model from section 5.1.1. (Eq. (5.10) with fitted bandwidth $D = 6.06\,\text{eV}$ and $V = U_0$.)

manner in both models.

The importance of the atomistic structure of the impurity for the creation of this midgap state can be inferred from the resonant energies of impurity states due to "double impurities" $V_{0,0} = V_{\text{d}} = U_0 \begin{pmatrix} 1 & 0 \\ 0 & 1 \end{pmatrix}$ acting on both sublattices within the unit cell at the origin. This pair of neighboring scatterers produces a resonance at the Dirac point for $U_0 = 3t \approx 8.1\,\text{eV}$ and E_{imp} changes sign, when U_0 passes through this value. This is in contrast to a single impurity, where $E_{\text{imp}} \to 0$ appears only in the limit of infinite potential strength and changing the sign of E_{imp} requires changing the sign of U_0.

This universal behavior of the single impurity is closely related to the real space shape of the created midgap state, i.e. the site dependence of impurity induced changes in the LDOS. In the tight binding formalism from above, the LDOS (as is the Green function) at a site i is 2×2 matrix $N(i,E) = -\frac{1}{\pi}\text{Im}\, G(i,i,E)$ in sublattice space. Its diagonal elements contain the LDOS projected on sublattice A (B) of the unit cell located at R_i. Introducing wave functions $\Phi_i(r)$ for the carbon p_z orbitals, this discrete LDOS can be converted to the continuous r-dependent LDOS $N(r,E) = -\frac{1}{\pi}\text{Im}\left(\sum_{i,j}\Phi_i(r)G(i,j,E)\Phi_j^\dagger(r)\right)$.

The LDOS in the vicinity of single and double impurities with resonances at $E_{\text{imp}} = -0.1\,\text{eV}$ are shown in Fig. 5.3. A strong single impurity in sublattice A induces an impurity state mostly localized in sublattice B and vice versa. A state localized in one sublattice can be realized only close to the Dirac point $E = 0$, as chirality of the Hamiltonian requires

$$\begin{aligned} E_{\text{imp}} \begin{pmatrix} 1 \\ 0 \end{pmatrix} &= H_k \begin{pmatrix} 1 \\ 0 \end{pmatrix} = -\sigma_3 H_k \sigma_3 \begin{pmatrix} 1 \\ 0 \end{pmatrix} \\ &= -E_{\text{imp}} \begin{pmatrix} 1 \\ 0 \end{pmatrix}. \end{aligned} \tag{5.12}$$

This result can be also viewed as manifestation of Lieb's theorem [131] in

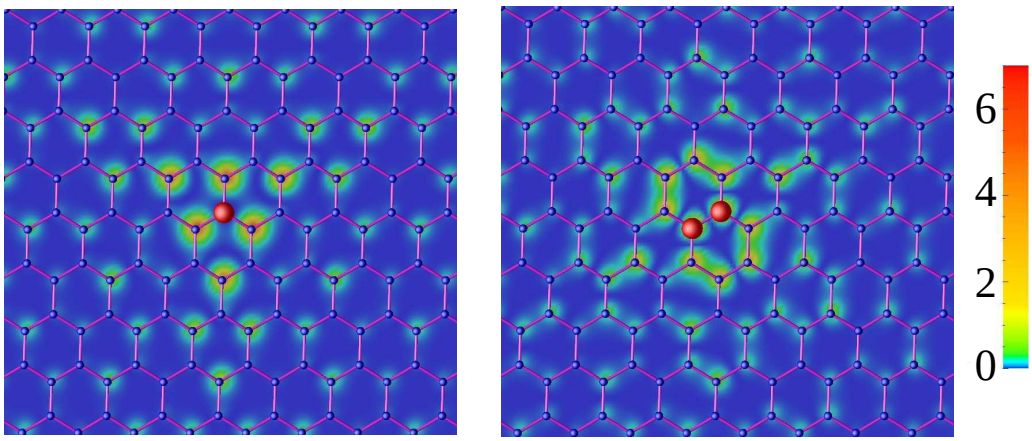

Figure 5.3: Real space properties of impurity states for different atomic structures of the impurity: The r-dependent LDOS at $E = E_{\mathrm{imp}} = -0.1\,\mathrm{eV}$ is shown for a single impurity with $U_0 = 45\,\mathrm{eV}$ (left) and for a scalar double impurity with $U_0 = 6.9\,\mathrm{eV}$ (right) encoded corresponding to the color bar. The impurity sites are marked as big red dots in the center of the images. The impurity state due to the single impurity in one sublattice is almost entirely localized in the other sublattice. Such a state can only exist very close to the Dirac point. (See Eq. (5.12).)

graphene: Having an infinitely strong potential acting at one site means decoupling this site from the rest of the system and thus having different numbers of atoms in sublattices A and B: $N_{\mathrm{A}} \neq N_{\mathrm{B}}$. Lieb's theorem states that any repulsive Hubbard model on a bipartite lattice will have a ground state with spin $S = 1/2|N_{\mathrm{A}} - N_{\mathrm{B}}|$. So, the impurity state with $E_{\mathrm{imp}} \to 0$ is the host of this magnetic moment.

As discussed in section 3.4, STM allows to image impurity states with very high spatial resolution. This high resolution is "enhanced" by the symmetry of graphene's electronic states at the Fermi level, which results in the impurity states depending strongly on microscopic details of the impurity like the adsorption site: As Fig. 5.3 shows, single and double impurities can be distinguished by the symmetry of the induced impurity state even if the resolution of the STM is not sufficient to resolve the difference between single and double impurities, directly. In section 6.5, we will find that the particular symmetries of graphene's low energy electronic states will allow to distinguish between different impurity orbitals causing a resonance.

Investigating the effect of impurities in graphene on the length scale of the lattice constant requires H_k from Eq. (3.2) as description of the pristine system, whereas at larger length scales H_{lin} from Eq. (3.4) suffices as unperturbed starting point. Using this linearized Hamiltonian, we will show in section 5.1.5 that the diagonal part of graphene's unperturbed real space Green function simplifies to

$$g_0(r,\omega) = \omega v_{\mathrm{f}}^2 \int \mathrm{d}p \frac{p J_0(pr)}{D^2(\omega^2 - v_{\mathrm{f}}^2 p^2)}$$

for large distances $r \gg \hbar v_{\mathrm{f}}/\omega$ from the impurity site. As a consequence, the

changes in LDOS decay according to a power law $\Delta N(r, E_{\text{imp}}) \propto 1/r$ for $E_{\text{imp}} \neq 0$ as found by several authors [88, 132, 92]. This is in contrast to a hard-wall impurity, i.e. $U_0 \to \infty$ and $E_{\text{imp}} = 0$, which has $1/r^2$ asymptotics of $\Delta N(r, E_{\text{imp}})$ [133].

5.1.3 Resonant impurities

So far, we considered impurities acting as potential scatterers in graphene. Many impurities contribute orbitals, $\hat{H}_{\text{imp}} = \epsilon_{\text{imp}} d^\dagger d$, with Fermi operator d and energy ϵ_{imp} which hybridize with the graphene bands, $\hat{V} = \sum_i \Psi_i^\dagger V_i d + \text{h.c.}$. This problem has been extensively discussed for normal metals and is often referred to as "non-interacting Anderson impurity model" [27].

Changing to the momentum space representation $\hat{V} = \int_{\Omega_B} \frac{\mathrm{d}^2 k}{\Omega_B} \Psi_k^\dagger V_k d + \text{h.c.}$ and evaluating the appropriate matrix elements in Eq. (5.2) leads to the coupled equations

$$(E - \epsilon_k) G_{k,k'}(E) = \delta_{k,k'} + V_{k'}^* G_{d,k'}(E) \tag{5.13}$$

$$(E - \epsilon_d) G_{d,d}(E) = 1 + \sum_k V_k G_{k,d}(E) \tag{5.14}$$

$$(E - \epsilon_k) G_{k,d}(E) = V_k^* G_{d,d}(E) \tag{5.15}$$

$$(E - \epsilon_d) G_{d,k}(E) = \sum_{k'} V_{k'} G_{k',k}(E), \tag{5.16}$$

where $k = (\vec{k}, \pm)$ includes crystal momentum $\vec{k}$ and band index $\pm$. These can be decoupled to

$$(E - \epsilon_k) G_{k,k'}(E) = \delta_{k,k'} + \sum_{k''} \frac{V_{k'}^* V_{k''}}{E - \epsilon_d} G_{k'',k'}(E) \tag{5.17}$$

and

$$(E - \epsilon_d) G_{d,d}(E) = 1 + \sum_k \frac{|V_k|^2}{E - \epsilon_k} G_{d,d}(E). \tag{5.18}$$

Eq. (5.17) shows that a resonant impurity acts on the graphene electrons like an energy dependent potential

$$V_{k,k'}(E) = \frac{V_{k'}^* V_{k'}}{E - \epsilon_d}. \tag{5.19}$$

Hence, all results for the potential impurities can be translated to resonant impurities. Combining Eqs. (5.10) and (5.19) yields possible resonant energies E_{imp} with corresponding resonance width Γ according to Eq. (5.11). Well defined impurity resonances with significant spectral weight in the graphene bands require that $\Gamma \ll |E_{\text{imp}} - \epsilon_d|$, i.e. that the singularity in the effective potential, Eq. (5.19), is well separated from the resonance.

An adsorbate having an orbital close to the Dirac point ($|\epsilon_d| \ll D$), which is strongly bond to one carbon atom in one sublattice only ($V_k = V \gtrsim D$), fulfills this condition and will act like a very strong static impurity potential in the vicinity

of the Dirac point. A chiral midgap state with $|E_{\text{imp}}| < |\epsilon_d|$ is created. A weakly hybridized impurity orbital ($V_k = V \to 0$) will lead to $E_{\text{imp}} \to \epsilon_d$ and $|E_{\text{imp}} - \epsilon_d| < \Gamma$. No strong resonance in the graphene bands will occur. However, depending on its filling a weakly hybridized impurity orbital can act as donor or acceptor level and create a charged impurity. We will encounter this situation in section 5.2.1.

5.1.4 Clusters and extended impurities

The impurities considered so far acted on the length scale of the graphene lattice constant and graphene prove insensitive to single weak perturbations at this length scale. We briefly turn now to potentials which act over bigger areas of the graphene sheet and which are smooth on the atomic scale. Such potentials are diagonal in the sublattice indices and enter the tight-binding model as $\hat{V}_{\text{pot}} = \sum_i V_i \Psi_i^\dagger \Psi_i$, with V_i being a real number varying slowly with site index i. Transferring to the long wavelength Dirac formalism yields smooth scalar potentials $V(r)\sigma_0$. These potentials shift the Dirac point locally, i.e. they lead to local doping if either the surrounding graphene sheet or the substrate can act as reservoir for electrons or holes. In this way, charge inhomogeneities can be created which are referred to as "electron and hole puddles" [134] if the averaged chemical potential is close to the Dirac point, $\bar{\mu} = 0$. These puddles are considered important for electron transport in the $\bar{\mu} = 0$ regime [83]. In this sense, weak extended potentials may strongly influence the electronic properties of a graphene sample.

Besides local doping effects, graphene's electronic properties turn out to be insensitive also to these extended potentials: As these potentials are diagonal in sublattice space, they cannot change the sublattice isospin of charge carriers upon scattering. This leads to a strong suppression of backscattering of electrons off potential barriers and all smooth barriers becoming fully transparent for electrons at normal incidence [83].

5.1.5 Impurities in superconducting graphene

In the preceding sections it has been discussed that certain impurities can substantially change clean graphene's linearly vanishing density of states: Strong impurities cause virtual bound states (VBS), i.e. resonances in the DOS, which may be arbitrarily sharp in the vicinity of the Dirac point.

Recently, proximity induced superconductivity in graphene has been demonstrated [135] and opened exciting opportunities for experiments: Superconducting graphene is an explicit example of valleytronics [136], where opposite valleys are nontrivially coupled. Understanding impurity effects is interesting in this context, for two reasons: First, it shows how the special low energy electronic properties of normal state graphene translate into other phases of this material. In addition, the possibility of intragap bound states is directly related to the stability of the superconducting state in graphene.

In this section, we theoretically investigate proximity induced superconductivity in graphene and study impurity effects on the LDOS. In the proximity effect, the pairing state of the Cooper pairs tunneling from the superconductor to graphene, will be controlled by the pairing state of superconductor. As in the case of the experiment by Heersche et. al.[135], we consider s-wave Cooper pairs in graphene. While intrinsic superconductivity in graphene is controversial [137] and no spectral gap in the samples has been measured to date, we note that Ti/Al bilayer contacts placed on the graphene sheet induce a measured supercurrent [135]. In presence of these *injected* Cooper pairs, any type of electron-electron interactions in graphene will produce a gap in the spectrum. This gap Δ will be proportional to the interaction strength and it remains to be seen how large it can be in graphene. Electron spectroscopy such as STM and/or planar tunneling into graphene in proximity to superconducting leads would be able to reveal this spectroscopic gap. We will treat Δ below as a phenomenological parameter that needs to be determined separately. Furthermore, we describe graphene in this proximity regime by Bogoliubov-de Gennes theory, since screening is rather efficient in this material [138].

As discussed in section 3.1, low energy electronic excitations in normal states graphene can be described by a Hamiltonian $H_{K^\pm} = v_\mathrm{f}\hbar(k_1\sigma_1 \mp k_2\sigma_2)$, where σ_i, $i = 1, 2, 3$, are Pauli matrices acting on the sublattice degrees of freedom, σ_0 is the identity matrix, and v_f is the Fermi velocity[1].

To understand impurities in superconducting graphene, we rewrite the above Hamiltonian to the Nambu formalism including both valleys:

$$\hat{H} = -i\hbar v_f \int \mathrm{d}^2x \hat{\Psi}^\dagger(x)(\partial_1\sigma_1 \otimes \tau_0 - \partial_2\sigma_2 \otimes \tau_3) \otimes \Lambda_0 \hat{\Psi}(x) \tag{5.20}$$

with $\hat{\Psi}(x)^\dagger = (\Psi^\dagger_{\downarrow K^+}(x), \Psi^\dagger_{\downarrow K^-}(x), \Psi_{\uparrow K^-}(x), \Psi_{\uparrow K^+}(x))$ and $\Psi_{\uparrow\downarrow K^\pm}(x)$ being field operators of electrons with a spin $\uparrow\downarrow$ and belonging to a valley $K^\pm$. τ_i and Λ_i with $i = 1, 2, 3$ are Pauli matrices acting on the valley and Nambu space, respectively. τ_0 and Λ_0 are the corresponding identity matrices. In this formalism the proximity induced pairing potential enters as $\Delta\sigma_3 \otimes \tau_0 \otimes \Lambda_1$ and results in electron dynamics being described by the Dirac-Bogoliubov-de Gennes (DBdG) Hamiltonian [139]:

$$H = -i\hbar v_f(\partial_1\sigma_1 \otimes \tau_0 - \partial_2\sigma_2 \otimes \tau_3) \otimes \Lambda_0 + \Delta\sigma_3 \otimes \tau_0 \otimes \Lambda_1. \tag{5.21}$$

The two valley Dirac Hamiltonian, Eq. (3.4), as well as the DBdG Hamiltonian, Eq. (5.21), allow for local impurities being parameterized by ten independent parameters [140]:

$$V = u_0(\sigma_0 \otimes \tau_0) + \sum_{s,l=1}^{3} u_{s,l}\sigma_s \otimes \tau_l. \tag{5.22}$$

Each of the parameters is associated with a particular scattering source. u_0, for instance, corresponds to an electrostatic potential averaged over one unit cell and

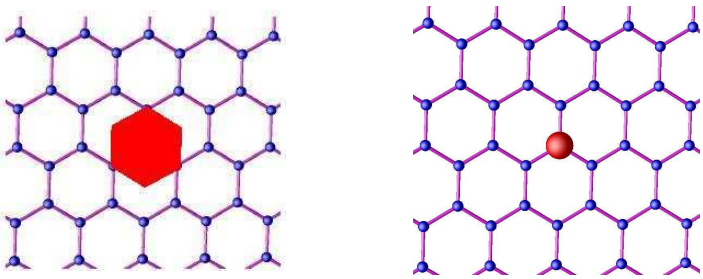

Figure 5.4: Among the various local impurities we discuss two limiting cases. The scalar impurity (left), V_s, corresponds to a uniform potential averaged over one unit cell, whereas the on-site impurity (right), V_o, acts on one sublattice only.

$u_{3,3}$ to different on-site energies in sublattice A and B. We discuss two limiting cases: a homogeneous potential acting within one unit cell V_s (”scalar impurity“) as well as a strongly localized impurity V_o (”on-site impurity“) acting only at sublattice A and giving rise to intervalley scattering. (See Fig. 5.4).

Starting from impurity operators in the tight-binding form of Section 5.1.2 and using the conventions of Eq. (5.21) we obtain the following explicit expressions for the impurity potentials in the adopted matrix notation:

$$V_\mathrm{s} = V_0\sigma_0 \otimes \tau_0 \otimes \Lambda_3 + V_1\sigma_0 \otimes \tau_0 \otimes \Lambda_0 \tag{5.23}$$

and

$$V_o = V_0(\sigma_3 + \sigma_0) \otimes (\tau_0 + \tau_1) \otimes \Lambda_3 + V_1(\sigma_3 + \sigma_0) \otimes (\tau_0 + \tau_1) \otimes \Lambda_0. \tag{5.24}$$

In both cases V_0 and V_1 describe the electrostatic and magnetic contribution to the impurity potential, respectively. The effect of these impurities on the local electronic properties of the superconducting graphene sheets is contained in the LDOS, which we calculate using the T-matrix approach as introduced in Section 5.1.1 or in Ref. [93].

Dealing with local impurities, it is convenient to adopt the position space representation. Therefore, the free x-dependent Green’s function $G(x,\omega)$ in polar coordinates, $x = x(r,\phi)$, is obtained from its momentum space counterpart

$$\begin{aligned} G^0(p,\omega) &= (\omega - H)^{-1} \\ &= \frac{(\omega\sigma_0 \otimes \tau_0 + v_\mathrm{f}[p_1\sigma_1 \otimes \tau_0 - p_2\sigma_2 \otimes \tau_3]) \otimes \Lambda_0 + \Delta\sigma_3 \otimes \tau_0 \otimes \Lambda_1}{\omega^2 - v_\mathrm{f}^2 p^2 - \Delta^2} \end{aligned}$$

by Fourier transformation

$$\begin{aligned} \hat{G}^0(x,\omega) &= \int \frac{\mathrm{d}^2 p}{\Omega_B}\, \hat{G}^0(p,\omega) e^{ipx} \\ &= g_0(r,\omega)(\omega\sigma_0 \otimes \tau_0 \otimes \Lambda_0 + \Delta\sigma_3 \otimes \tau_0 \otimes \Lambda_1) \\ &\quad + g_1(r,\omega)([\cos\phi\,\sigma_1 \otimes \tau_0 + \sin\phi\,\sigma_2 \otimes \tau_3] \otimes \Lambda_0) \end{aligned} \tag{5.25}$$

[1]Here, we define σ_i acting for both valleys, $K^\pm$, on pseudospinors of the form $\Psi_{K^\pm} = (\psi^A_{K^\pm}, \psi^B_{K^\pm})$, where A and B denote the two sublattices.

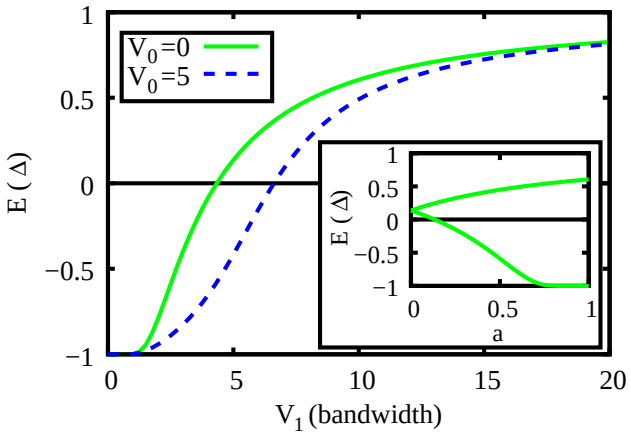

Figure 5.5: Energy of the impurity resonance for the scalar impurity as a function of the magnetic impurity potential V_1 for different electrostatic potentials V_0. The gap-parameter is $\Delta = W/10$. The lower right inset shows the splitting of the impurity state due to intervalley scattering. We model intervalley scattering as $V = V_1(\sigma_0 \otimes \tau_0 \otimes \Lambda_0 + a\sigma_0 \otimes \tau_1 \otimes \Lambda_0)$ with the strength of the intervalley scattering parameterized by a and $V_1 = 5W$. One split state is shifted to the gap edge, the other state remains an intragap state.

with

$$g_0(r,\omega) = v_\mathrm{f}^2 \int_0^{p_c} \mathrm{d}p\, p \frac{J_0(pr)}{W^2(\omega^2 - \Delta^2 - v_\mathrm{f}^2 p^2)} \tag{5.26}$$

and

$$g_1(r,\omega) = iv_\mathrm{f}^3 \int_0^{p_c} \mathrm{d}p\, p^2 \frac{J_1(pr)}{W^2(\omega^2 - \Delta^2 - v_\mathrm{f}^2 p^2)}, \tag{5.27}$$

where we expressed the Brillouin zone volume $\Omega_B = 2\pi W^2/v_\mathrm{f}^2$ in terms of the bandwidth W.

The Green function at $x = 0$ determines the LDOS of the clean system: $\hat{G}^0(0, \omega + i\delta) = M(\omega)(\omega\sigma_0 \otimes \tau_0 \otimes \Lambda_0 + \Delta\sigma_3 \otimes \tau_0 \otimes \Lambda_1)$. Here is $M(\omega) = M'(\omega) + iM''(\omega)$ with

$$M'(\omega) = \frac{1}{2W^2} \ln \left| \frac{\Delta^2 - \omega^2}{W^2 + \Delta^2 - \omega^2} \right| \tag{5.28}$$

and

$$M''(\omega) = \begin{cases} -\frac{\pi\,\mathrm{sgn}(\omega)}{2W^2} & \text{for } \Delta^2 < \omega^2 < \Delta^2 + W^2 \\ 0 & \text{else.} \end{cases} \tag{5.29}$$

The corresponding LDOS vanishes within the superconducting gap ($\omega^2 < \Delta^2$) and is given by $N_0(\omega) = \frac{4|\omega|}{W^2}$ outside the gap, which is quite different from usual BCS superconductors as there are *no* coherence peaks at the gap edge.

As discussed in Section 5.1.2, impurity resonances occur when the T matrix becomes (almost) singular, i.e. $\det(1 - G^0(0,\omega)V) = 0$. For the scalar impurity this secular equation yields

$$1 - 2M(\omega)\omega V_1 + M^2(\omega)(\omega^2 - \Delta^2)(V_1^2 - V_0^2) = 0 \tag{5.30}$$

with solutions that can be understood analytically in the following limiting cases: Firstly consider a solely magnetic impurity, i.e. $V_0 = 0$, with $V_1 > 0$. In the Born limit the solutions $\omega_0 = -\Delta \pm \delta\omega$ with

$$\delta\omega = \frac{W^2}{2\Delta} e^{-W^2/(\Delta V_1)} \tag{5.31}$$

give rise to intragap bound and virtual bound states in the continuum approaching the gap edge exponentially with decreasing V_1.

In the opposite limit of unitary scattering $\omega_0 = \pm\Delta - \delta\omega$ with

$$\delta\omega = -\frac{2W^2}{V_1 \ln\left(\frac{2\Delta}{V_1}\right)} \tag{5.32}$$

fulfills the secular equation, where the upper (lower) sign corresponds to an intragap bound (continuum virtual bound) state.

It is insightful to compare superconducting graphene to usual s-wave superconductors. Analogous arguments have shown that intragap bound states occur in these systems at $\omega_0 = \Delta - \delta\omega$ with

$$\delta\omega = \frac{2(\pi V_1 N_0/2)^2}{1 + (\pi V_1 N_0/2)^2}\Delta, \tag{5.33}$$

where N_0 is the density of states at the Fermi level of the normal state material [93]. Graphene has $N_0 \to 0$ resulting in the functional dependence of the resonance energies being different from Eq. (5.33). Superconducting graphene is not as sensitive to magnetic impurities as usual s-wave superconductors are: In the case of weak impurities resonant energies approach the gap edge exponentially, Eq. (5.31), in contrast to $\delta\omega \sim V_1^2$ in the usual s-wave case.

Numerical solutions to energies of the intragap bound states in graphene are shown in Fig. 5.5. They recover the limiting cases obtained analytically, Eq. (5.31)-(5.32) and demonstrate also the effect of an electrostatic contribution V_0 to the impurity potential: In the Born limit, the exponential dependence of $\delta\omega$ on the magnetic potential strength V_1 is dominant and suppresses any significant influence of V_0 on the impurity state energy. In the $V_1 \to \infty$ limit, V_0 leads to a renormalization of the *effective* magnetic potential strength $V_1 \to V_1(1 - \frac{V_0^2}{V_1^2})$. As Fig. 5.5 shows, the effect of an additional electrostatic potential becomes most pronounced in the intermediate region, where it reduces the effective magnetic potential strength most significantly. However, no qualitative changes regarding the resonant energies occur.

To elucidate the effect of intervalley scattering, we compare the strongly localized on-site impurities to the scalar impurities discussed above. Due to valley degeneracy, the scalar impurity gives rise to doubly degenerate intra gap bound states. This degeneracy is lifted by intervalley scattering, $V = V_1(\sigma_0 \otimes \tau_0 \otimes \Lambda_0 + a\sigma_0 \otimes \tau_1 \otimes \Lambda_0)$, as a is increased from 0 to 1. (See Fig. 5.5).

The secular equation for the on-site impurity, $a = 1$, reduces to that of a scalar impurity with the replacement $V_{0,1} \to 4V_{0,1}$. Thus, apart from lifting the valley degeneracy intervalley scattering results in a renormalization of the effective

impurity strength. Note, however, that although both valleys K and K' are nontrivially coupled by the superconducting pairing and despite the pseudo spin nature of the valley degree of freedom, only real magnetic impurities act as pair breakers — a consequence of the Anderson theorem [141].

We will now turn to the real space properties of impurity states in superconducting graphene and compare to usual s-wave-superconductors as well as normal state graphene. With the real-space Green's function $G(x,x',\omega) = G^0(x-x',\omega) + G^0(x,\omega)T(\omega)G^0(-x',\omega)$ one obtains the local density of states $N(x,\omega) = N_0(\omega) + \delta N(x,\omega) = -\frac{1}{\pi}\mathrm{Im}G(x,x,\omega)$ in presence of an impurity. As before, this LDOS is a matrix corresponding to the matrix structure of the Green function. Here, it accounts for the contributions from the different sublattices, valleys and the Nambu space. According to Eq. (5.21), the spin-up excitations are hole excitations yielding for each spin component the LDOS

$$N_{\downarrow\uparrow}(x,\omega) = \mathrm{Tr}\,\frac{\Lambda_0 \pm \Lambda_3}{2} N(x,\pm\omega), \tag{5.34}$$

where the trace involves either the spin-down or up part of the Nambu space. In the case of the scalar impurity, this yields the following corrections to the unperturbed LDOS

$$\delta N_{\downarrow\uparrow}(r,\pm\omega) = -\frac{4}{\pi}\mathrm{Im}\frac{a_{\downarrow\uparrow}g_0^2(r,\omega) + b_{\downarrow\uparrow}g_1^2(r,\omega)}{1 - 2M(\omega)\omega V_1 + M^2(\omega)(\omega^2-\Delta^2)(V_1^2 - V_0^2)} \tag{5.35}$$

with $a_{\downarrow\uparrow} = (\omega^2-\Delta^2)[\pm V_0 + M(\omega)\omega(V_0^2 - V_1^2)] + (\omega^2+\Delta^2)V_1$ and $b_{\downarrow\uparrow} = (\pm V_0 + V_1) + M(\omega)\omega(V_0^2 - V_1^2)$. By replacing $M(\omega) \to 4M(\omega)$ in these formula, one obtains the case of the strongly localized on-site impurity.

Due to Eq. (5.35), the asymptotic decay of impurity induced LDOS modulations at large distances from the impurity is governed by $g_0^2(r,\omega_0)$ and $g_1^2(r,\omega_0)$. Neglecting high-energy cut-off related oscillations at this length scale, one may extend the momentum space integrals in Eq. (5.25) to infinity. This yields modified Bessel functions, i.e. $g_0(r,\omega_0) = -\frac{1}{W^2}\mathrm{K}(0,\mathrm{r}\sqrt{\Delta^2-\omega_0^2}/\mathrm{v_f})$ and $g_1(r,\omega_0) = -\frac{i\sqrt{\Delta^2-\omega_0^2}}{W^2}\mathrm{K}(1,\mathrm{r}\sqrt{\Delta^2-\omega_0^2}/\mathrm{v_f})$. Therefore, the LDOS of impurity induced intragap states decays as

$$\delta N_{\downarrow\uparrow}(r,\pm\omega_0) \propto r^{-1}e^{-2r\sqrt{\Delta^2-\omega_0^2}/\mathrm{v_f}}. \tag{5.36}$$

The exponential decay is the same as in usual s-wave superconductors, whereas the $1/r$ prefactor is characteristic for two dimensional materials [130, 93].

As Fig. 5.6 (a) shows, impurity states in the gap can give rise to prominent features in the LDOS, which may be measured by STM: The density of the impurity state at the impurity site at $r = 0$ as well as the maximum of the density are strongly sensitive to the particular type of impurity. In general, impurity states with energies in the middle of the gap ($V_1 = 5W$ in Fig. 5.6 (la)) give rise to the sharpest maxima in the r-dependent LDOS. The ratio of the maximum density to the density at the impurity site increases with the potential strength V_1.

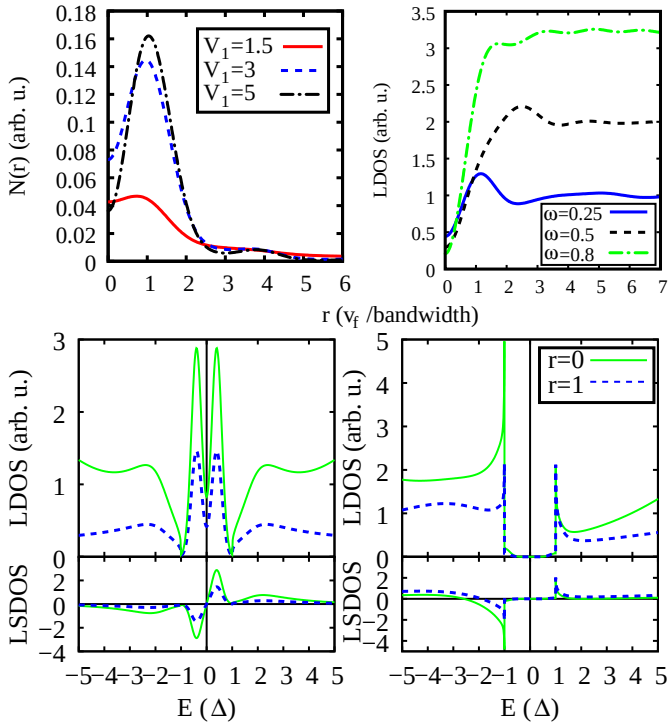

Figure 5.6: Upper panel: Left: Density N of the intra-gap bound states as a function of the distance r from the impurity for purely magnetic scalar impurities and different potentials V_1. The impurity strength is given in units of the bandwidth W. Right: Friedel oscillations in the local density of states (LDOS) around a scalar impurity at $r = 0$ with $V_0 = 0$ and $V_1 = 3W$. The different curves correspond to the energies $\omega = 0.8$, 0.5 and $0.25W$. In both panels, the gap-parameter is $\Delta = W/10$. Lower panel: The local density of states (LDOS, upper panel) and the local spin density of states (LSDOS, lower panel), $\delta N_\uparrow(r,\omega) - \delta N_\downarrow(r,\omega)$, at $r = 0$ and $r = 1$ is shown for scalar of impurities with different potentials: a purely magnetic impurity with $V_0 = 0$ and $V_1 = 3W$ (left) as well as an impurity with $V_0 = 2W$ and $V_1 = 1W$.

In the continuum, Eq. (5.35) encodes the real space shape of VBS around the impurities. As Fig. 5.6 (b) shows exemplary for a scalar impurity, the wavelength λ of these oscillations is always determined by the energy ω and the gap Δ: $\lambda = \pi v_f / \sqrt{\omega^2 - \Delta^2}$. Therefore, the asymptotic long range decay of LDOS oscillations in the continuum is qualitatively the same for normal state and superconducting graphene.

The most prominent differences between normal state and superconducting graphene appear in the energy dependence of the LDOS in the vicinity of an impurity:

In Fig. 5.6, the LDOS near a purely magnetic scalar impurity with $V_0 = 0$ and $V_1 = 3W$ is compared to an impurity contributing an electrostatic potential $V_0 = 2W$ and $V_1 = 1W$. The purely magnetic impurity, Fig. 5.6 (c), does not break particle hole symmetry and yields therefore a fully symmetric LDOS and a fully antisymmetric local spin density of states (LSDOS). This is in contrast to the more general second impurity, Fig. 5.6 (d), where the LDOS and LSDOS are

not symmetric under particle hole transformation.

Moreover, both *magnetic* impurities considered, here, lead to resonances in the continuum close to the superconducting gap-edge. Such resonances do not occur for normal states graphene and are very similar to the resonances occurring close the gap edges of the model semiconductor discussed in Section 5.1.1: The real parts of the local Green function of superconducting graphene (Eq. 5.28) and the model semiconductor are very similar as both diverge logarithmically at the gap edge.

5.2 Realistic impurity effects

In the previous sections we discussed different mechanisms of impurities interacting with graphene in terms of (semi)analytically solvable models. We now work out which of these models apply to which impurities present in real graphene samples and give an understanding of doping of graphene by adsorbates. To this end, we firstly consider the NO_2 system interacting with graphene and give a combined experimental and theoretical study. The experiments were carried out by K. Novoselov et al. in A. Geim's group at the University at Manchester. Afterwards we proceed with discussing the importance of substrate effects in the context of H_2O adsorbates on graphene. Afterwards, the relation of bonding mechanisms, migration barriers and the occurrence of chiral midgap states in graphene is studied.

5.2.1 The NO_2 system on graphene

Theoretically, the electronic and structural properties of the graphene adsorbate systems are addressed by means of DFT, as described in detail in my diploma thesis [142]. In short, all calculations are carried out with the VASP [48] using the projector augmented waves (PAW) [53, 52] basis sets (c.f. sections 2.3.3 and 2.4). As van der Waals forces are ill represented in the local density approximation (LDA) as well as in gradient corrected exchange correlation functionals (GGA) resulting in over- and underbonding, respectively [143], we apply both functionals to obtain upper and lower bounds for adsorption energies and related structural properties. The plane wave expansions of the Kohn-Sham orbitals were cut off at 875 eV in the GGA [42] and at 957 eV in the LDA-calculations.

In this periodic scheme, single NO_2 and N_2O_4 adsorbates are modelled in 3×3 and 4×4 graphene supercells, respectively. The ionic configurations presented here are fully relaxed with all forces being less than $0.02\,\mathrm{eV\,\AA^{-1}}$, and the convergence of subsequent total energy calculations is guaranteed by applying the tetrahedron method with Blöchl corrections on Γ-centered k-meshes denser than $30\times30\times1$, when folded back to the single graphene Brillouin zone. As in Ref. [144], the DOS obtained in our DFT calculations are the central quantities in the following discussion of the adsorbate effects on the electronic properties of the graphene sheets.

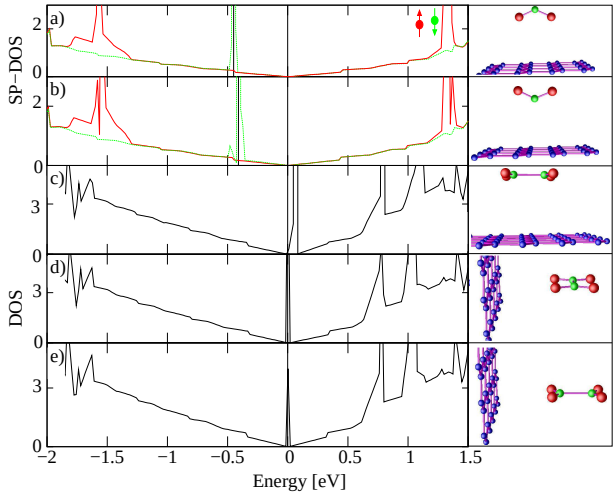

Figure 5.7: Left: Spin-polarized DOS of the graphene supercells with adsorbed NO_2, a) - b), and DOS of graphene with N_2O_4, c) - e), in various adsorption geometries. The energy of the Dirac points is defined as $E_D = 0$. In the case of NO_2 the Fermi level E_f of the supercell is below the Dirac point, directly at the energy of the spin down POMO, whereas for N_2O_4 E_f is directly at the Dirac points. Right: Adsorption geometries obtained with GGA. The carbon atoms are printed in blue, nitrogen green and oxygen red.

Gaseous NO_2 maintains equilibrium with its dimer N_2O_4 giving rise to various different adsorption mechanisms on graphene — similar to the case of graphite [145, 146]. For both, we obtained possible adsorption geometries as depicted in Fig. 5.7 right. The corresponding adsorption energies in GGA are 85 meV (a), 67 meV (b), 67 meV (c), 50 meV (d) and 44 meV (e) per molecule with sheet-adsorbate distances of 3.4 – 3.5Å for the monomer and 3.8 – 3.9Å for the dimer. As usual, LDA yields higher adsorption energies, approximately 169 – 181 meV for the monomer and 112 – 280 meV for the dimer, and favors the adsorbates by 0.5 – 1Å nearer to the sheet.

The spin-polarized DOS of the supercells containing NO_2, shown in Fig. 5.7 a) and b), reveals a strong acceptor level at 0.4 eV below the Dirac point in both adsorption geometries. The molecular orbitals of NO_2 correspond to flat bands and manifest themselves as peaks in the DOS. The energies of these peaks are virtually independent of the adsorbate orientation. Most important for doping effects is the partially occupied molecular orbital (POMO) of NO_2, which is split by a Hund like exchange interaction: The spin-up component of this orbital is approximately 1.5 eV below the Dirac point and fully occupied, as it is also for the case of free NO_2 molecule. The spin down component of the NO_2 POMO is *unoccupied* for free NO_2, but 0.4 eV below the Dirac point in the adsorbed configuration[2] — it gets populated by electrons from graphene.

By means of band structure calculations we investigated the band width and

[2]The energies of the POMO spin up and down orbitals relative to the Dirac points predicted by LDA are −0.5 eV and −1.4 eV, respectively, i.e. in almost quantitative agreement with the GGA results.

hybridization of the NO_2 acceptor bands with the graphene bands. It turns out that in a small region, less than 1% of the Brillouin zone, where the graphene and the NO_2 POMO bands come as close as 40 meV, these bands start mixing significantly. In the entire rest of the Brillouin zone, the acceptor band is localized almost entirely at the adsorbate. The band structure calculations yield $V_k/D < 0.1$ for V_k as entering Eq. (5.19). The acceptor level is weakly hybridized with the graphene bands and localized at the NO_2 adsorbate.

In contrast to the paramagnetic monomer, the dimer, N_2O_4, has no unpaired electrons and is diamagnetic: on formation from two monomers the two POMOs hybridize with the resulting bonding orbital being the highest occupied molecular orbital (HOMO). The possibility of doping effects due to adsorbed dimers has been investigated using the DOS depicted in Fig. 5.7 c) - e). Again, the molecular orbitals of the adsorbates are recognizable as sharp peaks in the supercell DOS. Similar to NO_2, band structure calculations reveal weak hybridization of the adsorbate and the graphene bands. The N_2O_4 HOMO is in all cases more than 3 eV below the Fermi level and therefore does not give rise to any doping. However, the lowest unoccupied molecular orbital (LUMO) is always quite near to the Dirac point, i.e. between 1 meV and 66 meV above it. Those initially empty N_2O_4 LUMOs can be populated by the graphene electrons due to thermal excitations and act consequently as acceptor levels.

So, density functional theory predicts the following experimentally checkable features: First, there will be two types of dopants, when graphene is exposed to NO_2: the monomer and the dimer giving rise to acceptor levels far below and rather close to the Dirac point, respectively. Furthermore, we find both acceptor states almost entirely localized at the adsorbate molecules and similarly weakly hybridized with the graphene p_z bands. Therefore electrons in both acceptor states should exhibit a similar electron mobility, which should be much less than the mobility of the electrons in the graphene bands.

These predictions have been examined experimentally by K. Novoselov and A. Geim at the University of Manchester by combining electric field effect and Hall measurements at different adsorbate concentrations. The results will be presented in the following part of this section. As described in [7, 147] Hall bar devices with Ti/Au (5nm/40nm) contacts were prepared from monolayer graphene flakes on heavily-doped oxidized (300nm SiO_2) silicon substrates. As prepared, the samples were unintentionally p-doped. This unintentional doping has been removed by annealing in vacuum for 2 hours at 410K [7].

Then the samples were exposed to NO_2 strongly diluted in nitrogen (100 ppm of NO_2) for 60 seconds at room temperature. After the exposure the chamber was evacuated and the samples were annealed in a number of annealing cycles while constantly kept under vacuum. During each annealing cycle the devices were heated up to 410K, kept at that temperature for some time, allowing for desorption of some NO_2 / N_2O_4 (such reducing the doping level slightly) and then cooled down to room temperature at which longitudinal R_{xx} and Hall R_{xy} resistances were measured at $B = 1$ T as a function of the gate voltage V_G.

This procedure allowed us to vary the level of doping gradually in the range

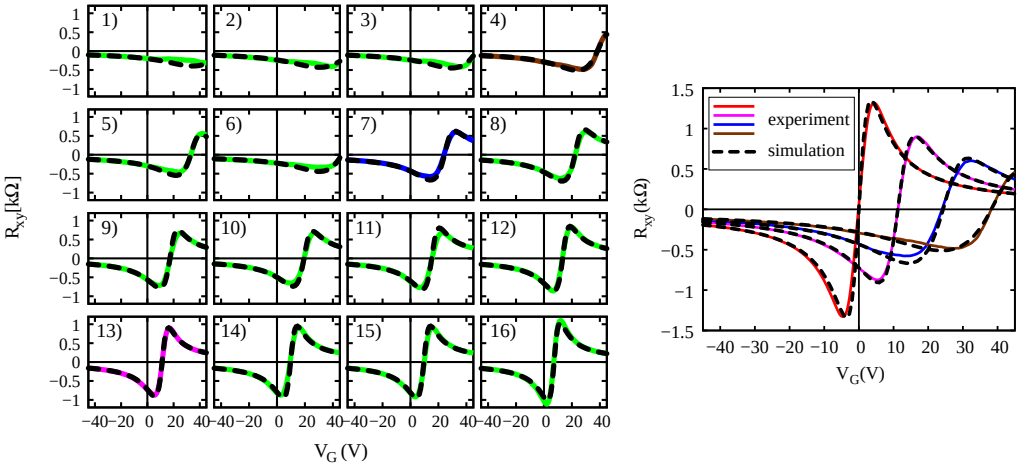

Figure 5.8: The Hall resistances, R_{xy}, as a function of the gate voltage, V_G, for a graphene sample with different levels of NO_2/N_2O_4 doping. The solid lines are the experimental results and the dashed lines are the simulations. They are fitted to the experimental curves by adjusting the dopant concentrations c_1 and c_2 for each curve. R_{xy} vs. V_G is shown for 16 different adsorbate concentrations in the left panel. The green curves are not shown in the right panel, the other correspond to the equally colored curves in the right panel. The simulation close to the red curve corresponds to undoped graphene, $c_1 = c_2 = 0$.

from $3{\cdot}10^{12}$ cm^{-2} down to practically pristine state with doping as low as 10^{11} cm^{-2} by controlling the time spent at 410K (varied from 2 minutes for the very first cycle and up to 16 hours for the last cycle, when the undoped state was reached). In total, 16 cycles and one measurement with the pristine sample have been made. (See Fig. 5.8.)

These R_{xy} vs. V_G measurements exhibit two characteristic features. Firstly, the curves move towards higher positive gate voltages with increasing NO_2/N_2O_4 doping. Secondly, the transition region, where R_{xy} depends linearly on the gate voltage (corresponding to the presence of both types of carriers), becomes wider, and simultaneously, the maximum R_{xy} achieved becomes lower for a higher amount of NO_2/N_2O_4 on the graphene sample. This is a clear evidence of the two distinct acceptor levels, as will be explained in the following.

Consider $1/R_{xy}$ as shown in Fig. 5.9. The deep acceptor level causes a solid shift at all V_G, while the acceptor level close to the Dirac point gives rise to an additional shift of the electron branch (straight line at negative $1/R_{xy}$). The curve for doped graphene (blue curve) exhibits these two shifts with respect to the red curve, which corresponds to undoped graphene. The NO_2-acceptor level shifts the entire doped curve to the right, whereas the additional shift of the electron branch reflects the presence of the N_2O_4 impurity level near the Dirac point. The latter additional shift in $1/R_{xy}$ displays as broadening of the transition region near the charge neutrality point in the R_{xy} curves, discussed above.

To make this analysis quantitative we give a simple model, which is based on the presence of four types of carriers: electrons and holes in graphene as well as electrons in the NO_2 and N_2O_4 acceptor states. Electrons and holes in graphene

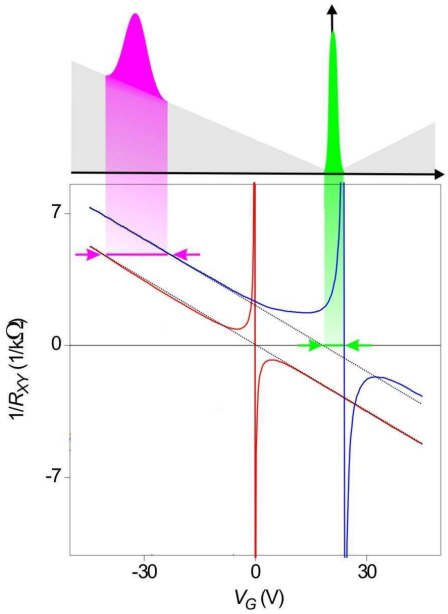

Figure 5.9: $1/R_{xy}$ for pristine (red curve) and doped (blue curve) graphene samples. Upper panel: schematic DOS of doped graphene (corresponds to the blue curve) with grey depicting DOS for pure graphene, the magenta peak representing the DOS for NO_2 and the green peak for N_2O_4. Shifting of the blue curve with respect to the undoped one (red) suggests the presence of the low-laying NO_2 peak, and the fact that the electron branch for blue curve is shifted with respect to the hole branch indicates the presence of the N_2O_4 peak.

have approximately the same, rather high mobility of about 5000 cm^2/Vs [7]. Our DFT calculations predict the acceptor bands to be both flat with a similar bandwidth and a similar, weak hybridization with the graphene bands is found. Thus, we expect the mobility μ of electrons in the impurity states to be much smaller than the mobility of the electrons in the graphene bands. Expressing the impurity state electron mobility μ in units of the graphene electron mobility, the Hall resistance is given by [148] $R_{xy} = \frac{B(\mu^2 c+n-p)}{e(\mu c+n+p)^2}$, where n (p) is the density of electrons (holes) in graphene and c is the density of electrons in the impurity states. As the gate voltage $V_G = \alpha\sigma$ is directly related to the total charge density of the sample $\sigma = e(c + n - p)$, where the prefactor α is determined by substrate properties as described in [7], we can simulate the Hall resistance as a function of V_G.

To this end, we adjust the global fit parameter α to the slope of the $|1/R_{xy}|$ curves. Once, the impurity state electron mobility μ and the impurity DOS N_{imp} are specified, R_{xy} and V_G are functions of the chemical potential, since n, p and c are determined by the graphene DOS and N_{imp}, respectively, via the Fermi distribution function. It turns out, that for reasonable agreement of *all* 17 experimental curves with the simulations $\mu \approx 0.1$ is required and $N_{imp}(E)$ has to be peaked around *two* distinct energies, $E_1 \leq -300\,\text{meV}$ and $E_2 \approx -40\,\text{meV}$. Taking in particular $N_{imp}(E) = c_1\delta(E - E_1) + c_2\delta(E - E_2)$, we simulate the R_{xy} vs. V_G mea-

surements with three global fit parameters α, μ and E_2 and two curve specific fit parameters, c_1 and c_2. $E_1 \leq -300\,\text{meV}$ corresponds to our DFT estimation of $E_1 \approx -400\,\text{meV}$.

The good agreement of simulations and experiment (see Fig. 5.8) confirms the presence of two distinct impurity levels due to the NO_2 and N_2O_4 as predicted by DFT. The coefficients c_1 and c_2 are measures of the density of electronic states due to the NO_2 and N_2O_4 adsorbates, respectively. From the fitting of the simulations to the experimental curves we obtain $c_1 = 1.7,\ 1.1,\ 0.6 \cdot 10^{12}\,\text{cm}^{-2}$ and $c_2 = 1.3,\ 0.9,\ 0.3 \cdot 10^{12}\,\text{cm}^{-2}$ for the brown, blue and magenta curve in Fig. 5.8, respectively, corresponding to 3000-10000 molecules on a device of $0.75\,\mu\text{m} \times 0.75\,\mu\text{m}$ in size.

The deep acceptor level at $E_1 \leq -300\,\text{meV}$ due to NO_2 is always fully occupied under our experimental conditions. In the limit of exposure to NO_2 strongly diluted in an inert gas atomsphere, the characteristic jumps in the Hall resistivity of graphene devices detected by Schedin et al. [15] correspond to single electrons being removed or introduced to the sample. The combined DFT and experimental results presented here suggest that these jumps correspond to the detection of single NO_2 molecules and lead to the picture that one electron is transferred from graphene to NO_2 per adsorbate molecule. NO_2 molecules cause doping but do not create any chiral midgap state in graphene. So, they are one example of the class of charged, weakly hybridized impurities, as discussed in Section 5.1.3.

5.2.2 Inert impurities

Experiments like those by Schedin et al. [15] show that graphene is sensitive to closed-shell molecules like H_2O, NH_3 and CO, as these adsorbates cause doping of graphene. The microscopic mechanism of this doping, however, has remained unclear and will be addressed in this section. Density functional theory calculations on single water molecule adsorbates on perfect free standing graphene [149] were in line with previous studies on carbon nanotubes (CNT) [150] and found H_2O physisorption but no H_2O induced impurity states close to the Fermi level. Therefore, the doping effects found experimentally [7, 15] are very likely due to more complicated mechanisms than interactions of graphene with single water molecules: Firstly, the experiments dealing with the effect of water on graphene were carried out using graphene on top of SiO_2 substrates. In addition, for finite concentrations of H_2O on graphene H_2O clusters might form.

In this section we study the substrate and cluster formation effects in the water-graphene-system by means of density functional theory (DFT). We show that both, highly oriented water clusters as well as water adsorbates in combination with a defective SiO_2 substrate can lead to doping of graphene. To this end, we consider model systems (see Fig. 5.10) for water and ice in different concentrations of free standing graphene as well as for water interacting with defective SiO_2 substrates. By analyzing the involved dipole moments and comparison to electrostatic force microscopy [151], we show that the SiO_2 substrate is crucial for obtaining doping by H_2O adsorbates on graphene.

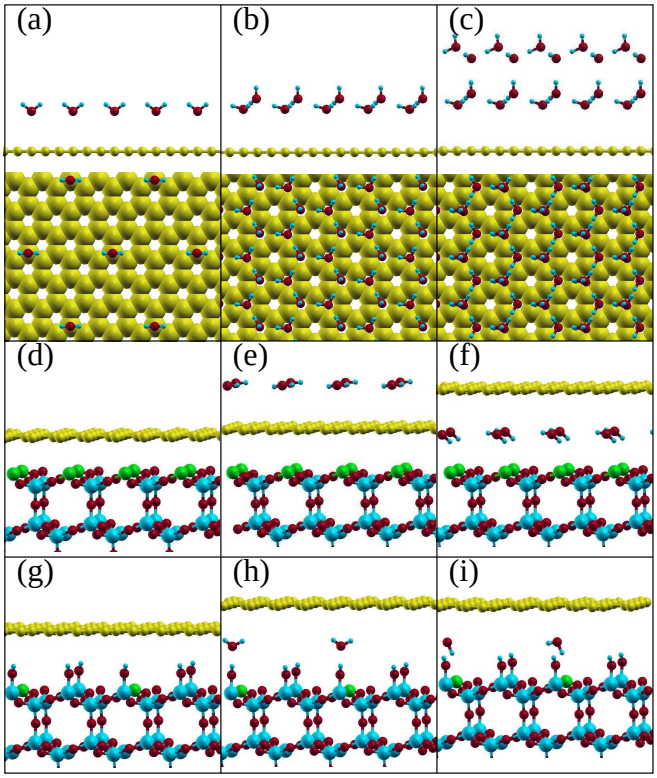

Figure 5.10: Model systems for water interacting with graphene. a-c: Free standing graphene with single water adsorbates (a), a bilayer (b) and a tetralayer (c) of ice Ih. Carbon atoms yellow, oxygen red and hydrogen small blue balls. d-i: graphene on top of SiO_2 with every second (d-f) or eighth (g-i) surface Si atom forming a Q_3^0 defect. Water adsorbates are considered on top of graphene (e), and between graphene and the substrate (f), (h), and (i). Fully coordinated Si atoms are depicted as big blue balls, Si atoms at Q_3^0 defects in green.

As in the previous DFT calculations presented in this thesis, the electronic and structural properties of the graphene-substrate-adsorbate systems are obtained using generalized gradient approximation (GGA)[42, 43] to the exchange correlation potential. For solving the resulting Kohn-Sham equation we used VASP [48] with the PAW [52, 53] basis sets and 875 eV as plane wave cut-off. The graphene-substrate-adsorbate systems are modeled using supercells containing up to 83 substrate atoms (Si, O and H), 12 adsorbate atoms, and 32 C atoms. In the total energy calculations and during the structural relaxations the k-meshes for sampling of the supercell Brillouin zone were chosen be as dense as a 24×24 and 12×12 k-mesh, respectively, when folded up to the simple graphene unit cell.

First, water adsorption on free standing graphene with different water concentrations is considered. To model a single H_2O molecule on graphene, 3×3 graphene supercells were used. Full relaxation of H_2O with oxygen or hydrogen nearest to the graphene yielded adsorbed configurations with binding energies of 40 meV and 36 meV and molecule sheet distances of 3.50 Å and 3.25 Å, respectively. These values are in the same order as those obtained by Leenaerts et. al.

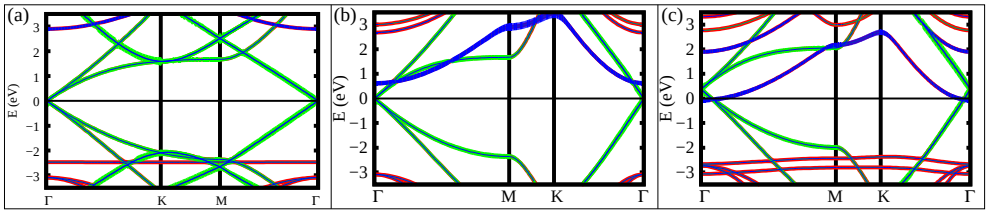

Figure 5.11: Bandstructures of supercells with fully relaxed single molecules (a), a bi-layer (b) and a tetralayer (c) of water on graphene, corresponding to Fig. 5.10 a-c), respectively, are shown. The graphene π bands are marked in green, the nearly free electron bands in blue. Due to the H_2O dipole moments, graphene's nearly free electron band is shifted with respect to its π bands.

[149] indicating physisorption of single water molecules on graphene. Analyzing the density of states/band structures for these two adsorption geometries we find qualitative agreement with Ref. [149]: None of these configurations exhibits energy levels due to the adsorbate near the Dirac point, as shown in Fig. 5.11 a) for the configuration with oxygen closest to graphene. The HOMO of H_2O is more than 2.4 eV below the Fermi energy and its LUMO more than 3 eV above it. The absence of any additional impurity level close to the Dirac point shows that single water molecules on perfect free standing graphene sheets do not cause any doping.

The supercell applied here, corresponds to an adsorbate concentration of $n = 2\,\mathrm{nm}^{-2}$, which is well inside the range of concentrations (1-10 nm^{-2}) found experimentally in Ref. [151]. The lateral dimension $a = 4.5\,\text{Å}$ of the hexagonal ice Ih (0001)-surface unit cell corresponds to a concentration of 5.7 $H_2O\,\mathrm{nm}^{-2}$ per layer. Thus, increasing the H_2O concentration significantly above the $n = 2\,\mathrm{nm}^{-2}$ from above leads to water clusters or ice like structures, rather than isolated molecules.

To gain insight into doping of graphene by water clusters and ice overlayers we studied fully relaxed bi-layers and four layers of ice Ih adsorbed on graphene. These overlayer structures have been proposed as basis of ice growth on various hexagonal metal surfaces [152, 153] and can be modeled as $(\sqrt{3}\times\sqrt{3})\,\mathrm{R30}^\circ$ overlayer on the simple graphene unit cell. The lattice mismatch in this configuration is 0.23 Å — on the same order as found for water overlayers on Ni(111) [152] — and therefore a reasonable starting point for studying ice on graphene.

The supercell bandstructures (Fig. 5.11 b) and c)) show that the electric field by proton-ordered ice on top of graphene changes the energy of graphene's nearly free electron bands. In contrast to pristine graphene, where these bands start at 3eV above the Dirac point or in the case of single H_2O adsorbates on graphene (Fig. 5.11 a)), their bottom is at 0.6eV above and 0.1eV below the Dirac point for a bi- and a tetralayer of ice Ih on top of graphene. This shift is due to electrostatic fields induced by the H_2O dipole moments and results in hole doping for the tetralayer of ice on graphene.

The water adlayers cause a change in contact potential $\delta\phi$, which can be esti-

mated using the H_2O dipole moment $p = 6.2\times10^{-30}$ Cm and the relaxed structures to be $\delta\phi = 1.4$V and 5.4V for a water bi- and tetralayer, respectively. While only the latter structure causes doping, the corresponding change in contact potential exceeds the experimental value, $\delta\phi_{\text{exp}} = 1.3\,\text{V}$, from Ref. [151] by more than a factor of 4. However, water strongly diluted in N_2 has been found to cause hole doping in graphene on SiO_2[15]. Given these two experiments, doping due to multiple fully oriented ice overlayers as in Fig. 5.11 is likely not the most important interaction mechanism for water and graphene.

We now turn to studying the effect of the SiO_2 substrate in the water-graphene interplay. The experiments with graphene on top of SiO_2 used substrates, which were created by plasma oxidation of Si. [15, 151] The SiO_2 surface created in this way is amorphous and its electronic, structural and chemical properties are challenging to model from first principles. To obtain, qualitative insight to the most important physical mechanisms it is, however, a reasonable starting point to consider crystalline SiO_2 in the β-cristobalite form as a substrate [154].

The (111) surface of this modification can be used to create the most likely defects on SiO_2 amorphous surfaces: These are so called Q_3^0 and Q_4^1 defects [155] having one under coordinated silicon and oxygen atom, respectively. Furthermore, the unit cell of this surface is nearly commensurate with the graphene lattice: The lattice constant $a_{\text{SiO}_2} = 7.13\,\text{Å}$ [156] results in a surface unit cell $a_{\text{SiO}_2}/\sqrt{2} = 5.04\,\text{Å}$, which is 4% larger than twice the lattice constant $2a_0 = 4.93\,\text{Å}$ of graphene. As the SiO_4 tetrahedra in SiO_2 are known to adjust to external strain easily, we model graphene on SiO_2 by 2×2 or 4×4 graphene supercells with lateral dimension $2a_0$ or $4a_0$. As substrate we put 4% laterally strained and hydrogen passivated β-cristobalite with 6 Si atoms per surface unit cell in vertical direction. We then created the defects by removing H passivation atoms, added the H_2O adsorbates and relaxed until all forces were less than $0.08\,\text{eV}\cdot\text{Å}^{-1}$. In this way, we consider passivated and defective SiO_2 surfaces — the latter containing either undercoordinated silicon or oxygen atoms — as substrate for graphene. The effect of water exposure is simulated by putting water molecules on top of graphene as well as between graphene and the substrate.

Graphene on top of fully passivated SiO_2 means two inert systems in contact with each other. Consequently, there are no bands in addition to graphene's Dirac bands at the Fermi level and no doping occurs. (The band structure is not shown here, for brevity.) This changes strongly for graphene on defective SiO_2. As a model system, we study Q_3^0 defects in β-cristobalite (111)-surfaces. Depending on the supercell size, 2×2 and 4×4, in these periodic structures every second and eighth surface Si atom is under coordinated, respectively, and forms a Q_3^0 defect. (See Fig. 5.10 (d-i).)

These defects lead to additional states in the vicinity (±1eV) around the Fermi level. (See Fig. 5.12 a) and d).) The avoided crossing in Fig. 5.12 a) indicates significant hybridization of the defect and the graphene bands and demonstrate the impurity state's importance for conduction electron scattering in graphene. In the pure SiO_2 graphene model systems (Fig. 5.12 a) and d)), the impurity bands do not cross the Fermi level. This situation can be changed by water adsorbates,

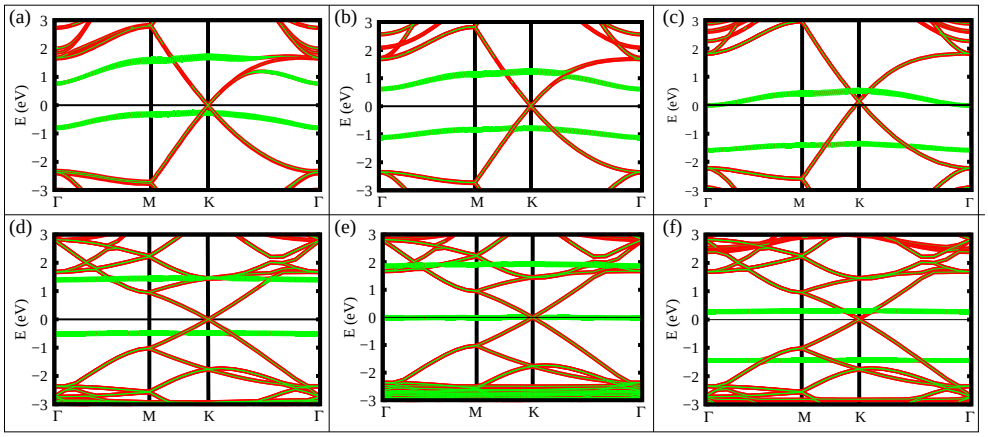

Figure 5.12: Band structures for graphene on defective SiO_2 substrates. (a-c) 2×2 and (d-f) 4×4 graphene supercells with every second, (a-c), or eighth, (d-f) surface Si atom forming a Q_3^0 defect. The corresponding geometries are shown in Fig. 5.10 d-i), respectively. Spin up and down bands are shown at the same time. Contributions at the defect site are marked as green fatbands. a) and d) without water adsorbates. b) with water on top of graphene. c), e), and f) with water between graphene and the substrate. c), f) H_2O dipole moment pointing tilted downwards. e) H_2O dipole moment pointing upwards.

which may sit either in between graphene and the substrate (Fig. 5.12 c), e) and f) or on top of graphene (Fig. 5.12 b)). In all cases, the electrostatic dipole moment of the water adsorbates comes along with strong local electrostatic fields, which allow to shift the impurity bands significantly with respect to the graphene bands. As Fig. 5.12 demonstrates, this shift strongly depends on the place of adsorption and the orientation of the water molecules leading, either to hole doping (Fig. 5.12 c) and f)) or electron doping (Fig. 5.12 e)).

Similar effects of water can be found for graphene on the (0001)-plane of α-quartz or β-cristobalite with Q_4^1 defects. Although the interaction mechanisms of water, SiO_2 and graphene presented here are not exhaustive, the comparison of water adsorption on perfect free standing graphene to water adsorption on graphene lying on a (defective) SiO_2 substrate allows the following conclusions: Perfect free standing graphene may have water adsorbates on top but its electronic transport properties are insensitive against perturbations by the water adsorbates. Single molecules will not create any impurity states close to the Dirac point. For obtaining doping effects, one needs highly ordered H_2O cluster or ice structures.

The substrate changes the situation completely. The dipole moments of H_2O adsorbates cause local electrostatic fields that can shift the substrate's defect states with respect to the graphene electrons and cause doping.

This microscopic view of H_2O pushing electrons to the substrate is well in line with EFM [151]: The graphene contact potential changes by about +1 V upon water adsorption (exposure to moist N_2 with 50% relative humidity), whereas the SiO_2 substrate contact potential stays almost constant during this procedure. This change in contact potential $\Delta\phi$ can be converted into doping of graphene (expressed in terms of a surface charge density σ) knowing the sepa-

ration d of the compensation charges in the substrate from the graphene sheet: $\sigma = \epsilon_0\epsilon_r\Delta\phi/d \approx 2 \times 10^{13}\text{e}\cdot\text{cm}^{-2}$ for $d = 1\,\text{nm}$ and $\epsilon_r = 3.9$, which is the dielectric constant of SiO_2. Typical experimental values $\sigma \sim 10^{12}\text{e}\cdot\text{cm}^{-2}$ suggest $d \sim 20\,\text{nm}$. Thus, the DFT simulations as well as the EFM experiments suggest that H_2O induced doping is mediated by electrostatic dipole fields and that the separation between the compensation charges and the graphene sheet is significantly larger than the typical 2 Å found e.g. for doping by K adatoms, which are discussed in the following section. This difference can be expected to manifest in electron scattering with indirect dopants leading to much weaker scattering than direct dopants.

5.2.3 Midgap states and migration barriers

For judging which impurities might determine electron scattering in graphene and for optimizing chemical functionalization, the mechanisms determining the impurity mobility, i.e. their migration barriers and binding energies, need to be known: Firstly, the migration barriers decide at which temperatures impurities will start moving along the graphene sheet resulting in possible cluster formation. Indeed, it has been shown that clusters of (charged) impurities lead to weaker electron scattering than the same amount of randomly distributed impurities [157]. Moreover, the migration barriers and adsorption energies allow to judge at which temperature impurities can be removed from the graphene sheets, e.g., by annealing. In this section, we first consider monovalent adsorbates and show that these can be divided into two separate groups regarding the bonding mechanism: ionically and covalently bond impurities. To this end, we present ab-initio calculations on H, Li, Na, K, Cs, F, Cl, Br, I, CH_3, and OH adsorbates on graphene. For these systems the electronic structure (section 5.2.3) and migration barriers (section 5.2.3) are analyzed. The covalently bond impurities cause a characteristic midgap state derived from the graphene electrons. This state turns out to be very stable, as graphene's conjugated π bonds enhance the migration barriers of neutral covalently bond impurities. In section 5.2.3, the experimentally important case of oxygen ad-atoms is discussed.

For a first principles description of the graphene adsorbate systems we performed GGA [42, 43] calculations on 4×4 graphene supercells containing one impurity. As in the previous sections, VASP [48] with PAW [52, 53] basis sets has been used. We obtained relaxed structures for the graphene adsorbate systems, total energies, and orbitally resolved LDOS. In the total energy calculations and during the structural relaxations the k-meshes for sampling of the supercell Brillouin zone were chosen be as dense as a 24×24 and 12×12 k-mesh, respectively, when folded up to the simple graphene unit cell.

To find migration barriers for ionically bond impurities it is sufficient to perform structural relaxations with the impurities in three different high symmetry adsorption sites: on top of a C-atom (t-site), in the middle of a hexagon (h-site) and above the middle of a nearest neighbor C-C bond (b-site). The covalent impurities cause strong distortions of the nearby bonds and require the minimum

energy paths to be calculated using the nudged elastic band method [158]. As starting guess a linear interpolation between two adjacent stable configurations with three or more intermediate points has been chosen. To check for convergence of the migration barriers with the supercell size, we performed also calculations with 3×3 as well as 5×5 supercells for H ad-atoms and reproduced the barrier from the 4×4 supercell within an accuracy of 4%. Moreover, the convergence of the local density of states close to the impurity with the supercell size has been assured in this way.

Electronic structure of monovalent impurities on graphene

The local electronic structure of graphene in the vicinity of adsorbates (Fig. 5.13) can be grouped into two classes. The LDOS in the vicinity of adsorbates like Li or Cl exhibits a sharp resonance close to Fermi level which is almost entirely localized at the impurity. Besides this peak, the LDOS at the nearest neighbor and at the next nearest neighbor of the impurity exhibits the pseudogap characteristic for graphene.

This is qualitatively different for the second group of impurities (Fig. 5.13 c) and d)). H and F adatoms cause a midgap state characteristic for Dirac fermions: With the bonding partner of the impurity in sublattice A the impurity state is localized in sublattice B and at the impurity atom.

Every stable atomic configuration under investigation can be strictly grouped either into the class of strongly or weakly hybridized impurities, as can be seen from Fig. 5.13 e)-f): Ionically bond impurities give rise to a sharp acceptor (donor) level below (above) the Dirac point at $E_\mathrm{D} = 0$. The LDOS of covalently bond impurities is much broader and exhibits characteristic resonances far below the Fermi level (between -10 eV and -4 eV) as well as a midgap state at the Fermi level.

As regards electron scattering this midgap state is mainly independent of the particular type of covalent impurity. The supercell band structures for H, CH_3, OH, and F covalently bond to graphene are shown in Fig. 5.14. The band structure of graphene with adsorbed H and CH_3 as well as those for graphene with F and OH adsorbates coincide close to the Fermi level despite the different internal structure of the adsorbates. The coupling of the midgap state and the graphene bands can be quantified in an *effective* impurity model $H = H_\mathrm{D} + H_\mathrm{imp}$, where the unperturbed graphene bands are described by

$$H_D = \sum_k \epsilon(k) d_k^\dagger d_k \tag{5.37}$$

and the perturbation by

$$H_\mathrm{imp} = \epsilon_\mathrm{imp} c^\dagger c + V\left(\sum_k c^\dagger d_k + \mathrm{H.c.}\right). \tag{5.38}$$

Here, the index $k = (\vec{k}, \nu)$ denotes crystal momentum $\vec{k}$ and band number $\nu = \pm$. $\epsilon(k)$ is the unperturbed graphene dispersion. The effective impurity is charac-

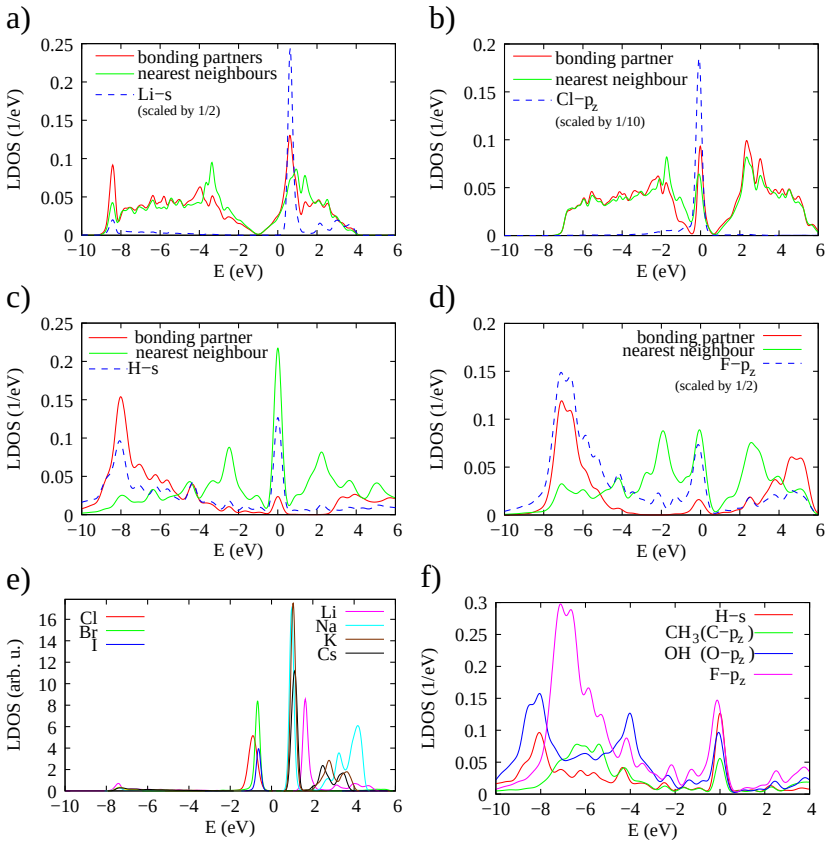

Figure 5.13: LDOS in different graphene adsorbate systems. (a-b) ionically bond impurities, (c-d) covalently bond impurities. a) Graphene + Li, b) Graphene + Cl, c) Graphene + H d) Graphene + F. For the impurity's bonding partner in graphene and its nearest neighbor the p_z projected LDOS is shown. The valence electron LDOS at the impurity site for ionically bond impurities is depicted in (e) and for covalently bond impurities in (f). In (a-d) and (f) the Fermi level is at $E = 0$; in (e) the Dirac point is at $E = 0$.

terized by its energy ϵ_{imp} and its hybridization V with the graphene bands. In a supercell calculation at the backfolded Dirac points $\vec{k} = K^{\pm}$, this model simplifies to

$$H = \begin{pmatrix} \epsilon_{\text{imp}} & A & B \\ A^* & 0 & 0 \\ B^* & 0 & 0 \end{pmatrix}, \tag{5.39}$$

where the zero block stems from the graphene bands at the Dirac point and A (B) are the components of V_k in the two different sublattices A (B). This allows to derive the coupling strengths $|V| = \sqrt{|A|^2 + |B|^2}$ and ϵ_{imp} from the DFT energies of the three bands closest to the Fermi level in the supercell calculation: We identify the energies of these bands at the supercell Brillouin zone K-point, $E_1 \leq E_2 \leq E_3$, with the eigenvalues of H from Eq. (5.39): $\epsilon_0 = 0$, $\epsilon_{\pm} = \epsilon_{\text{imp}}/2 \pm \sqrt{|\epsilon_{\text{imp}}/2|^2 + |V|^2}$. By letting $\epsilon_0 = E_2$ (i.e. choosing the energy offset such that $E_2 = 0$), $\epsilon_- = E_1$ and $\epsilon_+ = E_3$ and solving for ϵ_{imp} and $|V|^2$, we obtain the impurity energies and coupling strengths as shown in table 5.1.

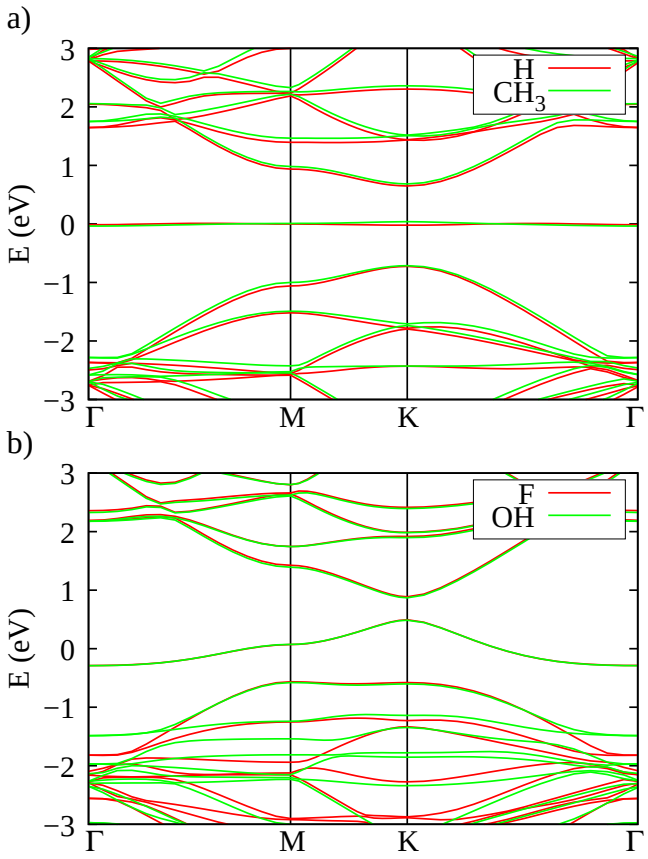

Figure 5.14: Supercell band structure of (a) H and CH_3 on graphene as well as (b) F and OH bond covalently to graphene. Bands coincide close to the Fermi level ($E = 0$) despite the different internal structure of the impurities.

The coupling $|V|$ is mainly independent of the internal structure of the covalently bond impurities. Hence, this midgap state appears as a universal feature of all monovalent impurities which are strongly bond to one of graphene's carbon atoms.

Bonding of H-atoms to graphene and related electron scattering has been analyzed in [159, 160, 161]. For the bonding partner of H, the π bond to its nearest carbon neighbors is broken and a σ bond with the H ad-atom is formed. The carbon bonding partner of H atoms has been found to be decoupled from the graphene π-electron system and the resulting local imbalance between the number of atoms belonging to each of the two sublattices causes a midgap state. The band structures from Fig. 5.14 and the coupling constants from Table 5.1 show that same mechanism is effective for all monovalent covalently bond impurities on graphene.

It might appear surprising that F forms a covalent bond with graphene, while Cl becomes charged and bonds ionically. This is caused by the inertness of graphene's sp^2 network, which has to be broken upon formation of a covalent bond. For Cl having one completely filled inner electronic shell the typical covalent radius is 1.02Å (see Ref. [162]), which is almost twice more than for F. Thus,

Table 5.1: Impurity energy and hybridization for the effective impurity model of the midgap state for different impurities. All impurities are placed on top of a C atom, which is at the total energy minimum for the covalently bond impurities and the anions Cl / Br but not for the cations Li and Na.

	ϵ_{imp} (eV)	$\|V\|$ (eV)		ϵ_{imp} (eV)	$\|V\|$ (eV)
H	-0.03	0.69	Li	1.17	0.11
CH_3	-0.11	0.70	Na	0.93	0.07
OH	-0.70	0.65	Cl	-0.79	0.21
F	-0.67	0.65	Br	-0.73	0.09

Table 5.2: Minimum energy sites, bonding energies E_b, and migration barriers ΔE for ionically and covalently bond impurities.

	site	E_b (eV)	ΔE (eV)		site	E_b (eV)	ΔE (eV)
H	t	0.80	1.01	Li	h	1.08	0.31
CH_3	t	0.27	0.63	Na	h	0.48	0.09
OH	t	0.91	0.53	K	h	0.81	0.06
F	t	1.99	0.29	Cs	h	0.96	0.04
O	b	2.43	0.74	Cl	t,b	0.80	< 0.005
				Br	t,b	0.54	< 0.005
				I	t,b	0.31	< 0.005

a significantly lower covalent binding energy can be expected for Cl than for F, which — as our calculations show — unables Cl to break graphene's sp^2 network. For the same reason, NO_2 does not bind covalently to graphene.

Migration barriers and chemical bonding

In the following we show, that the creation of the midgap state by a neutral impurity covalently bond to one carbon atom and high migration barriers are closely related. A comparison to ionically bond impurities is given.

In agreement with [163], we find the energy minimum for the alkali cations at the h-sites and barriers as shown in table 5.2. The barriers decrease with cation size and are all (except for the special case of Li) below 0.1 eV.

The potential energy landscape for the cations consists of dips in the center of the hexagons bordered by a hexagonal net of banks. Within this net spanned by the nearest neighbor carbon bonds, the variation of potential energy is by a factor of more than 5 smaller than between the h-site and the t/b-sites.

This landscape is reversed for the anions: Having their energy minima on the net and maxima in the center of the hexagons, the anions can freely move on the graphene sheets. The fact that the height of the impurity above the sheet is always minimized in center of the hexagon, would result in the energy minimum being in the center of the hexagon for all ionically bond impurities if atomic scale inhomogeneities in the screening charge of the impurities were negligible. The anions preferring the t- and b-sites over the h-sites shows that inhomogeneities in

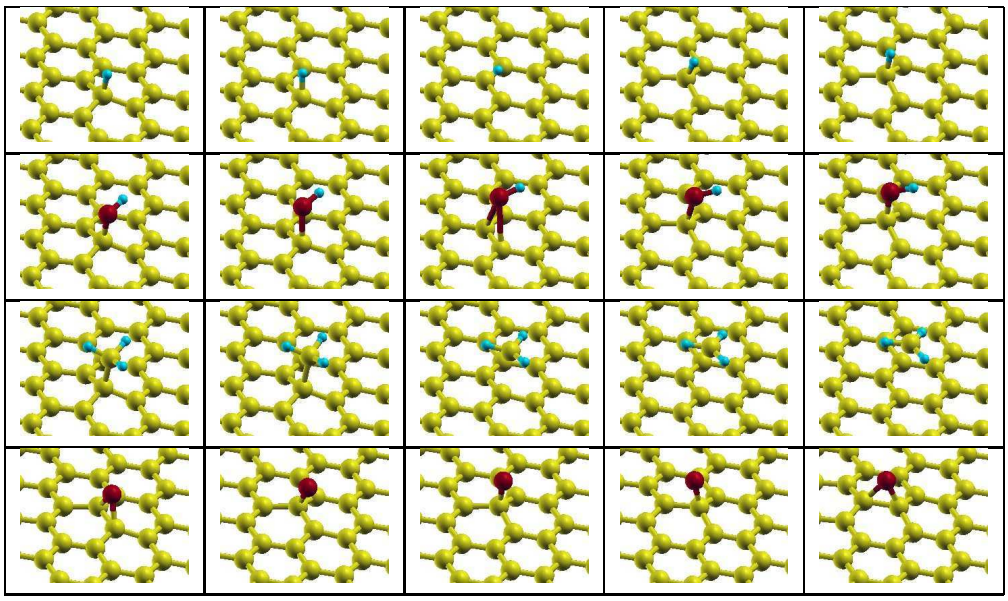

Figure 5.15: Stable and transition state geometries for H, OH, CH_3 and O (from top to bottom) on graphene. For H, OH and O, two neighboring stable adsorption geometries are in the very right and left and the saddle point transition state in the middle. Transition of CH_3 from one stable adsorbed geometry to a neighboring requires desorption. For CH_3, desorption with the saddle point configuration being in the middle is shown. In the minimum energy adsorbed configuration of CH_3 the H-C-H bond angles are 109.2°, suggesting sp^3 hybridization of C in the CH_3 group, whereas the desorbed CH_3 is flat corresponding to sp^2 hybridization.

the screening charge corrugate the potential energy landscape of the ions on the order of some 10 meV.

The total bonding energy, E_b (see table 5.2), is for each the cationic species about 3 times to an order of magnitude bigger than its migration barrier, ΔE. For the anions the ratio $E_b/\Delta E \sim 10^2$ is even larger. While the typical ionic bonding energies on the order of a few 100 meV to 1 eV prevent desorption a room temperature, the migration barriers are significantly smaller, make most ions mobile on graphene and let cluster formation appear possible at room temperature.

This in strong contrast to covalently bond impurities: our calculations show that the potential energy landscape for these impurities is by an order of magnitude more corrugated. We find migration barriers between 0.29 eV for F and 1.01 eV for H. Notably, F has highest absolute binding energy ($E_b = 1.99$ eV) of all monovalent impurities considered, here, but it has the smallest migration barrier within the group of covalent impurities. For F and OH we find the saddle point energy of the transition path significantly below the desorption energy, which is $E_b = 0.91$ eV for OH. This is in strong contrast to H and CH_3: For H the energy of the saddle point state is only 4 meV below the desorption barrier and moving a CH_3-group from one carbon atom to its nearest neighbor requires even overcoming the desorption barrier of 0.63 eV. No saddle point configuration with the CH_3-group in the middle of two neighboring C-atoms except for the CH_3

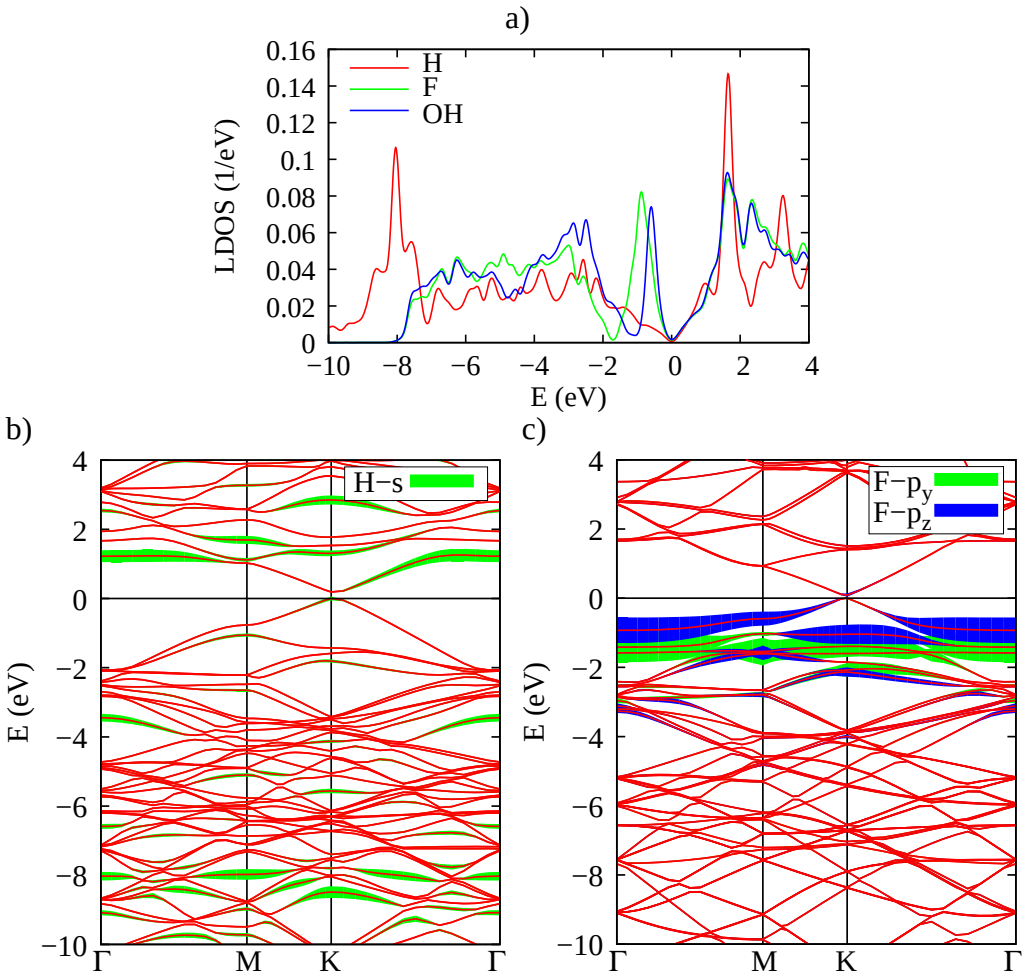

Figure 5.16: Electronic structure in the transition state. a) p_z-LDOS at a carbon atom next to the impurity. Lower part: Band structures of graphene supercells with b) H and c) F impurities in transition state configuration. Contributions from the impurity atoms are marked as fatbands. In all panels, the Dirac point is defined to be at $E = 0$.

being fully desorbed from the graphene sheet could be found.

The transition paths between adjacent stable adsorption sites of H, OH, and CH_3 are depicted in Fig. 5.15. In agreement with previous studies [159], we find significant out-of-plane lifting (0.4 – 0.5 Å) of the impurity's bonding partner in the minimum energy configurations.

H, F, and OH are above a bridge site in saddle point of the transition path. In this configuration, the OH group is oriented perpendicular to the C-C bond of the two neighboring carbon atoms. For F, OH, and H the nature of chemical binding in the saddle point configuration can be understood from the supercell electronic properties shown in Fig. 5.16. The LDOS at the carbon atoms next to the F and OH impurities is very similar to the LDOS in the vicinity of *ionically* bond impurities like Cl or Br (see Fig. 5.13b). This is in contrast to the case of H, where in addition to a resonance at 2 eV, the LDOS at the carbon neighbor of the impurity is broadened and exhibits a peak at −8 eV — similar to all covalently

bond impurities in their minimum energy configuration. The H-impurity causes a donor level and is at the same time covalently bond, as the supercell band structure with contributions from the H impurity marked as fat bands further illustrates. There are contributions from the H *s*-orbital over the energy range from −10 eV up to +3 eV, indicating strong hybridization of the impurity orbital with the graphene bands. This is very different from F in the saddle point configuration with its valence orbitals contributing significantly within an energy interval which is an order of magnitude smaller. In the transition state F and OH are ionically bond to graphene.

The high barrier for H suggests that the formation of a strong covalent bond in the transition state is highly unfavorable. The origin of this effect can be understood from the model Hamiltonian, Eq. (5.39): With the impurity on top of the bridge site, sublattice symmetry is preserved: $A = B$ in Eq. (5.39). The symmetric combination of the two C-p_z orbitals adjacent to the impurity $\phi_+ = \frac{1}{\sqrt{2}}(0, 1, 1)$ will couple to the impurity $\phi_{\text{imp}} = (1, 0, 0)$. The antisymmetric combination $\phi_- = \frac{1}{\sqrt{2}}(0, 1, -1)$ is decoupled and forms the analog of the midgap state occurring for the impurity on top of a carbon atom: In the latter case, with the impurity's bonding partner in sublattice A, one obtains $B = 0$ and finite A in Eq. (5.39). Thus, $\phi_0 = (0, 0, 1)$ is decoupled from the impurity in the stable configuration. ϕ_0 is non-bonding and is therefore at the energy of the Dirac point. $\phi_- = \frac{1}{\sqrt{2}}(0, 1, -1)$, however, is an antibonding combination of neighboring C-p_z orbitals. The ab-initio calculations show that the resonances derived from this state are more than 1 eV above the Dirac point, unoccupied and not available for screening the additional positive charge brought by the H-impurity. Thus, the creation of a local charge is enforced by graphene's electronic structure for the impurity in a b-site saddle point configuration. As a consequence, a strong tendency to ionic bonding with graphene *decreases* migration barriers, while migration preferably neutral covalently bond impurities is suppressed.

Oxygen impurities on graphene

In the previous sections, we showed with the model system of monovalent impurities that covalently bond impurities exhibit higher migration barriers than ionically bond impurities. With increasing number of chemically active orbitals, as, e.g., for transition metal adsorbates with partially filled 3d shells, the situation can become arbitrarily complicated (see section 6.5). We now show, however, that the experimentally and technically important case of oxygen ad-atoms is well in line with the results on monovalent impurities.

Oxygen being divalent, adsorbs to bridge sites on graphene with migration from one stable configuration to the next involving the path depicted in Fig. 5.16. In the stable adsorbed configuration, it binds covalently to graphene with decoupling its two carbon bonding partners from the graphene π electronic system (see Fig. 5.17). The LDOS at these carbon atoms is strongly depleted in the vicinity of the Fermi level and exhibits the typical shape of sp^3 bonded carbon — very similar to the situation for monovalent covalently bond impurities on graphene discussed

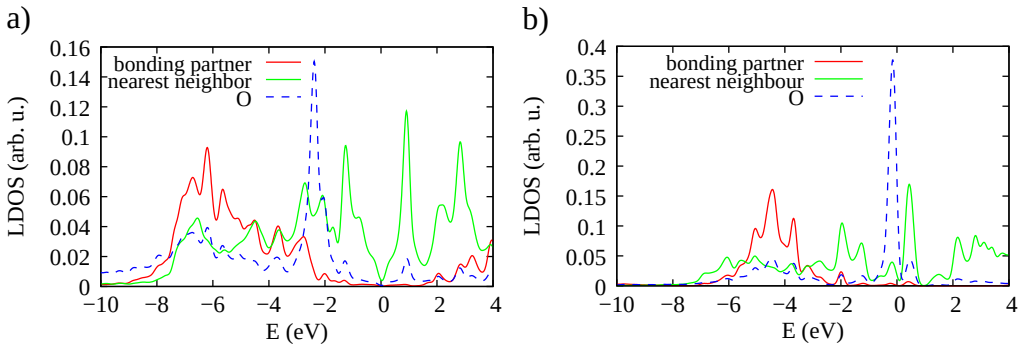

Figure 5.17: Electronic structure of graphene with adsorbed oxygen in the minimum energy configuration (a) and in the transition state configuration (b). The p_z projected LDOS at a carbon bonding partner of oxygen, one of its nearest neighbors, and the LDOS at the oxygen ad-atom are shown.

before.

However, no midgap state is created by oxygen ad-atoms in their minimum energy configuration as both graphene sublattices are affected equally by the oxygen ad-atoms. There are resonances in the LDOS of nearest neighbors at $E = -1.2\,\text{eV}$ and $E = 0.9\,\text{eV}$, but the LDOS vanishes linearly at the Fermi level $E_\text{F} = 0$. This is because O represents a ”double impurity” in terms of a tight-binding model (see section 5.1.2) and strong double impurities do not universally create midgap states.

For migration of oxygen from one stable configuration to a neighboring, one of its two bonds to graphene has to be broken. In the saddle point state, oxygen is forming a single covalent bond to one carbon atom. This results in a midgap state of the same nature as in the case of covalently bonding monovalent impurities in their stable configuration. The midgap state is slightly above the Fermi level, as the non-bonding orbital of oxygen (sharp peak below $E_\text{F} = 0$ in Fig. 5.17 b) is fully below E_F and accepts one electron from the midgap state. So, O binds partially covalent and partially ionically to graphene in the saddle point configuration.

As in the case of monovalent impurities, the requirement of breaking one covalent bond results in the rather high migration barrier of 0.74 eV for oxygen on graphene, which is however smaller than the adsorption energy of 2.43 eV. In this sense O is similar to OH or F on graphene, which are all able to form a (partially) ionic bond in the saddle point configuration.

The investigation various examples of monovalent impurities on graphene in this subsection allowed us to establish a relation between their type of chemical bonding, the occurrence of chiral midgap states and their migration barriers. We showed that migration barriers of ionically bond impurities are significantly lower than than their binding energies, $\Delta E \ll E_b$, which is in contrast to covalently bond impurities having typical migration barriers on the order of some 100 meV to 1 eV and $\Delta E \sim E_b$.

This tendency explains experimental findings of charged impurities moving

almost freely on graphene [15, 164] and experiments suggesting considerable migration barriers for H adsorbates [110, 87]. The fact that clusterization of impurities on graphene strongly suppresses their contribution to the resistivity [157] makes covalently bond impurities one natural candidate to the main source of scattering limiting the electron mobility in graphene. It is essential that, as demonstrated here, these impurities frequently have quasilocal peaks nearby the neutrality point — not accidentally but enforced by symmetry.

Chapter 6

Correlated magnetic nanosystems

In the preceding chapters we studied the influence of inhomogeneities on the electronic properties on graphene. These systems appeared to be well described within the picture of non-interacting quasiparticles obtained from LDA/GGA. Here, we aim at an understanding of how the atomic composition determines the electronic and magnetic properties of nanosystems where the independent particle picture breaks down. We focus on magnetic ad-atoms and nanostructures on metal surfaces as well as on graphene and perform semianalytic and LDA++ based studies. In all examples discussed, here, Kondo physics will play an important role. The Kondo effect will be introduced together with the Anderson impurity model in section 6.1. Afterwards, Ce atoms on different metal hosts are investigated in a joint theoretical and experimental study (section 6.2). An ab-initio based theory for resonant valence photoemission spectra is given and a substrate dependent transition of the Ce f-electron character from localized to delocalized is explained. Co ad-atoms in Cu hosts have been subject of numerous STM experiments and present a model system for investigating the Kondo effect. In particular, the influence of local coordination on the Kondo effect has been studied experimentally in this system, whereas a full theoretical ab-initio based understanding is still unavailable. This motivates the first-principles studies of Co in different Cu environments (section 6.4). First, single Co atoms in bulk Cu are compared to Co inside a Cu (111) surface and adsorbed on Cu (111). Afterwards, coordination effects in magnetic $CoCu_n$ nanostructures are investigated by combining STM and first-principles theory. The last part of this chapter (Sec. 6.5) is devoted to the study of Co ad-atoms on graphene. In graphene, *all* quasiparticles at the Fermi level belong to a non-trivial representation of the crystal point symmetry group. This makes graphene very different from usual metal surfaces and we will work out the consequences for STM experiments: It will be shown that the coupling of the impurity to graphene depends unusually strong on the symmetry of the active impurity orbitals. This strongly affects q-factors seen in STM as well as Kondo temperatures.

6.1 The Anderson Impurity Model and the Kondo effect

Historically, the motivation for the Anderson Impurity model (AIM) goes back to the 1930s, when a resistance minimum has been observed in some metals like Au [165]. This minimum was in opposition to the usually monotonically decreasing resistance, when the temperature is lowered and its origin was totally obscure at that time [27]. In the 1960s a correlation between the resistance minimum and the existence of localized magnetic moments has been found [166], which finally motivated Kondo's study of magnetic impurities in non-magnetic metallic hosts: Using a perturbative approach Kondo explained the minimum in the resistance due to contributions from magnetic impurities [167].

During that time Anderson addressed the question of how localized magnetic moments can be formed in metallic hosts [168]. The insight, that a spin-down electron hopping onto a spin-up impurity will experience not only the exchange repulsion but also the Hartree repulsion of the spin-up electron already residing there, while the spin-up electron does not see this repulsion, lead to the formulation of AIM Hamiltonian[1]:

$$\hat{H}_{\mathrm{AIM}} = \sum_{k,\sigma} \epsilon_k c^\dagger_{k,\sigma} c_{k,\sigma} + \sum_{k,m,\sigma} \left(V_{km} c^\dagger_{k,\sigma} d_{m,\sigma} + \mathrm{H.c.} \right) + \hat{H}_{\mathrm{at}} \tag{6.1}$$

with

$$\hat{H}_{\mathrm{at}} = \sum_{\sigma} \epsilon_{d,m} d^\dagger_{m,\sigma} d_{m,\sigma} + \frac{1}{2} \sum_{\substack{m,m,'m'',m''' \\ \sigma,\sigma'}} U_{mm'm''m'''} d^\dagger_{m,\sigma} d^\dagger_{m',\sigma'} d_{m'',\sigma'} d_{m''',\sigma}. \tag{6.2}$$

It describes an impurity characterized by quantum numbers, (m, σ) (orbital and spin), with corresponding Fermi operators, $d_{m,\sigma}$, on-site energies $\epsilon_{d,m}$ and local Coulomb interaction $U_{mm'm''m'''}$. This impurity is embedded in a sea of conduction electrons described by Fermi operators, $c_{k,\sigma}$, and energies, ϵ_k, where k includes crystal momentum and band index. The coupling of the impurity and the conduction electrons is provided by the hopping V_{km}.

This model explains how local moments are formed and how they are eventually screened at low temperatures. Its physics can be approached from the non-interacting limit, $U_{mm'm''m'''} \to 0$, and from the atomic limit, $V_{km} \to 0$. In section 5.1.3, the non-interacting limit has been studied with the main result being the occurrence of virtual bound states: Defining the hybridization function (cf. Eq. (5.18)),

$$\Delta_{mm'}(\omega) = \sum_k \frac{V^*_{km} V_{km'}}{\omega + i\delta - \epsilon_k}, \tag{6.3}$$

it can be shown that the LDOS at the impurity site consists of a resonance at $\epsilon_{\mathrm{imp}} = \epsilon_m + \mathrm{Re}\,\Delta_{mm}(\epsilon_{\mathrm{imp}})$ of width[2] $\Gamma = -\mathrm{Im}\,\Delta_{mm}(\omega)$. The impurity does not have

[1] Here, the mulitorbital AIM is given. The original AlM included one impurity orbital.

[2] This statement holds if $\Delta_{mm'}$ is diagonal and if Γ is small as compared to the distance of ϵ_{imp} to the closest Van Hove singularity in the bare conduction electron DOS.

a magnetic moment in this case, i.e. it does not contribute a Curie-Weiss term to the magnetic susceptibility.

We now turn to the atomic limit, consider an impurity with one orbital and skip orbital quantum numbers in the following. The impurity Hamiltonian simplifies to $\hat{H}_{\text{at}} = \sum_\sigma \epsilon_d n_{d,\sigma} + U n_{d,\uparrow} n_{d,\downarrow}$, which has four eigenstates $|0\rangle, |\uparrow\rangle = d_\uparrow^\dagger|0\rangle, |\downarrow\rangle = d_\downarrow^\dagger|0\rangle$, and $|\uparrow\downarrow\rangle = d_\uparrow^\dagger d_\downarrow^\dagger|0\rangle$. The empty impurity, $|0\rangle$, and the double occupied impurity are non-magnetic with energies $E_0 = 0$ and $E_2 = 2\epsilon_d + U$, respectively. In the case of single occupation, $|\uparrow\rangle$ or $|\downarrow\rangle$, the energy is $E_1 = \epsilon_d$ and the impurity possesses a magnetic moment corresponding to a spin $\frac{1}{2}$. For given chemical potential, μ, the impurity is hence magnetic if $E_1 - E_0 < \mu$ and $E_2 - E_1 > \mu$, i.e.

$$\epsilon_d < \mu < \epsilon_d + U. \tag{6.4}$$

The spectral function, $N(\omega)$, of such a magnetic impurity consists two δ-peaks at ϵ_d and $\epsilon_d + U$,

$$N(\omega) = \frac{1}{2}\delta(\epsilon_d - \omega) + \frac{1}{2}\delta(\epsilon_d + U - \omega), \tag{6.5}$$

corresponding to the removal and the addition of an electron, respectively.

The behavior of the impurity in between these two limiting cases can be grouped in different parameter regimes: The first qualitative insight from Anderson's original work [168] using a static mean field theory is that a finite magnetic moment at the impurity site forms if $-\pi \operatorname{Im}\Delta(\mu) < U$ and Eq. (6.4) are fulfilled. If, in particular, $\epsilon_d + U - \mu \gg |\operatorname{Im}\Delta(\mu)|$ and $\mu - \epsilon_d \gg |\operatorname{Im}\Delta(\mu)|$, the Anderson model can be mapped to the s-d model [27], $\hat{H} = \hat{H}_0 + \hat{H}_{\text{sd}}$ with $H_0 = \sum_{k,\sigma} \epsilon_k c_{k,\sigma}^\dagger c_{k,\sigma}$ and

$$\hat{H}_{\text{sd}} = \sum_{k,k'} J_{k,k'} \left(S^+ c_{k,\downarrow}^\dagger c_{k',\uparrow} + S^- c_{k,\uparrow}^\dagger c_{k',\downarrow} + S_z (c_{k,\uparrow}^\dagger c_{k',\uparrow} - c_{k,\downarrow}^\dagger c_{k',\downarrow}) \right), \tag{6.6}$$

where S_z and $S^\pm = S_x \pm i S_y$ are spin operators of a spin S localized at the impurity site. For a single orbital impurity, the exchange coupling is given by

$$J_{k,k'} = V_k^* V_{k'} \left(\frac{1}{U + \epsilon_d - \epsilon_k'} + \frac{1}{\epsilon_k - \epsilon_d} \right). \tag{6.7}$$

For electrons at the Fermi level, this coupling is antiferromagnetic due to Eq. (6.4). Upon reducing the AIM to the s-d model an additional potential scattering term, $\hat{V}_{\text{pot}}$ occurs. This term can be accounted for by including it into $\hat{H}_0 \to \hat{H}_0 + \hat{V}_{\text{pot}}$ and considering $c_{k,\sigma}$ as Fermi operators of the exact eigenstates of $\hat{H}_0 + \hat{V}_{\text{pot}}$. This entire transformation from the AIM to the s-d model is called Schrieffer-Wolff transformation. The so-called local moment regime is defined as the regime in which a Schrieffer-Wolff transformation is possible and the s-d model is adequate to describe the low energy physics of the system.

Starting from the local moment regime and increasing either Δ or letting ϵ_d or $\epsilon_d + U$ approach the Fermi level, such that $\mu - \epsilon_d \sim |\operatorname{Im}\Delta|$ or $\epsilon_d + U - \mu \sim |\operatorname{Im}\Delta|$ valance fluctuations can no longer be considered as virtual processes and eliminated by the Schrieffer-Wolff transformation. This regime is called intermediate

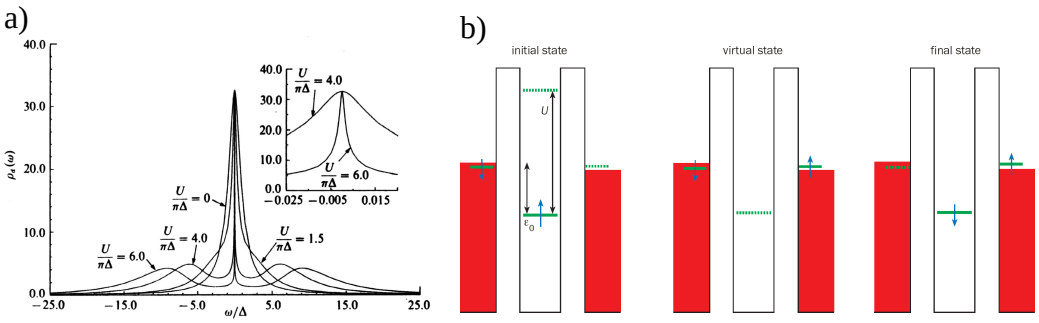

Figure 6.1: (a) Schematic illustration of the evolution of the impurity spectral function $\rho_d(\omega) \equiv N(\omega)$ as interaction strength U is turned on continuously, maintaining a constant impurity occupancy. The noninteracting resonance at $U = 0$ splits into an upper and lower atomic peak at $\epsilon_d + U$ and ϵ_d, respectively. From [27]. (b) Illustration of the one orbital AIM. The magnetic impurity is assumed to have one electron level with energy $\epsilon_0 = \epsilon_d$ below the Fermi energy $\mu = 0$ of the metal (red). This level is assumed to be occupied by one spin-up electron (blue). Adding another electron is requires bring up the Coulomb energy, U, while it would cost at least $|\epsilon_0|$ to remove the electron. However, the system can tunnel between this and the *energetically degenerate* configuration with flipped spin: The spin-up electron can hop off the impurity site to briefly occupy a classically forbidden virtual state outside the impurity, and then be replaced by a spin-down electron from the metal. From [169]

valence or mixed valence regime. Finally, there are two non-magnetic regimes, the empty orbital- and the double occupancy regime, in the cases of $\epsilon_d - \mu \gg |\mathrm{Im}\,\Delta|$ and $\mu - \epsilon_d - U \gg |\mathrm{Im}\,\Delta|$, respectively. In the following sections we will study systems covering the local moment and the intermediate valence regimes and address their spectral properties.

A mean-field treatment does not resolve the question of how the spectral and thermodynamic properties translate from the atomic to the strongly hybridized limit and how the atomic "ionisation" peaks in the spectrum — called Hubbard bands — evolve into a single resonance: upon turning on the hybridization of the impurity to the conduction electrons a many-body resonance, the so-called Abrikosov-Suhl-Kondo resonance, develops at the Fermi level. Conversely, upon turning on the interaction the two Hubbard bands are split off the virtual bound state peak, which narrows and evolves into the Abrikosov-Suhl-Kondo resonance if the local moment regime is entered. (See Fig. 6.1 (a).) This resonance originates from the impurity spin being screened by conduction electron spins and the corresponding coherent tunneling of the impurity spin between spin-up and spin-down configurations as illustrated in Fig. 6.1 (b).

The width of the resonance is defined as Kondo temperature $k_\mathrm{B}T_\mathrm{K}$. Calculating T_K for a *realistic* system is a formidable problem and will be faced in the following sections. It is worth noting that even the question of which type of Kondo model is appropriate to describe a given realistic impurity can be extremely difficult, in general. For the classical example of Fe impurities in bulk Au, this question has only been answered very recently [170]. There are, however, well-defined model

systems, where the dependence of T_K on the model parameters is known. For an s-d model with constant bare DOS of the host, ρ_0, conduction electron bandwidth D and k-independent exchange coupling $J = J_{k,k'}$ one obtains [27]

$$k_B T_K \sim D|2J\rho_0|^{1/2} e^{-1/2J\rho_0}. \tag{6.8}$$

The single orbital Anderson model in the local moment regime with constant hybridization Δ, chemical potential $\mu = 0$ and bandwidth D such that $|\epsilon_d|, |\epsilon_d + U| \gg D$, can be reduced to above the s-d model. Applying the Schrieffer-Wolff transformation, Eq. (6.7), and substituting into Eq. (6.8) yields

$$k_B T_K \sim D\left(\frac{\Delta U}{|\epsilon_d||\epsilon_d + U|}\right)^{1/2} e^{-\pi|\epsilon_d||\epsilon_d+U|/2\Delta U}. \tag{6.9}$$

The screening of the impurity spin by the conduction electron spins leading to the formation of the Abrikosov-Suhl-Kondo resonance is called Kondo effect. The energy gain upon screening and formation of the resulting many body ground state is on the order of T_K. Hence, the Kondo effect disappears at high temperatures $T \gg T_K$, where the impurity spin and the conduction electrons lose their correlations.

In the AIM only the impurity site is subject to a quartic interaction term, whereas the bath of conduction electrons assumed to be non-interacting. Using the action formalism introducted in section 2.5 (see [55] or [171] for a detailled derivation), the non-interacting (Gaussian) bath degrees of freedom can be integrated out and local electronic properties of the impurity can be described by the effective action

$$S_{\text{eff}} = -\sum_{\alpha,\beta} \int_0^\beta \mathrm{d}\tau \int_0^\beta \mathrm{d}\tau' d^*_\alpha(\tau) \mathcal{G}^{-1}_{0,\alpha\beta}(\tau,\tau') d^*_\beta(\tau') + \int_0^\beta H_{\text{at}}(d^*_\alpha(\tau), d_\beta(\tau)) \tag{6.10}$$

with

$$\mathcal{G}^{-1}_{0,\alpha\beta}(i\omega_n) = (i\omega + \mu) - \Delta_{\alpha\beta}(i\omega_n). \tag{6.11}$$

The hybridization function, defined in Eq. (6.3), mimics the effect of the conduction electron bath on impurity degrees of freedom as a frequency dependent complex valued potential. It will be therefore a central quantity in the discussion of realistic impurity effects in the following sections.

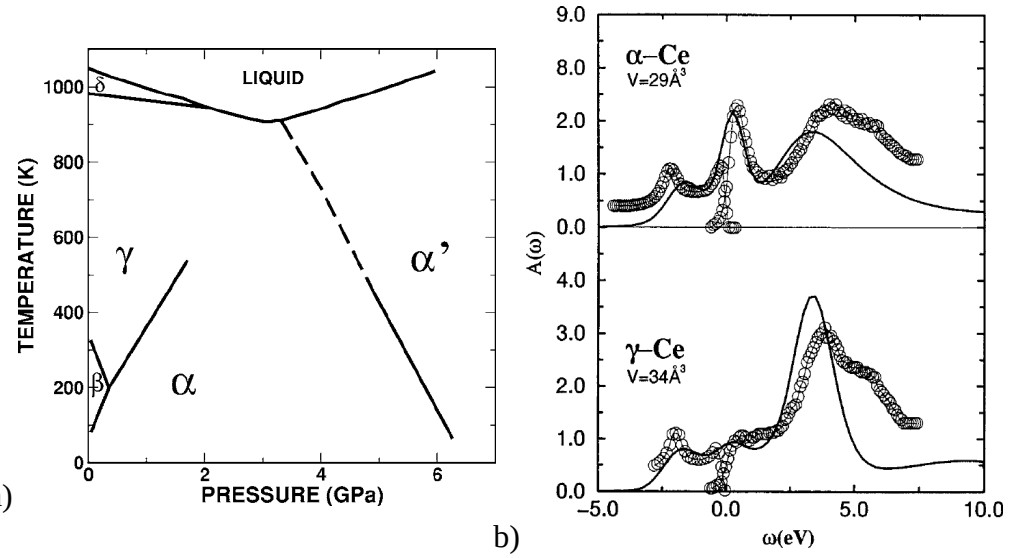

Figure 6.2: (a) The phase diagram of bulk cerium. From [173, 31]. (b) $spdf$-density of states of α and γ as obtained from experiments (circles) and LDA+DMFT (solid lines). Upon volume collapse, spectral weight is transferred to the Abrikosov-Suhl resonance at the Fermi level. From [175].

6.2 Ce ad-atoms on metal surfaces

Isolated Ce atoms coupled to a metallic host are an emblematic case for the physics quantum impurity problems introduced in the last section. The valence electrons of rare earth elements exhibit a very distinct character: the $4f$-derived states are localized, experience strong electron-electron interaction and usually possess a magnetic moment, while $5d6s$-states are extended and participate in the chemical bonding. Ce is a particular interesting case, since its $4f$ shell is at the borderline between localization and itinerancy: bulk Ce undergoes a pressure induced isostructural first-order volume collapse transition, the Ce $\alpha \rightarrow \gamma$ transition, with the change in volume being on the order of 15%. (See Fig. 6.2, Refs. [172, 173, 174, 175], and references therein.) In the large volume γ-phase, the $4f$ spectrum is split into Hubbard bands and a local $4f$ magnetic moment is present. When reducing the volume on entering the α-phase, an Abrikosov-Suhl resonance develops at the Fermi level and the local moment disappears [31]. The Ce $\alpha \rightarrow \gamma$ transition is, therefore, intimately connected with transition of the 4f electrons from delocalized to localized.

Similarly, isolated Ce atoms coupled to metallic hosts display very different behavior depending on their atomic environments: Ce atoms diluted in bulk metals have been found to cover the hole range, from magnetic Ce with atomic-like electronic Ce^{3+} configuration in hosts like Ag to non-magnetic in, e.g. Rh or W, as well as intermediate cases in between [176]. The mechanisms behind this behavior have been revealed by extensive photoemission studies of Ce impurities in bulk metals as well as Ce intermetallic compounds and a theory developed by Gunnarsson and Schönhammer [64]. Depending on the hybridization of the Ce

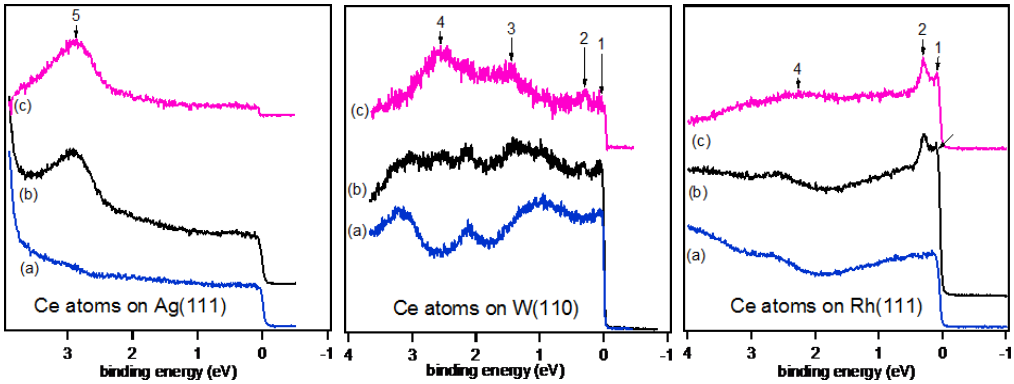

Figure 6.3: Valence photoelectron energy distribution curves for the clean Ag(111), W(110), and Rh(111) surfaces ((a)) and in presence the of Ce ad-atoms (0.001 ML coverage) ((b)). The curves labelled by (c) are the differences between the corresponding spectra (b) and (a).

atoms with their environment and the bare Ce 4f energy w.r.t. the Fermi level of the host, Ce appears to be either in the local moment or in the mixed valence regime.

It is now investigated how the effect of reduced coordination affects the spectral properties of isolated Ce atoms on metal surfaces. Firstly, photoemission experiments on Ce ad-atoms on Ag(111), W(110), and Rh(111) surfaces performed by Gardonio and Carbone (ELETTRA, Trieste) are described. In bulk, these materials are known to span all the range from weak hybridization (Ag), with via the intermediate case (W), to strong hybridization (Rh). Afterwards, a theoretical investigation of Ce on these surfaces is given.

6.2.1 Photoemission spectroscopy of Ce

The photoemission experiments were performed at SuperESCA beamline at the ELETTRA Synchrotron Radiation facility in Trieste. Ag(111), W(110) and Rh(111) substrates were prepared by a standard procedure and monitored by LEED. Isolated Ce ad-atoms were obtained by depositing Ce at a substrate temperature of 20K in a coverage regime ranging from one thousandth to few tenth of a monolayer (statistical growth regime). The major difficulty of photoemission experiments on such systems is that spectroscopic signature of magnetic impurities in the 0.01-0.001 ML coverage range can be obtained only for those combination of impurity/substrates for which the signal of the impurity is comparable to the host. I.e. there needs to be a photon energy such that the correlated impurity orbital cross section is much larger than the cross sections for the other channels. Resonant photoemission across the $4d \rightarrow 4f$ threshold of Ce is one of the few cases where this requirement is fulfilled.

Fig. 6.3 shows the resonant photoelectron spectra measured at the Ce $4d \rightarrow 4f$ absorption threshold for Ce isolated atoms on Ag(111), W(110) and Rh(111) surfaces. In order to better distinguish between the photoemission signal derived

from the Ce ad-atoms and the substrate contribution, the photoemission spectra before (curves (a)) and after (curves (b)) deposition of the Ce atoms are compared and the difference spectra (curves (c)) are taken for each host. The spectra of isolated Ce atoms are found to be clearly different on the three substrates and a clear trend when going from Ag to Rh is visible: On Ag(111) only a peak around 2.9 eV is present, while on W(110) peaks at binding energies of 1.5 and 2.3 eV as well as two smaller peaks close to the Fermi level, at 0.0 and 0.25 eV, contribute spectral weight. On Rh(111) the major contribution is derived from structures close to the Fermi level, the peaks labelled 1 and 2, a small and broad peak around 2.3 eV is still present. I.e. the $4f$ electrons of Ce seem to undergo a transition from localized to delocalized when going from Ce on Ag (111) to Ce on Rh (111) via the intermediate case of Ce on W (110). In the intermediate case, the deep ionization peak appears to be split up into two peaks.

To understand the origin of these entirely different distributions of Ce $4f$ spectral weight and to explain why the ionization peak is split up on W (110), we present first-principles calculations in the following subsection.

6.2.2 Simulation of Ce ad-atom photoemission spectra

To investigate the electronic properties of Ce on the three substrates theoretically with the detailled atomistic environment of Ce being taken into account, we proceed in two steps: First, DFT calculations are carried out to obtain relaxed geometries and the hybridization functions for single Ce-atoms on Ag(111), W(110), and Rh(111). These hybridization functions are afterwards used to calculate the valence electron photoemission spectra following Gunnarsson and Schönhammer, Ref. [64].

The DFT calculations have been carried out using VASP and PAW implemented in there. (See sections 2.3.3 and 2.4.) In these calculations, single Ce atoms on Ag(111), W(110) and Rh(111) have been modeled using 2×2 surface supercells with slab thicknesses of 7 layers and all crystal structures have been relaxed until the forces acting on each atom were less than 0.02eV/Å. The relaxed structures are depicted in Fig 6.4. In all cases Ce adsorbs to high symmetry positions, which are close to the continued bulk lattice on Ag(111) and W(110). On the Rh (111) surface, Ce adsorption to an hcp site is by ~ 250 meV more favorable than the fcc site.

The corresponding LDOS (see 6.4), projected on the Ce *s*-, *p*-, and *d*-orbitals, shows that the *s*- and *p*-states of Ce appear to be similarly broad and delocalized on all substrates and their LDOS extends over $\gtrsim 10$ eV in energy. This indicates strong metallic bonding Ce to the substrate. The Ce 5*d* states slightly broaden when going from Ce on Ag (111) to Ce on Rh (111) but the characteristic width of the LDOS in the 5d states is in all cases on the order of some eV. Hence, the picture of Ce having delocalized outer s-, p-, and d-electrons developed for Ce in bulk metals can be well transferred to isolated Ce atoms on Ag (111), W(110) and Rh (111).

The Ce 4f electrons can be expected to be subject of strong correlations which

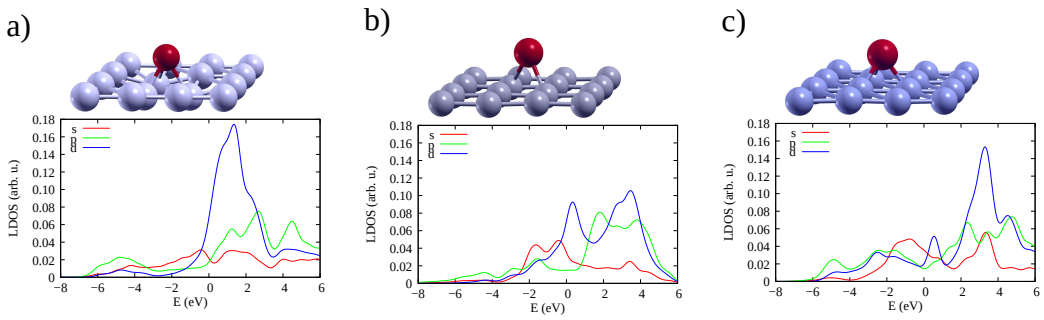

Figure 6.4: Upper panel: Fully relaxed adsorption geometries of (a) Ce on Ag (111), (b) W(110) and (c) Rh (111). On Ag(111) and W(110), Ce occupies positions close to the continued bulk lattice. On the (111) surface of fcc Rh, Ce stacks close to an hcp site. Lower panel: LDOS of the Ce *s*-, *p*-, and *d*-orbitals on Ag (111), W(110) and Rh (111). The Ce 6*s*-, 6*p*-, and 5*d*-electrons are strongly hybridized with the substrate conduction bands and contribute to the LDOS over an energy range on the order of some eV.

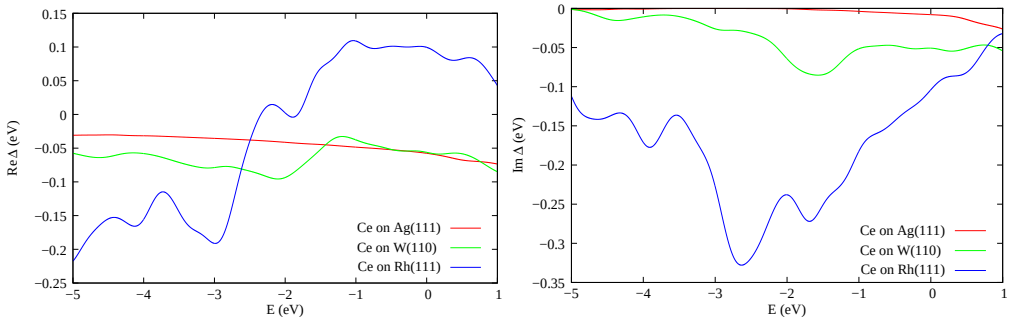

Figure 6.5: Calculated Ce 4 f-electron hybridization functions for isolated adatoms on Ag(111), W(110), and Rh(111). The real parts are shown in in the left and the imaginary parts in the right panel.

require a description in terms of an LDA++ based approach (see section 2.5.3). For the description of the isolated Ce ad-atoms we choose "first-principles Anderson models" with the hybridization functions, $\Delta_{mm'}(\omega)$, Eq. (6.3), being obtained from DFT. The PAW basis sets provide intrinsically projections onto localized atomic orbitals, which we use to extract the hybridization functions. The procedure to obtain hybridization functions or Green functions from projector quantities calculated in VASP has been implemented during this thesis and is explained in appendix A.

Following Gunnarsson and Schönhammer, [64], we assume $\Delta_{mm'}(\omega) = \Delta(\omega)\delta_{mm'}$, i.e. diagonal and orbitally independent hybridization, which we obtain from the full LDA hybridization, $\Delta^{\mathrm{LDA}}_{mm'}(\omega)$ by averaging over all Ce f-orbitals, $\Delta(\omega) = \frac{1}{7}\sum_m \Delta^{\mathrm{LDA}}_{mm}(\omega)$. The resulting $\Delta(\omega)$ for Ce on the three different substrates are shown in Fig. 6.5.

The imaginary part of the Ce 4f-hybridization, $\mathrm{Im}\,\Delta(\omega)$, on the Ag (111) is at all energies below the Fermi level more than an order of magnitude smaller than the corresponding 4f-hybridizations of Ce on W(110) or Rh (111). Obviously, Ce

on Rh (111) exhibits by far the strongest hybridization, which gives the first hint, why the ionization peak of Ce on Rh (111) is most strongly smeared out and why the quasi-particle peak at the Fermi level might be strongest for Ce on Rh (111). In the intermediate case of Ce on W(110), there is a peak in $\mathrm{Im}\,\Delta(\omega)$ extending from $\omega = -1$ eV to -2 eV. This resonance is caused by bonding to t_{2g} d-orbitals of neighboring W-atoms.

The real parts of the Ce $4f$-hybridization functions are shown in Fig. 6.5. They are related to $\mathrm{Im}\,\Delta(\omega)$ by the Hilbert transform

$$\mathrm{Re}\,\Delta(\omega) = -\frac{1}{\pi}\mathcal{P}\int \mathrm{d}\omega' \frac{\mathrm{Im}\,\Delta(\omega')}{\omega - \omega'}.$$

Hence, peaks in the imaginary part cause steps in the real part. The step in $\mathrm{Re}\,\Delta(\omega)$ in the energy range of -2.1 until -1.3 eV for Ce on W(110), will be proven responsible for the peak splitting observed in photoemission (see Fig. 6.3).

In the sudden approximation, the photoemission intensity, $\rho(\epsilon)$ we aim to calculate is given by expectation values of the resolvent operator of the many body Hamiltonian:

$$\rho(\epsilon) \sim \frac{1}{\pi}\sum_{\nu} \mathrm{Im}\langle\phi_0|\psi_\nu^\dagger \frac{1}{\epsilon - i0^+ - E_0 + \hat{H}}\psi_\nu|\phi_0\rangle. \tag{6.12}$$

Here, $|\phi_0\rangle$ is the many body ground state of $\hat{H}$ and E_0 the corresponding ground state energy. ψ_ν is defined to be the Fermi operator removing one electron from a Ce $4f$ state labelled by the quantum number ν, i.e. $\psi_\nu = d_{m,\sigma}$ with $\nu = (m, \sigma)$ in terms of Eq. (6.1). The idea of the approach from Ref. [64] is to calculate the ground variationally and introduce a many body basis set $\{|i\rangle\}$, which is approximately complete in the subspace describing the photoemission experiment, $1 \approx \sum |i\rangle\langle i|$, so that it can be used to evaluate the resolvent operator from Eq. (6.12):

$$\rho(\epsilon) \sim \frac{1}{\pi}\sum_{\nu,i,j} \mathrm{Im}\langle\phi_0|\psi_\nu^\dagger|i\rangle\langle i| \frac{1}{\epsilon - i0^+ - E_0 + \hat{H}}|j\rangle\langle j|\psi_\nu|\phi_0\rangle. \tag{6.13}$$

To proceed, we note that in valence electron photoemission of Ce mainly processes involving $f^1 \to f^0$ or $f^1 \to f^1$ transitions can be expected to contribute [64]. Therefore, we consider the limit $U \to \infty$ and restrict the Ce 4f occupancy to 0 and 1. To construct $|\phi_0\rangle$ and the basis set $\{|i\rangle\}$, we rewrite the AIM in the form

$$H = \sum_{\nu=1}^{N_f} \epsilon_f n_\nu + \int \epsilon \psi_{\epsilon\nu}^\dagger \psi_{\epsilon\nu}\mathrm{d}\epsilon + \int [V(\epsilon)\psi_\nu^\dagger \psi_{\epsilon\nu} + \mathrm{H.c.}]\mathrm{d}\epsilon + U\sum_{\nu<\mu} n_\nu n_\mu, \tag{6.14}$$

where $U \to \infty$ is implied, $n_\nu = \psi_\nu^\dagger\psi_\nu$, ϵ_f is the bare on-site Ce $4f$ energy[3], and the conduction electron states with corresponding Fermi operators $\psi_{\epsilon\nu}$ are relabelled according to their bare energy ϵ and the f-orbital ν they couple to. The conduction electrons not coupling to the Ce 4f orbitals can be omitted.

[3] In our LDA++ approach, ϵ_f is used to absorb the double counting terms and left as fitting parameter.

We introduce a "Fermi-vacuum" state

$$|0\rangle = \left(\prod_{\nu, \epsilon < \epsilon_F} \psi^\dagger_{\epsilon\nu} \right) |\text{vacuum}\rangle, \tag{6.15}$$

with all conduction electron state below the Fermi level filled and all Ce 4f states empty. In lowest order, $\hat{H}$ couples this state to states of the form

$$|\epsilon\rangle = \frac{1}{\sqrt{N_f}} \sum_\nu \psi^\dagger_\nu \psi_{\epsilon\nu} |0\rangle. \tag{6.16}$$

For $U \to \infty$ and

$$N_f \to \infty \text{ with } N_f V(\epsilon) = \text{const.} \tag{6.17}$$

it can be shown that the *exact* many body ground state takes the form

$$|\phi_0\rangle = A \left[|0\rangle + \int_{-\infty}^0 a(\epsilon) |\epsilon\rangle \mathrm{d}\epsilon \right], \tag{6.18}$$

where the Fermi level is $\epsilon_F = 0$ and the constant $A = \left(1 + \int_{-\infty}^0 |a(\epsilon)|^2 \mathrm{d}\epsilon\right)^{-1/2}$ ensures normalization. Defining

$$\Delta E = \langle \phi_0 | H | \phi_0 \rangle - \langle 0 | H | 0 \rangle, \tag{6.19}$$

the coefficients $a(\epsilon)$ are obtained from minimization of ΔE, which implies the secular equations

$$\Delta E = \sqrt{N_f} \int V^*(\epsilon) a(\epsilon) \mathrm{d}\epsilon \tag{6.20}$$

$$(\Delta E - \epsilon_f + \epsilon) a(\epsilon) = \sqrt{N_f} V(\epsilon). \tag{6.21}$$

The solution to these equations yields

$$\Delta E = N_f \int_{-\infty}^0 \frac{|V(\epsilon)|^2}{\Delta E - \epsilon_f + \epsilon} \mathrm{d}\epsilon \tag{6.22}$$

and the occupancy of the Ce f-shell,

$$n_f = A^2 \int_{-\infty}^0 |a(\epsilon)|^2 \mathrm{d}\epsilon = \frac{C}{C+1}, \tag{6.23}$$

with

$$C = N_f \int_{-\infty}^0 \frac{|V(\epsilon)|^2}{(\Delta E - \epsilon_f + \epsilon)^2} \mathrm{d}\epsilon. \tag{6.24}$$

This specifies all ground state properties up to correction on the order of $1/N_f$. We now construct the basis $\{|i\rangle\}$ for the photoexcited state. Ce $4f$ photoemission creates states of the form $\psi_\nu |\phi_0\rangle$ (c.f. Eq. (6.13)), which can be represented as

$$\psi_\nu |\phi_0\rangle = \frac{A}{\sqrt{N_f}} \int_{-\infty}^0 \mathrm{d}\epsilon a(\epsilon) |\epsilon, \nu\rangle, \tag{6.25}$$

where the states, $|\epsilon, \nu\rangle = \psi_{\epsilon,\nu}|0\rangle$, contain one hole in the conduction band. These states couple to states of the form

$$|\epsilon, \epsilon', \nu; 1\rangle = \frac{1}{\sqrt{N_f - 1}} \sum_{\nu \neq \nu'} \psi^\dagger_{\nu'} \psi_{\epsilon',\nu'} \psi_{\epsilon,\nu} |0\rangle \tag{6.26}$$

with matrix elements $\langle \epsilon, \epsilon', \nu; 1|H|\epsilon'', \nu\rangle = \sqrt{N_f - 1} V(\epsilon')\delta(\epsilon - \epsilon'')$, which remain finite in the limit of Eq. (6.17). The states $|\epsilon, \epsilon', \nu; 1\rangle$ have the Ce $4f$ shell singly occupied and two holes in the conduction band. All other states, including, e.g., those with a particle-hole pair in the conduction band, $\psi^\dagger_{E,\nu'} \psi_{\epsilon',\nu'} \psi_{\epsilon,\nu}|0\rangle$, can be shown to couple to states of type $|\epsilon, \nu\rangle$ or $|\epsilon, \epsilon', \nu; 1\rangle$ with a strength $V(\epsilon'')$, which goes to zero in the limit of Eq. (6.17). Therefore, $\{|\epsilon, \nu\rangle, |\epsilon, \epsilon', \nu; 1\rangle\} = \{|i\rangle\}$ yields the desired basis for describing the photoemission experiment up to order $1/N_f$.

Evaluating Eq. (6.13) in this subspace and accounting for the spin-orbit splitting $\Delta\epsilon_f = 0.25\,\mathrm{eV}$ of the Ce $4f$ orbitals[4] yields

$$\rho(\epsilon) \sim A^2 \int_{-\infty}^{0} \mathrm{d}\epsilon' |V(\epsilon')|^2 \left(\frac{N_{f1}}{(\epsilon' - \delta)^2} + \frac{N_{f2}}{(\epsilon' - \delta - \Delta\epsilon_f)^2} \right) \mathrm{Im}\, \tilde{g}(z + \delta - \epsilon'), \tag{6.27}$$

where $z = \epsilon - i0^+$ and $\delta = \epsilon_f - \Delta E$. $N_{f1} = 6$ and $N_{f2} = 8$ are the degeneracies of the Ce 4f spin-orbit multiplets with $j = 5/2$ and $j = 7/2$, respectively, and

$$\tilde{g}(z) = \frac{1}{z - \epsilon_f - N_{f1}\tilde{\Gamma}(z) - N_{f2}\tilde{\Gamma}(z + \Delta\epsilon_f)}. \tag{6.28}$$

The function $\tilde{\Gamma}(z)$ plays the role hybridization function in the truncated Hilbert space

$$\tilde{\Gamma}(z) = \int_{-\infty}^{0} \mathrm{d}\epsilon \frac{|V(E)|^2}{z - \epsilon}. \tag{6.29}$$

By construction, we have $|V(\epsilon)|^2 = -\frac{1}{\pi} \mathrm{Im}\, \Delta(\epsilon)$, which forms the interface of the first-principles hybridization functions $\Delta(\epsilon)$ and the Gunnarsson-Schöhammer treatment of the AIM presented above. With the on-site f-energy being the only fitting parameter and using the established value of 250meV for the spin-orbit splitting between the $f_{5/2}$ and $f_{7/2}$ states, the groundstate and the spectral properties of the Ce adatoms are obtained by firstly solving the generalized form[4] of Eq. (6.22) numerically and then evaluating the integrals in Eqs. (6.27) and (6.29) numerically. This has been implemented in a FORTRAN-program, which carefully treats the nearly singular integrands.

Fig. 6.6 shows the calculated Ce $4f$ spectra for all substrates and different on-site energies ϵ_f. The spectra of Ce on Ag(111) exhibit one sharp peak close to the bare f-electron energy, which corresponds to the ionization process $f^1 \to f^0$. Independent of ϵ_f the spectral weight of this main peak dominates the spectrum and is by orders of magnitude larger than the weight of a possible Kondo peak:

[4] See Ref. [64] for details. ΔE is affected by including spin-orbit coupling. Therefore, we use the generalization of Eq. (6.22) to include spin-orbit coupling, as given explicitly in Eq. (A1) of Ref. [64].

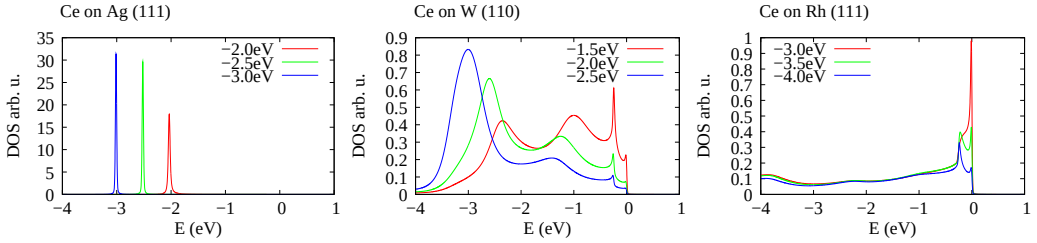

Figure 6.6: Calculated $4f$-spectra for single Ce atoms on Ag(111), W(110) and Rh(111) surfaces. The dependence of the spectra on the on-site energies ϵ_f is illustrated by showing spectra obtained with different ϵ_f. All cureves are labelled by the corresponding ϵ_f.

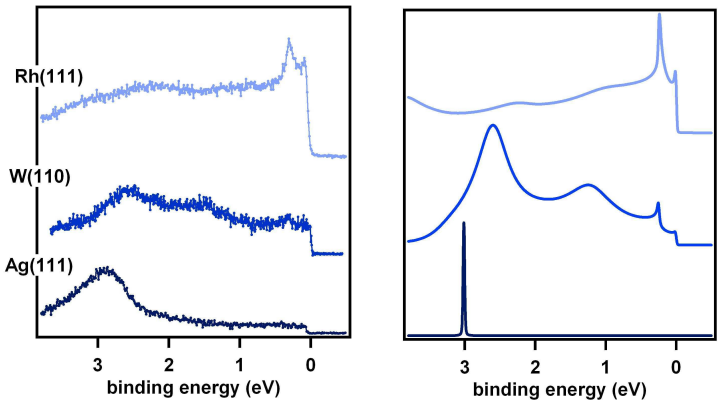

Figure 6.7: Comparison of experimental photoemission spectra (a) in the valence band of Ce ad-atoms on Ag(111), W(110) and Rh(111) surfaces to the theoretical Ce 4f-spectra (b). The theoretical spectra have been obtained with $\epsilon_f = 3.0\,\text{eV}$, $1.7\,\text{eV}$, and $3.7\,\text{eV}$ for Ce on Ag(111), W(110) and Rh(111), respectively.

within the entire range of ϵ_f considered in Fig. 6.6 we find $1 - n_f < 10^{-4}$. This presents a measure for the weight Z of the Kondo peak, as $Z = 1 - n_f$ for vanishing spin-orbit splitting $\Delta\epsilon_f = 0$ [64, 27].

For the case of Ce on Rh(111), the Kondo or the spin-orbit peak ($f_{5/2} \rightarrow f_{7/2}$ around the energy $-\Delta\epsilon_f$) dominate the spectrum for all ϵ_f shown in Fig. 6.6 and the ionization peak is always broadened to a wide continuum. Here, the main effect of changing ϵ_f is changing the relative weight of the spin-orbit peak as compared to the Kondo peak.

The spectra of Ce on W(110) lie in between these two extreme cases with the ionization peak being remarkably split-up into two separate peaks at $E > -1.5\,\text{eV}$ and $E < -2.3\,\text{eV}$ in all cases. In this intermediate regime, the on-site-energy strongly affects the ratio of spectral weight in the ionization peak to the amount of weight in the the Kondo and the spin-orbit peak.

The comparison of theoretical and experimental spectra given in Fig. 6.7 shows that theory and experiment are in very good agreement with each other. This suggests that the physical processes determining the photoemission spectra of isolated Ce ad-atoms on the different surfaces are well described within our

model. All trends including the peak splitting in the case of Ce on W(110) are understandable from the structure of the hybridization functions shown in Fig. 6.5. On the ionization peak, the hybridization acts like a self-energy term on a resonant level (c.f. Eq. (6.28)) with the real part shifting the level and the imaginary part broadening it. The Ag(111) and Rh(111) surfaces are forming the two extreme cases of weak and strong hybridization, respectively, and lead to correspondingly sharp / broadened ionization peaks. The resonance near $\omega = -1.6\,\mathrm{eV}$ in the hybridization of Ce on W(110) splits the ionization peak: the step in the real part causes spectral weight being shifted to lower energies below the resonance and to higher energies above it.

For Ce on Rh (111), there is an even larger step in $\mathrm{Re}\,\Delta(\omega)$ extending from $\omega = -3\,\mathrm{eV}$ to $-2\,\mathrm{eV}$. This large step results in a significant amount of weight being being pushed to that high energies, that it contributes to the peaks close to the Fermi level but does not form a second separate ionization peak as in the case of Ce on W(110). This effect occurring in the case of strong hybridization, has been similarly observed in the bulk compound $CeNi_2$ [177, 27].

As in the case of bulk alloys [177], the hybridization of the Ce 4f states with the conduction electron states can induce strong structures in the Ce 4f spectral function for isolated atoms on surfaces. The results from above demonstrates that the LDA++ approach followed, here, is ideally suited to either predict these structures or to reveal the hybridization mechanisms responsible for structures in experimentally measured spectra. For the case of Ce on Ag (111), photoemission and theory found concordantly no significant Kondo like contribution to the spectra. This is in contrast to the Kondo effect of Ce on Ag (111) reported in early STM experiments [178]. The Kondo temperature $T_K = 5\,\mathrm{K} = 0.4\,\mathrm{meV}/k_B$ reported there is far off the value $T_K \sim \delta \ll 10^{-2}\mathrm{meV}$ for all $\epsilon_f < 1\,\mathrm{eV}$ found here by combining photoemission and first-principles calculations. Hence, our results support the conjecture (c.f. Ref [179]) that the STM experiments from Ref. [178] were measuring rather Ce clusters than isolated atoms on Ag (111). This demonstrates that the combination of photoemission spectroscopy and first-principles theory can provide an important complementary view on the physics of magnetic nanostructures.

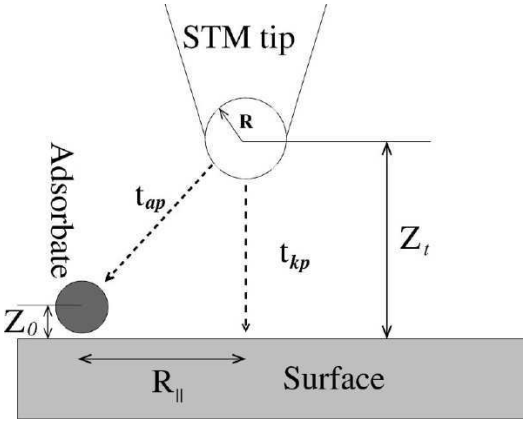

Figure 6.8: Schematic illustration of an STM experiment on a nanostructure adsorbed on a surface. The tunneling current is caused by hopping from the tip to the surface and to the adsorbate. From [180].

6.3 Scanning tunneling spectroscopy of adsorbate resonances

We now turn to an investigation of local electronic properties of magnetic nanostructures and their manifestation in scanning tunneling spectroscopy experiments. We are particularly interested in setups as depicted in Fig. 6.8, where a tunneling current I is measured as function of bias voltage V. To calculate$I = I(V)$ and the differential tunneling conductance $\mathrm{d}I/\mathrm{d}V$, we follow the standard tunneling Hamiltonian approaches from Refs. [115, 180, 181]: the system without the STM tip is described by the Anderson impurity model in the form of Eq. (6.1) and the isolated tip is modelled in terms of non-interacting electrons with the Hamiltonian

$$\hat{H}_{\mathrm{t}} = \sum_{p,\sigma} \epsilon_p t^{\dagger}_{p,\sigma} t_{p,\sigma}, \tag{6.30}$$

where $t_{p,\sigma}$ denotes the Fermi operators for electrons with spin σ in a states p in the tip. The energy of electrons in the tip is ϵ_p and p is a general quantum number.

When the tip is brought close to the surface, a tunneling current can flow and the interaction of tip and sample expressed by the tunneling Hamiltonian,

$$\hat{M} = \sum (M_{mp} d^{\dagger}_{m,\sigma} t_{p,\sigma} + \mathrm{H.c.}) + \sum (M_{kp} c^{\dagger}_{k\sigma} t_{p,\sigma} + \mathrm{H.c.}). \tag{6.31}$$

Here, M_{mp} and M_{kp} are the tunneling matrix elements describing hopping of electrons from a tip state p into an adsorbate orbital m and an conduction electron state k, respectively.

Using the continuity equation, the current from the tip to the sample can be expressed as

$$I = -e\langle \dot{n}_t \rangle, \tag{6.32}$$

where $n_t = \sum_{p,\sigma} t^{\dagger}_{p,\sigma} t_{p,\sigma}$ is the number operator for electrons in the tip. The time derivative is given by the Heisenberg equation for n_t w.r.t. the full Hamiltonian

$\hat{H} = \hat{H}_{\mathrm{AIM}} + \hat{H}_{\mathrm{t}} + \hat{M}$:

$$\begin{aligned} I &= -e\left\langle \frac{i}{\hbar}\left[\hat{H}, n_t\right]\right\rangle = -e\left\langle \frac{i}{\hbar}\left[\hat{M}, n_t\right]\right\rangle \\ &= \frac{2e}{\hbar}\mathrm{Im}\left\{\sum M_{mp}\langle d^{\dagger}_{m,\sigma} t_{p,\sigma}\rangle + \sum M_{kp}\langle c^{\dagger}_{k\sigma} t_{p,\sigma}\rangle\right\}. \end{aligned} \tag{6.33}$$

In general, the expectation values in Eqs. (6.32) and (6.33) are with respect to a time-dependent non-equilibrium state of the tip-sample system and the current has to be calculated by means of non-equilibrium Green functions as outlined in Ref. [180]. Standard scanning tunneling spectroscopy experiments work at tip-sample separations on the order of $5 - 10\,\text{Å}$ and moderate bias voltages $\lesssim 1\,\mathrm{eV}$, where the tunneling matrix elements define the smallest energy scale of the Hamiltonian and tunneling currents are so small that the tip and the sample are each in *local* equilibrium. In this situation the manifestation of non-equilibrium driving the current between tip and sample is that the chemical potential of tip, μ_t, and sample, μ_s, differ by the bias voltage $eV = \mu_t - \mu_s$. I.e. the bias is accounted for by the state of the system when evaluating the average in Eq. (6.33).

Following Ref. [28] we adopt the interaction representation with $\hat{K}' = \hat{H}_{\mathrm{AIM}} + \hat{H}_t - \mu_t n_t - \mu_s n_s$ governing the time dependence of all operators and $n_s = \sum_{k,\sigma} c^{\dagger}_{k\sigma} c_{k\sigma}$. Expanding to lowest order in the tunneling Hamiltonian, Eq. (6.31), yields the tunneling current

$$I = \frac{ie}{\hbar}[U_{\mathrm{ret}}(eV) - U_{\mathrm{adv}}(eV)], \tag{6.34}$$

where U_{ret} (U_{adv}) is a retarded (advanced) correlation function related via analytic continuation, $i\omega_n \to \omega \pm i0^+$, to the Matsubara correlation function

$$\begin{aligned} U(i\omega_n) = -\int_0^{\beta} \mathrm{d}\tau e^{i\omega_n \tau} \Big\{ & M_{kp} M^*_{k'p'} \langle T_\tau c^{\dagger}_{k\sigma}(\tau) t_{p,\sigma}(\tau) t^{\dagger}_{p',\sigma'} c_{k'\sigma'}\rangle \\ & + M_{mp} M^*_{m'p'} \langle T_\tau d^{\dagger}_{m,\sigma}(\tau) t_{p,\sigma}(\tau) t^{\dagger}_{p',\sigma'} d_{m',\sigma'}\rangle \\ & + M_{kp} M^*_{m'p'} \langle T_\tau c^{\dagger}_{k\sigma}(\tau) t_{p,\sigma}(\tau) t^{\dagger}_{p',\sigma'} d_{m',\sigma'}\rangle \\ & + M_{mp} M^*_{k'p'} \langle T_\tau d^{\dagger}_{m,\sigma}(\tau) t_{p,\sigma}(\tau) t^{\dagger}_{p',\sigma'} c_{k'\sigma'}\rangle \Big\}. \end{aligned} \tag{6.35}$$

Summation over all quantum numbers is understood, here. The first two terms of this expression correspond to direct tip-conduction electron state and tip-adsorbate state tunneling, the latter two are quantum interference terms. For the setup under investigation, i.e. an STM tip several Å away from the surface it is reasonable to assume no interaction between the tip- and the sample-electrons[5]. Hence, the state of the tip-sample system can be decomposed into a single product state and the correlation function factors into a product of Green functions for tip and sample.

[5] This assumption is already contained in the particular form of $\hat{K}'$.

For the first term in Eq. (6.35) this yields

$$\begin{aligned} X(i\omega_n) &= -\int_0^\beta \mathrm{d}\tau e^{i\omega_n\tau}\langle T_\tau c^\dagger_{k\sigma}(\tau)t_{p,\sigma}(\tau)t^\dagger_{p',\sigma'}c_{k'\sigma'}\rangle \\ &= \int_0^\beta \mathrm{d}\tau e^{i\omega_n\tau}\langle T_\tau c_{k'\sigma'}c^\dagger_{k\sigma}(\tau)\rangle\langle T_\tau t_{p,\sigma}(\tau)t^\dagger_{p',\sigma'}\rangle \\ &= \frac{1}{\beta}\sum_{i\omega_n'} G^{\sigma'\sigma}_{k'k}(i\omega_n' - i\omega_n)G^{\sigma\sigma'}_{pp'}(i\omega_n') \\ &= \int \frac{\mathrm{d}\epsilon_s}{2\pi}A^{\sigma'\sigma}_{k'k}(\epsilon_s)\int \frac{\mathrm{d}\epsilon_t}{2\pi}A^{\sigma\sigma'}_{pp'}(\epsilon_t)\frac{n_\mathrm{F}(\epsilon_t)-n_\mathrm{F}(\epsilon_s)}{i\omega_n+\epsilon_t-\epsilon_s}, \end{aligned} \tag{6.36}$$

where a Lehmann representation of the Matsubara Green functions has been used: $G(i\omega_n) = \int \frac{\mathrm{d}\epsilon}{2\pi}\frac{A(\epsilon)}{i\omega_n-\epsilon}$. Comparison with Eq. (6.34) shows that terms of the type

$$\begin{aligned} &X(eV+i0^+) - X(eV-i0^+) \\ &\quad = -2\pi i\int \frac{\mathrm{d}\epsilon_s}{2\pi}A^{\sigma'\sigma}_{k'k}(\epsilon_s)\int \frac{\mathrm{d}\epsilon_t}{2\pi}A^{\sigma\sigma'}_{pp'}(\epsilon_t)(n_\mathrm{F}(\epsilon_t)-n_\mathrm{F}(\epsilon_s))\delta(eV+\epsilon_t-\epsilon_s) \\ &\quad = -2i\int \frac{\mathrm{d}\epsilon_s}{2\pi}A^{\sigma'\sigma}_{k'k}(\epsilon_s)A^{\sigma\sigma'}_{pp'}(\epsilon_s-eV)(n_\mathrm{F}(\epsilon_s-eV)-n_\mathrm{F}(\epsilon_s)) \end{aligned} \tag{6.37}$$

enter the expression for the current. Inserting these into Eq. (6.34) yields

$$\begin{aligned} I = \frac{2e}{\hbar}\int \frac{\mathrm{d}\epsilon_s}{2\pi}\Big\{ & M_{kp}M^*_{k'p'}A^{\sigma'\sigma}_{k'k}(\epsilon_s)A^{\sigma\sigma'}_{pp'}(\epsilon_s-eV) \\ &+ M_{mp}M^*_{m'p'}A^{\sigma'\sigma}_{m'm}(\epsilon_s)A^{\sigma\sigma'}_{pp'}(\epsilon_s-eV) \\ &+ M_{mp}M^*_{k'p'}A^{\sigma'\sigma}_{k'm}(\epsilon_s)A^{\sigma\sigma'}_{pp'}(\epsilon_s-eV) \\ &+ M_{kp}M^*_{m'p'}A^{\sigma'\sigma}_{m'k}(\epsilon_s)A^{\sigma\sigma'}_{pp'}(\epsilon_s-eV)\Big\}(n_\mathrm{F}(\epsilon_s-eV)-n_\mathrm{F}(\epsilon_s)). \end{aligned} \tag{6.38}$$

For approximately constant tip density of states within the range of applied bias voltages and neglecting higher order contributions of the tip-sample coupling, the differential tunneling conductance is consequently given by

$$\begin{aligned} \frac{\mathrm{d}I}{\mathrm{d}V} \sim A^{\sigma\sigma'}_{pp}(\epsilon_\mathrm{F})\Big\{ & M_{kp}M^*_{k'p}A^{\sigma'\sigma}_{k'k}(eV) + M_{mp}M^*_{m'p}A^{\sigma'\sigma}_{m'm}(eV) \\ &+ M_{mp}M^*_{k'p}A^{\sigma'\sigma}_{k'm}(eV) + M_{kp}M^*_{m'p}A^{\sigma'\sigma}_{m'k}(eV)\Big\}. \end{aligned} \tag{6.39}$$

In absence of external magnetic fields, the Hamiltonian is time reversal symmetric and all matrix elements can be defined in terms of real numbers. Omitting the tip density of states, yields the compact expression for the differential conductance

$$\frac{\mathrm{d}I}{\mathrm{d}V} \sim -\,\mathrm{Im}\left\{\mathbf{M}^\dagger\mathbf{G}^R(eV)\mathbf{M}\right\}, \tag{6.40}$$

$$\mathbf{G}^R(eV) = \begin{pmatrix} G^R_{k'k}(eV) & G^R_{k'm}(eV) \\ G^R_{m'k}(eV) & G^R_{m'm}(eV) \end{pmatrix}, \tag{6.41}$$

$$\mathbf{M} = \begin{pmatrix} M_{kp} \\ M_{mp} \end{pmatrix}, \tag{6.42}$$

where $\mathbf{G}^R$ is the retarded Green function of the sample in matrix form. Using a standard equation of motion technique [180], this Green function matrix can be expressed entirely in terms of the unperturbed conduction electron Green function $G^{R0}_{k'k}(\omega) = \delta_{k,k'} G^{R0}_k(\omega)$, the full interacting impurity Green function $G^R_{m'm}(eV)$ and the hybridization matrix elements V_{km} from Eq. (6.1):

$$G^R_{k'k}(\omega) = \delta_{k,k'} G^{R0}_k(\omega) + G^{R0}_{k'}(\omega) \sum_{mm'} \left[V_{k'm'} G^R_{m'm}(\omega) V_{mk} \right] G^{R0}_k(\omega) \tag{6.43}$$

$$G^R_{m'k}(\omega) = \sum_m G^R_{m'm}(\omega) V_{mk} G^{R0}_k(\omega) \tag{6.44}$$

$$G^R_{k'm}(\omega) = G^{R0}_{k'}(\omega) \sum_{m'} V_{k'm'} G^R_{m'm}(\omega). \tag{6.45}$$

This can be used together with Eq. (6.40) to show that the differential conductance is

$$\frac{\mathrm{d}I}{\mathrm{d}V} \sim -\mathrm{Im}\, T^R(eV), \tag{6.46}$$

$$T^R = \sum_{k,p} |M_{kp}|^2 G^{R0}_k + \sum_{m,m',p} \tilde{M}_{pm} G^R_{m'm} \tilde{M}_{m'p}, \tag{6.47}$$

$$\tilde{M}_{pm} = M_{pm} + \sum_k M_{pk} G^{R0}_k V_{km}. \tag{6.48}$$

We now turn to the situation of a resonance in one of the impurity orbitals, m_0, at energy ϵ_r of width Γ with spectral weight Z: $G^R_{m_0m_0}(\omega) = \frac{Z}{\omega - \epsilon_r + i\Gamma}$. Moreover, we assume smooth density of states in all other channels and $\tilde{M}_{pm_0} = \tilde{M}_{m_0}$ being equal for all tip states in the energy range of interest. Then, up to a constant background the conductance close to $eV = \epsilon_r$ takes the form

$$\frac{\mathrm{d}I}{\mathrm{d}V} \sim -\,\mathrm{Im}\left\{ \tilde{M}_{m_0} G^R_{m_0m_0}(eV) \tilde{M}_{m_0} \right\} \tag{6.49}$$

$$= -\left\{ (\mathrm{Re}^2[\tilde{M}_{m_0}] - \mathrm{Im}^2[\tilde{M}_{m_0}]) \mathrm{Im}[G^R_{m_0m_0}(eV)] + 2\mathrm{Re}[\tilde{M}_{m_0}] \mathrm{Im}[\tilde{M}_{m_0}] \mathrm{Re}[G^R_{m_0m_0}(eV)] \right\}$$

$$\sim -\left\{ (q^2 - 1) \mathrm{Im}[G^R_{m_0m_0}(eV)] - 2q\,\mathrm{Re}[G^R_{m_0m_0}(eV)] \right\}$$

$$\sim -\frac{1}{\tilde{\omega}^2 + 1} \left\{ -(q^2 - 1) - 2q\tilde{\omega} \right\} = \frac{(\tilde{\omega} + q)^2}{\tilde{\omega}^2 + 1} - 1, \tag{6.50}$$

where we defined $\tilde{\omega} = (\omega - \epsilon_r)/\Gamma$ and

$$q = -\frac{\mathrm{Re}\, \tilde{M}_{m_0}}{\mathrm{Im}\, \tilde{M}_{m_0}}. \tag{6.51}$$

As Eq. (6.50) shows, the impurity resonance manifests in STS like a Fano resonance with the asymmetry factor, q, given by Eq. (6.51).

To calculate the q-factor for a particular realistic situation the structure the STM tip has to be known and conduction electron states, $\psi_k(r)$ and (magnetic) impurity states $\psi_m(r)$ have to be disentangled. This poses two problems: First

the exact shape of the tip and its apex orbitals is usually unknown. Second, the distinction between impurity and conduction electron states is not fully natural: The impurity and the conduction electron states hybridize, leading to the Kohn-Sham eigenstates of the adsorbate impurity-system being mixtures of both. The definition of the impurity orbitals is therefore not unique.

One way to deal with these problems is joining first-principles theory with model calculations and making assumption on the unknown parameters like tip wave functions based on physical intuition. In this way, Fano factors for Co on Cu(111) and Cu(100) have been addressed in Ref. [182]. In this work, the impurity and conduction electron states have been separated by first obtaining the Kohn-Sham eigenstates of the clean surfaces and then evaluating the Kohn-Sham Hamiltonian of the surface with impurity in the basis given by low energy ($|\epsilon - \epsilon_F| \lesssim 1\,\mathrm{eV}$) clean surface eigenstates. Assuming an s-wave tip and choosing one atomic like Co 3d-orbital for being active in the Kondo effect, the dependence of the Fano q-factor on parallel tip surface distance, $R_\parallel$ has been calculated. At $R_\parallel < 6\,\text{Å}$ the authors find qualitative agreement for their q-factors with experimental data from Ref. [183]. In this approach, the disentangling of the correlated impurity and the conduction electron states by taking a small energy window eigenstates from the clean surface might seem a drastic approximation, since the *s*- and *p*-states of Co the impurity are strongly hybridizing with the Cu atoms in the vicinity. The Co *s*- and *p*-orbitals are consequently part of "the" conduction electrons in the vicinity of the impurity but not included in the conduction electron basis set from Ref. [182]. Similarly, the potential scattering between the conduction electron states off the impurity potential is not necessarily small as compared to the scale given by the energy window of ±1 eV.

Working with basis sets truncated in the way of Ref. [182] to describe the conduction electron states may appear unsatisfactory, as these states are usually well described in DFT with full potential basis sets like FLAPW or PAW. In LDA++ approaches as discussed in section 2.5.3 or 6.2 a correlated subspace is selected. Within this LDA++ philosophy, projecting the correlated subspace out of the Kohn-Sham Hamiltonian is the most natural way of obtaining "the" conduction electron wave functions and energies. Indeed, this projecting out of correlated states can be viewed as the direct complement of projecting correlations in, as done in basis independent formulations of LDA+DMFT [184].

This projecting out strategy can be followed on different levels of approximation. First, all matrix elements V_{km} as well as the bare conduction electron Green function G^0_k could be obtained in this way and interfaced e.g. with a QMC solution of the resulting AIM. While this might be conceptionally the most consequent way of calculating the q-factor and probably a way to make predictions in the future, it might be not the most transparent way to shed light on experimental observations and to explain trends observed in experiments: (V_{km}) is usually a high dimensional matrix with the conduction electron quantum number k including a few hundred different bands in typical supercell calculations.

It is therefore useful to make additional assumptions on the particular form of the matrix elements in Eq. (6.1) and (6.31). We follow two complementary

series of approximations based on different physical assumptions. In all cases, we consider the tip directly above the magnetic ad-atom or nanostructure and assume that the magnetic moment is localized in atomic 3d orbitals of the impurity[6].

To obtain our first approach to the q-factor, we note that the *atomic* impurity *s*- and *p*-orbitals mainly contribute to the conduction electron states at the impurity site and it is therefore reasonable to construct a basis of conduction electron states in the vicinity of the impurity from these *s*- and *p*-orbitals. Then, for the *d*-type magnetic orbitals strongly localized at the impurity site, the hybridization matrix elements are given by

$$V_{km} = \int \mathrm{d}^3 r \psi_k(r) V(r) \psi_m(r) \approx \langle \psi_k | \mathcal{P}_{sp} V | \psi_m \rangle, \tag{6.52}$$

where V is the full Kohn-Sham potential and $\mathcal{P}_{sp}$ is a projector on the *s*- and *p*-orbitals of the impurity. For the tip directly above the ad-atom the tunneling amplitude of conduction electron states to the tip is likely dominated by the amplitude of the conduction electron wave functions at the impurity site, which is topmost point of the sample[7]. The conduction electron tunnelling matrix elements fulfill therefore

$$M_{kp} \approx \langle \psi_k | \mathcal{P}_{sp} H_T | \psi_p \rangle, \tag{6.53}$$

where H_T is the Kohn-Sham Hamiltonian of the tip-sample system without hybridization V_{km}.

The full Kohn-Sham Greenfunction G_{KS} is related to the unhybridized Kohn-Sham Green function $G^0_{\mathrm{KS}} \equiv G^{R0}$ occurring in Eq. (6.48) by the Dyson equation $G_{\mathrm{KS}} = G^0_{\mathrm{KS}} + G^0_{\mathrm{KS}} V G^0_{\mathrm{KS}} + G^0_{\mathrm{KS}} V G^0_{\mathrm{KS}} V G^0_{\mathrm{KS}} + \cdots$. As G^0_{KS} is by definition block diagonal in the conduction and impurity states, we have $\langle i | G_{\mathrm{KS}} | j \rangle = \langle i | G^0_{\mathrm{KS}} | j \rangle + O(V^2)$ for *s*- and *p*-atomic states, $|i\rangle$ and $|j\rangle$, at the impurity site.

Inserting this to Eq. (6.48) yields

$$\tilde{M}_{pm} \approx M_{pm} + \langle \psi_p | H_T \mathcal{P}_{sp} G_{\mathrm{KS}} \mathcal{P}_{sp} V | \psi_m \rangle. \tag{6.54}$$

Obviously, $\mathcal{P}_{sp} G_{\mathrm{KS}} \mathcal{P}_{sp}$ is the local Kohn-Sham Green function of the s- and p-impurity orbitals. In the simplest approximation, all dependencies on impurity orbitals s, p_x, p_y, p_z are neglected and the local Green function is replaced by an average, $\bar{G}_{\mathrm{KS}} = \frac{1}{4} \mathrm{Tr} \mathcal{P}_{sp} G_{\mathrm{KS}} \mathcal{P}_{sp}$, over all impurity *s*- and *p*-orbitals. This yields

$$\tilde{M}_{pm} \approx M_{pm} + M_0 V_0 \bar{G}_{\mathrm{KS}}, \tag{6.55}$$

and

$$q = -\frac{M_{pm} + M_0 V_0 \mathrm{Re} \bar{G}_{\mathrm{KS}}}{M_0 V_0 \mathrm{Im} \bar{G}_{\mathrm{KS}}}, \tag{6.56}$$

[6] In this work, Co on Cu(111) as well as Co on graphene is considered. We therefore restrict the discussion to 3d states carrying the magnetic moment, since the generalization to f-states is straight forward.

[7] This process should not be confused with "tunneling through impurity orbitals". The impurity *s*- and *p*-orbitals, are part of the conduction electrons.

where M_0 and V_0 are constants. Note, that this approximation to the q-factor can also be derived along the lines of Ref. [180] by assuming a particular form of the conduction electron wave functions. In this sense, Eq. (6.56) is equivalent to Eq. (3.21) from Ref. [180].

The other "projecting out" approach to the q-factor aims at the case, where the resonance is formed by a set of impurity orbitals with well defined symmetry, S, which is also a symmetry of the clean surface as well as of the surface with an impurity on top. In this case, the conduction electron states can be labelled in terms of irreducible representations m of the symmetry S and the conduction electron quantum numbers can chosen to contain m, $k = (m, \tilde{k})$, with $G^{0R}_{kk'} \sim \delta_{kk'}$ being still diagonal. With the notion that the impurity is again the topmost point of the sample, the tunneling amplitude of conduction electron states to the tip is again dominated by the impurity site it is reasonable to assume $M_{kp} = \frac{M_0}{V_0} V_{km}$ for tip orbitals, p, transforming under S also according to m. With the definition of the hybridization function, Eq. (6.3), this leads to

$$q = -\frac{M_{pm} + (M_0/V_0)\mathrm{Re}\,\Delta}{(M_0/V_0)\mathrm{Im}\,\Delta}. \tag{6.57}$$

We will encounter this high symmetry situation for Co on graphene and use Eq. (6.57) in section 6.5.

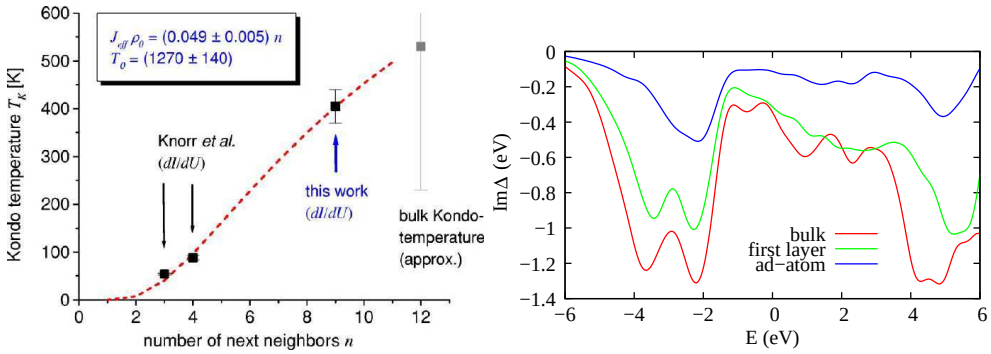

Figure 6.9: Left: Kondo temperatures for Co in different Cu environments with Co coordination number n = 3, 4, 9 and 12 for Co on the Cu (111) and Cu (100) surfaces, in the Cu (111) surface and in bulk Cu, respectively. The dashed line is a fit of T_K according to Eq. (6.58) and $J\rho(\epsilon_F, r) \sim n$ to the experimental Kondo temperature data. The simple scaling of appears to be well followed by the experimental data points. From Ref. [185]. Right: Orbitally averaged hybridization functions for Co in bulk Cu, in the first layer of the Cu (111) and as ad-atom on Cu (111). The imaginary part, Im Δ, is shown.

6.4 Co atoms in Cu environments

Co atoms coupled to metallic Cu hosts may be regarded as the "drosophila fly" for experiments of how localized electrons interact with delocalized electrons. In different Cu environments, Co is known act as Kondo impurity and Kondo temperatures have been measured for Co in bulk, for Co on the Cu (111) and Cu (100) surfaces as well as for Co in the Cu (111) surface [183, 185]. These experiments showed that within these four configurations the Kondo temperatures appear to scale with the coordination number n of Co according to

$$T_K = T_0 \exp(-1/J\rho(\epsilon_F, r)), \tag{6.58}$$

where the product of the effective exchange interaction J and the local density of states at the impurity site $\rho(\epsilon, r)$ fulfills $J\rho(\epsilon_F, r) \sim n$. This simple relation appears to hold despite all multiorbital effects and the intricate local electronic structure for Co in different Cu environments (see Fig. 6.9).

This is indeed surprising, as detailled descriptions of these experiments appeared complicated and quite contradictory: Early interpretations of Co on Cu (111) Kondo effect were based on the assumption that only surface states of Cu (111) are involved in the scattering of electron waves by the Co adatoms [186, 187, 188]. These interpretations were particularly, successful in explaining the observations of "quantum mirages" [189] in corral structures on the Cu (111) surface. However, later experiments with Co atoms on the Cu (100) surface (that does not have any surface state) [183], or on Ag (111) but close to atomic surface steps (that affect the surface states) [190] have indicated that bulk rather than surface states are responsible for the Kondo effect in these situations.

We turn now to an investigation to which extent the realistic atomic geometry of Kondo systems plays a crucial role in determining the complex electronic

properties and to which extent details of the intraatomic Coulomb interaction are important in these systems.

6.4.1 QMC study of Co coupled to Cu hosts

We first present an LDA++ type investigation of the spectra on Co in bulk Cu, in the Cu (111) surface and on the Cu (111) surface, which has been done in collaboration with E. Gorelov.[8] These Co-Cu systems are treated as five-orbital Anderson impurity models representing 3*d* electronic shell of the cobalt atom hybridized with a bath of a conduction Cu electrons. These AIMs are solved using the recently developed Continuous Time Quantum Monte Carlo (CT-QMC) method in the weak coupling formulation [191].

The details of the CT-QMC method are described elsewhere [191, 192, 193]. We apply it here, since it is capable of dealing with an arbitrary local Coulomb interaction matrix, which allows us to compare results with a full rotationally invariant Coulomb interaction matrix to on-site Coulomb interaction containing only density-density type terms. The input of the CT-QMC calculations are bath Green functions as defined in Eq. (6.11), which are related to the hybridization functions as explained in section 6.1. The latter are used for a qualitative discussion.

For all Co-Cu systems studied here, the bath Green functions and the hybridization functions were obtained using the DFT within the supercell approach using the VASP package (see section 2.4) with the projector augmented wave (PAW) basis sets (c.f. Ref. [52] and section 2.3.3). For the simulation of a cobalt impurity in the bulk we employed a $CoCu_{63}$ supercell structure with the lattice constant corresponding to pure copper. The surfaces were modeled by supercells of Cu (111) slabs containing 5 Cu layers with 2×2 and 3×4 lateral extension for Co in and on the surface, respectively.

We obtained the Co 3*d* bath Green function matrix,

$$\mathcal{G}_{0,ij}(i\omega_n) = \sum_{n\mathbf{k}} \frac{\langle d_i|\psi_{n\mathbf{k}}\rangle \left\langle \psi_{n\mathbf{k}}|d_j\right\rangle}{i\omega_n + \mu - \varepsilon_{n\mathbf{k}}}, \tag{6.59}$$

and the related hybridization function using the projectors $\langle d_i|\psi_{n\mathbf{k}}\rangle$ provided by the PAW basis sets (see appendix A). In this way, we avoid a truncation of the Kohn-Sham Hilbert space like in Ref. [182], where Co on Cu (111) has been discussed. Moreover, we treat all Co 3d orbitals on the same footing and do not restrict our considerations to the $d_{3z^2-r^2}$ orbital as in Ref. [182].

The orbitally averaged Co 3*d*-hybridization functions for the three different Co-Cu systems are shown in Fig. 6.9. The experimental trend of increasing Kondo temperatures with increasing coordination is in agreement with increasing hybridization strength when going from Co ad-atoms, to Co inside the surface

[8] The CT-QMC results presented here have been obtained by E. Gorelov, who wrote the CT-QMC code and performed the CT-QMC calculations. The author of this thesis performed the DFT calculations, which yielded the bath Green functions used as input for the CT-QMC calculations and the hybridization functions discussed in this section.

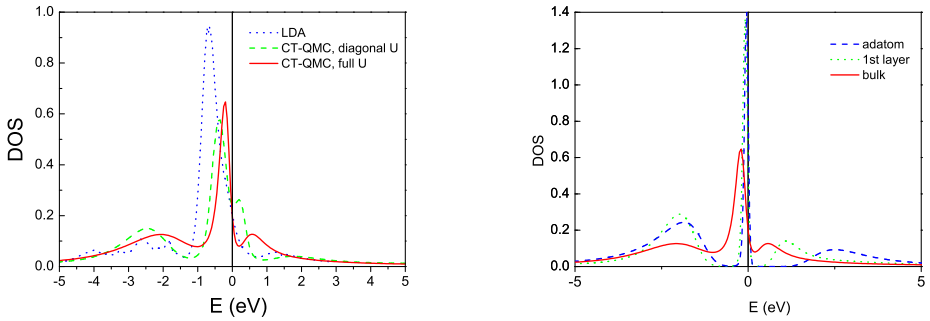

Figure 6.10: Total DOS of the Co 3d orbitals. Left: For Co embedded in bulk Cu the DOS as obtained from CT-QMC calculations with full and diagonal Coulomb vertex and $U = 4$ eV, $J = 0.7$ eV, $\beta = 10$ eV^{-1} in close to Co d^7 configuration is compared to the LDA Co DOS. Right: Comparison of of a Co atom embedded in the bulk of Cu to Co in the 1-st layer and a Co-adatom on the Cu(111) surface. The curves show CT-QMC results for $U = 4$ eV, $J = 0.7$ eV, $\beta = 10$ eV^{-1} with the impurity in d^7 configuration.

layer of Cu (111) to Co in bulk Co. When comparing Eq. (6.8) to Eq. (6.9), on sees that the Schrieffer Wolf transformation leads to $J\rho \sim \Delta$. Our calculations yield $\mathrm{Im}\,\Delta_{\mathrm{ad-atom}}(\epsilon_f) : \mathrm{Im}\,\Delta_{\mathrm{first-layer}}(\epsilon_f) : \mathrm{Im}\,\Delta_{\mathrm{bulk}}(\epsilon_f) = 1 : 2.8 : 3.1$, which is roughly in line with the experimental data suggesting the corresponding rations of the hybridization strengths on the order of $1 : 3 : 4$.

For the many-body calculations of the Co impurity in the Cu matrix we need to find the effective d-orbital chemical potential which defines the number, n_d, of 3d-electrons of cobalt. The particular electronic configuration of a Co atom in a copper matrix is unknown, and obtaining it in a systematic first-principles way is equivalent to solving the double counting problem discussed in section 2.5.3. Here, DFT yields $n_d = 7.3 - 7.4$, which suggests that the realistic Co 3d occupation is likely close to the d^7 configuration. Therefore we performed all impurity calculations for Co in d^7 configuration. The DOS being discussed in the following have been obtained from the QMC Matsubara Green functions by analytical continuation using the maximum entropy method [194].

The results of the CT-QMC calculations with full and density-density type Coulomb vertex for a cobalt impurity in the bulk with $U = 4$ eV and $J = 0.7$ eV are presented in Fig. 6.10 and compared to the bare impurity density of states. There is a pronounced difference between the Kondo-like resonances near the Fermi level. In the case of the full U-vertex it becomes more narrow and located much closer to the Fermi level. The sign problem for a Co impurity in the bulk is not large and the average sign is between 0.90 and 0.97 depending on the simulation temperature.

We also performed CT-QMC calculations of a cobalt impurity on the surface of Cu(111) and embedded into the first copper layer. In contrast to the bulk system, in or on the surface one has a large sign problem, related with the relatively large non-diagonal elements of the bath Green functions. Although changing of

the sign is a very rare event (less than 0.03% of the accepted steps), we had to do constrained sign calculations [192, 193]. The sign problem prevents us from calculating at sufficiently low temperatures, which would be required for reliably obtaining a quantitative value of the width of the Kondo resonance. However, a qualitative study of how the local coordination affects the spectral properties of the impurity is possible at $\beta = 10\,\mathrm{eV}^{-1}$: A comparison of the different spectral functions for the bulk, surface and first-layer cobalt impurity is presented in Fig. 6.10. One can see clearly the change of the Kondo resonance width as a function of reduced dimensionality, i.e. when going from the bulk into or on the surface. At our simulation temperature, the width of the Kondo resonance of Co in and on the surface appears to be similar. However, the high energy features of the spectra differ markedly between Co on and in the surface. The upper Hubbard peak is shifted to higher energies upon reducing the coordination.

This study leads to the conclusions, that non-density-density terms in the Coulomb vertex are required to obtain quantitative predictions of spectral functions and related properties, as can been seen from the position of the Hubbard peaks and the quasiparticle peak in Fig. 6.10 left. However, hybridization effects like bringing the Co impurity from bulk to the surface can be quite drastic: As a comparison of the two panels in Fig. 6.10 shows, the sharpening of the Kondo resonance and the shifting of the Hubbard bands is much stronger when going from bulk to the surface than on switching on the non-diagonal part of Coulomb matrix. So, the qualitative overall shape of the DOS and its response to strong hybridization changes appear to be well described by density-density type terms of the Coulomb vertex.

6.4.2 The Kondo effect in $CoCu_n$ clusters

In the last section we found that experiment and theory appear to agree on the trend that increasing coordination leads to higher Kondo temperatures. We now report on a joint experimental[9] and theoretical study of $CoCu_n$ clusters on the Cu (111) surface: The clusters containing a single magnetic impurity were investigated by scanning tunneling microscopy, spectroscopy, and *ab initio* electronic structure calculations. Surprisingly, the Kondo temperatures of the Co atom embedded in the Cu clusters on Cu(111) exhibit a non-monotonic variation with the cluster size. This is at variance with previously discussed models which are typically invoked to interpret the Kondo effect of a single adsorbed atom (adatom). We perform DFT calculations to model the experimental observations and demonstrate the importance of the local inhomogeneous electronic structure for correlation effects in small clusters.

The details of the experimental procedure are given in Ref. [195]. For here, it is important to note that the scanning tunneling microscope was operated at 7 K and in ultra-high vacuum with a base pressure of 10^{-9} Pa. The $CoCu_n$ nanostructures were created by first evaporating individual Co atoms on the Cu (111)

[9]The experiments presented in this section were done by N. Néel, J. Kröger and R. Berndt at the Institut für Experimentelle und Angewandte Physik, Christian-Albrechts-Universität zu Kiel.

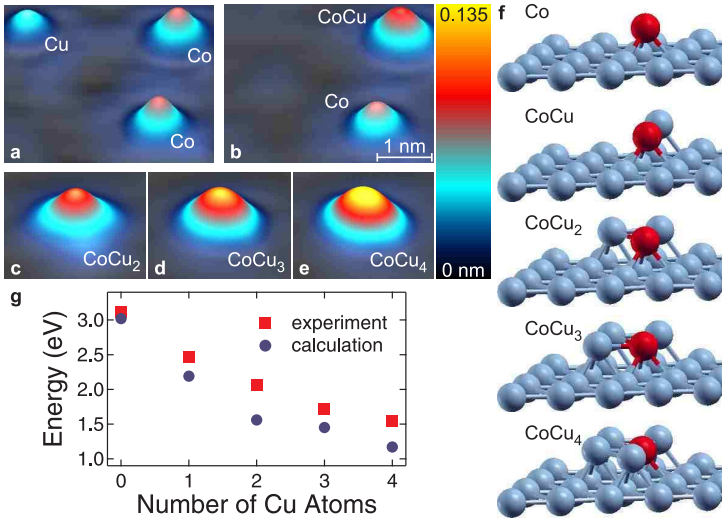

Figure 6.11: (a) STM image of Co and Cu atoms on Cu(111) prior to fabricating $CoCu_n$ clusters. (b) - (e) Sequence of STM images showing $CoCu_n$ clusters. The same lateral and height scale was used for all images. Images were acquired at a sample voltage of 100 mV and a tunneling current of 0.1 nA. (f) Ball-and-stick models of fully relaxed adsorption structures of $CoCu_n$ on Cu(111). Only the uppermost substrate layer is shown for clarity. (g) Experimental energy of unoccupied cluster state versus cluster size. The size of the symbols (squares) corresponds to the uncertainty of the energies. Calculated energies are depicted as dots.

surface and then placing Cu atoms around Co by atomic manipulation with the STM tip. Spectroscopy of the differential conductance (dI/dV) was performed by a lock-in technique.

Figures 6.11(a)-(e) show a series of constant-current STM images, which illustrates fabrication of a CoCu cluster (Figs. 6.11(a), (b)) and dimensions of $CoCu_n$ ($n = 1, \ldots, 4$) clusters (Figs. 6.11(b)-(e)). In STM images acquired at a sample voltage of 100 mV Co atoms appear higher than Cu atoms (Fig. 6.11(a)). The stick-and-ball models of the clusters used for the calculations are presented in Fig. 6.11(f).

Spectroscopy of dI/dV performed with the tip positioned above the cluster center reveals an unoccupied state whose energy decreases with increasing number of Cu atoms (squares in Fig. 6.11(g)). Our calculations (see below) show that this resonance is of p_z character and are in agreement with experimental data (circles in Fig. 6.11(g)). This resonance serves to confirm the calculated relaxed structures.

Figure 6.12 shows a sequence of dI/dV spectra acquired on a single Co atom (lower curve, $n = 0$) and above the center of $CoCu_n$ clusters with n ranging between 1 and 4. Starting from a sharp indentation of the differential conductance close to the Fermi level (0 mV) which is the spectroscopic signature of the single-Co Kondo effect on Cu(111), the dI/dV curve broadens appreciably upon adding two Cu atoms to the Co atom. Surprisingly, upon increasing the number of Cu atoms to three and four, the resonance sharpens again, in contrast to the mono-

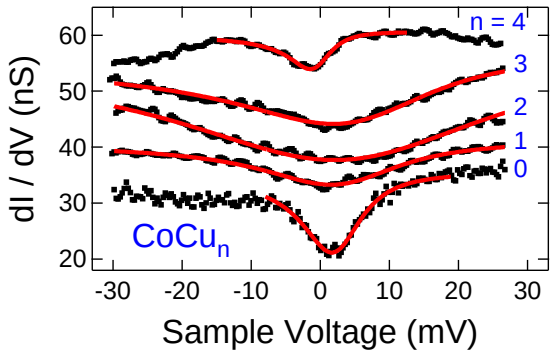

Figure 6.12: Spectroscopy of dI/dV of CoCu$_n$ clusters around the Fermi level. The spectroscopic feature is the Abrikosov-Suhl resonance induced by the Kondo effect. Lines depict fits of Fano lines, Eq. (6.50), to experimental data. Spectra for $n = 1, \ldots, 4$ are vertically offset by 5, 10, 20, 25 nS, respectively.

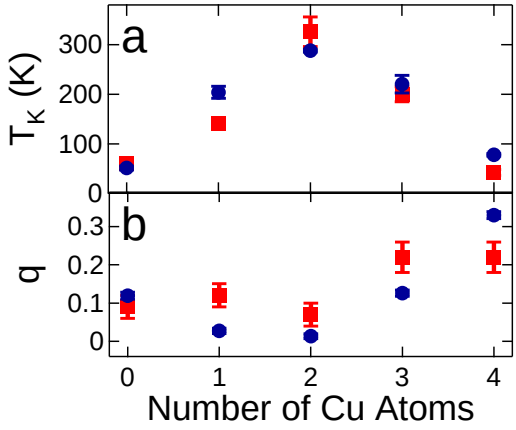

Figure 6.13: (Color online) Kondo temperatures (a) and asymmetry parameters (b) as a function of cluster size from experiments (squares) and calculations (dots).

tonic behavior of the unoccupied p_z-like state with the number of copper atoms (Fig. 6.11(g)).

To quantify the broadening of the resonances at the Fermi level we described experimental data by a Fano line shape as in Eq. (6.50) with q the asymmetry parameter of the Fano theory and width $\Gamma = k_B T_K$. The profiles of Fano line shapes according to Eq. (6.50) and fitted to dI/dV data are presented as lines in Fig. 6.12. The striking change of the width of the Abrikosov-Suhl resonance is reflected by the Kondo temperature T_K plotted in Fig. 6.13 (a). While the single Co adatom exhibits $T_K = (61 \pm 4)$ K, in agreement with Ref. [183], for CoCu$_2$ we find (326 ± 30) K which then decreases again to (43 ± 6) K for CoCu$_4$. Figure 6.13(b) shows the evolution of the asymmetry parameter with the cluster size. For $n = 0, 1, 2$ the asymmetry parameter varies weakly around 0.1. It increases steeply by ≈ 100 % upon adding a third Cu atom. Kondo temperatures and asymmetry

Table 6.1: Experimental and calculated Kondo temperatures (T_K) and asymmetry parameters (q) of $CoCu_n$ extracted from fits of the Fano lines, Eq. (6.13), to measured Kondo resonances shown in Fig. 6.12. Experimental uncertainty margins correspond to standard deviations obtained by a statistical analysis of a variety of fits. Calculated T_K and q are the arithmetic mean of values obtained by a Gaussian broadening of the *sp* local density of states by 100 meV and 50 meV. The uncertainty margins reflect the deviations of the arithmetic mean from data obtained by 100 meV and 50 meV broadening.

	Experiment		Calculation	
n	T_K (K)	q	T_K (K)	q
0	61 ± 4	0.09 ± 0.03	52 ± 4	0.12 ± 0.01
1	142 ± 10	0.12 ± 0.03	204 ± 12	0.03 ± 0.01
2	326 ± 30	0.07 ± 0.03	288 ± 3	0.01 ± 0.01
3	200 ± 15	0.22 ± 0.04	221 ± 18	0.13 ± 0.01
4	43 ± 6	0.22 ± 0.04	79 ± 3	0.33 ± 0.01

parameters for the various clusters are summarized in Table 6.1.

The peculiar behavior of the Kondo resonance with cluster size is at variance with the monotonic dependence of T_K on the coordination from the surface Kondo models discussed in Refs. [183, 185] and in the preceding section. Given the complications and controversy in gaining theoretical understanding of the Kondo effect of single Co atoms on the Cu (111) surface (c.f. section 6.4 and Refs. [186, 187, 188, 183, 190]), *ab initio* electronic structure calculations which are not restricted by specific model assumptions can be very useful. Here, we perform accurate calculations of the local electronic structure of clusters on the copper surface.

We use these calculations together with Eq. (6.8) to obtain a theoretical estimate of how the Kondo temperature should vary with cluster size. Since the *sp*-*d* exchange interaction is local, ρ_0 in Eq. (6.8) is the LDOS of conduction electrons at the magnetic atom at the Fermi level. Within the approximations discussed in section 6.3, the asymmetry parameter, q, is also determined by the local electronic structure: q can be expressed according to Eq. (6.56) and rewritten as

$$q = -[\mathrm{Im}\,\bar{G}_{KS}(\epsilon_F)]^{-1}[\gamma + \mathrm{Re}\,\bar{G}_{KS}(\epsilon_F)], \tag{6.60}$$

where $\bar{G}_{KS}$ is the local Green's function of the conduction electrons at the impurity site and $\gamma = M_{pm}/M_0V_0$ is a measure for the ratio of the coupling of the STM tip to conduction electron states and to the strongly localized Co *d* states.

To realistically describe the $CoCu_n$ clusters on Cu(111) we calculated their electronic and structural properties by means of DFT using the generalized gradient approximation to the exchange correlation potential [42] with PAW basis sets (350 eV plane wave cut-off) [52] as implemented in VASP [53]. (See sections 2.2, 2.3.3, and 2.4 for details.) We modeled the $CoCu_n$ structures using 4×3 supercells of Cu(111) slabs containing up to 7 Cu layers. Guided by the apparent heights and symmetries from the STM images, we chose flat $CoCu_n$ clusters with the Co atom at high symmetry positions in the center of the cluster as a starting point. These

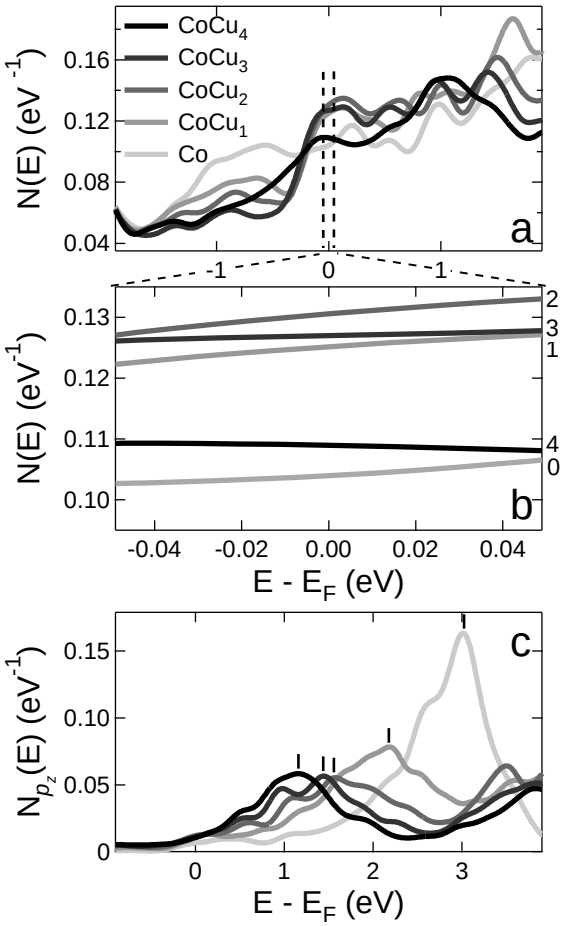

Figure 6.14: Calculated local density of states (LDOS) at the Co site for $CoCu_n$ assemblies. (a) *sp* LDOS, $N(E)$, plotted for energies between $-1.9\,\text{eV}$ and $1.9\,\text{eV}$ with respect to the Fermi energy. (b) Close-up view of (a) showing the energy range of the Kondo resonance. (c) p_z LDOS, $N_{p_z}(E)$, with indicated energies of unoccupied cluster resonances shown in Fig. 6.11(g).

structures haven been fully relaxed with the requirement that all forces are less than $0.02\,\text{eV}\,\text{Å}^{-1}$ and were then used to calculate the LDOS. The supercell Brillouin zone integrations for obtaining the LDOS have been performed using the tetrahedron-method on 6×6 k meshes with subsequent 50 - 100 meV Gaussian broadening. Below, we use both, 50 and 100 meV smearing, to provide an uncertainty margin for the derived Kondo temperatures and asymmetry parameters[10].

The relaxed structures, Fig. 6.11(f), show that the distance of the Co atom to the Cu surface increases monotonically upon adding Cu atoms to the cluster. However, the local electronic structure at the Fermi level and at the Co site varies in a

[10]These uncertainty margins naturally do not contain uncertainties, which are due to the models, Eqs. (6.8) and (6.60), used to obtain Kondo temperatures and Fano factor from the first-principles calculations. These margins give only an estimate of intrinsic DFT errors due to e.g. the finite k-mesh used in the Brillouin zone integration.

non-monotonic way with increasing number of Cu atoms. The substrate conduction band states extend to the Co adatom site where they interact with localized Co 3d electrons. In the simple model of Eq. (6.8), this interaction is quantified by the Co sp-projected LDOS, $N(E) = N_s(E) + N_p(E)$, which is shown in Figs. 6.14(a) and 6.14(b). The dependence of $N(E_\mathrm{F})$ on the number of Cu atoms is non-monotonic[11], Fig. 6.14 (b), and leads, according to Eq. (6.8), to the experimentally observed non-monotonic behavior of the Kondo temperature (Fig. 6.13): we used $W = 20\,\mathrm{eV}$ and $J = 1.3\,\mathrm{eV}$ as fitting parameters to obtain the theoretical estimates for the Kondo temperatures shown in Table 6.1 and Fig. 6.13. Moreover, with $\gamma = 0.22\,\mathrm{eV}^{-1}$ in Eq. (6.60) the variation of $\bar{G}_\mathrm{KS}(E_\mathrm{F}) = \int \mathrm{d}\epsilon' \frac{N(\epsilon')}{E_\mathrm{F}-\epsilon'+i\delta}$ with the number Cu atoms also reproduces the non-monotonic trend of q observed in the experiments., Fig. 6.13 (b). Figure 6.14 (c) shows that the p_z-projected LDOS at the Co site, N_{p_z}, exhibits an unoccupied state resonance and its evolution with the number of Cu atoms. The resonances appear as peaks in the calculated N_{p_z} whose energies show the same monotonic behavior as in the experiment, Fig. 6.11 (g).

This trend in N_{p_z} is representative for all contributions to $N(E)$. Upon adding more Cu atoms to the cluster spectral weight and resonance energies are shifted to lower energies. Like N_{p_z} the other Co p orbitals have their main spectral weight above E_F, whereas N_s has its main peaks below E_F, which is characteristic for transition metals. Consequently, there is an decrease (increase) of N_s (N_p) at E_F with increasing cluster size. When these contributions to $N(E_\mathrm{F})$ are almost balanced but non-uniform, a non-monotonic dependence of $N(E_\mathrm{F})$ on the cluster size occurs, as is the case here. The details of the non-monotonic behavior are related to the specific nature of cluster resonances and chemical bonds in the system. The Fermi level of Cu lies in the region of non-bonding sp states. This region is characterized by numerous cluster resonances lying close in energy and being therefore very sensitive to changes of the environment. While non-monotonic variation of $N(E_\mathrm{F})$ with cluster size is likely to occur, predicting its detailed behavior requires accounting for the full geometry of the clusters.

In summary, we have shown in this section that the Kondo effect in clusters depends crucially on their detailed geometric structure. Atom by atom manipulation changes the local density of conduction electron states at the magnetic site and thus varies the Kondo temperature in rather broad limits.

[11] The same non-monotonic variation of $N(E_\mathrm{F})$ is obtained in LDA and in spin-polarized GGA calculations with *a posteriori* spin averaging.

6.5 Co on graphene

Graphene differs from usual metals or semiconductors in three important aspects: It is a truly two-dimensional material [7] with the charge carriers resembling massless Dirac fermions [81, 82, 11] and the chemical potential being tunable by gate voltages [7].

Recently, scanning tunneling spectroscopy experiments of graphene opened the exciting possibility to address its electronic properties locally and to study the interaction of graphene with magnetic ad-atoms. For single Co atoms adsorbed on heavily doped graphene, the observation of Kondo resonances with Kondo temperatures of the order of $T_K = 15K$ has been reported [196]. Theoretically, Kondo physics in "Dirac materials" defined as class of materials with low energy Dirac type excitations has been first addressed in the context of high Tc superconductors [197, 198, 199, 200, 93]. It has been demonstrated that even in the undoped case a Kondo effect can exist above a certain critical coupling between the impurity spin and the Dirac electrons [197, 198].

The dependence of the critical coupling, Kondo temperatures and impurity spectral functions on doping and localized impurity states has been studied in terms of theoretical model systems like single orbital Anderson models or SU(2) Kondo models [201, 202, 203, 204, 205, 206]. All these studies ignored, however, the importance of orbital physics for the Kondo effect of magnetic ad-atoms on graphene. It arises because localized spins in magnetic ions occur almost exclusively in partially filled d or f shells. For graphene the same two-dimensional representations of the hexagonal C_{6v} symmetry group, that determines the orbital degeneracies of ad-atoms in high-symmetry locations, is also responsible for the band degeneracies in graphene at the two Dirac points. Accordingly, the spin of an ad-atom in the center of a carbon hexagon can only couple efficiently by superexchange to graphene bands close to the Dirac point, if it is localized in orbitally degenerate levels. Therefore, the orbital degree of freedom and also spin-orbit coupling can be naturally expected to govern the Kondo physics in graphene. In general one can expect that correlation effects will entangle fluctuating orbital [18] and spin degrees of freedoms. This can lead to an SU(4) Kondo effect [207, 208].

In the next subsections, we show that symmetry and orbital selection rules govern not only the coupling to the graphene bands close to the Dirac points but also to high-energy van-Hove singularities. We find that virtual high-energy fluctuations control the size of the Kondo temperature, and, in turn, can lead to a strongly asymmetric gate-voltage dependence of T_K, that would be characteristic for a specific set of orbitals. First, we investigate the adsorption of Co ad-atoms on graphene by means of DFT (section 6.5.1). In section 6.5.2, we develop a *first-principles* based model describing the Kondo physics of Co on graphene. Finally, we predict desinct signatures of the Kondo resonances due to Co on graphene in scanning tunneling experiments.

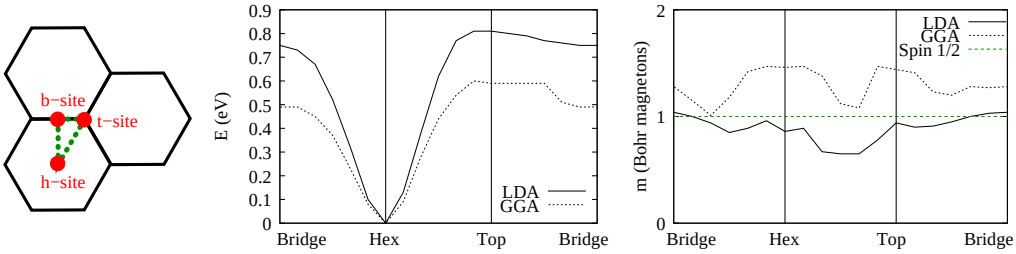

Figure 6.15: Left: Schematic illustration high symmetry adsorption sites for Co ad-atoms on graphene (red) and paths connecting these sites (green). Middle: Total energy, E, of graphene with a Co ad-atom as function of the Co position along the path depicted in the left panel. Energies obtained with GGA and LDA are shown. The energy for Co at an h-site is defined as $E = 0$. Right: Total magnetic moment of the graphene supercell with adsorbed Co as function of the Co position.

6.5.1 Adsorption geometries and magnetic states

For an ab-initio description of Co on graphene we performed DFT calculations on 3×3, 4×4, 5×5 and 6×6 graphene supercells containing one Co ad-atom using the Vienna Ab Initio Simulation Package (VASP) [48] with the projector augmented wave (PAW) [52, 53] basis sets. To judge the role of on-site Coulomb interactions, we employed a generalized gradient approximation functional (GGA) [42] as well as GGA+U with $U = 2\,\text{eV}$, $J = 0.9\,\text{eV}$ and $U = 4\,\text{eV}$, $J = 0.9\,\text{eV}$. In addition, LDA calculations were performed. The calculations were done with plane wave cut-offs 800 eV and 928 eV for the GGA and LDA functionals, respectively. We obtained fully relaxed structures for all of these functionals with the forces acting on each atom less than $0.02\,\text{eV}\text{Å}^{-1}$.

To judge which adsorption geometries are possible, we firstly relaxed Co ad-atoms adsorbed to high-symmetry sites the graphene lattice: Co above the center of a hexagon (h-site), Co on top of a C-atom (t-site) and above a bridge site (b-site). Using a 4×4 graphene supercell, 100 meV first order Methfessel-Paxton smearing and a 3×3 k-mesh for sampling the supercell Brillouin zone, we calculated to total-energy and the total magnetic moment of the supercell for the Co atom being moved along the path connecting the relaxed adsorption geometries[12].

As can be seen from Fig. 6.15, LDA as well as GGA predict Co adsorbing to a h-site with t-site or b-site adsorption being $\gtrsim 0.5\,\text{eV}$ higher in energy. In all cases, the electronic configuration of Co close to spin $S = 1/2$. These results are in agreement with prior studies published in Ref. [209]. Moreover, our results suggest that neither t-site nor b-site adsorption gives rise to metastable structures that are separated from the h-site total energy minimum by a significant energy barrier.

The h-site adsorption geometry is C_{6v} symmetric, which leads to degener-

[12]The paths were obtained by linearly interpolating between the relaxed adsorption geometries and using 5 images in between each of the relaxed geometries.

	Energy (eV)		
U (eV)	h-site	t-site	b-site
0.0	0.00	0.60	0.47
2.0	0.00	0.04	0.23
4.0	0.00	-0.22	-0.08

	magnetic moment (μ_B)		
U (eV)	h-site	t-site	b-site
0.0	1.11	1.25	1.23
2.0	1.18	1.94	1.55
4.0	1.93	1.95	1.97

Table 6.2: Left: Total energy in eV of relaxed structures with Co at different adsorption sites as function of on-site Coulomb repulsion U. For each value of U, the energy for Co at an h-site is defined as $E = 0$. Right: Magnetic moment in μ_B of Co $3d$ electrons as function of U and adsorption site.

ate states in the vicinity of the Fermi level (see below). This naturally rises the question of the stability against Jahn-Teller distortions. Such distortions are suppressed: Small displacements of the Co ad-atom from its symmetric adsorption site do not change the crystal field the Co orbitals at the Fermi level and their hybridization for with the low energy graphene bands to linear order. Also assymmetric out-of plane motions of the adjacent C-atoms lifting the C_{6v} symmetry did not yield any energy gain in our GGA calculations.

In GGA+U, the potential energy landscape for Co appears much more complicated. The GGA+U functional has various almost isoenergetic self-consistent solutions at the same adsorption site which makes optaining a transition path as for the GGA calculations highly error-prone and computationally inefficient. Therefore, we obtained fully relaxed geometries for Co at h-, t- and b-sites and analysed the forces for small displacements from the relaxed positions: For $U = 2\,\text{eV}$, $J = 0.9\,\text{eV}$ h-site adsorption is still the global total energy minimum with the Co $3d$ electrons giving rise either to spin $S_d = 1/2$ or spin $S_d = 1$. At this value of U, there exists also a metastable configuration for Co at a t-site with $3d$ electron spin $S_d = 1$, which is 0.04 eV higher in energy than the $S_d = 1/2$ h-site configuration. In the $S_d = 1$ t-site configuration, an additional unpaired electron mainly localized in the Co $4s$-orbital an contributing another spin $1/2$ occurs, such that the total Co spin is $S = 3/2$. For $U = 4\,\text{eV}$, $J = 0.9\,\text{eV}$ the global minimum energy is found for Co with $S = 3/2$ on a t-site, which is 0.2 eV and 0.08 eV lower in energy than the h- and b-sites, respectively. These results are summarized in table 6.2. While pure GGA or LDA strongly suggests Co adsorbing to h-sites in a spin $1/2$ state, from GGA+U both h-site as well as a t-site adsorption in low or high spin-configurations appear possible. In the following we discuss the electronic structure and discuss the possibility of a Kondo effect for all relevant cases: first $S = 3/2$ on the t-site, then $S_d = 1$ on the h-site and, finally, $S_d = 1/2$ on the h-site as the most interesting case.

6.5.2 Kondo models from first-principles

To understand the electronic structure of Co adsorbed to h- and t-sites on graphene, we consider the LDOS obtained from GGA+U with $U = 2\,\text{eV}$, $J = 0.9\,\text{eV}$ in these adsorption geometries and discuss the effect of spin-orbit coupling

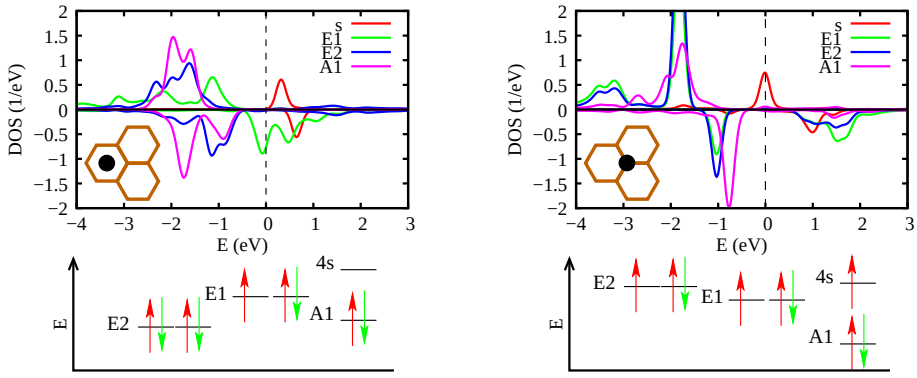

Figure 6.16: Upper panel: Orbitally resolved spin-polarized local density of states (LDOS) for a Co ad-atom at an h-site (left) and a t-site (right) for $U = 2\,\text{eV}$ and $J = 0.9\,\text{eV}$. At the h-site, Co has spin 1/2 due to one hole in the 3*d*-orbitals with E1 symmetry (d_{xz}, d_{yz}). For Co on a t-site we find spin 3/2 due to two holes in the Co 3*d*-orbitals and one electron in the Co 4*s*-orbital. Lower panel: Energy level diagrams of Co at a graphene h-site (left) and a t-site (right).

(SOC).

For Co adsorbed on a t-site the crystal fields have C_{3v} symmetry: the 5 Co *d*-orbitals split into two orbital doublets corresponding to the two-dimensional representation (E) of C_{3v} and a singlet of the one-dimensional representation (A1). As can be seen from the LDOS (Fig. 6.16), the spin 3/2 of the Co atom is made up by a spin 1 residing in the Co 3*d*-orbitals of E symmetry ferromagnetically coupled to a spin 1/2 mainly from the Co 4*s*-orbital. The four low-energy graphene bands close to the Dirac points can also be decomposed into one two-dimensional and two one-dimensional representations which hybridize efficiently with the E and A1 orbitals, respectively. In the absence of spin-orbit coupling (SOC) one can, therefore, expect a two-stage Kondo effect: first, the direct coupling of the s-orbital to the C atom beneath quenches 1/2 of $S = 3/2$ resulting in a spin 1 coupling to the two bands of E symmetry via the next-nearest C atoms which screen the remaining spin in a second stage.

To estimate the strength of SOC in this configuration, we calculate the magnetic anisotropy, $E_{\text{MAE}} = E_{\parallel} - E_{\perp} \approx 1.0\,\text{meV}$, as the energy difference between magnetization parallel and perpendicular to the graphene plane in GGA+U with $U = 4.0\,\text{eV}$ and $J = 0.9\,\text{eV}$.[13] This translates into different energies, $E_{|S_z|=1/2} - E_{|S_z|=3/2} \approx 1.3\,\text{meV}$, depending on the z-component, S_z, of the Co spin $S = 3/2$ in this configuration. Ignoring Kondo physics, the ground state has $|S_z| = 3/2$ and exhibits Kramers degeneracy but spin flips $S_z = 3/2 \rightarrow S_z = -3/2$ induced by conduction electron scattering are only possible in higher order processes. Hence, the Kondo effect is efficiently suppressed for Co in this configu-

[13] These calculations were done with a 3×3 graphene supercell, which has been fully relaxed for Co at a t-site in a spin-collinear GGA+U calculation with $U = 4.0\,\text{eV}$ and $J = 0.9\,\text{eV}$. The magnetic anisotropy has been calculated by constraining the direction of magnetization at the Co site but allowing for all other electronic degrees of freedom to relax to a self-consistent solution.

ration, as soon as $T_K \ll 1.3\,\text{meV} \approx 15\,\text{K}$. For a (first stage) Kondo temperature of the order of 15 K or above a definite determination of the relevant low-energy model is very difficult, but a possible scenario is that first the Kondo effect partially screens $1/2$ out of $S = 3/2$, then spin-orbit coupling stabilizes a low energy doublet ($S_z = \pm 1$), which is finally screened at very low temperatures by an anisotropic Kondo effect.

For Co at an h-site, the situation is more interesting and a quantitative analysis easier: here, the crystal fields have C_{6v} symmetry and decompose the d-orbitals into two non-equivalent two-dimensional irreducible representations E1 (d_{xz}, d_{yz}) and E2 ($d_{x^2-y^2}$, d_{xy}) plus one one-dimensional representation A1 ($d_{3z^2-r^2}$). For both the $S_d = 1/2$ and the $S_d = 1$ configuration, the spin degree mainly resides in the E1 orbitals, as shown for $S_d = 1/2$ in Fig. 6.16. The Co 4*s*-orbital is unoccupied in this configuration. To estimate the strength of the SOC for the Co 3*d* electrons in this configuration, we extract the coupling constant λ occuring in the single particle SOC operator $H_{\text{SOC}} \approx \lambda \mathbf{l} \cdot \mathbf{s}$, with $\mathbf{l}$ and $\mathbf{s}$ being the orbital and spin angular momentum operators, respectively, from VASP. With the self-consistent GGA charge density we obtain $\lambda = 60\,\text{meV}$.

Moreover, in the GGA calculations we obtained the crystal field splitting from the d-level energies as $\epsilon_{E2} - \epsilon_{E1} = -0.8\,\text{eV}$ and $\epsilon_{A1} - \epsilon_{E1} = -0.56\,\text{eV}$ for Co at the h-site. Diagonalizing the 3*d* subspace of the Co atom with $S_d = 1$ in d^8 configuration in this crystal field yields a singlet as the ground state, which is separated by about $0.008\,\text{eV} \approx 90\,\text{K}$ from a doublet of first excited states. Hence, for a high-spin Co at an h-position an $S_d = 1$ Kondo effect is quenched if $T_K \lesssim 90\,\text{K}$ and a much lower T_K [196] is only consistent with the low-spin configuration.

For Co at an h-site with $S = 1/2$ in d^9 configuration (see Fig. 6.16) one obtains a four-fold degenerate state. SOC lifts this degeneracy, resulting in a twice degenerate atomic ground state, which is separated from a doublet of excited states by an energy of the order of λ. In this more than half-filled regime, the spin- and orbital moment are aligned in parallel (c.f. Hund's 3rd rule). The d-hole resides in the highest crystal field orbitals, $E1$, which have $|l_z| = 1$. Hence, the Zeeman splitting for out-of-plane magnetic fields, B_z, is $\Delta E = \mu_B B_z (g_l s_z + g_l l_z)/\hbar = \pm \mu_B 2 B_z$ resulting in the effective g-factor of $g|s_z|/\hbar = 2$. We will see that the SOC induced lifting from four fold to two fold degeneracy will lead to SU(4) Kondo physics above the scale of λ and SU(2) Kondo physics at lower energies.

To predict the behavior of the Kondo temperatures with the gate voltage in this configuration, we describe the Co at an h-site in terms of an Anderson impurity model: The conduction electrons residing in graphene's π-bands are modeled by a tight-binding Hamiltonian of the form[14]

$$\hat{H}_0 = t \sum_{<\mathbf{i},\mathbf{j}>} c_{\mathbf{i}}^\dagger c_{\mathbf{j}} + t' \sum_{\ll\mathbf{i},\mathbf{j}\gg} c_{\mathbf{i}}^\dagger c_{\mathbf{j}} + t'' \sum_{\lll\mathbf{i},\mathbf{j}\ggg} c_{\mathbf{i}}^\dagger c_{\mathbf{j}} \tag{6.61}$$

[14] To obtain the correct energies of both π-band van-Hove singularities and the correct slope of the π-bands close to the Dirac points we go beyond the nearest neighbor tight-binding model introduced in section 3.1, Eqs. (3.1) and (3.2), and consider up to third nearest neighbor hopping as suggested in Ref. [73].

with $t = -2.97\,\mathrm{eV}$, $t' = -0.073\,\mathrm{eV}$, and $t'' = -0.33\,\mathrm{eV}$ quantifying the nearest, next-nearest and next-to-next nearest neighbor hopping, respectively [73]. Here, $c_{\mathbf{i}}$ denotes the Fermi operator for an electron in the carbon p_z orbital at site $\mathbf{i}$, where the index $\mathbf{i} = (i, A/B)$ labels the sublattice (A,B) and the unit cell, i, centered at R_i. In analogy to Eq. (3.2), Fourier transformation, $c_{\mathbf{i}} = \sum_i e^{ikR_i}(c_{k,A}, c_{k,B})^T \equiv \sum_i e^{ikR_i} c_{\mathbf{k}}$ leads to $\hat{H}_0 = \int \mathrm{d}k\, c^\dagger_{\mathbf{k}} H_k c_{\mathbf{k}}$ with

$$H_k = \begin{pmatrix} \eta(k) & \xi(k) \\ \xi^*(k) & \eta(k) \end{pmatrix}, \tag{6.62}$$

where $\xi(k) = t\sum_{j=1}^3 e^{ik(b_j - b_1)} + t''\sum_{j=1}^3 e^{ik(b''_j - b_1)}$ and $\eta(k) = t\sum_{j=1}^6 e^{ikb'_j}$ with b_j, b'_j and b''_j denoting vectors, which connect nearest, next-to-nearest and third nearest neighbors in the graphene lattice, respectively.

For the Co atom, we consider its $3d$-orbitals, $\hat{H}_{\mathrm{at}} = \sum_{m,\sigma} \epsilon_{|m|} n_{m,\sigma} + \frac{U}{2}\sum_{(m,\sigma)\neq(m',\sigma')} n_{m,\sigma} n_{m',\sigma'}$ with $n_{m,\sigma} = d^\dagger_{m,\sigma} d_{m,\sigma}$, where m is the quantum number of the z-component of the orbital momentum, $d_{m,\sigma}$ are Fermi operators, U is the local Coulomb repulsion and $\epsilon_{|m|}$ are the bare on-site energies. Here, we include hopping from the localized d-orbital to the nearest-neighbor C-atoms and use the C_{6v} symmetry to write the coupling of Co to graphene in the form

$$\hat{V} = \sum_{m,\sigma} V_{|m|} c^\dagger_{m,\sigma} d_{m,\sigma} + \mathrm{H.c.}, \tag{6.63}$$

where $c_{m,\sigma} = \sum_{<\mathbf{j}>} e^{im\phi_{\mathbf{j}}} c_{\mathbf{j},\sigma}/\sqrt{6}$, $c_{\mathbf{j},\sigma}$ is the Fermi operator of electrons at carbon atom at site $\mathbf{j}$ and $\phi_{\mathbf{j}}$ is the angle between a fixed crystalline axis and the bond from site $\mathbf{j}$ to the Co impurity.

As explained in section 6.1, all local physics is contained in the local Hamiltonian, $\hat{H}_{\mathrm{at}}$, and the hybridization function $\Delta_{mm'}(\omega)$ defined in Eq. (6.3). Here, we have $\Delta_{mm'}(i\omega) = V_{|m|} G^0_{mm'}(i\omega) V_{|m'|}$, where

$$G^0_{mm'}(i\omega) = \int \mathrm{d}k \langle m|\mathbf{k}\rangle (i\omega - H_k)^{-1} \langle \mathbf{k}|m'\rangle \tag{6.64}$$

is the bare graphene electron Green function of the states c_m. $\Delta_{mm'}(i\omega) = \Delta_m(i\omega)\delta_{mm'}$ is diagonal and $\Delta_m(i\omega) = \Delta_{-m}(i\omega)$ by symmetry.

The hybridization functions for different values of $|m| = 0, 1, 2$ are subject to selection rules imposed by the matrix elements $\langle m|\mathbf{k}\rangle$: The eigenstates of $\hat{H}_0$ close to the Dirac points, K and $K' = -K$, transform according to E1 and E2 under C_{6v} with the E1 and E2 being degenerate at the Dirac point. Hence, hybridization with $m = 0$ states is cubically suppressed, $\mathrm{Im}\,\Delta_{m=0}(\omega) \sim |\omega|^3$ and

$$\mathrm{Im}\,\Delta_{|m|=1}(\omega)/V_1^2 = \mathrm{Im}\,\Delta_{|m|=2}(\omega)/V_2^2 \approx -\pi \frac{\sqrt{3}|\omega|}{2\pi(t-2t'')^2} \tag{6.65}$$

to leading order in ω.

In contrast to the particle hole symmetry for $\omega \to 0$, the hybridization functions are largely asymmetric at higher energies. This is caused by the E1 and the

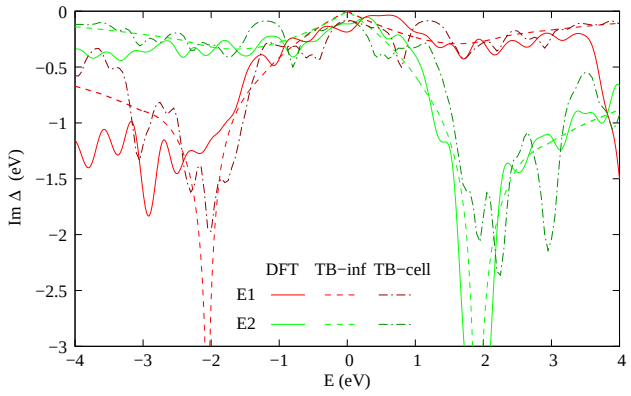

Figure 6.17: Imaginary part, $\mathrm{Im}\,\Delta_{|m|}(E)$, of the hybridization functions of the E1 ($|m| = 1$) and E2 orbitals ($|m| = 2$) of a Co ad-atom adsorbed to a graphene h-site. Hybridization functions obtained from DFT and tight-binding (TB) models of one Co on an infinite graphene sheet (TB-inf) as well as the same supercell (TB-cell) as used in DFT with $V_1 = 1.4\,\mathrm{eV}$ and $V_2 = 1.5\,\mathrm{eV}$ are shown.

E2 impurity orbitals coupling each to only one of the van-Hove singularities resulting from the graphene bands at the Brillouin zone M point: The E1 impurity orbitals as well as the graphene valence electron wave functions at the M point are odd under 180° rotation about the h-site, whereas the E2 orbitals and conduction electron wave functions at the M point are even under this transformation. Hence, the E1 hybridization exhibits a logarithmic singularity,

$$\Delta_1(\omega) \sim \ln|\omega - E_{M-}|, \tag{6.66}$$

at $E_{M-} = t + t' - 3t'' \approx -2.1\,\mathrm{eV}$. However, there is no singularity in the E1 hybridization at the energy of the conduction band van-Hove singularity, $E_{M+} = -t + t' + 3t'' \approx 1.9\,\mathrm{eV}$. For the E2 orbitals, the situation is reversed:

$$\Delta_2(\omega) \sim \ln|\omega - E_{M+}| \tag{6.67}$$

for $\omega \to E_{M+}$.

To obtain realistic hybridization strengths, V_1 and V_2, we calculate Δ_m by means of DFT as described in appendix A and fit the tight-binding hybridizations via V_1 and V_2 (see Fig. 6.17). The tight-binding (TB) hybridizations were obtained in two ways: (1) by directly evaluating Eq. (6.64), which models one Co ad-atom on an infinite graphene sheet, and (2) by employing the same 6×6 supercell as in the DFT calculations and performing the same supercell Brillouin zone integration.

The high energy particle-hole / E1-E2 asymmetry is striking the DFT as well as in both TB hybridization functions. The DFT hybridization functions display small wiggles and the van-Hove singularities appear to be smeared out. Comparison of the DFT hybridization to the TB supercell hybridization shows that these two effects are supercell artifacts. The tight-binding curves can be well fitted to

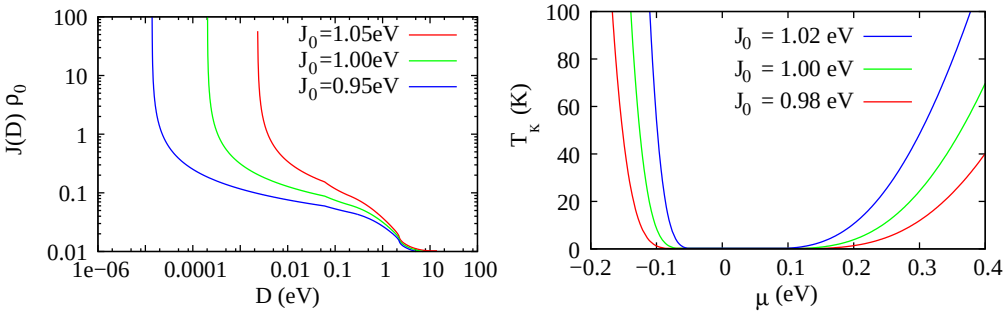

Figure 6.18: Left: Renormalized effective coupling strength, $J(D)\frac{\rho(\mu-D)+\rho(\mu+D)}{2} \equiv J(D)\rho_0$, as function of the high energy cut-off D for the chemical potential $\mu = 0.20\,\text{eV}$ and three different bare couplings $J_0 = 1.05$, 1.00, and 0.95 eV. Right: Kondo temperatures T_K as function of μ for $J_0 = 1.02$, 1.00, and 0.98 eV. The Kondo temperatures are remarkably asymmetric for electron and hole doped graphene.

DFT[15] with $V_1 = 1.4\,\text{eV}$ and $V_2 = 1.5\,\text{eV}$. For energies above 3.4 eV and below $-3.1\,\text{eV}$ also further bands contribute to $\Delta_m(\omega)$. They contribute to screening and lead to a (finite) renormalization of the exchange coupling which we absorb in a redefinition of the bare exchange coupling J_0 used below.

To estimate Kondo temperatures and their gate voltage dependence, we solve the scaling equation[16] [27, 210]

$$\frac{\mathrm{d}J(D)}{\mathrm{d}D} = -N(D)J^2(D)\frac{\rho(\mu-D)+\rho(\mu+D)}{2D}, \tag{6.68}$$

where $J(D)$ is the renormalized exchange coupling, D is the high energy cut-off, μ is the chemical potential in graphene and $\rho(\omega) = -\mathrm{Im}\Delta_1(\omega)/(\pi V_1^2)$. The degeneracy factor, $N(D) = 4$ for $D > \lambda$ and $N(D) = 2$ else [210], accounts for locking the orbital- to the spin-degree of freedom below the energy scale of the spin-orbit coupling.

Varying J_0 for $\mu = 0.2\,\text{eV}$ (as in the experiment reported in Ref.[196]), we find the Kondo temperature[17] changing by an order of magnitude for varying J_0 within a few percent. (See Fig. 6.18 left.) While this hinders predictions of the absolute value of the Kondo temperature, the trend of how the Kondo temperature depends on the chemical potential in graphene is robust w.r.t. changes in J_0: Leaving J_0 as fitting parameter, we predict the gate voltage-dependence of T_K as shown in Fig. 6.18 right.

Note that the used values for $J_0 \approx 1\text{eV}$ are of order V_1^2/U for realistic values of V_1 and U. The remarkable asymmetry of the hybridization function leads to a

[15] Note that only *one* fitting parameter is employed per curve. Including an on-site potential at the adjacent C-atoms allows to bring even the energy positions of the wiggles in the TB supercell and the DFT hybridization functions into agreement. Here, we focus on qualitative consequences of the particle hole asymmetry in the hybridization function and do not include a second fitting parameter.

[16] This scaling analysis has been contributed by A. Rosch (University of Cologne).

[17] We extract the Kondo temperatures, T_K, from the scaling analysis, as value of the high energy cut-off $D = k_B T_K$, where $J(D)$ diverges.

highly asymmetric dependence of the Kondo temperatures on the gate voltages. If the E2 orbitals were carrying the magnetic moment instead of E1 this asymmetry would be reversed.

Interestingly, for $J > J_c \approx 1.1\,\mathrm{eV}$ we find that the Kondo effect persists even for vanishing doping. This implies that by relative small changes (e.g. using different substrates) it may be possible to realize the quantum critical point of the pseudogap Kondo problem [197, 198, 93, 199, 200].

6.5.3 Fourier transformed STM and Fano lineshapes

We will now discuss how the symmetry of Co orbital carrying the magnetic moment can be probed by FT-STS. Afterwards, we explain how the Fano asymmetry factor arising in STS of Kondo resonances is affacted by the special electronic structure and the particular symmetries of Co at an h-site on graphene.

In the simplest model (see e.g. [88]), FT-STS measures the Fourier transform of the local density of states, $|\rho_k(E)|$, in the vicinity of an impurity with the constant background of a clean sample being substracted:

$$\rho_k(E) = -\frac{1}{\pi}\int \mathrm{d}^2 r e^{ikr}\,\mathrm{Im}\,(G(r,r,E) - G^0(r,r,E)). \tag{6.69}$$

Using the T-matrix formalism as in section 5.1.1 in the discrete position space representation of section 5.1.2 and representing the carbon p_z orbitals by δ-functions in real space, Eq. (6.69) simplifies to

$$\rho_k(E) = -\frac{1}{\pi}\sum_j \int \mathrm{d}^2 k' e^{ikr_j}\frac{1}{i}\left[\delta G_{k',k'+k}(E) - \delta G^*_{k'+k,k'}(E)\right]_{jj}, \tag{6.70}$$

where the index j labels the two atoms per graphene unit cell, r_j their position w.r.t. the unit cell origin and the k' integral extends over the first Brillouin zone. The Green functions occuring in Eq. (6.70) are 2×2 matrices in sublattice space and obtained from the unperturbed graphene Green functions $G^0_k(E)$ with the T-matrix: $\delta G_{k',k'+k}(E) = G^0_{k'}(E)T_{k',k'+k}(E)G^0_{k'+k}(E)$.

In a resonant level model for the Kondo peak, we consider orbitals of E1 and E2 symmetry to derive the FT-STS patterns from Eq. (6.70) using a corresponding T-matrix with phase $\pi/2$. To this end, we implement Eq. (6.70) in Mathematica and use a $\sqrt{3}\times\sqrt{3}\ R30^\circ$ graphene supercell which allows us to obtain k and k' independent T matrices for h-site impurity resonances.

This leads to the Fourier transformed LDOS as depicted in Fig. 6.19. As the Kondo impurity on the h-site couples equally strong to both K and K' points, the inter-valley scattering is very strong. Due to the two sublattices, it depends however strongly on the energy E and the phase shift δ to which extent this K-K' scattering leads to FT-STS intensity at the K and K' points. As Fig. 6.19 shows, there is a double arc structure of intensity around K / K' for $E = 0.4\,\mathrm{eV}$ with the radius given by twice the Fermi wave vector. These structures disappear for $E \to 0$. The orbital symmetries manifest in distinct FT-STS maps with characteristic

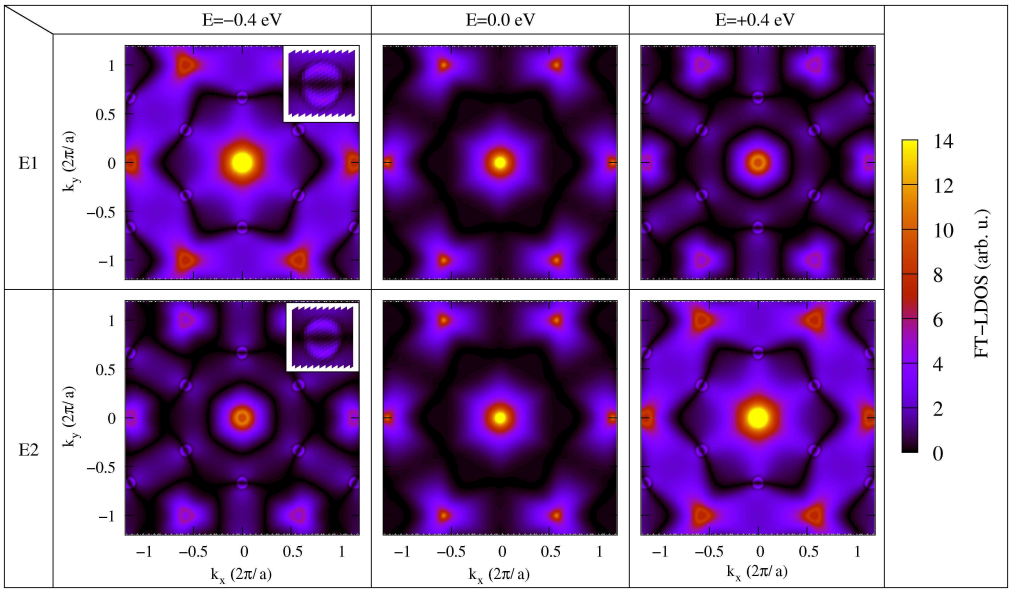

Figure 6.19: Fourier transformed LDOS for resonances of E1 (upper panel) and E2 symmetry (lower panel) at energies $E = -0.4,\ 0.0$, and $0.4\,\mathrm{eV}$ for a phase $\pi/2$ of the T-matrix at these energies. The reciprocal lattice vectors are $(2/\sqrt{3}, 0)$ and $(1/\sqrt{3}, 1)$ in units of $2\pi/a$, where $a = 2.465$Å is the lattice constant. The bright spots close to the panel boundaries are centers of higher Brillouin zones. The insets show close-up views of the K/K' points which are at symmetry equivalent positions of $(0, 2/3)$.

gate voltage and tunneling bias dependence: Upon energy, $E \to -E$ (and phase shift reversal, $\pi/2 + \eta \to \pi/2 - \eta$) the FT-STS patterns of resonances with E2 and E1 symmetry interchange.

We now turn to the Fano q-factors arising in STS. To this end it is instructive, to compare Fano factors arising at impurity resonances in graphene to the case of normal metal hosts. The magnetic orbitals of the ad-atom are usually strongly localized resulting in the direct tunneling of electrons from the impurity orbtials to the tip being much weaker than tunneling via the substrate: $|M_{pm}| \ll |M_{pk}|$ in Eq. (6.48) and $|M_{pm}| \ll |M_0 V_0 \bar{G}_{\mathrm{KS}}|$ in Eq. (6.56). Negelcting, thus, direct tunneling from the impurity to the tip, Eq. (6.56) simplifies to

$$q \approx -\mathrm{Re}\, G(E_\mathrm{F})/\mathrm{Im}\, G(E_\mathrm{F}). \tag{6.71}$$

In a metal with bandwidth D and constant DOS in the vicinity of the impurity[18], $\mathrm{Im}\, G(\epsilon) = -\pi/2D$ if $-D < \epsilon < D$, we obtain $q \approx \frac{1}{\pi} \ln \left| \frac{D+E_\mathrm{F}}{D-E_\mathrm{F}} \right| \approx \frac{2E_\mathrm{F}}{\pi D}$. Hence, $|q| < 1$ and the Kondo effect manifests in STM on normal metals as anti-resonance close to E_F as long as $|M_{dt}| \ll |M_{kt}|$.

This is very different for graphene: The graphene DOS is linear and in the simplest model given by $N_0^\mathrm{g}(E) = \frac{|E|}{D^2} \cdot \Theta(D - |E|)$ resulting $G(E) = \frac{E}{D^2} \ln \left| \frac{E^2}{D^2 - E^2} \right| -$

[18] See also section 5.1.1 and Fig. 5.1 for the model Green functions of simple metals and graphene discussed, here.

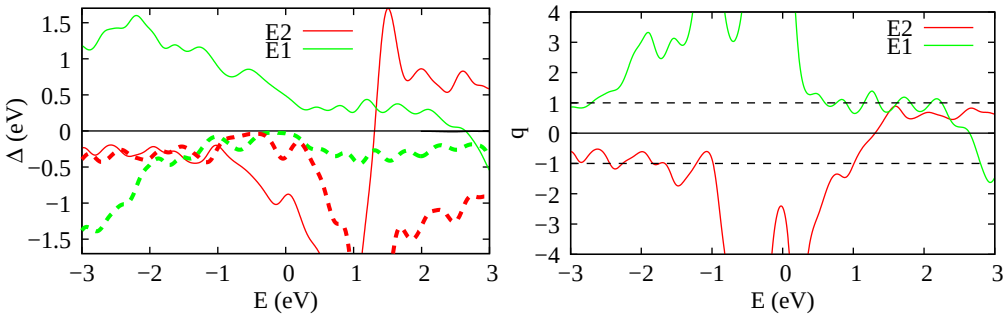

Figure 6.20: Hybridization functions, Δ, (left) and Fano asymmetry factors, q, (right) for Co on graphene as obtained from our first principles calculations. The q-factors have been calculated from the hybridization functions using Eq. (6.57). For the hybridization functions $\mathrm{Re}\,\Delta$ is plotted as solid line, $\mathrm{Im}\,\Delta$ dashed. The energy $E = 0$ corresponds to the Fermi level of the charge neutral supercell.

$i\pi N_0^{\mathrm{g}}(E)$ and

$$q \approx \frac{2\,\mathrm{sign}\,(E_F)}{\pi} \ln\left|\frac{E_{\mathrm{F}}}{D}\right|. \tag{6.72}$$

This result follows directly from linearity of $N_0^{\mathrm{g}}(E)$ and the Kramers-Kronig relations. As $D \approx 6\,\mathrm{eV}$[19] and usually $E_{\mathrm{F}} \lesssim 0.5\,\mathrm{eV}$, the q-factor can be $q \gg 1$ and the Kondo effect may manifest in STM as *resonance* instead of an anti-resonance, even for $|M_{dt}| \ll |M_{kt}|$. This is in contrast to a normal metal, where predominant tunneling into the conduction electron states results in a Kondo-antiresonance in STM.

As the real part of the Green function enters Eq. (6.71), the q-factor carries information about high energy features of the local electronic structure which is in general beyond effective low energy theories. To understand the role of such contributions to the q-factor, we illustrate the situation for the experimentally important case of Co on graphene. We assume Co adsorption to an h-site. Using the hybridization functions obtained from DFT and Eq. (6.57), we simulate the q-factor for E1 and E2 type resoances.

As Fig. 6.20 shows, we have $|\mathrm{Im}\,\Delta(\epsilon)| \ll |\mathrm{Re}\,\Delta(\epsilon)|$ in the vicinity of the Fermi level of the charge neutral supercell, $E = 0$. As a consequence, one obtains $q > 1$ in a wide energy rage and q is strongly energy dependent. So, q is expected to be strongly sensitive to local changes in the chemical potential of graphene, which can be caused by gate voltages, chemical doping or substrate effects. Apart from $|q| \gg 1$ for $E \to 0$, we find the q-factor for resonances with E1 and E2 symmetry displaying markedly different and asymmetric energy dependences. The orgin of these asymmetric q-factors is the same as for the asymmetric Kondo temperatures: States of E1 symmetry couple to the valence band van-Hove singularity but not to the conduction band van-Hove singularity, whereas for the E2 type impurity states the situation is reversed. All these effects are well beyond a Dirac type linearized

[19] Assuming linear dispersion in the entire Brillouin zone and approximating the Brillouin zone by circles around the two nonequivalent Dirac points results in $D \approx 6\,\mathrm{eV}$ [92].

dispersion analysis.

In summary, we showed in the last three subsections that the Kondo effect of Co ad-atoms on graphene is controlled by the particular symmetries of the Co 3*d*-orbitals originating from graphene crystal field splitting. Based on first-principles calculations we found different possible scenarios with *t*− or *h*-site adsorption of Co and consequences for the Kondo physics. For Co at an *h*-site we found a surprising asymmetry of Kondo temperatures and Fano q-factors w.r.t. the chemical potential and predicted characteristic FT-STS patterns. All these effects can be probed by STM.

Chapter 7

Summary and Outlook

In this thesis we investigated the electronic properties of different nano scale solid state systems, in particular graphene and magnetic nanostructures on surfaces. Graphene differs from usual metal or semiconductor surfaces in that its low energy electronic quasiparticles are entirely located in the Brillouin zone corners with band degeneracies being enforced by the high symmetries of the honeycomb lattice. We found that this specialty, presents a common background for huge inelastic contributions to STS of clean graphene and an orbitally controlled Kondo effect of Co ad-atoms on graphene.

Zone corner phonons can couple the low energy electronic states states from K/K' to high energy states from the Brillouin zone center and circumvent the so-called momentum space selection rule for tunnelling into graphene. There are two different phonons with energy $\hbar\omega = 67$ meV and 151 meV which may by symmetry assist electron tunneling into graphene. Our density functional calculations showed that the inelastic tunneling channel due to the 67 meV phonon is by a factor of ~ 15 more efficient than the 151 meV channel. This is in good accordance with recent experiments [117] and allowed to disentangle different many body contributions to graphene's electronic structure by means of STS.

For Co ad-atoms adsorbed to the center of a graphene hexagon, the same two-dimensional representations of the hexagonal symmetry group, that are responsible for the band degeneracies in graphene, also determine the orbital degeneracies of the ad-atoms. Hence, efficient superexchange coupling of the ad-atom spin to the graphene bands, requires it to reside in degenerate orbitals. This notion leads to the general prediction that orbital fluctuations and also spin-orbit coupling naturally control the Kondo physics of any magnetic ad-atom adsorbing to a high symmetry position on graphene. For case of Co on graphene, we find that the interplay of the orbital Co physics and the peculiar band-structure of graphene leads to a gate-voltage dependence of the Kondo temperature, of the Fano q-factor and of the FT-STS patterns displaying a very strong, characteristic particle-hole asymmetry. This will allow to probe experimentally, which orbitals are involved in the Kondo effect of the magnetic impurity.

The study of general inhomogeneity and impurity effects in graphene presented here revealed how graphene interacts with its environment and how midgap

states that likely present important sources of electron scattering can be created. Investigating the electronic properties of corrugated graphene, we showed by means of first-principles calculations how rippling-induced pseudo-magnetic fields alter graphenes low-energy electronic properties and justified an extended low energy effective field theory. The formation of flat bands near the Fermi level corresponding to pseudo-Landau levels has been confirmed for quenched ripples but relaxation of in-plane strains turned out to destroy these states. This may be an important statement in light of the hypothesis [123] that quenched ripples are a major source of scattering in graphene and the observation that annealing of a freely hanged graphene membrane can increase drastically its mobility [12]. However, this issue is still speculative and there is yet no real theory that explains why ripple structures should become quenched. Further investigations are needed on this question. An alternative source of midgap states can be resonant impurities. Our studies of monovalent impurities showed, that these impurities frequently cause quasilocal states nearby the Dirac point — not accidentally but enforced by symmetry. These chiral midgap states are often accompanied by high migration barriers of the impurities, which makes these impurities very stable and lets them appear as a very natural source of electron scattering in graphene. When studying doping mechanisms for gas molecule adsorbates on graphene, inert and open shell adsorbates turned out to be fundamentally different: While open-shell species like NO_2 appear to accept electrons directly from graphene, doping effects due to inert molecules like H_2O require additional reservoirs for electrons or holes like the substrate, for example.

The magnetic nanostructures investigated in the last part of this thesis demonstrated how sensitive magnetic atoms are to their particular environment. For isolated Ce atoms on different surfaces, we found the $4f$ electrons showing all the range from localized to delocalized behavior and pronounced changes in the spectral function with the substrate. A similarly high degree of tunability has been found for the $CoCu_n$ clusters on Cu (111) surfaces, where atom-by-atom manipulation was proven to cause non-monotonic variations in the local electronic structure and varied the Kondo temperature in rather broad limits.

Great progress in the understanding of the electronic structure of nano scale electronic systems has been achieved during the last years but widespread applications of these systems require a theory capable of “predictive nanostructure design”. Reduced symmetries at surfaces often hinder reliable predictions, in particular if many-body phenomena at low temperatures play a decisive role. The example of Co on graphene shows that incorporating this material into the field of correlated magnetic nanosystems may change this situation due to its the well defined and highly symmetric low energy excitations. First studies exploring these possibilities are on the way.

Appendix A

LDA++ calculations using VASP

The ab-initio treatment of correlated systems (see sections 2.5.2, 2.5.3, and 6.1) requires the calculation of Green functions or hybridization functions in terms of local orbitals. Following Ref. [184], the desired quantity is a projection $\mathcal{P}^{\mathcal{C}} = \sum_L |L\rangle\langle L|$ of the full Kohn-Sham Green function $\hat{G}_{KS}(\mathrm{E})$ on a set of localized orbitals $\{|L\rangle\}$:

$$\hat{G}^{\mathcal{C}}_{KS}(\mathrm{E}) = \mathcal{P}^{\mathcal{C}}\hat{\mathrm{G}}_{\mathrm{KS}}(\mathrm{E})\mathcal{P}^{\mathcal{C}}. \tag{A.1}$$

The subspace $\mathcal{C} = \mathrm{span}(\{|L\rangle\})$ is usually termed correlated subspace. In plane wave based calculations, $\hat{G}_{\mathrm{KS}}(E)$ is available in terms of a (truncated) set of Bloch states $|K\rangle$ that are eigenstates $H_{\mathrm{KS}}|K\rangle = \epsilon_K|K\rangle$:

$$\hat{G}_{\mathrm{KS}}(E) = \sum_K \frac{|K\rangle\langle K|}{E + i0^+ - \epsilon_K}. \tag{A.2}$$

Inserting Eq. (A.2) into Eq. (A.1) shows that one needs to evaluate projectors of the type $\langle L|K\rangle$ in order to access the matrix elements $(\hat{G}^{\mathcal{C}}_{KS}(\mathrm{E}))_{\mathrm{LL}'}$ of the local Green function.

In most cases the correlated orbitals are d- or f-orbitals, which are to a good approximation localized inside the PAW augmentation spheres. Using the PAW decomposition, Eqs. (2.52) and (2.56), of the Bloch state $|K\rangle = \mathcal{T}|\tilde{K}\rangle = |\tilde{K}\rangle + \sum_i(|\phi_i\rangle - |\tilde{\phi}_i\rangle)\langle\tilde{p}_i|\tilde{K}\rangle$ one obtains for a converged partial wave expansion $\langle L|K\rangle = \sum_i\langle L|\phi_i\rangle\langle\tilde{p}_i|\tilde{K}\rangle$. The index i of the augmentation functions $|\phi_i\rangle$ includes site μ, angular momentum l and m as well as an index ν labelling the radial function: $i = (\mu, l, m, \nu)$. In practice, the localized orbitals can be also chosen to be angular momentum eigenstates at a given site μ, which leads to

$$\langle L|K\rangle = \sum_\nu \langle L|\phi_\nu\rangle\langle\tilde{p}_\nu|\tilde{K}\rangle \tag{A.3}$$

with ν abbreviating $i = (\mu, l, m, \nu)$ where μ, l, and m are fixed. In the PAW approach, the first augmentation function, $\nu = 0$, for each channel is usually taken to be in atomic eigenfunction (c.f. section 2.3.3 and Ref. [52]). Defining the correlated subspace in terms of atomic eigenfunctions leads consequently to $|L\rangle = |\phi_{\nu=0}\rangle$. As higher augmentation functions, $\nu > 0$, are in general not

orthogonal to the $|\phi_{\nu=0}\rangle$ states, evaluation of Eq. (A.3), requires accounting for the overlaps of the form $\langle\phi_{\nu=0}|\phi_{\nu'}\rangle$. This approach has been implemented to the AB-INIT code by Amadon [211].

We implemented an LDA+U inspired approximation to extract local Green functions from VASP. As in the LDA+U scheme implemented in VASP [212], we choose

$$|\langle L|K\rangle|^2 = \sum_{\nu,\nu'} \langle\tilde{K}|\tilde{p}_\nu\rangle\langle\phi_\nu|\phi_{\nu'}\rangle\langle\tilde{p}_{\nu'}|\tilde{K}\rangle. \tag{A.4}$$

Hence, the absolute value of the projectors is in this scheme given by the projection onto a subspace of augmentation channels with given angular momentum, (l, m). The phase is determined by

$$\arg\left(\langle L|K\rangle\right) = \arg\left(\sum_\nu \langle\tilde{p}_\nu|\tilde{K}\rangle\right). \tag{A.5}$$

If higher augmentation channels are negligible, $|\langle\tilde{p}_{\nu=0}|\tilde{K}\rangle| \gg |\langle\tilde{p}_{\nu>0}|\tilde{K}\rangle|$, Eq. (A.3) and Eqs. (A.4)-(A.5) become equivalent and both approaches yield the same Green functions. This is usually the case for states close to the Fermi level, where the projection $\langle\tilde{p}_{\nu=0}|\tilde{K}\rangle$ presents normally the major contribution to the PAW partial wave expansion. The LDA+DMFT implementation based on the projectors from Eqs. (A.4)-(A.5) has been compared to NMTO [213, 214] and other plane wave Wannier function based LDA+DMFT implementations [215] for the test cases of $YTiO_3$ and NiO, where the results turned out to be in good accordance [216].

As constructed, the projectors in Eq. (A.3) as well as in Eqs. (A.4) and (A.5) are not properly normalized to two reasons: (1) the Bloch basis is incomplete and (2) the PAW augmentation functions are not orthonormal. In our implementation we orthonormalize the projectors by the following Wannier type construction: By definition, the localized states $|L\rangle$ are labelled by site and angular momentum indices: $L = (\mu, l, m)$. We split the site index $\mu = R + T$ such that R labels the position within the unit cell and T is the Bravais lattice vector of the unit cell in which μ is located. This allows us to construct the Bloch transform of the localized states,

$$|L_k\rangle = \sum_T e^{ikT}|L_T\rangle, \tag{A.6}$$

where k is from the first Brillouin zone and $|L_T\rangle \equiv |L\rangle = |\mu, l, m\rangle$ with $\mu = R + T$. The sum in Eq. (A.6) runs over the Bravais lattice. Labelling the Bloch states $|K\rangle = |k, n\rangle$ by their crystal momentum, k, and band index, n, we normalize the our projectors $\mathcal{P}^{\mathcal{C}}_{Ln}(k) = \langle L_k|k, n\rangle$ using the overlap operator

$$O_{LL'}(k) = \sum_n \mathcal{P}^{\mathcal{C}}_{Ln}(k)\left(\mathcal{P}^{\mathcal{C}}_{L'n}(k)\right)^* \tag{A.7}$$

in

$$\bar{\mathcal{P}}^{\mathcal{C}}_{Ln}(k) = \sum_{L'} [O(k)]^{-1/2}_{LL'}\, P^{\mathcal{C}}_{L'n}(k). \tag{A.8}$$

In many parts of this work, we use hybridization functions instead of local Green functions. These functions are related to each other by

$$G^{-1}(\epsilon) = \epsilon + i\delta - \epsilon_d - \Delta(\epsilon), \tag{A.9}$$

where ϵ_d is the static crystal field. Eq. (A.9) is a matrix equation with G, Δ, and ϵ_d being (dim C) $\times$ (dim C) matrices, in general. To separate the hybridization from the static LDA crystal field, we numerically evaluate the limit $\epsilon \to \infty$, where $\epsilon - G^{-1}(\epsilon) \to \epsilon_d$.

Appendix B

Second quantized interacting electron Hamiltonians

We consider an interacting electron Hamiltonian in the form of Eqs. (2.1)-(2.4) in Born-Oppenheimer approximation

$$\hat{H} = \sum_i \frac{\hat{p}_i^2}{2m_\mathrm{e}} + \sum_i V(\hat{r}_i) + \sum_{j>i} \frac{e^2}{|\hat{r}_i - \hat{r}_j|} \tag{B.1}$$

and aim to rewrite it in the form of Eq. (2.5). Here, $V(\hat{r}_i)$ is a one-electron potential as following from Eq. (2.4) for frozen nuclei. Following Ref. [217] we employ the field operators, $\Psi_\sigma(r)$, for electrons with spin σ to write the one electron operators in second quantized form

$$\hat{H}_1 = \sum_\sigma \int \mathrm{d}^3 r\, \Psi_\sigma^\dagger(r) \left(-\frac{\hbar^2}{2m_\mathrm{e}} \nabla^2 + V(r) \right) \Psi_\sigma(r). \tag{B.2}$$

This operator is spin-independent and diagonal in spin indices. Spin-orbit coupling or magnetic fields transverse to the spin quantization axis can lead to terms which are off-diagonal in the spin indices. The Coulomb interaction is spin-independent and reads in terms of the field operators as

$$\hat{H}_2 = \frac{1}{2} \sum_{\sigma,\sigma'} \int \mathrm{d}^3 r\, \mathrm{d}^3 r'\, \Psi_\sigma^\dagger(r)\, \Psi_{\sigma'}^\dagger(r') \frac{e^2}{|r - r'|} \Psi_{\sigma'}(r') \Psi_\sigma(r). \tag{B.3}$$

The field operators, $\Psi_\sigma^\dagger(r)$, create electrons in position eigenstates $|r\rangle \otimes |\sigma\rangle$ with spin σ. Changing from position space eigenstates to a different one electron basis $\{|\alpha\rangle \otimes |\sigma\rangle\}$ is achieved by reexpressing the field operators:

$$\Psi_\sigma(r) = \sum_\lambda \langle r|\alpha\rangle c_{\alpha,\sigma}, \tag{B.4}$$

where $c_{\alpha,\sigma}$ is the annihilation operator of an electron in a state described by the wave function $\phi_\alpha(r) = \langle r|\alpha\rangle$ with spin σ. This yields

$$\hat{H}_1 = \sum_{\sigma,\alpha,\beta} c_{\beta,\sigma}^\dagger t_{\beta,\alpha} c_{\alpha,\sigma} \quad \text{with} \quad t_{\beta,\alpha} = \int \mathrm{d}^3 r\, \phi_\beta^*(r) \left(-\frac{\hbar^2}{2m_\mathrm{e}} \nabla^2 + V(r) \right) \phi_\alpha(r), \tag{B.5}$$

and

$$\hat{H}_2 = \frac{1}{2} \sum_{\substack{\sigma,\sigma' \\ \alpha,\alpha',\beta,\beta'}} U_{\alpha,\beta,\beta',\alpha'} c^\dagger_{\alpha,\sigma} c^\dagger_{\beta,\sigma'} c_{\beta',\sigma'} c_{\alpha',\sigma} \tag{B.6}$$

with

$$U_{\alpha,\beta,\beta',\alpha'} = \int \mathrm{d}^3 r \, \mathrm{d}^3 r' \phi^*_\alpha(r) \phi^*_\beta(r') \frac{e^2}{|r - r'|} \phi_{\beta'}(r') \phi_{\alpha'}(r). \tag{B.7}$$

Introducing superindices $i = (\alpha_i, \sigma_i)$ combining orbital and spin degrees of freedom, Eqs. (B.5)-(B.7), take the form of Eq. (2.5) with

$$t_{ij} = t_{\alpha_i,\alpha_j} \delta_{\sigma_i,\sigma_j} \tag{B.8}$$

and

$$U_{ijkl} = U_{\alpha_i,\alpha_j,\alpha_k,\alpha_l} \delta_{\sigma_i,\sigma_l} \delta_{\sigma_j,\sigma_k}. \tag{B.9}$$

Due to the spin-independence of the Coulomb interaction the matrix elements U_{ijkl} factorize into an orbital dependent part, $U_{\alpha_i,\alpha_j,\alpha_k,\alpha_l}$, and the Kronecker symbols in spin-space, $\delta_{\sigma_i,\sigma_l} \delta_{\sigma_j,\sigma_k}$.

In Eqs. (B.3) and (B.7) we considered the bare two-body Coulomb interaction $V(r, r') = \frac{e^2}{|r-r'|}$. It should be noted that the discussion presented here, is not restricted to any particular type of interaction. The only formal property we exploited in Eq. (B.7) is the spin-independence. Hence, the above discussion holds also for any other spin-independent two body interaction like a screened Coulomb interaction.

Appendix C

The Nambu formalism for superconducting graphene

We derive a Hamiltonian of graphene in proximity of a superconducting material and the Nambu formalism as used in section 5.1.5, Eqs. (5.20)-(5.21), is introduced. The discussion of superconductivity is following Refs. [218] and [93]. In a basic model, normal state graphene can be described by the tight-binding Hamiltonian defined in Eqs. (3.1) and (3.2). We use the same conventions as in section 3.1 to label operators, sublattices etc. but now the electron spin degree of freedom is written, explicitly: $a_{i,\varsigma}$ and $b_{i,\varsigma}$ denote the Fermi operators of electrons localized at sublattice atoms A and B in the cell at R_i with spin $\varsigma \in \{\uparrow, \downarrow\}$, respectively.

We consider a local electron-electron interaction in graphene[1] of the form

$$\hat{H}_{\text{int}} = -\frac{1}{2} V \sum_{\varsigma,\varsigma'} \int \mathrm{d}^3 r \, \Psi^\dagger_\varsigma(r) \, \Psi^\dagger_{\varsigma'}(r) \Psi_{\sigma'}(r) \Psi_\varsigma(r), \tag{C.1}$$

with the field operators, $\Psi_\varsigma(r)$, as defined in appendix B. Following the standard BCS mean field treatment, this interaction is decoupled to a sum of quadratic terms (c.f. Eqs. (2.2)-(2.4) of Ref. [93])

$$\hat{H}_{\text{BCS}} = \frac{1}{2} \sum_{\varsigma,\varsigma'} \int \mathrm{d}^3 r \, \Psi^\dagger_{\varsigma'}(r) \bar{V}_{\varsigma,\varsigma'}(r) \Psi_\varsigma(r) + \Delta(r) \Psi^\dagger_\uparrow(r) \Psi^\dagger_\downarrow(r) + \Delta^*(r) \Psi_\downarrow(r) \Psi_\uparrow(r), \tag{C.2}$$

where $\bar{V}_{\sigma,\sigma'}$ contains the usual Hartree-Fock terms and

$$\Delta(r) = -V \left\langle \Psi_\downarrow(r) \Psi_\uparrow(r) \right\rangle \tag{C.3}$$

is the pair potential. In normal state graphene the superconducting order parameter vanishes, $\langle \Psi_\downarrow(r) \Psi_\uparrow(r) \rangle = 0$, but in contact with a superconductor a superconducting correlations and a pairing potential are introduced by the proximity effect. In the tight-binding basis of graphene, the proximity induced superconducting

[1] In the case of proximity induced superconductivity the electron-electron interaction can have arbitrary sign. Here, s-wave pairing as in the experiment by Heersche et al., Ref. [135], is discussed.

conducting correlations lead to finite order parameters of the form $\langle a_{i,\downarrow} a_{i,\uparrow}\rangle$ and $\langle b_{i,\uparrow} b_{i,\downarrow}\rangle$. Assuming the resulting pairing potential to be real and skipping the Hartree-Fock contributions of the local electron-electron interaction, we arrive at

$$\hat{H}_{\mathrm{SC}} = \sum_i \Delta \left(a_{i,\uparrow} a_{i,\downarrow} + b_{i,\uparrow} b_{i,\downarrow}\right) + \mathrm{H.c.} \tag{C.4}$$

for describing s-wave superconducting pairing in graphene.

We now translate this pairing to the low energy Dirac description of electrons in graphene. Setting the graphene lattice constant as unit of length, $a_0 = 2.46\text{Å} \equiv 1$, and introducing a coordinate frame such that the vectors connecting nearest neighbor atoms are $b_1 = (-1/\sqrt{3}, 0)$, $b_2 = (1/2\sqrt{3}, 1/2)$, and $b_3 = (1/2\sqrt{3}, -1/2)$, a Taylor expansion of the tight-binding Hamiltonian, Eq. (3.2) around the two non-equivalent nodal points, $K^{\pm} = \pm q_1 = \pm(4\pi/\sqrt{3})\left\{1/2, 1/2\sqrt{3}\right\}$, yields

$$\hat{H}_0 = \sum_{\varsigma\in\{\uparrow,\downarrow\}} \int \mathrm{d}^2k\, \Psi^{\dagger}_{K^+,\varsigma}(k) H_{K^+} \Psi_{K^+,\varsigma}(k) + \Psi^{\dagger}_{K^-,\varsigma}(k) H_{K^-} \Psi_{K^-,\varsigma}(k) \tag{C.5}$$

with $H_{K^{\pm}}(k) = \hbar v_f (k_1\sigma_1 \mp k_2\sigma_2)$, $\hbar v_f = \sqrt{3}t/2$, and $\Psi_{K^{\pm},\varsigma}(k) = \begin{pmatrix} a_{k\pm q_1,\varsigma} \\ i b_{k\pm q_1,\varsigma} \end{pmatrix}$, where σ_i are Pauli matrices acting on the sublattice degrees of freedom.

Following Nambu, we introduce a spinor $\hat{\Psi}^{\dagger}(k) = (\Psi^{\dagger}_{K^+,\downarrow}(k), \Psi^{\dagger}_{K^-,\downarrow}(k), \Psi_{K^-,\uparrow}(-k), \Psi_{K^+,\uparrow}(-k))$ creating particle and the time reversed hole excitations. The particle-hole space is called Nambu space, and we define Λ_i with $i = 1, 2, 3$ as Pauli matrices acting within this space. Moreover, we introduce Pauli matrices τ_i acting within the valley $K^{\pm}$-space. τ_0 and Λ_0 are the corresponding identity matrices. This allows us to rewrite the graphene Hamiltonian in Nambu space: The pairing reads as

$$\begin{aligned}
\hat{H}_{\mathrm{SC}} =& \int \mathrm{d}^2k\, (a_{k+q_1,\uparrow}, b_{k+q_1,\uparrow}, a_{k-q_1,\uparrow}, b_{k-q_1,\uparrow}) \begin{pmatrix} \Delta & 0 & 0 & 0 \\ 0 & \Delta & 0 & 0 \\ 0 & 0 & \Delta & 0 \\ 0 & 0 & 0 & \Delta \end{pmatrix} \begin{pmatrix} a_{-k-q_1,\downarrow} \\ b_{-k-q_1,\downarrow} \\ a_{-k+q_1,\downarrow} \\ b_{-k+q_1,\downarrow} \end{pmatrix} + \mathrm{H.c.} \\
=& \Delta \int \mathrm{d}^2k\, \hat{\Psi}^{\dagger}(k) \begin{pmatrix} 0 & 0 & \sigma_3 & 0 \\ 0 & 0 & 0 & \sigma_3 \\ \sigma_3 & 0 & 0 & 0 \\ 0 & \sigma_3 & 0 & 0 \end{pmatrix} \hat{\Psi}(k) \qquad \text{(C.6)} \\
=& \Delta \int \mathrm{d}^2k \hat{\Psi}^{\dagger}(k)\, \sigma_3 \otimes \tau_0 \otimes \Lambda_1 \hat{\Psi}^{\dagger}(k). \qquad \text{(C.7)}
\end{aligned}$$

Rewriting Eq. (C.5) in Nambu space yields

$$\begin{aligned}\hat{H}_0 &= \int \mathrm{d}^2k\, \hat{\Psi}^\dagger(k) \begin{pmatrix} H_{K^+}(k) & 0 & 0 & 0 \\ 0 & H_{K^-}(k) & 0 & 0 \\ 0 & 0 & -H_{K^+}(-k) & 0 \\ 0 & 0 & 0 & -H_{K^-}(-k) \end{pmatrix} \hat{\Psi}(k) \\ &= \int \mathrm{d}^2k\, \hat{\Psi}^\dagger(k) \begin{pmatrix} H_{K^+}(k) & 0 & 0 & 0 \\ 0 & H_{K^-}(k) & 0 & 0 \\ 0 & 0 & H_{K^+}(k) & 0 \\ 0 & 0 & 0 & H_{K^-}(k) \end{pmatrix} \hat{\Psi}(k). \end{aligned} \tag{C.8}$$

In the continuum Dirac theory of graphene, the site index i is replaced by a continuous position space coordinate x. Changing to position space representation and combining Eqs. (C.7) and (C.8) leads to

$$\begin{aligned} H_{\text{eff}} &= \int \mathrm{d}^2x\, \hat{\Psi}^\dagger(x) \begin{pmatrix} H_{K^+}(x) & 0 & \Delta\sigma_3 & 0 \\ 0 & H_{K^-}(x) & 0 & \Delta\sigma_3 \\ \Delta\sigma_3 & 0 & H_{K^+}(x) & 0 \\ 0 & \Delta\sigma_3 & 0 & H_{K^-}(x) \end{pmatrix} \hat{\Psi}(x) \\ &= \int \mathrm{d}^2x\, \hat{\Psi}^\dagger(x)(-i\hbar v_f(\partial_1\sigma_1 \otimes \tau_0 - \partial_2\sigma_2 \otimes \tau_3) \otimes \Lambda_0 + \Delta\sigma_3 \otimes \tau_0 \otimes \Lambda_1)\hat{\Psi}(x). \end{aligned} \tag{C.9}$$

This is exactly the Dirac-Bogoliubov-de-Gennes Hamiltonian, Eq. (5.21), used in section 5.1.5.

Bibliography

[1] K. v. Klitzing, G. Dorda, and M. Pepper, *New Method for High-Accuracy Determination of the Fine-Structure Constant Based on Quantized Hall Resistance*, Phys. Rev. Lett. **45**, 494 (1980).

[2] D. M. Eigler and E. K. Schweizer, *Positioning Single Atoms with a Scanning Tunneling Microscope*, Nature **344**, 524 (1990).

[3] M. F. Crommie, C. P. Lutz, and D. M. Eigler, *Confinement of Electrons to Quantum Corrals on a Metal Surface*, Science **262**, 218 (1993).

[4] C. R. Moon, L. S. Mattos, B. K. Foster, G. Zeltzer, and H. C. Manoharan, *Quantum holographic encoding in a two-dimensional electron gas*, Nature Nanotech. **4**, 167 (2009).

[5] International Technology Roadmap for Semiconductors, 2007 ed. Available from the International Technology Roadmap for Semiconductors web site, http://public.itrs.net/.

[6] R. E. Smalley, *Discovering the Fullerenes*, in *Nobel Lectures in Chemistry 1996-2000*, edited by I. Grenthe (World Scientific Publishing Co., 2003).

[7] K. S. Novoselov, A. K. Geim, S. V. Morozov, D. Jiang, Y. Zhang, S. V. Dubonos, I. V. Grigorieva, and A. A. Firsov, *Electric Field Effect in Atomically Thin Carbon Films*, Science **306**, 666 (2004).

[8] K. S. Novoselov, D. Jiang, F. Schedin, T. J. Booth, V. V. Khotkevich, S. V. Morozov, and A. K. Geim, *Two-dimensional atomic crystals*, Proc. Natl. Acad. Sci. USA **102**, 10451 (2005a).

[9] A. K. Geim and K. S. Novoselov, *The rise of graphene*, Nature Mater. **6**, 183 (2007).

[10] M. I. Katsnelson, *Graphene: carbon in two dimensions*, Mat. Today **10**, 20 (2007).

[11] A. H. Castro Neto, F. Guinea, N. M. R. Peres, K. S. Novoselov, and A. K. Geim, *The electronic properties of graphene*, Rev. Mod. Phys. **81**, 109 (2009).

[12] K. I. Bolotin, K. J. Sikes, Z. Jiang, M. Klima, G. Fudenberg, J. Hone, P. Kim, and H. L. Stormer, *Ultrahigh electron mobility in suspended graphene*, Solid State Commun. **146**, 351 (2008).

[13] X. Du, I. Skachko, A. Barker, and E. Y. Andrei, *Approaching ballistic transport in suspended graphene*, Nature Nanotech. **3**, 491 (2008).

[14] Y.-M. Lin, K. A. Jenkins, A. Valdes-Garcia, J. P. Small, D. B. Farmer, and P. Avouris, *Operation of Graphene Transistors at Gigahertz Frequencies*, Nano Lett. **9**, 422 (2009).

[15] F. Schedin, A. K. Geim, S. V. Morozov, E. W. Hill, P. Blake, M. I. Katsnelson, and K. S. Novoselov, *Detection of individual gas molecules adsorbed on graphene*, Nature Mater. **6**, 652 (2007).

[16] K. S. Kim, Y. Zhao, H. Jang, S. Y. Lee, J. M. Kim, K. S. Kim, J.-H. Ahn, P. Kim, J.-Y. Choi, and B. H. Hong, *Large-scale pattern growth of graphene films for stretchable transparent electrodes*, Nature **457**, 706 (2009).

[17] S. H. Pan, E. W. Hudson, K. M. Lang, H. Eisaki, S. Uchida, and J. C. Davis, *Imaging the effects of individual zinc impurity atoms on superconductivity in* $Bi_2Sr_2CaCu_2O_{8+\delta}$, Nature **403**, 746 (2000).

[18] O. Kolesnychenko, R. de Kort, M. Katsnelson, A. Lichtenstein, and H. van Kempen, *Real-space imaging of an orbital Kondo resonance on the Cr(001) surface*, Nature **415**, 507 (2002).

[19] P. Gambardella, S. Rusponi, M. Veronese, S. S. Dhesi, C. Grazioli, A. Dallmeyer, I. Cabria, R. Zeller, P. H. Dederichs, K. Kern, et al., *Giant Magnetic Anisotropy of Single Cobalt Atoms and Nanoparticles*, Science **300**, 1130 (2003).

[20] V. Madhavan, W. Chen, T. Jamneala, M. F. Crommie, and N. S. Wingreen, *Tunneling into a Single Magnetic Atom: Spectroscopic Evidence of the Kondo Resonance*, Science **280**, 567 (1998).

[21] P. Wahl, L. Diekhöner, M. A. Schneider, L. Vitali, G. Wittich, and K. Kern, *Kondo Temperature of Magnetic Impurities at Surfaces*, Phys. Rev. Lett. **93**, 176603 (2004).

[22] J. Kübler, *Theory of Itinerant Electron Magnetism* (Oxford University Press, 2000).

[23] J. M. Ziman, *Prinzipen der Festkörpertheorie* (Verlag Harri Deutsch, 1992).

[24] R. O. Jones and O. Gunnarsson, *The density functional formalism, its applications and prospects*, Rev. Mod. Phys. **61**, 689 (1989).

[25] W. M. C. Foulkes, L. Mitas, R. J. Needs, and G. Rajagopal, *Quantum Monte Carlo simulations of solids*, Rev. Mod. Phys. **73**, 33 (2001).

[26] F. Aryasetiawan and O. Gunnarsson, *The GW method*, Reports on Progress in Physics **61**, 237 (1998).

[27] A. C. Hewson, *The Kondo problem to heavy fermions* (Cambridge University Press, 1993).

[28] G. D. Mahan, *Many-Particle Physics* (Kluwer Academic/Plenum Publishers, 2000), 3rd ed.

[29] A. Georges, G. Kotliar, W. Krauth, and M. J. Rozenberg, *Dynamical mean-field theory of strongly correlated fermion systems and the limit of infinite dimensions*, Rev. Mod. Phys. **68**, 13 (1996).

[30] G. Kotliar and D. Vollhardt, *Strongly Correlated Materials: Insights From Dynamical Mean-Field Theory*, Physics Today **57**, 53 (2004).

[31] G. Kotliar, S. Y. Savrasov, K. Haule, V. S. Oudovenko, O. Parcollet, and C. A. Marianetti, *Electronic structure calculations with dynamical mean-field theory*, Rev. Mod. Phys. **78**, 865 (2006).

[32] A. I. Lichtenstein and M. I. Katsnelson, *Antiferromagnetism and d-wave superconductivity in cuprates: A cluster dynamical mean-field theory*, Phys. Rev. B **62**, R9283 (2000).

[33] G. Kotliar, S. Y. Savrasov, G. Pálsson, and G. Biroli, *Cellular Dynamical Mean Field Approach to Strongly Correlated Systems*, Phys. Rev. Lett. **87**, 186401 (2001).

[34] M. Potthoff, M. Aichhorn, and C. Dahnken, *Variational Cluster Approach to Correlated Electron Systems in Low Dimensions*, Phys. Rev. Lett. **91**, 206402 (2003).

[35] T. Maier, M. Jarrell, T. Pruschke, and M. H. Hettler, *Quantum cluster theories*, Rev. Mod. Phys. **77**, 1027 (2005).

[36] A. N. Rubtsov, M. I. Katsnelson, and A. I. Lichtenstein, *Dual fermion approach to nonlocal correlations in the Hubbard model*, Phys. Rev. B **77**, 033101 (2008).

[37] V. I. Anisimov, A. I. Poteryaev, M. A. Korotin, A. O. Anokhin, and G. Kotliar, *First-principles calculations of the electronic structure and spectra of strongly correlated systems: dynamical mean-field theory*, Journal of Physics: Condensed Matter **9**, 7359 (1997a).

[38] A. I. Lichtenstein and M. I. Katsnelson, *Ab initio calculations of quasiparticle band structure in correlated systems: LDA++ approach*, Phys. Rev. B **57**, 6884 (1998).

[39] R. M. Martin, *Electronic Structure: Basic Theory and Practical Methods* (Cambridge University Press, 2004).

[40] U. v. Barth and L. Hedin, *A local exchange-correlation potential for the spin polarized case. I*, J. Phys. C **5**, 1629 (1972).

[41] D. Joubert, ed., *Density Functionals: Theory and Applications* (Springer, Berlin, 1998).

[42] J. P. Perdew, J. A. Chevary, S. H. Vosko, K. A. Jackson, M. R. Pederson, D. J. Singh, and C. Fiolhais, *Atoms, molecules, solids, and surfaces: Applications of the generalized gradient approximation for exchange and correlation*, Phys. Rev. B **46**, 6671 (1992).

[43] J. P. Perdew, K. Burke, and M. Ernzerhof, *Generalized Gradient Approximation Made Simple*, Phys. Rev. Lett. **77**, 3865 (1996).

[44] P. E. Blöchl, C. J. Först, and J. Schimpl, *The Projector Augmented Wave Method: ab-initio molecular dynamics with full wave functions* (2002), cond-mat/0201015.

[45] M. Payne, M. Teter, D. Allan, T. Arias, and J. Joannopoulos, *Iterative minimization techniques for ab initio total-energy calculations: molecular dynamics and conjugate gradients*, Rev. Mod. Phys. **64**, 1045 (1992).

[46] S. Blügel and G. Bihlmayer, *Full-Potential Linearized Augmented Planewave Method*, (lecture notes) availble at http://www.fz-juelich.de/iff/S_Bluegel_lec/.

[47] S. G. Louie, K.-M. Ho, and M. L. Cohen, *Self-consistent mixed-basis approach to the electronic structure of solids*, Phys. Rev. B **19**, 1774 (1979).

[48] G. Kresse and J. Hafner, *Norm-conserving and ultrasoft pseudopotentials for first-row and transition elements*, J. Phys.: Condes. Matter **6**, 8245 (1994).

[49] O. K. Andersen, *Linear methods in band theory*, Phys. Rev. B **12**, 3060 (1975).

[50] J. M. Soler and A. R. Williams, *Simple formula for the atomic forces in the augmented-plane-wave method*, Phys. Rev. B **40**, 1560 (1989).

[51] E. Wimmer, H. Krakauer, M. Weinert, and A. J. Freeman, *Full-potential self-consistent linearized-augmented-plane-wave method for calculating the electronic structure of molecules and surfaces: O_2 molecule*, Phys. Rev. B **24**, 864 (1981).

[52] P. E. Blöchl, *Projector augmented-wave method*, Phys. Rev. B **50**, 17953 (1994).

[53] G. Kresse and D. Joubert, *From ultrasoft pseudopotentials to the projector augmented-wave method*, Phys. Rev. B **59**, 1758 (1999).

[54] G. Kresse, *Pseudopotentials (Part I)*, transparancies from VASP workshop. http://cms.mpi.univie.ac.at/vasp-workshop/slides/pseudopp1.pdf, Accessed 17-August-2009.

[55] J. W. Negele and H. Orland, *Quantum many-particle systems* (Addison-Wesley, Redwood City, California, 1988).

[56] A. Georges, *Strongly Correlated Electron Materials: Dynamical Mean-Field Theory and Electronic Structure*, AIP Conference Proceedings **715**, 3 (2004).

[57] V. I. Anisimov, I. V. Solovyev, M. A. Korotin, M. T. Czyżyk, and G. A. Sawatzky, *Density-functional theory and NiO photoemission spectra*, Phys. Rev. B **48**, 16929 (1993).

[58] V. I. Anisimov, F. Aryasetiawan, and A. I. Lichtenstein, *First-principles calculations of the electronic structure and spectra of strongly correlated systems: the LDA+ U method*, J. Phys.: Condens. Matter **9**, 767 (1997b).

[59] V. I. Anisimov, J. Zaanen, and O. K. Andersen, *Band theory and Mott insulators: Hubbard U instead of Stoner I*, Phys. Rev. B **44**, 943 (1991).

[60] A. B. Shick, A. I. Liechtenstein, and W. E. Pickett, *Implementation of the LDA+U method using the full-potential linearized augmented plane-wave basis*, Phys. Rev. B **60**, 10763 (1999).

[61] F. Lechermann, M. Fähnle, B. Meyer, and C. Elsässer, *Electronic correlations, magnetism, and structure of Fe-Al subsystems: An LDA + U study*, Phys. Rev. B **69**, 165116 (2004).

[62] O. Bengone, M. Alouani, P. Blöchl, and J. Hugel, *Implementation of the projector augmented-wave LDA+U method: Application to the electronic structure of NiO*, Phys. Rev. B **62**, 16392 (2000).

[63] A. N. Rubtsov, V. V. Savkin, and A. I. Lichtenstein, *Continuous-time quantum Monte Carlo method for fermions*, Phys. Rev. B **72**, 035122 (2005a).

[64] O. Gunnarsson and K. Schönhammer, *Electron spectroscopies for Ce compounds in the impurity model*, Phys. Rev. B **28**, 4315 (1983).

[65] N. D. Mermin, *Crystalline Order in Two Dimensions*, Phys. Rev. **176**, 250 (1968).

[66] D. Nelson, T. Piran, and S. Weinberg, eds., *Statistical Mechanics of Membranes and Surfaces* (World Scientific, Singapore, 2004).

[67] A. Fasolino, J. H. Los, and M. I. Katsnelson, *Intrinsic ripples in graphene*, Nature Mater. **6**, 858 (2007).

[68] J. C. Meyer, A. K. Geim, M. I. Katsnelson, K. S. Novoselov, T. J. Booth, and S. Roth, *The structure of suspended graphene sheets*, Nature **446**, 60 (2007).

[69] D. A. Dikin, S. Stankovich, E. J. Zimney, R. D. Piner, G. H. B. Dommett, G. Evmenenko, S. B. T. Nguyen, and R. S. Ruoff, *Preparation and characterization of graphene oxide paper*, Nature **448**, 457 (2007).

[70] Y. Hernandez, V. Nicolosi, M. Lotya, F. M. Blighe, Z. Sun, S. De, I. T. McGovern, B. Holland, M. Byrne, Y. K. Gun'ko, et al., *High-yield production of graphene by liquid-phase exfoliation of graphite*, Nature Nanotech. **3**, 563 (2008).

[71] A. Reina, X. Jia, J. Ho, D. Nezich, H. Son, V. Bulovic, M. S. Dresselhaus, and J. Kong, *Large Area, Few-Layer Graphene Films on Arbitrary Substrates by Chemical Vapor Deposition*, Nano Lett. **9**, 30 (2009).

[72] P. R. Wallace, *The Band Theory of Graphite*, Phys. Rev. **71**, 622 (1947).

[73] S. Reich, J. Maultzsch, C. Thomsen, and P. Ordejón, *Tight-binding description of graphene*, Phys. Rev. B **66**, 035412 (2002).

[74] G. W. Semenoff, *Condensed-Matter Simulation of a Three-Dimensional Anomaly*, Phys. Rev. Lett. **53**, 2449 (1984).

[75] J. L. M. nes, F. Guinea, and M. A. H. Vozmediano, *Existence and topological stability of Fermi points in multilayered graphene*, Phys. Rev. B **75**, 155424 (2007).

[76] D. M. Basko, *Theory of resonant multiphonon Raman scattering in graphene*, Phys. Rev. B **78**, 125418 (2008).

[77] S. Das Sarma, A. K. Geim, P. Kim, and A. H. MacDonald, eds., *Exploring graphene - Recent research advances* (2007), vol. 143 of *Solid State Commun.*, pp. 1 – 125.

[78] M. I. Katsnelson and K. S. Novoselov, *Graphene: New bridge between condensed matter physics and quantum electrodynamics*, Solid State Commun. **143**, 3 (2007).

[79] Y. Zheng and T. Ando, *Hall conductivity of a two-dimensional graphite system*, Phys. Rev. B **65**, 245420 (2002).

[80] V. P. Gusynin and S. G. Sharapov, *Unconventional Integer Quantum Hall Effect in Graphene*, Phys. Rev. Lett. **95**, 146801 (2005).

[81] K. S. Novoselov, A. K. Geim, S. V. Morozov, D. Jiang, M. I. Katsnelson, I. V. Grigorieva, S. V. Dubonos, and A. A. Firsov, *Two-dimensional gas of massless Dirac fermions in graphene*, Nature **438**, 197 (2005b).

[82] Y. Zhang, Y.-W. Tan, H. L. Stormer, and P. Kim, *Experimental observation of the quantum Hall effect and Berry's phase in graphene*, Nature **438**, 201 (2005).

[83] M. I. Katsnelson, K. S. Novoselov, and A. K. Geim, *Chiral tunnelling and the Klein paradox in graphene*, Nature Phys. **2**, 620 (2006).

[84] K. S. Novoselov, Z. Jiang, Y. Zhang, S. V. Morozov, H. L. Stormer, U. Zeitler, J. C. Maan, G. S. Boebinger, P. Kim, and A. K. Geim, *Room-Temperature Quantum Hall Effect in Graphene*, Science **315**, 1379 (2007).

[85] L. Brey and H. A. Fertig, *Electronic states of graphene nanoribbons studied with the Dirac equation*, Phys. Rev. B **73**, 235411 (2006).

[86] Y.-W. Son, M. L. Cohen, and S. G. Louie, *Energy Gaps in Graphene Nanoribbons*, Phys. Rev. Lett. **97**, 216803 (2006).

[87] D. C. Elias, R. R. Nair, T. M. G. Mohiuddin, S. V. Morozov, P. Blake, M. P. Halsall, A. C. Ferrari, D. W. Boukhvalov, M. I. Katsnelson, A. K. Geim, et al., *Control of graphene properties by reversible hydrogenation: Evidence for graphane*, Science **323**, 610 (2009).

[88] C. Bena and S. A. Kivelson, *Quasiparticle scattering and local density of states in graphite*, Phys. Rev. B **72**, 125432 (2005).

[89] N. M. R. Peres, F. Guinea, and A. H. C. Neto, *Electronic properties of disordered two-dimensional carbon*, Phys. Rev. B **73**, 125411 (2006).

[90] Y. V. Skrypnyk and V. M. Loktev, *Impurity effects in a two-dimensional system with the Dirac spectrum*, Phys. Rev. B **73**, 241402 (R) (2006).

[91] V. V. Cheianov and V. I. Fal'ko, *Friedel Oscillations, Impurity Scattering, and Temperature Dependence of Resistivity in Graphene*, Phys. Rev. Lett. **97**, 226801 (2006).

[92] T. O. Wehling, A. V. Balatsky, M. I. Katsnelson, A. I. Lichtenstein, K. Scharnberg, and R. Wiesendanger, *Local electronic signatures of impurity states in graphene*, Phys. Rev. B **75**, 125425 (2007).

[93] A. V. Balatsky, I. Vekhter, and J.-X. Zhu, *Impurity-induced states in conventional and unconventional superconductors*, Rev. Mod. Phys. **78**, 373 (2006).

[94] J. Kong, N. R. Franklin, C. Zhou, M. G. Chapline, S. Peng, K. Cho, and H. Dai, *Nanotube Molecular Wires as Chemical Sensors*, Science **287**, 622 (2000).

[95] P. G. Collins, K. Bradley, M. Ishigami, and A. Zettl, *Extreme Oxygen Sensitivity of Electronic Properties of Carbon Nanotubes*, Science **287**, 1801 (2000).

[96] W. Kim, A. Javey, O. Vermesh, Q. Wang, Y. Li, and H. Dai, *Hysteresis Caused by Water Molecules in Carbon Nanotube Field-Effect Transistors*, Nano Lett. **3**, 193 (2003).

[97] S. Heinze, J. Tersoff, R. Martel, V. Derycke, J. Appenzeller, and P. Avouris, *Carbon Nanotubes as Schottky Barrier Transistors*, Phys. Rev. Lett. **89**, 106801 (2002).

[98] T. Ohta, A. Bostwick, T. Seyller, K. Horn, and E. Rotenberg, *Controlling the Electronic Structure of Bilayer Graphene*, Science **313**, 951 (2006).

[99] S. Y. Zhou, D. A. Siegel, A. V. Fedorov, and A. Lanzara, *Metal to Insulator Transition in Epitaxial Graphene Induced by Molecular Doping*, Phys. Rev. Lett. **101**, 086402 (2008).

[100] J. H. Chen, C. Jang, S. Adam, M. S. Fuhrer, E. D. Williams, and M. Ishigami, *Charged-impurity scattering in graphene*, Nature Phys. **4**, 377 (2008).

[101] M. Ishigami, J. H. Chen, W. G. Cullen, M. S. Fuhrer, and E. D. Williams, *Atomic Structure of Graphene on SiO_2*, Nano Lett. **7**, 1643 (2007).

[102] E. Stolyarova, K. T. Rim, S. Ryu, J. Maultzsch, P. Kim, L. E. Brus, T. F. Heinz, M. S. Hybertsen, and G. W. Flynn, *High-resolution scanning tunneling microscopy imaging of mesoscopic graphene sheets on an insulating surface*, Proc. Natl. Acad. Sci. USA **104**, 9209 (2007).

[103] G. M. Rutter, J. N. Crain, N. P. Guisinger, T. Li, P. N. First, and J. A. Stroscio, *Scattering and Interference in Epitaxial Graphene*, Science **317**, 219 (2007).

[104] V. W. Brar, Y. Zhang, Y. Yayon, T. Ohta, J. L. McChesney, A. Bostwick, E. Rotenberg, K. Horn, and M. F. Crommie, *Scanning tunneling spectroscopy of inhomogeneous electronic structure in monolayer and bilayer graphene on SiC*, Appl. Phys. Lett. **91**, 122102 (2007).

[105] P. Lauffer, K. V. Emtsev, R. Graupner, T. Seyller, L. Ley, S. A. Reshanov, and H. B. Weber, *Atomic and electronic structure of few-layer graphene on SiC(0001) studied with scanning tunneling microscopy and spectroscopy*, Phys. Revl B **77**, 155426 (2008).

[106] Y. Zhang, V. W. Brar, F. Wang, C. Girit, Y. Yayon, M. Panlasigui, A. Zettl, and M. F. Crommie, *Giant Phonon-induced Conductance in Scanning Tunneling Spectroscopy of Gate-tunable Graphene*, Nature Phys. **4**, 627 (2008).

[107] I. Brihuega, P. Mallet, C. Bena, S. Bose, C. Michaelis, L. Vitali, F. Varchon, L. Magaud, K. Kern, and J. Y. Veuillen, *Quasiparticle Chirality in Epitaxial Graphene Probed at the Nanometer Scale*, Phys. Rev. Lett. **101**, 206802 (2008).

[108] V. Geringer, M. Liebmann, T. Echtermeyer, S. Runte, M. Schmidt, R. Rückamp, M. C. Lemme, and M. Morgenstern, *Intrinsic and extrinsic corrugation of monolayer graphene deposited on SiO_2*, Phys. Rev. Lett. **102**, 076102 (2009).

[109] G. Li, A. Luican, and E. Y. Andrei, *Scanning Tunneling Spectroscopy of Graphene on Graphite*, Phys. Rev. Lett. **102**, 176804 (2009).

[110] J. C. Meyer, C. O. Girit, M. F. Crommie, and A. Zettl, *Imaging and dynamics of light atoms and molecules on graphene*, Nature **454**, 319 (2008).

[111] B. C. Stipe et al., *Single-Molecule Vibrational Spectroscopy and Microscopy*, Science **280**, 1732 (1998).

[112] A. V. Balatsky et al., *Inelastic tunneling spectroscopy in a d-wave superconductor*, Phys. Rev. B **68**, 214506 (2003).

[113] J. Lee et al., *Interplay of electron-lattice interactions and superconductivity in $Bi_2Sr_2CaCu_2O_{8+\delta}$*, Nature **442**, 546 (2006).

[114] G. Csanyi, P. B. Littlewood, A. H. Nevidomskyy, C. J. Pickard, and B. D. Simons, *The role of the interlayer state in the electronic structure of superconducting graphite intercalated compounds*, Nature Phys. **1**, 42 (2005).

[115] J. Tersoff and D. R. Hamann, *Theory of the scanning tunneling microscope*, Phys. Rev. B **31**, 805 (1985).

[116] M. Mohr, J. Maultzsch, E. Dobardzic, S. Reich, I. Milosevic, M. Damnjanovic, A. Bosak, M. Krisch, and C. Thomsen, *Phonon dispersion of graphite by inelastic x-ray scattering*, Phys. Rev. B **76**, 035439 (2007).

[117] V. W. Brar, S. Wickenburg, M. Panlasigui, C.-H. Park, T. O. Wehling, Y. Zhang, R. Decker, C. Girit, A. V. Balatsky, S. G. Louie, et al., *Observation of Carrier-density-dependent Many-body Effects in Graphene via Tunneling Spectroscopy* (2009), (PRL accepted).

[118] W. A. Harrison, *Electronic Structure and the Properties of Solids - The physics of the chemical bond* (W. H. Freeman and Company, 1980).

[119] E.-A. Kim and A. H. C. Neto, *Graphene as an electronic membrane*, Europhys. Lett. **84**, 57007 (2008).

[120] M. S. Foster and I. Aleiner, *Graphene via large N: A renormalization group study*, Phys. Rev. B **77**, 195413 (2008).

[121] S. V. Morozov, K. S. Novoselov, M. I. Katsnelson, F. Schedin, L. A. Ponomarenko, D. Jiang, and A. K. Geim, *Strong Suppression of Weak Localization in Graphene*, Phys. Rev. Lett. **97**, 016801 (2006).

[122] F. Guinea, M. I. Katsnelson, and M. A. H. Vozmediano, *Midgap states and charge inhomogeneities in corrugated graphene*, Phys. Rev. B **77**, 075422 (2008).

[123] M. I. Katsnelson and A. K. Geim, *Electron scattering on microscopic corrugations in graphene*, Phil. Trans. R. Soc. A **366**, 195 (2008).

[124] T. Stauber, N. M. R. Peres, and F. Guinea, *Electronic transport in graphene: A semi-classical approach including midgap states*, Phys. Rev. B **76**, 205423 (2007).

[125] J. Röhrl, M. Hundhausen, K. V. Emtsev, T. Seyller, R. Graupner, and L. Ley, *Raman spectra of epitaxial graphene on SiC(0001)*, Appl. Phys. Lett. **92**, 201918 (2008).

[126] H. Ajiki and T. Ando, *Lattice distortion of metallic Carbon nanotudes induced by magnetic-fields*, J. Phys. Soc. Jpn. **64**, 260 (1995).

[127] H. Brune, M. Giovannini, K. Bromann, and K. Kern, *Self-organized growth of nanostructure arrays on strain-relief patterns*, Nature **394**, 451 (1998).

[128] T. O. Wehling, A. V. Balatsky, A. M. Tsvelik, M. I. Katsnelson, and A. I. Lichtenstein, *Midgap states in corrugated graphene: Ab initio calculations and effective field theory*, Europhys. Lett. **84**, 17003 (2008a).

[129] L. D. Landau and E. M. Lifschitz, *Lehrbuch der Theoretischen Physik, Band 7, Elastizitätstheorie* (Akademie-Verlag, Berlin, 1989).

[130] R. Joynt, *Bound States and Impurity Averaging in Unconventional Superconductors*, J. Low Temp. Phys. **109**, 811 (1997).

[131] E. H. Lieb, *Two theorems on the Hubbard model*, Phys. Rev. Lett. **62**, 1201 (1989).

[132] D.-H. Lin, *Friedel theorem for two-dimensional relativistic spin-(1/2) systems*, Phys. Rev. A **73**, 044701 (2006).

[133] V. M. Pereira, F. Guinea, J. M. B. L. dos Santos, N. M. R. Peres, and A. H. C. Neto, *Disorder Induced Localized States in Graphene*, Phys. Rev. Lett. **96**, 036801 (2006).

[134] J. Martin, N. Akerman, G. Ulbricht, T. Lohmann, J. H. Smet, K. von Klitzing, and A. Yacoby, *Observation of electron-hole puddles in graphene using a scanning single-electron transistor*, Nature Phys. **4**, 144 (2008).

[135] H. B. Heersche, P. Jarillo-Herrero, J. B. Oostinga, L. M. K. Vandersypen, and A. F. Morpurgo, *Bipolar supercurrent in graphene*, Nature **446**, 56 (2007).

[136] A. Rycerz, J. Tworzydlo, and C. W. J. Beenakker, *Valley filter and valley valve in graphene*, Nature Phys. **3**, 172 (2007).

[137] B. Uchoa and A. H. Castro Neto, *Superconducting States of Pure and Doped Graphene*, Phys. Rev. Lett. **98**, 146801 (2007).

[138] The dielectric constant of graphene is $\epsilon \approx 6$ and implies good screening, see T. Ando, J. Phys. Soc. Jpn. **75**, 074716 (2006).

[139] C. W. J. Beenakker, *Specular Andreev Reflection in Graphene*, Phys. Rev. Lett. **97**, 067007 (2006).

[140] E. McCann, K. Kechedzhi, V. I. Fal'ko, H. Suzuura, T. Ando, and B. L. Altshuler, *Weak-Localization Magnetoresistance and Valley Symmetry in Graphene*, Phys. Rev. Lett. **97**, 146805 (2006).

[141] P. W. Anderson, *Theory of dirty superconductors*, J. Phys. Chem. Solids **11**, 26 (1959).

[142] T. O. Wehling, *Impurity effects in graphene*, Fachbereich Physik, Universität Hamburg (2006), Diplomarbeit.

[143] E. J. Meijer and M. Sprik, *A density-functional study of the intermolecular interactions of benzene*, J. Chem. Phys. **105**, 8684 (1996).

[144] S. Santucci, S. Picozzi, F. D. Gregorio, L. Lozzi, C. Cantalini, L. Valentini, J. M. Kenny, and B. Delley, *NO2 and CO gas adsorption on carbon nanotubes: Experiment and theory*, J. Chem. Phys. **119**, 10904 (2003).

[145] P. Sjovall, S. K. So, B. Kasemo, R. Franchy, and W. Ho, *NO_2 adsorption on graphite at 90 K*, Chem. Phys. Lett. **172**, 125 (1990).

[146] R. Moreh, Y. Finkelstein, and H. Shechter, *NO_2 adsorption on Grafoil between 297 and 12 K*, Phys. Rev. B **53**, 16006 (1996).

[147] T. O. Wehling, K. S. Novoselov, S. V. Morozov, E. E. Vdovin, M. I. Katsnelson, A. K. Geim, and A. I. Lichtenstein, *Molecular Doping of Graphene*, Nano Lett. **8**, 173 (2008b).

[148] J. S. Kim, *A matrix formalism for the Hall effect in multicarrier semiconductor systems*, Journal of Applied Physics **86**, 3187 (1999).

[149] O. Leenaerts, B. Partoens, and F. M. Peeters, *Adsorption of H_2O, NH_3, CO, NO_2, and NO on graphene: A first-principles study*, Phys. Rev. B **77**, 125416 (2008).

[150] J. Zhao, A. Buldum, J. Han, and J. P. Lu, *Gas molecule adsorption in carbon nanotubes and nanotube bundles*, Nanotechnology **13**, 195 (2002).

[151] J. Moser, A. Verdaguer, D. Jimenez, A. Barreiro, and A. Bachtold, *The environment of graphene probed by electrostatic force microscopy*, Appl. Phys. Lett. **92**, 123507 (2008).

[152] T. Lankau, *A Computational Analysis of Hydrogen-Bonded Networks*, Department of Chemistry, University of Hamburg (2004), habilitation thesis.

[153] S. Meng, E. Kaxiras, and Z. Zhang, *Water wettability of close-packed metal surfaces*, J. Chem. Phys. **127**, 244710 (2007).

[154] P. Carrier, L. J. Lewis, and M. W. C. Dharma-wardana, *Electron confinement and optical enhancement in Si/SiO_2 superlattices*, Phys. Rev. B **64**, 195330 (2001).

[155] M. Wilson and T. R. Walsh, *Hydrolysis of the amorphous silica surface. I. Structure and dynamics of the dry surface*, J. Chem. Phys. **113**, 9180 (2000).

[156] A. Wright and A. Leadbetter, *Structures of β-cristobalite phases of SiO_2 and $AlPO_4$*, Philos. Mag. **31**, 1391 (1975).

[157] M. I. Katsnelson, F. Guinea, and A. K. Geim, *Scattering of electrons in graphene by clusters of impurities*, Phys. Rev. B **79**, 195426 (2009).

[158] H. Jónsson, G. Mills, and K. W. Jacobsen, in *Classical and Quantum Dynamics in Condensed Phase Simulations*, edited by B. J. Berne, G. Ciccotti, and D. F. Coker (World Scientific, 1998), p. 385.

[159] D. W. Boukhvalov, M. I. Katsnelson, and A. I. Lichtenstein, *Hydrogen on graphene: Electronic structure, total energy, structural distortions and magnetism from first-principles calculations*, Phys. Rev. B **77**, 035427 (2008).

[160] S. Casolo, O. M. L. vvik, R. Martinazzo, and G. F. Tantardini, *Understanding adsorption of hydrogen atoms on graphene*, J. Chem. Phys. **130**, 054704 (2009).

[161] J. P. Robinson, H. Schomerus, L. Oroszlány, and V. I. Fal'ko, *Adsorbate-Limited Conductivity of Graphene*, Phys. Rev. Lett. **101**, 196803 (2008).

[162] B. Cordero, V. Gomez, A. E. Platero-Prats, M. Reves, J. Echeverria, E. Cremades, F. Barragan, and S. Alvarez, *Covalent radii revisited*, Dalton Transactions pp. 2832–2838 (2008).

[163] K. T. Chan, J. B. Neaton, and M. L. Cohen, *First-principles study of metal adatom adsorption on graphene*, Phys. Rev. B **77**, 235430 (2008).

[164] M. Caragiu and S. Finberg, *Alkali metal adsorption on graphite: a review*, J. Phys: Condens. Matter **17**, R995 (2005).

[165] W. de Haas, J. de Boer, and G. van dën Berg, *The electrical resistance of gold, copper and lead at low temperatures*, Physica **1**, 1115 (1934).

[166] M. P. Sarachik, E. Corenzwit, and L. D. Longinotti, *Resistivity of Mo-Nb and Mo-Re Alloys Containing 1% Fe*, Phys. Rev. **135**, A1041 (1964).

[167] J. Kondo, *Resistance Minimum in Dilute Magnetic Alloys*, Prog Theor. Phys. **32**, 37 (1964).

[168] P. W. Anderson, *Localized Magnetic States in Metals*, Phys. Rev. **124**, 41 (1961).

[169] L. Kouwenhoven and L. Glazman, *Revival of the Kondo effect*, Physics World **14**, 33 (2001).

[170] T. A. Costi, L. Bergqvist, A. Weichselbaum, J. von Delft, T. Micklitz, A. Rosch, P. Mavropoulos, P. H. Dederichs, F. Mallet, L. Saminadayar, et al., *Kondo Decoherence: Finding the Right Spin Model for Iron Impurities in Gold and Silver*, Phys. Rev. Lett. **102**, 056802 (2009).

[171] H. Hafermann, Ph.D. thesis, Universität Hamburg (2009).

[172] B. Johansson, *The - transition in cerium is a Mott transition*, Philos. Mag. **30**, 469 (1974).

[173] D. C. Koskenmaki and K. A. Gschneidner, Jr., in *Handbook on the Physics and Chemistry of Rare Earths: Metals*, edited by K. A. Gschneidner, Jr. and L. Eyring (North-Holland, Amsterdam, 1981), vol. 1, chap. 4.

[174] J. W. Allen and R. M. Martin, *Kondo Volume Collapse and the $\gamma \rightarrow \alpha$ Transition in Cerium*, Phys. Rev. Lett. **49**, 1106 (1982).

[175] A. K. McMahan, K. Held, and R. T. Scalettar, *Thermodynamic and spectral properties of compressed Ce calculated using a combined local-density approximation and dynamical mean-field theory*, Phys. Rev. B **67**, 075108 (2003).

[176] H. J. Barth, M. Luszik-Bhadra, and D. Riegel, *Formation of Local Magnetic Moments of Ce in Metallic Elements*, Phys. Rev. Lett. **50**, 608 (1983).

[177] J. W. Allen, S. J. Oh, O. Gunnarsson, K. Schönhammer, M. B. Maple, M. S. Torikachvili, and I. Lindau, *Electronic structure of cerium and light rare-earth intermetallics*, Adv. Phys. **35**, 275 (1986).

[178] J. Li, W.-D. Schneider, R. Berndt, and B. Delley, *Kondo Scattering Observed at a Single Magnetic Impurity*, Phys. Rev. Lett. **80**, 2893 (1998).

[179] M. Ternes, A. J. Heinrich, and W.-D. Schneider, *Spectroscopic manifestations of the Kondo effect on single adatoms*, J. Phys.: Condens. Matter **21**, 053001 (2009).

[180] M. Plihal and J. W. Gadzuk, *Nonequilibrium theory of scanning tunneling spectroscopy via adsorbate resonances: Nonmagnetic and Kondo impurities*, Phys. Rev. B **63**, 085404 (2001).

[181] V. Madhavan, W. Chen, T. Jamneala, M. F. Crommie, and N. S. Wingreen, *Local spectroscopy of a Kondo impurity: Co on Au(111)*, Phys. Rev. B **64**, 165412 (2001).

[182] C.-Y. Lin, A. H. C. Neto, and B. A. Jones, *First-Principles Calculation of the Single Impurity Surface Kondo Resonance*, Phys. Rev. Lett. **97**, 156102 (2006).

[183] N. Knorr, M. A. Schneider, L. Diekhöner, P. Wahl, and K. Kern, *Kondo Effect of Single Co Adatoms on Cu Surfaces*, Phys. Rev. Lett. **88**, 096804 (2002).

[184] F. Lechermann, A. Georges, A. Poteryaev, S. Biermann, M. Posternak, A. Yamasaki, and O. K. Andersen, *Dynamical mean-field theory using Wannier functions: A flexible route to electronic structure calculations of strongly correlated materials*, Phys. Rev. B **74**, 125120 (2006).

[185] N. Quaas, M. Wenderoth, A. Weismann, R. G. Ulbrich, and K. Schönhammer, *Kondo resonance of single Co atoms embedded in Cu(111)*, Phys. Rev. B **69**, 201103 (2004).

[186] G. A. Fiete and E. J. Heller, *Colloquium: Theory of quantum corrals and quantum mirages*, Rev. Mod. Phys. **75**, 933 (2003).

[187] O. Agam and A. Schiller, *Projecting the Kondo Effect: Theory of the Quantum Mirage*, Phys. Rev. Lett. **86**, 484 (2001).

[188] D. Porras, J. Fernández-Rossier, and C. Tejedor, *Microscopic theory for quantum mirages in quantum corrals*, Phys. Rev. B **63**, 155406 (2001).

[189] H. C. Manoharan, C. P. Lutz, and D. M. Eigler, *Quantum mirages formed by coherent projection of electronic structure*, Nature **403**, 512 (2000).

[190] L. Limot and R. Berndt, *Kondo effect and surface-state electrons*, Appl. Surf. Sci. **237**, 572 (2004).

[191] A. N. Rubtsov, V. V. Savkin, and A. I. Lichtenstein, *Continuous-time quantum Monte Carlo method for fermions*, Phys. Rev. B **72**, 035122 (2005b).

[192] E. Gorelov, Ph.D. thesis, Universität Hamburg (2007).

[193] E. Gorelov, T. O. Wehling, A. N. Rubtsov, M. I. Katsnelson, and A. I. Lichtenstein, *Relevance of complete Coulomb interaction matrix for the Kondo problem: Co impurity on Cu(111)*, Phys. Rev. B **80**, 155132 (2009).

[194] M. Jarrell and J. E. Gubernatis, *Bayesian inference and the analytic continuation of imaginary-time quantum Monte Carlo data*, Phys. Rep. **269**, 133 (1996).

[195] N. Néel, J. Kröger, R. Berndt, T. O. Wehling, A. I. Lichtenstein, and M. I. Katsnelson, *Controlling the Kondo Effect in $CoCu_n$ Clusters Atom by Atom*, Phys. Rev. Lett. **101**, 266803 (2008).

[196] L. S. Mattos et al. (2009), To be published. See also APS March Meeting 2009, contribution T25.00009.

[197] C. R. Cassanello and E. Fradkin, *Kondo effect in flux phases*, Phys. Rev. B **53**, 15079 (1996).

[198] K. Ingersent, *Behavior of magnetic impurities in gapless Fermi systems*, Phys. Rev. B **54**, 11936 (1996).

[199] M. Vojta and R. Bulla, *Kondo effect of impurity moments in d-wave superconductors: Quantum phase transition and spectral properties*, Phys. Rev. B **65**, 014511 (2001).

[200] L. Fritz and M. Vojta, *Phase transitions in the pseudogap Anderson and Kondo models:Critical dimensions, renormalization group, and local-moment criticality*, Phys. Rev. B **70**, 214427 (2004).

[201] K. Sengupta and G. Baskaran, *Tuning Kondo physics in graphene with gate voltage*, Phys. Rev. B **77**, 045417 (2008).

[202] M. Hentschel and F. Guinea, *Orthogonality catastrophe and Kondo effect in graphene*, Phys. Rev. B **76**, 115407 (2007).

[203] P. S. Cornaglia, G. Usaj, and C. A. Balseiro, *Localized Spins on Graphene*, Phys. Rev. Lett. **102**, 046801 (2009).

[204] H.-B. Zhuang, Q. feng Sun, and X. C. Xie, *Scanning tunneling spectroscopy of a magnetic atom on graphene in the Kondo regime*, Europhys. Lett. **86**, 58004 (2009).

[205] B. Uchoa, L. Yang, S.-W. Tsai, N. M. R. Peres, and A. H. C. Neto, *Theory of Scanning Tunneling Spectroscopy of Magnetic Adatoms in Graphene*, Phys. Rev. Lett. **103**, 206804 (2009).

[206] L. Dell'Anna, *Kondo impurity on the honeycomb lattice at half-filling* (2009), `arXiv.org:0911.1255`.

[207] L. Borda, G. Zaránd, W. Hofstetter, B. I. Halperin, and J. von Delft, *SU(4) Fermi Liquid State and Spin Filtering in a Double Quantum Dot System*, Phys. Rev. Lett. **90**, 026602 (2003).

[208] P. Jarillo-Herrero, J. Kong, H. S. van der Zant, C. Dekker, L. P. Kouwenhoven, and S. De Franceschi, *Orbital Kondo effect in carbon nanotubes*, Nature **434**, 484 (2005).

[209] Y. Mao et al., *Density functional calculation of transition metal adatom adsorption on graphene*, J. Phys.: Condens. Matter **20**, 115209 (2008).

[210] Y. Kuramoto, *Perturbative renormalization of multi-channel Kondo-type models*, Eur. Phys. J. B **5**, 457 (1998).

[211] B. Amadon, F. Lechermann, A. Georges, F. Jollet, T. O. Wehling, and A. I. Lichtenstein, *Plane-wave based electronic structure calculations for correlated materials using dynamical mean-field theory and projected local orbitals*, Phys. Rev. B **77**, 205112 (2008).

[212] A. Rohrbach, J. Hafner, and G. Kresse, *Electronic correlation effects in transition-metal sulfides*, J. Phys.: Condens. Matter **15**, 979 (2003).

[213] E. Pavarini, S. Biermann, A. Poteryaev, A. I. Lichtenstein, A. Georges, and O. K. Andersen, *Mott Transition and Suppression of Orbital Fluctuations in Orthorhombic* 3*d*1 *Perovskites*, Phys. Rev. Lett. **92**, 176403 (2004).

[214] E. Pavarini, A. Yamasaki, J. Nuss, and O. K. Andersen, *How chemistry controls electron localization in 3d1 perovskites: a Wannier-function study*, New Journal of Physics **7**, 188 (2005).

[215] D. Korotin, A. V. Kozhevnikov, S. L. Skornyakov, I. Leonov, N. Binggeli, V. I. Anisimov, and G. Trimarchi, *Construction and solution of a Wannier-functions based Hamiltonian in the pseudopotential plane-wave framework for strongly correlated materials*, Eur. Phys. J. B **65**, 91 (2008).

[216] M. Karolak, *Ab-Initio study of the Metal-insulator transition in* $Ca_{2-x}Sr_xRuO_4$, Fachbereich Physik, Universität Hamburg (2009), Diplomarbeit.

[217] F. Schwabl, *Quantenmechanik für Fortgeschrittene (QM II)* (Springer Berlin Heidelberg, 2008), 5th ed.

[218] P. G. de Gennes, *Superconductivity of Metals and Alloys* (W. A. Benjamin, New York, 1966).

Acknowledgements

Many people have contributed to this thesis to whom I would like to express my gratitude, here. First, I would like to thank Prof. A. Lichtenstein for the possibility of performing exciting research in his group, for enduring support and numerous discussions. Moreover, he facilitated me to participate in many workshops, conferences and international collaborations, which lead to many decisive inspirations for this work.

I thank JP. F. Lechermann for acting as the second referee for this thesis, for many discussions on correlated electron systems and for providing me the projection module, which has been used to interface VASP with many-body approaches.

I am grateful to Prof. M. Katsnelson for acting as referee for the defense of my doctoral thesis and for initiating a large amount of the research projects presented in this thesis. His suggestions and comments contributed at various stages to the success of this work.

Many projects were done in close collaboration with Prof. A. Balatsky. I would like to thank him for hospitality, when I was visting Los Alamos National Laboratory. I am particularly thankful for numerous hours of in-depth physics discussions, stimulating large amounts of the work and teaching me a lot of condensed matter physics.

The work on NO_2 adsorbates on graphene was done in collaboration with the group of Prof. A. Geim. I would like to thank Prof. A. Geim, Dr. K. Novoselov, and Prof. I. Grigorieva for hospitality during my vistit to Manchester and various stimulating discussions on graphene physics. I am grateful to Prof. K. Scharnberg for the fruitful collaboration on impurity effects in graphene and many general discussions on impurity physics during the last years. I thank Prof. R. Berndt, Dr. J. Kröger, and Dr. N. Néel for the collaboration on the Kondo effect in $CoCu_n$ clusters and for showing us recent unpublished experimental results. In this context, I am also grateful to PD. S. Kettemann for very helpful discussions. Moreover, I would like to thank Dr. S. Gardonio and Prof. C. Carbone for providing us their photoemission data on isolated Ce atoms on different substrates and for the collaborative work on this subject. The project on the Kondo effect of Co ad-atoms on graphene was done together with Prof. A. Rosch. I am thankful to him for inviting me to Cologne and for taking a lot of time to explain Kondo physics to me. His expertise in Kondo physics and many stimulating questions were decisive for the success of this project. In this context, I am also thankful to Prof. H. Manoharan for sharing his experimental results with us. I would like to thank Prof. A. Tsvelik for the collaboration on graphene ripples and discussing details of the field theoretical model employed there. Moreover, I would like to express my thankfulness to Dr. A. Landa for inviting me to Livermore and the possibility of using the supercomputer at Lawrence Livermore National Laboratory. I am grateful to Prof. A. Rubstov, A. Antipov and I. Krivenko for hospitality while visiting Moscow State University. I thank Prof. U. Bovensiepen and Dr. A. Melnikov for the invitations to Berlin, the collaboration and the fruitful discussions on two side projects not presented, here. I am grateful to Prof. M. Crommie and

Dr. V. Brar for the collaboration on the phonon mediated tunneling into graphene and for sharing their experimental data with us.

Special thanks are dedicated to “Deutsche Forschungsgemeinschaft” for financial support within SFB 668-TP A3.

I am thankful to the 1st Institute for Theoretical Physics in Hamburg and, in particular, the entire group “th1-li” for the very good working environment and good atmosphere. First, I would like to thank H. Hafermann for interesting physics and non-physics discussions while sharing the office, on conferences or on airplanes with damaged wings as well as for lots of programming and LaTeX tips. I thank the diploma students F. Binder, M. Karolak, and B. Sachs for fruitful joint work and the further development of helpful VASP postprocessing tools. I am grateful to Dr. K. Patton for various discussions on STM theory and his introduction to different facets of the US culture including some skiing slopes in Colorado. I thank Dr. E. Gorelov, Dr. S. Brener, and C. Jung for their viewpoints on various physics questions and the former two for their introduction to basics of the Russian language.

Without my family this thesis would have never been possible. I would like to thank my parents for supporting and backing me throughout my life. Julia, thank you for always being there for me, your huge amount of patience and your love.

List of publications

[1] T. O. Wehling, A. V. Balatsky, M. I. Katsnelson, A. I. Lichtenstein, K. Scharnberg, and R. Wiesendanger, *Local electronic signatures of impurity states in graphene*, Phys. Rev. B **75**, 125425 (2007).

[2] T. O. Wehling, K. S. Novoselov, S. V. Morozov, E. E. Vdovin, M. I. Katsnelson, A. K. Geim, and A. I. Lichtenstein, *Molecular Doping of Graphene*, Nano Lett. **8**, 173 (2008).

[3] T. O. Wehling, H. P. Dahal, A. I. Lichtenstein, and A. V. Balatsky, *Local impurity effects in superconducting graphene*, Phys. Rev. B **78**, 035414 (2008).

[4] B. Amadon, F. Lechermann, A. Georges, F. Jollet, T. O. Wehling, and A. I. Lichtenstein, *Plane-wave based electronic structure calculations for correlated materials using dynamical mean-field theory and projected local orbitals*, Phys. Rev. B **77**, 205112 (2008).

[5] T. O. Wehling, I. Grigorenko, A. I. Lichtenstein, and A. V. Balatsky, *Phonon-Mediated Tunneling into Graphene*, Phys. Rev. Lett. **101**, 216803 (2008).

[6] T. O. Wehling, A. I. Lichtenstein, and M. I. Katsnelson, *First-principles studies of water adsorption on graphene: The role of the substrate*, Appl. Phys. Lett. **93**, 202110 (2008).

[7] T. O. Wehling, A. V. Balatsky, A. M. Tsvelik, M. I. Katsnelson, and A. I. Lichtenstein, *Midgap states in corrugated graphene: Ab initio calculations and effective field theory*, Europhys. Lett. **84**, 17003 (2008).

[8] A. Melnikov, I. Radu, A. Povolotskiy, T. Wehling, A. Lichtenstein, and U. Bovensiepen, *Ultrafast dynamics at lanthanide surfaces: microscopic interaction of the charge, lattice and spin subsystems*, J. Phys. D **41**, 164004 (2008).

[9] N. Néel, J. Kröger, R. Berndt, T. O. Wehling, A. I. Lichtenstein, and M. I. Katsnelson, *Controlling the Kondo Effect in $CoCu_n$ Clusters Atom by Atom*, Phys. Rev. Lett. **101**, 266803 (2008).

[10] T. O. Wehling, M. I. Katsnelson, and A. I. Lichtenstein, *Adsorbates on graphene: Impurity states and electron scattering*, Chem. Phys. Lett. **476**, 125 (2009).

[11] T. O. Wehling, M. I. Katsnelson, and A. I. Lichtenstein, *Impurities on graphene: Midgap states and migration barriers*, Phys. Rev. B **80**, 085428 (2009).

[12] E. Gorelov, T. O. Wehling, A. N. Rubtsov, M. I. Katsnelson, and A. I. Lichtenstein, *Relevance of complete Coulomb interaction matrix for the Kondo problem: Co impurity on Cu(111)*, Phys. Rev. B **80**, 155132 (2009).